Copyright
by
Peter Barry Clarke
2015

The Dissertation Committee for Peter Barry Clarke
certifies that this is the approved version of the following dissertation:

A Discrete Velocity Method for the Boltzmann Equation with Internal Energy and Stochastic Variance Reduction

Committee:

Philip Varghese, Co-Supervisor

David Goldstein, Co-Supervisor

Irene Gamba

Thierry Magin

Laxminarayan Raja

A Discrete Velocity Method for the Boltzmann Equation with Internal Energy and Stochastic Variance Reduction

by

Peter Barry Clarke, B.S.As.E.

DISSERTATION

Presented to the Faculty of the Graduate School of

The University of Texas at Austin

in Partial Fulfillment

of the Requirements

for the Degree of

DOCTOR OF PHILOSOPHY

THE UNIVERSITY OF TEXAS AT AUSTIN

December 2015

Dedicated to my parents, siblings, and Naomi

Acknowledgments

The work presented in this dissertation was only made possible through the support, guidance, and collaboration of many people including, but not limited to, the faculty here at The University of Texas at Austin, my colleagues, family, and friends.

I would like to start by thanking my advisors Dr. Philip Varghese and Dr. David Goldstein for the support they have provided throughout this research. I thank them for the many lessons they have taught me about how to be a researcher and a student. I am grateful to my PhD committee, Dr. Laxminarayan Raja, Dr. Irene Gamba, and Dr. Thierry Magin, for their interest in my research and time commitment to my education. I wish to extend a special thanks to Dr. Magin for his willingness to cross the globe for the defense of this work. Additionally, the discussions and collaborations with Dr. Gamba and Dr. Magin which have taken place both here and abroad at several conferences have always been of great benefit to me.

I must take time to recognize the most generous funding I have received in the pursuit of this work. Parts of my degree program were supported by PECOS and the NSF, but the majority of the work has been supported by the NASA Space and Technology Research Fellowship (NSTRF). The fellowship not only provided funding, but provided the opportunity to spend multiple summers at the NASA Ames Research Center as well.

I wish to acknowledge the previous work done by Dr. Aaron Morris that formed the foundation for most of this dissertation. Along with Dr. Morris's contributions, the research efforts of David Hegermiller should also be recognized for their influence on my own work. Special thanks to my peers

for listening to my questions, helping establish a strong research environment, and providing the necessary distractions which made long days seem short.

I could never have completed this work without the support and advice of my father and mother. Their love and respect of education has been an inspiration throughout my entire life. Finally, eternal thanks for the support of my girlfriend throughout the course of my graduate pursuits.

A Discrete Velocity Method for the Boltzmann Equation with Internal Energy and Stochastic Variance Reduction

Peter Barry Clarke, Ph.D.
The University of Texas at Austin, 2015

Co-Supervisors: Philip Varghese
David Goldstein

The goal of this work is to develop an accurate and efficient flow solver based upon a discrete velocity description of the Boltzmann equation. Standard particle based methods such as Direct Simulation Monte Carlo (DSMC) have a number of difficulties with complex and transient flows, stochastic noise, trace species, and high level internal energy states. To address these issues, a discrete velocity method (DVM) was developed which models the evolution of a flow through the collisions and motion of variable mass quasi-particles defined as delta functions on a truncated, discrete velocity domain.

The work is an extension of a previous method developed for a single, monatomic species solved on a uniformly spaced velocity grid. The collision integral was computed using a variance reduced stochastic model where the deviation from equilibrium was calculated and operated upon. This method produces fast, smooth solutions of near-equilibrium flows.

Improvements to the method include additional cross-section models, diffuse boundary conditions, simple realignment of velocity grid lines into non-uniform grids, the capability to handle multiple species (specifically trace

species or species with large molecular mass ratios), and both a single valued rotational energy model and a quantized rotational and vibrational model. A variance reduced form is presented for multi-species gases and gases with internal energy in order to maintain the computational benefits of the method. Every advance in the method allows for more complex flow simulations either by extending the available physics or by increasing computational efficiency. Each addition is tested and verified for an accurate implementation through homogeneous simulations where analytic solutions exist, and the efficiency and stochastic noise are inspected for many of the cases. Further simulations are run using a variety of classical one-dimensional flow problems such as normal shock waves and channel flows.

Table of Contents

Acknowledgments **v**

Abstract **vii**

List of Tables **xiii**

List of Figures **xiv**

Chapter 1. Introduction **1**
1.1 Motivation 1
1.2 Overview 5
1.3 Outline 7

Chapter 2. Literature Review **8**
2.1 Model Equation Methods 10
2.2 The Discrete Velocity Method (DVM) 11
2.3 Direct Simulation Monte Carlo (DSMC) 15
2.4 Variance Reduction in DSMC 16
2.5 Lattice Boltzmann 17
2.6 Spectral Methods 18
2.7 Internal Energy Models in a Dilute Gas 19
2.7.1 Multi-Temperature Models 20
2.7.2 State-to-state Models 20

Chapter 3. The Discrete Boltzmann Equation **23**
3.1 The Velocity Distribution Function 23
3.2 Moments and Other Properties 24
3.3 Collision Cross-Section 25
3.4 The Boltzmann Equation 27
3.5 Scaling 28
3.6 Discretization 29

3.7 Scaling and Discretizing the Macroscopic Properties 33
3.8 Time Scales 34
3.9 The Maxwellian Distribution Function 35
3.10 The Bobylev-Krook-Wu Solution 36
3.11 1D Shock Wave Theory 38
3.12 Channel Flow 40

Chapter 4. Implementation for Monatomic Gases 44
4.1 Elastic Collision Theory 46
4.1.1 Full Monte Carlo Depletion 49
4.1.2 Variance Reduction 54
4.1.3 Replenishment 59
4.1.4 Negative Value of The Velocity Distribution Function . 69
4.2 Collision Cross-Section 70
4.2.1 Hard Sphere Model 70
4.2.2 Pseudo-Maxwell Model 72
4.2.3 The Variable Hard Sphere (VHS) Model 72
4.2.4 The Variable Soft Sphere (VSS) Model 73
4.2.5 Other Cross-Section Models 74
4.3 Convection 75
4.4 Boundary Conditions 77
4.4.1 Wall Reflection BCs 77
4.4.2 Fixed Properties Boundary Condition 81
4.4.3 Zero Gradient Boundary Condition 82
4.5 Results 82
4.5.1 BKW Relaxation 82
4.5.2 Collision Cross-Section Models in a 1D Shock 86
4.5.3 Channel Flows 89
4.5.4 Expansion into a Vacuum 95
4.6 Conclusions 99

Chapter 5. Nonuniform Velocity Grids **100**
5.1 Definition of the Volume Element 102
5.2 Non-Uniform Remapping 105
5.2.1 Equal Density Remapping 106
5.2.2 Equal Momentum Remapping 108
5.2.3 Equal Energy Remapping 110
5.2.4 Selection of a Method 111
5.3 Results 112
5.4 Conclusions 118

Chapter 6. Multiple Species **119**
6.1 The Velocity Domain and Boltzmann Equation 120
6.2 Mixture Properties 122
6.3 Time stepping 124
6.4 Full Monte Carlo 125
6.5 Variance Reduction 128
6.6 Replenishment 132
6.7 Results 133
6.8 Conclusions 143

Chapter 7. The Discrete Boltzmann Equation for Gases with Internal Energy **144**
7.1 The Dunham Equation and Decoupling Rotational and Vibrational Energy 146
7.2 Nuclear Spin 150
7.3 Scaling of Internal Energy Properties and Constants 152
7.4 Internal Energy Form of The Distribution Function, Boltzmann Equation, and Collision Integral 152
7.5 Macroscopic Properties Related to Internal Energy 155
7.6 Inelastic Interactions 157
7.6.1 Relaxation Rates 158
7.6.2 Landau-Teller Relaxation 160
7.6.3 Larsen-Borgnakke Approximation 161
7.6.4 Other Models 168

Chapter 8. Implementation for Gases with Internal Energy 169
8.1 Depletion Splitting 169
8.2 Replenishment 172
8.3 Single Valued Rotational Energy 174
8.3.1 Full Monte Carlo Depletion 176
8.3.2 Variance Reduced Depletion 177
8.3.3 Rotation-Translation Energy Exchange 181
8.3.4 Replenishment Adjustments 182
8.3.5 Results 182
8.4 Quantized Internal Energy 186
8.4.1 Full Monte Carlo Depletion 187
8.4.2 Variance Reduced Model for Quantized Internal Energy 191
8.4.3 Energy Exchanges 202
8.4.4 Results 202
8.5 Conclusions 219

Chapter 9. Conclusions 220
9.1 Summary 220
9.2 Future Work 224

Appendices 227

Appendix A. Gas Properties 228

Appendix B. Evaluation of the Depletion Integral Term 230
B.1 Monatomic Full Monte Carlo 230
B.2 Diatomic Variance Reduction 232

Appendix C. Non-Uniform Remapping 236
C.1 Equal Density 236
C.2 Equal Momentum 237
C.3 Equal Energy 239

Appendix D. Larsen-Borgnakke for Quantized Rotation 241

Bibliography 245

List of Tables

2.1 Methods for solving the Boltzmann equation and modeling inelastic collisions 9

4.1 Inherited and current work for monatomic species 45
4.2 Computation time for a BKW relaxation solved with standard full Monte Carlo and variance reduced models 84
4.3 Argon, Mach 2, 1D shock conditions 87
4.4 Couette flow conditions 91

5.1 Non-uniform grid properties for a BKW relaxation 113
5.2 Argon, Mach 9, 1D shock velocity grid structure 115
5.3 Argon, Mach 9, 1D shock conditions 115
5.4 Computation time for a Mach 9 shock with uniform and non-uniform velocity grids 117

6.1 Xe-He, Mach 3.9, 1D shock conditions 134
6.2 Xe-He, Mach 3.9, velocity domain 134
6.3 C_{AB} values for Xe-He beam simulation 138

8.1 N_2, Mach 2.6, 1D shock conditions for single valued rotation . 186
8.2 Comparison of computation times for various methods for homogeneous relaxation of N_2 210
8.3 N_2, Mach 12, 1D shock conditions 212

A.1 Molecular properties 228
A.2 Characteristic temperatures 228
A.3 Spectroscopic constants and nuclear spin statistical weights . . 229
A.4 Constants for rotational and vibrational relaxation rate calculations 229

List of Figures

1.1 Local Knudsen number regions for flow models 3
1.2 Particle and discrete velocity viewpoints of a molecular gas . . 5

3.1 Collision cross-section geometry 26
3.2 Schematic showing the production of delta functions at discrete velocity locations from a continuous function 30
3.3 Continuous distribution and the corresponding discrete distribution approximation 31
3.4 1D slice of the discrete, truncated Maxwellian distribution function 36
3.5 1D slice of the discrete, truncated Bobylev-Krook-Wu distribution function 37
3.6 Stationary, 1D, normal shock schematic 38
3.7 Couette flow schematic 41
3.8 Fourier flow schematic 43

4.1 DVM flow chart 46
4.2 DVM flow chart: Collision routine 48
4.3 Example of a collision velocity selection from a cumulative distribution function 51
4.4 Example of a collision velocity selection from a cumulative distribution function with a reference vector. 52
4.5 Depletion schematic 54
4.6 Example 1D slice of original, equilibrium, and deviation velocity distribution functions 55
4.7 DVM flow chart: Replenishment routine 60
4.8 3D Coordinate system 61
4.9 Monatomic collision sphere (2D slice) 62
4.10 Remapping scheme stencil on a uniform grid 64
4.11 Collision sphere and remapping stencil for a post-collision velocity located outside the velocity domain 66

4.12 2D schematic showing use of interior points whose distance from the origin is bounded by the distance from the edge of the domain of the post-collision velocity 68
4.13 Maxwellian distribution showing boundary blow-up for a fine grid and stable boundaries for the expanded stencil scheme . . 68
4.14 Effect of a depletion from positive and negative distribution function values 69
4.15 DVM flow chart: Convection routine 76
4.16 1D spatial grid with a wall boundary 78
4.17 Specular reflection schematic and example 79
4.18 Diffuse reflection schematic and example 80
4.19 Accommodated reflection schematic and example 81
4.20 Evolution of the moments for the BKW solution for standard full Monte Carlo and variance reduced methods 83
4.21 Difference between the analytic solution to the BKW relaxation and DVM solutions for the standard FMC and variance reduced collision models 84
4.22 Evolution of entropy in comparison to the number of collisions for the standard full Monte Carlo and the variance reduced methods 85
4.23 Evolution of the 4th and 6th moments for the BKW relaxation with coarse velocity grids 86
4.24 Argon, Mach 2, 1D shock profiles for hard sphere, pseudo-Maxwell, VHS, and VSS collision models 88
4.25 Number of collisions simulated using a variance reduced method in an argon, Mach 2, 1D shock 89
4.27 Comparison of steady-state, macroscopic property profiles for a range of Knudsen numbers in a Couette flow 91
4.28 Evolution of y-velocity in a Couette flow for $Kn = 0.1$ 92
4.29 Evolution of temperature and heat-flux in a Couette flow for $Kn = 0.1$ 93
4.30 Comparison of steady-state temperature and heat flux profiles for a range of Knudsen numbers in a Fourier flow 94
4.31 Evolution of temperature and number density in a Fourier flow for $Kn = 0.1$ 95
4.32 Schematic of 1D expansion of argon into a vacuum 95
4.33 Number density profiles over time for expansion into a vacuum 97
4.34 X-velocity profile over time for expansion into a vacuum . . . 98

4.35 Force exerted on a diffuse wall due to particles expanding into a vacuum 98

5.1 Mach 9 upstream and downstream distribution functions illustrating the high resolution and large domain needed to properly visualize both regimes 101
5.2 Example of a realigned velocity grid 102
5.3 Volume elements in a non-uniform grid 104
5.4 Remapping stencil for a non-uniform velocity grid 106
5.5 Remapping scheme result with equal mass sent to each external point 108
5.6 Remapping scheme result with equal momentum sent to each external point 109
5.7 Remapping scheme result with equal energy sent to each external point 111
5.8 Relation between the closeness of external points to the origin with respect to internal points and the remapping fraction at each stencil location 112
5.9 Nonuniform velocity grid used for the grid comparison test and 4th and 6th moments of fine and coarse uniform velocity grids and a non-uniform velocity grid 114
5.10 Uniform and Non-uniform velocity grids used to simulate a Mach 9 shock 116
5.11 Argon, Mach 9, 1D shock profiles for a uniform and non-uniform velocity grid 116

6.1 2D schematic of a Maxwellian for a high molecular mass species and a low molecular mass species 121
6.2 RMS noise in a two species gas due to a range of C_{AB} values . 127
6.3 Multi-species, variance reduction schematic 130
6.4 Multi-species collision sphere (2D slice) 133
6.5 Xe-He, Mach 3.9, 1D shock profiles 135
6.6 Xe-He, Mach 3.9, 1D shock profile showing the number of simulated collisions 136
6.7 3D velocity distribution functions of helium in a helium beam simulation 139
6.8 Temperature profile of xenon due to the effects of a helium beam and the number of simulated collisions for Xe-Xe, Xe-He, and He-He collision types 141

6.9 Temperature and bulk velocity profiles for the relaxation of helium in a helium beam simulation 142

7.1 Diatomic rotation and vibration schematic 144
7.2 Rotational energy level spacing 149
7.3 Vibrational energy level spacing 150
7.4 Scaled vibrational and rotational energy distributions 154
7.5 Rotational and vibrational temperature curve fits 157

8.1 Depletion splitting schematic 170
8.2 Internal energy collision sphere (2D slice) 174
8.3 Single valued rotational energy distribution 175
8.4 Depletion for a single valued rotation model 176
8.5 Schematic decomposition of a distribution function for the variance reduced model for single valued rotation 179
8.6 0D, N_2, rotational temperature relaxation for single valued rotation 183
8.7 0D, N_2, relaxation of the velocity distribution function for single valued rotation 184
8.8 0D, N_2, relaxation of rotational distribution functions for single valued rotation 185
8.9 Normalized density and temperature profiles for a Mach 2, 1D, N_2 shock 186
8.10 Elastic depletion schematic 189
8.11 Inelastic depletion schematic 190
8.12 Decompositions of the vibrational distribution function 193
8.13 Homogeneous relaxation of rotation-only N_2 for various collision models 204
8.14 Original and normalized rotational energy distribution during rotation-only relaxation of N_2 205
8.15 Homogeneous relaxation of rotation-only N_2 for the rigid rotor and non-rigid rotor models 206
8.16 Homogeneous relaxation of vibration-only N_2 for various collision models 207
8.17 Normalized vibrational energy distribution during vibration-only relaxation of N_2 208
8.18 Homogeneous relaxation of vibration-only N_2 for the simple harmonic and anharmonic oscillators 209
8.19 Homogeneous relaxation of rotation-only N_2 210

8.20 Normalized density and temperature profiles of a cold Mach 12 N_2 shock 213
8.21 Upstream velocity and rotation distribution functions for a cold, Mach 12, N_2 shock 214
8.22 Downstream velocity and rotation distribution functions for a cold, Mach 12, N_2 shock 215
8.23 Velocity and rotation distribution functions at a mid-shock location for a cold, Mach 12, N_2 shock 215
8.24 Rotational distributions at a variety of velocity locations in a mid-shock velocity distribution function for a cold, Mach12, N_2 shock 217

D.1 Comparison of the most probable rotational level for rigid rotor and non-rigid rotor models 244

Nomenclature

λ	Mean free path
L	Characteristic length scale
Kn	Knudsen number
$f(\eta)$	Velocity distribution function
$\varphi(\eta)$	Density weighted velocity distribution function $(n \cdot f)$
η, ζ	3D velocity coordinates (x, y, z)
η', ζ'	Post-collision 3D velocity coordinates (the $'$ symbol signifies a post-collision value)
t	Time
x_i	Spatial (physical) location, $i \in (0 : N_p)$
g	Relative velocity between η and ζ
σ_T	Total collision cross-section, integrated over all scattering angles
n	Number density
T	Temperature
p	Pressure
u_i	Bulk velocity, $i \in x, y, z$
d	Molecular diameter
m	Molecular mass
m_r	Reduced mass
χ	Collision scattering angle
M	Mach number
s	Entropy
Q^k	k^{th} moment of the distribution function
$\Delta\varphi$	Depletion number density per collision
β	Velocity grid spacing
N_v	Total number of velocity grid points
$N_{x,y,z}$	Number of velocity grid points in x,y,z directions
N_p	Number of spatial points
N_s	Number of species
$nint(x)$	Function returns the nearest integer to x
$sgn(x)$	Function returns the sign of x (± 1)
θ_v	Vibrational characteristic temperature

θ_r	Rotational characteristic temperature
ν	Vibrational level number
J	Rotational level number
N_ν	Number of vibrational levels
N_J	Number of rotational levels
$\epsilon_v(\nu)$	Vibrational energy level
$\epsilon_r(J)$	Rotational energy level
$\psi_v(\nu)$	Density weighted vibrational distribution function at a single velocity location $(\varphi(\eta) \cdot f_v(\nu)$
$f_v(\nu)$	Vibrational distribution function at a single velocity location
$\psi_r(J)$	Density weighted rotational distribution function at a single velocity location $(\varphi(\eta) \cdot f_r(J)$
$f_r(J)$	Rotational distribution function at a single velocity location
q	Degeneracy
ξ_v	Vibrational degrees of freedom
ξ_r	Rotational degrees of freedom
$\hat{\varphi}_t^E$	Equilibrium density at a single velocity location
$\hat{\varphi}_t^d$	Deviation density at a single velocity location
$\hat{\varphi}_r^d$	Sum over the absolute values of the rotation deviation distribution at a single velocity location
$\hat{\varphi}_v^d$	Sum over the absolute values of the vibration deviation distribution at a single velocity location
$\hat{\varphi}_{rv}^d$	Sum over the absolute values of the vibration deviation distribution at a single velocity location
n_{rv}^d	Total absolute deviation in rotational and vibration at a single spatial location

Chapter 1

Introduction

1.1 Motivation

The motivation for this work is to develop an accurate and efficient flow solver based upon a discrete velocity model of the governing kinetic equations. According to kinetic theory, at the microscopic level the state of a system is defined by the motion of molecules and their interactions through collisions, and the nature of these interactions is determined by the intermolecular potentials of colliding molecules. Exchanges of mass (in chemical reactions), momentum, and translational and sometimes internal energy may occur between molecules during collisions, and the motion of molecules between collision events serves to diffuse information throughout the flow domain.

The thermal non-equilibrium flow regime is characterized by the mean free path, λ, being the same order or greater than the characteristic length scale for macroscopic gradients, L. Defining the Knudsen number as the ratio between λ and L, a generally accepted condition for thermal non-equilibrium in a gas flow is:

$$Kn = \frac{\lambda}{L} \geq O(0.01) \tag{1.1}$$

Under the condition in equation 1.1, the flow is considered rarefied and certain assumptions can be made. One assumption is that the gas is made up of point-like structureless molecules and they interact through short range,

two-body potentials. Furthermore, according to the molecular chaos hypothesis, called the Stosszahlansatz in the writings of Boltzmann, the velocities of molecules before colliding are uncorrelated and independent of position but highly correlated after a collision due to conservation of mass, momentum, and energy [1]. A result of this assumption is that interactions between molecules in a dilute gas can be approximated by binary collisions alone, and the mean time between collisions is much greater than the duration of a collision.

The Navier-Stokes (continuum) equations fail to accurately represent a flow when equation 1.1 is satisfied, and different governing equations which remove the continuum constraint and model the gas on a microscopic level are needed. The Boltzmann equation describes the statistical behavior of a gas in thermal non-equilibrium by modeling the individual interactions between molecules during collisions, and the equation is usually used when the Navier-Stokes equations fail. In fact, the Boltzmann equation could be used across the entire range of Knudsen numbers seen in Figure 1.1, but because molecular interactions are tracked, finding a solution to the Boltzmann equation is inherently less efficient than for continuum equations. However, conditions of thermal non-equilibrium which require solutions to the Boltzmann equation may occur in micro- and nano-scale devices, shocks, satellite attitude control thruster plumes, around satellites in low-earth orbit, and during hypersonic re-entry. These flows can be very complex and might include changes to internal energy states, radiation, unsteadiness, gas chemistry, phase change, and intricate geometries.

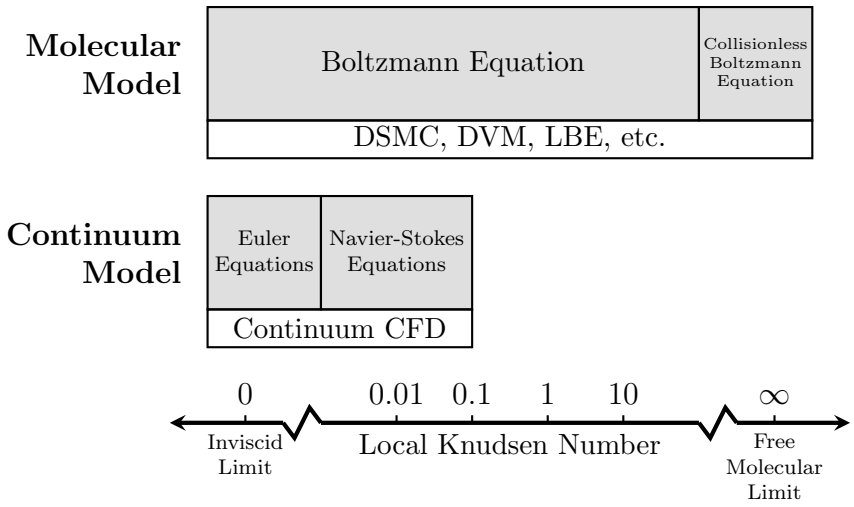

Figure 1.1: Local Knudsen number regions for continuum and molecular flow equations. Corresponding computation models are shown underneath.

The traditional standard for solving the Boltzmann equation for rarefied gas flows is the Direct Simulation Monte Carlo method (DSMC) [2]. However, there are several issues with the technique. DSMC can be costly for a variety of conditions including near-continuum, low-speed, and unsteady flows, it suffers from statistical fluctuations, and the potentially costly process of ensemble averaging may be necessary to produce a smooth solution, especially for unsteady flows. This leads to a related issue: DSMC coupled with other flow solvers feeds fluctuations across the solver boundaries. The fluctuations may degrade the accuracy of computations by causing numerical instabilities, and may make it difficult to provide accurate instantaneous flow properties, especially for transient problems. The DSMC method also encounters difficulties when investigating problems where a relatively minor constituent has significant effects on flow physics. For example, species with low mole fractions may have major chemistry implications, high vibrational energy levels can be important even at low temperatures when the density fractions are small, and small concentrations of charged particles can be very

important to ionization. Weighting schemes and other methods have been used to mitigate some of these issues but the implementation can be messy and difficult. Finally, DSMC suffers from a dependence on phenomenological models and empirical fits to available data.

Because of the problems associated with DSMC, the development of an efficient, low noise, rarefied gas solver could be beneficial to the scientific and engineering community. This work outlines a discrete velocity method, called DVM, that has been developed for flows requiring a solution to the Boltzmann equation. DVM models the evolution of a flow through collisions and motion of fixed velocity, variable mass quasi-particles (Figure 1.2b) as opposed to the fixed mass, variable velocity molecules (Figure 1.2a) of traditional particle based methods like DSMC. The quasi-particles are defined on set velocity locations in phase space and the weight of a quasi-particle represents the number density of a species of a particular velocity class. This representation has no restriction on particle weight and the mass of particles of a certain velocity class may take on any value within the precision of the computer being used.

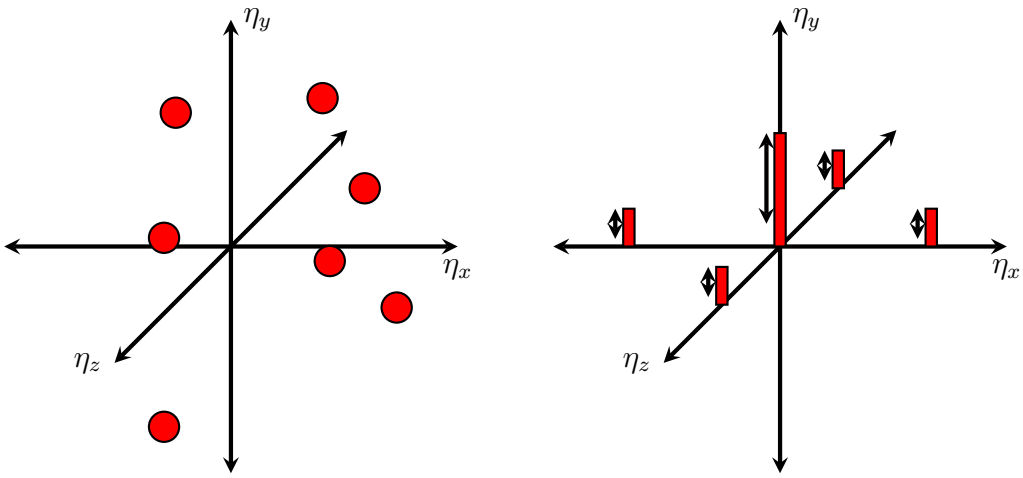

Figure 1.2: The (a) Lagrangian particle viewpoint of a molecular gas with fixed mass, variable velocity particles vs the (b) discrete velocity viewpoint with fixed velocity quasi-particles.

In a similar manner to DSMC, a stochastic (Monte Carlo based) method is used to compute the effect of molecular collision. The method used is based on a relatively new method for DSMC called full Monte Carlo with variance reduction [3, 4]. Variance reduction both decreases computation time and greatly decreases statistical noise as the distribution being modeled approaches equilibrium.

1.2 Overview

The scope of this work is limited to an extension of DVM in several key areas important to the future growth of the method and related code. The method inherited from A. Morris's Masters thesis work [5] was limited to a single, monatomic species interacting as pseudo-Maxwell molecules with no external forces, and the velocity domain was restricted to uniformly spaced grids in every coordinate direction. The collision integral was solved by a

variance reduction model [6], and post-collision molecules where mapped back onto the grid using a mass, momentum, and energy conservative scheme [7].

Since the start of the current work, the method has been extended and improved in a multitude of ways. Alongside a variety of minor changes to improve computational performance, major extensions to the DVM approach were made in the following areas:

- The variable hard sphere (VHS) model and variable soft sphere (VSS) model were implemented as approximations for the collision cross-section of molecules.
- A variety of new boundary conditions were added including diffuse and accommodated wall reflection.
- Using simple realignment of grid lines, non-uniform velocity grids were implemented with the intention of focusing computational effort in a more efficient manner.
- Inelastic collisions with a simple Landau-Teller-like model to approximate energy transfers between translational and rotational modes where added to allow for polyatomic molecules.
- The method was extended to include gas mixtures. A major focus of this work was on mixtures with large number density or molecular mass ratios.
- The final improvement to the discrete velocity method was the implementation of a quantized internal energy model where full rotational and vibrational distributions are stored and updated during elastic and inelastic collisions.

A variance reduced model was formulated for each major contribution, and the method was validated with a range of 0D and 1D steady and unsteady flows. Results were compared to analytic, numerical, Direct Simulation Monte Carlo, and previously verified DVM solutions.

1.3 Outline

The general outline of this work is to first overview the relevant kinetic theory on a topic and then describe the methodology of various related improvements that opened the door to new capabilities in the DVM approach. At the end of each individual methods section, results are shown illustrating the improvement discussed, and simple examples are used in order to highlight important benefits and/or limitations to the method. Before moving into the present DVM theory and method, Chapter 2 will briefly overview the history of discrete velocity methods and make comparisons to a variety of other techniques used to solve rarefied gas flow problems. The Boltzmann equation and its properties are discussed in Chapter 3 along with the scaling used in DVM and the method of discretization. Chapter 4 goes over the methodology for treating a single, monatomic species. Most of Chapter 4 is a review of the work inherited at the start of the current research. Chapter 5 introduces an extension of the velocity grid discretization from uniform Cartesian grids to non-uniform Cartesian grids. Chapter 6 introduces multiple species into the method. Chapter 7 outlines the theory behind the simulation of diatomic molecules in a rarefied gas flow and describes the form of the Boltzmann equation when internal energy is included. Chapter 8 describes different DVM methods to solving the Boltzmann equation with diatomic molecules. Finally, Chapter 9 summarizes the work and discusses future research needed to expand the DVM approach.

Chapter 2

Literature Review

This chapter describes work related to numerical solutions of the Boltzmann equation, the discrete velocity method, and models for vibrational and rotational energy. A variety of methods for solving the Boltzmann equation are described including: model equations, discrete velocity methods (DVM), Direct Simulation Monte Carlo (DSMC), the Lattice Boltzmann Equation (LBE), and various spectral methods. The benefits and limitations of each method are highlighted throughout the discussion. The final section briefly highlights several methods for approximating the effects of inelastic collisions using multi-temperature models or state-to-state models.

Table 2.1: Methods for solving the Boltzmann equation and modeling inelastic collisions

Solution Method	**Related Work**
Model Equations	• Grad • BGK • Other
Discrete Velocity Method	• Original work • University of Texas (DVM) • Discrete ordinance method (DOM)
Direct Simulation Monte Carlo	• Bird's DSMC • Other DSMC • Variance reduced model
Lattice Boltzmann Equation	• Lattice gas cellular automata (LGCA) • Lattice Boltzmann equation (LBE)
Spectral Methods	• Initial spectral methods • Spectral-Lagrangian method

Internal Energy Model	**Related Work**
Multi-Temperature Models	• Two-temperature
State-to-state Models	• Pseudo-species • Forced Harmonic Oscillator (FHO) • Anderson's model (Energy Gap) • Larsen-Borgnakke • Rovibrational models

2.1 Model Equation Methods

One of the primary difficulties in solving the Boltzmann equation is finding an accurate approximation to the nonlinear collision integral. The first work on solving this problem consisted of approximating the distribution function by a series of polynomials [8, 9] and later the collision integral by a model equation [10–12]. These equations allow for complex solutions because they are simpler to solve than the original collision integral, but they suffer under the limits and approximations of the model used.

Probably the most famous model was presented by Bhatnagar, Gross, and Krook [10]. Called the BGK method, it assumes a linearized approximation of the collision integral where the difference between local and equilibrium (Maxwellian) distributions determines the change in the velocity distribution function due to collisions. The rate of relaxation for the method is proportional to the collision time, τ. The collision integral is modified into a simple relation, and the method can provide integral equations for macroscopic variables in some cases [13]. It is best applied to cases of weak non-equilibrium [14]. However, the parameter τ has a somewhat arbitrary definition in the BGK method, while in reality it should be a complicated functional of the distribution function [15]. As a result, the correct relaxation rate is not guaranteed, and for flows with strong dependence on the relaxation rate, such as strong shocks [16], the BGK method will calculate inaccurate flow structures. The model also fails to produce the correct Prandtl number, and an adjustment to the method called ES-BGK (ellipsoidal statistical model) is commonly used which addresses the issue [17]. Further discussion of weak non-equilibrium and the BGK operator can be found in Chapman & Cowling [14]. Despite their inaccuracies, the BGK and ES-BGK operator and other model equations are used in a significant number of rarefied gas solvers due to their low cost, simple implementation, and generally acceptable accuracy for specific flow problems.

2.2 The Discrete Velocity Method (DVM)

Motivated by the inaccuracies of model equation methods in highly non-equilibrium flows, deterministic methods for the full Boltzmann equation were developed. Discrete velocity methods are computational schemes where the velocity domain is discretized into a finite set of grid points, and particles are limited to velocity values that lie on the grid. The collision integral is then solved using one of several methods including direct integration or stochastic analysis. Such methods have been used in a wide range of work to solve a variety of problems, especially within the rarefied gas regime, but the following literature review focuses on those methods which are important to the field or which directly influenced the current work.

Restricting velocities to a finite set was first proposed by Krook [18] in 1955 in relation to work on approximations for radiative transfer problems, and Gross mentioned the problem again in 1960 [19]. However, the idea was first implemented by Broadwell for low Mach number Couette and Rayleigh flows in 1964 [20], and Broadwell later extended the method to calculating high Mach number shock structures [21]. The original method limited velocity space to 6 or 8 velocities and gains and losses were directly calculated through analysis of all possible collision results.

The Hicks-Yen-Nordsieck (HYN) method [22, 23] used a discrete velocity grid and approximated the collision integral with a Monte Carlo method in 1966. The HYN method allowed mixed continuum and rarefied flow problems to be solved more easily [24], and allowed for implicit time schemes which provide faster convergence and larger time steps (advantages can be seen in other methods of the same type as HYN [25, 26]). However, the method did not directly enforce conservation of mass, momentum, or energy because the collision integral was approximated. A correction scheme was used to enforce conservation, but the corrections limited the accuracy of the solutions.

Integer DSMC

Expanding on the work of Broadwell [20, 21], Goldstein [27] developed a discrete velocity particle method where every particle has an integer velocity both before and after a collision. The basic method was very similar to Direct Simulation Monte Carlo (DSMC), but with significant memory savings due to possible molecular velocities being restricted to a discrete set of values. Post-collision velocities were determined by rotating the relative velocity of colliding particles to another set of allowed grid points. Available post-collision grid points could be pre-tabulated in a look-up table, but as simulations became more complex, the tables became large. This was especially true for flows with internal energy where the relative velocity vector could be adjusted in length (e.g. flows with inelastic collisions). However, successful results were shown for N_2 & O_2 mixture using a variable hard sphere collision model.

DVM at the University of Texas at Austin

At the same time as Goldstein, Tan and Varghese [28] outlined a discrete velocity method which truncated the velocity domain where the value of the distribution function fell below a prescribed threshold. Removing very small values of the distribution increased the efficiency by reducing the required number of stored velocity locations. The collision integral was solved directly, and in a similar manner to Goldstein [29], post collision velocities are restricted to the set of discrete velocity nodes which conserve mass, momentum, and kinetic energy. The method showed favorable results for high Mach number flows and high efficiency for unsteady problems when compared to DSMC, but was less efficient than DSMC based methods for steady state problems. Expanding on his work with Tan, Varghese [30] later addressed the issue of post-collision velocities being restricted to grid nodes. The work presented a scheme for projecting off-grid post-collision velocities back onto grid

nodes while conserving mass, momentum, and energy. The scheme removed the need for tabulating possible post-collision velocities and reduced statistical error for coarser velocity grids.

Further progressing the work of Goldstein, Tan, and Varghese, Morris developed a discrete velocity method in his Master's work at The University of Texas at Austin [5, 31]. Along with implementing Varghese's remapping method [7], Morris approximated the collision integral through a partially stochastic method where each velocity node is collided with a random sampling of other nodes. A variance reduction technique described by Baker and Hadjiconstantinou [3] was also implemented which allowed for low noise, low cost solutions to a variety of homogeneous and 1D shock simulations [6]. The current work described in this proposal is an expansion of the method developed by Morris, and a more in-depth discussion of the scheme will be presented in the following sections.

Some of the code structure and methodology used in the current work is based on the Master's work of Hegermiller done at The University of Texas at Austin [32]. Hegermiller attempted to create a discrete velocity method for a simple diatomic gas with rotational energy. A single value of rotational energy representative of the average energy was stored at each velocity location and a Landau-Teller-like method was used to calculate changes in energy due to inelastic collisions. Simulations were run for homogeneous relaxations and low Mach number 1D shocks. The results showed the correct macroscopic equilibrium values but incorrect relaxation rates. The rates were incorrect due to errors in the definition of rotational energy in a collision and the incorrect implementation of Z_r, the rotational relaxation rate. A method was used where every collision was inelastic and $1/Z_r$ of the rotational energy change in a collision was applied. While this method does produce a relaxation to the correct equilibrium value, it has been shown to violate detailed balance

[33]. A second problem with the method was that solutions to the 1D shock problem would sometimes become unstable due to velocity locations having positive rotational energy but no mass or negative mass. This was caused by two separate factors. The remapping scheme used for post-collision velocities allowed reductions in mass combined with increases in energy, and the method used for approximating collisions between equilibrium distributions in variance reduced calculations created large regions of negative or zero valued mass. Despite these problems, the framework developed by Hegermiller provided a foundation for the internal energy schemes discussed in Chapter 8.

DVM at other Institutions

A similar numerical scheme to our discrete velocity method was developed independently by Tcheremissine [34] called the discrete-ordinate method (DOM). In the original work [35], post-collision velocities were projected onto the grid using a method dependent on both colliding particles instead of just one particle as in the work of Varghese [30]. The projection method restricted the scheme to uniform grids and small mass ratio mixtures since each species had to reside on the same velocity grid. Extensions to the work by Aristov and Tcheremissine showed that complex molecular potentials such as the Lennard-Jones potential could be used in discrete velocity methods without a significant increase in computation time [36]. Favorable results using the scheme were shown for both high speed [37] and low speed [38] flows. The need for uniform grids was relaxed by Kolobov [39] by using a correction factor but at the cost of exact conservation. The correction factor included accounting for an inverse collision originating from the closest node to the post-collision velocity locations.

Moderate to large mass ratios were used by Dodulad and Tcheremissine [40] during investigations into various projection methods for remapping post-

collision velocities. The projection methods, an extension of the work by Varghese [30] and Morris [31], allowed separate grid spacing for individual species.

Tcheremissine later showed solutions to the Boltzmann equation for polyatomic gases using the DOM he developed [41]. The work explored several different models for rotational energy exchange which reduced the number of rotational energy levels or approximated rotation as a two level model where $\epsilon_2 > kT_{max}$. A more extensive look at various discrete velocity models can be found in Aristov's book [42].

2.3 Direct Simulation Monte Carlo (DSMC)

At the same time as the first deterministic methods were proposed, stochastic particle-based methods were introduced to address initial limits to computational power. In the 1960's, G. Bird developed the Direct Simulation Monte Carlo (DSMC) method to model gas flows at the microscopic level [2]. The molecules in the flow are modeled directly by seeding the domain with a number of simulated molecules, each one representing a pre-determined number of real molecules. Interactions between molecules are described through probabilistic models and molecule movements through physical space are simulated realistically. The DSMC method can be used to simulate flows in any flow regime from continuum to free-molecular but is generally used for transitional and rarefied flow fields due to the high computational cost in the continuum regime [2]. Separate Monte Carlo based methods were introduced by Nanbu and Babovsky [43,44] where the collision process was derived directly from the Boltzmann equation, but the primary simulation method within the rarefied gas flow community remains Bird's DSMC.

DSMC is a mature method with a wide range of physics and flow con-

ditions available [2, 45], but there are several issues inherent to the method which may limit its application. Instantaneous flow properties are subject to statistical fluctuations, and in conditions where molecules with a low mole ratio are disproportionately important to quantities of interest this can wash out important flow features. DSMC can also be expensive for near-continuum, low-speed, and unsteady flows due to the large number of simulated molecules needed for an accurate representation of the flow [2], and statistical fluctuations can make hybrid continuum solvers difficult to implement [46]. Despite the difficulties for certain conditions, the method has been shown to be robust and accurate [47], and it can be applied to multi-dimensional rarefied flows due to relatively recent improvements in computational resources [47, 48]. A complete description of the DSMC method used in this work can be found in Bird's work [2, 45].

2.4 Variance Reduction in DSMC

An important inspiration to the work described is the development of a variance reduced form of DSMC. Traditional DSMC has difficulty simulating flows where the noise in the flow is of a greater magnitude than the changes in the properties of the flow. Examples include near continuum, low Mach number, and small-scale heat transfer flows. However, many of these flows have a significant portion of the gas close to equilibrium and these portions can be rapidly evaluated with a variance reduced method. The concept, originally postulated by Baker [3], is based on the near-equilibrium nature of most flows. As the flow approaches equilibrium the deviations from equilibrium become very small, and it was shown that operating on the deviation from equilibrium instead of the entire velocity distribution function can result in significant computational savings and reduction of statistical noise by Hadjiconstantinou, Baker, and Homolle [3, 4].

Radtke *et al* [49] split variance reduced methods into two primary groups: deviational methods and weight based methods. Weight based methods assign weights to individual particles reflecting the deviation from equilibrium in a gas, but require particle splitting and recombination steps [50, 51]. Deviational methods simulate only the deviational part of a gas distribution function with single weight particles [3, 4].

The variance reduced DSMC method has also been extended to the BGK collision model, and a more thorough analysis of using global vs. local equilibrium was conducted [52]. Present work on variance reduced DSMC has generally been limited to simulations of the linear term (particles drawn from the equilibrium colliding with particles drawn from the deviation), and the nonlinear term (both colliding particles drawn from the deviation) has only recently been extended to include mass conservation [49].

2.5 Lattice Boltzmann

A relatively recent addition to the discrete velocity family of methods is the Lattice Boltzmann method (LBE). The method started as an extension to lattice gas cellular automata (LGCA), first presented by Frisch, Hasslacher, and Pomeau in 1986 [53]. The method describes a gas on a lattice grid where particles have a fixed mass and can move on the lattice to any connecting point based on their velocity vector but could not move shorter or longer than a connecting point on the lattice. Because of the on/off nature of particles, Boolean operators could be used to describe particles. The method had several significant problems including high statistical noise, impracticality for multi-dimension flows, a high viscosity barrier, and low Reynolds numbers [54].

The Lattice Boltzmann method was first developed by McNamara and Zanetti in 1988 [55] in response to the problem of high statistical noise in

LGCA. The method expanded LGCA from the Boolean description to a value representing the ensemble average of the density distribution function. The multi-dimension problem was solved by describing the collision by the difference between the distribution and the equilibrium distribution [55–57]. LBE finally became fully independent from LGCA by removing the dependence of collisions on the LGCA Boolean microdynamics [58]. The current state of the LBE method uses the BGK operator to determine the results of collisions between distribution functions. An extensive discussion on the LBE method can be found in Succi [54].

The Lattice Boltzmann method is promising for multiphase or multicomponent flows, high Knudsen number flows such as those found in microfluidics, and a variety of other complex flow conditions. However the method suffers the limitations imposed by the BGK operator, has difficulties with high Mach number flows, and must be coupled with a thermal specific solution to enable heat transfer [54].

2.6 Spectral Methods

Discrete velocity grids have been used in conjunction with a variety of spectral methods for solving the Boltzmann equation as well. These methods transform the collision operator into phase-space and use a finite difference, finite volume, or discontinuous Galerkin method to solve the convection operator. The first deterministic spectral methods for the Boltzmann equation came from the work of Bobylev [59, 60]. He showed the Fourier transformed Boltzmann equation takes a closed form for Maxwell molecules whose angular cross-sections were integrable, and numerical methods based on Bobylev's work were first implemented by Pareschi and Perthame [61]. The method was further extended by Bobylev, who used Maxwell molecules and hard spheres to derive a weighted convolution structure for the collision in-

tegral [62]. However, initial work did not allow for the exact conservation of mass, momentum, and energy [63] and could not be extended to arbitrary cross-section models [62, 63]. In response, Gamba and Tharkabhushanam proposed a spectral-Lagrangian method [64] to address the issue of conservation and Haack and Gamba later extended the method to include angular dependent cross-sections [65]. Spectral methods have also been used by Heintz [66] and Alekseenko and Josyula [67] to solve space-homogeneous problems. The spectral-Lagrangian method has even more recently been extended to multiple species and gases with discrete internal energies in the work of Munafo [68]. Deterministic methods have an advantage over stochastic methods that the solutions are not affected by noise. However, deterministic methods have significant difficulty with the high dimensionality of the problem, and computations are generally solved in $O(N^{2d})$, except for some special cases such as hard spheres in 3D which can be solved quicker [69].

2.7 Internal Energy Models in a Dilute Gas

When describing many flows it is sometimes necessary to include internal energy states such as rotation and vibration, and one of the first extensions of the Boltzmann equation to include internal energy was by Wang Chang and Uhlenbeck in 1951 [70]. The WCU equation defines the collision kernel of the Boltzmann equation using cross sections defined for every possible change in energy level and satisfies micro-reversibility. A rather informative review of the WCU equation can be found in Dellacherie [71]. A similar form of the Boltzmann equation was independently derived for quantum mechanics by Waldmann [72] and Snider [73]. The main difficulty in solving either the WCU or Waldmann-Snider equation is accurately describing the process for exchanges of energy between energy modes. The methods used can be classified under two headings: multi-temperature models where kinetic, rotational,

and vibrational energy and temperature components undergo direct relaxation or state-to-state models where individual energy level populations are tracked.

2.7.1 Multi-Temperature Models

Starting from the work of Appleton and Bray [74], much of the initial work on simulating internal energy involved assuming Boltzmann distributions for rotational and vibrational energy and representing each mode by an individual temperature such as in the work of Park [75–77]. This method is typically referred to as the two- or multi-temperature model. Mass, momentum, and energy conservation were supplemented with equations for conservation of internal energy components when a gas is in non-equilibrium. The additional conservation equations had energy transfer source terms associated with the production/destruction of internal energy due to collisions [77–80]. Energy exchanges between modes were typically represented by models based on Landau-Teller's theory [77, 79, 81]. Formulation of energy transfer terms accounted only for mono-quantum transitions [77, 82]. However, the assumption fails immediately behind a shock for example [77], since collisions in these conditions are energetic enough for multi-quantum jumps [82]. Further limits are discussed by Park [76].

Extensive improvements and tunings were made to multi-temperature models to account for the effects of dissociation, but since such considerations are outside the scope of this work, they will be left unreviewed. A more complete review of multi-temperature models can be found in Losev [83].

2.7.2 State-to-state Models

State-to-state models were proposed in response to the deficiencies and limitations of multi-temperature models [82, 84]. The fundamental difference between the two models is each internal energy level of a polyatomic

species is treated as a separate pseudo-species. This framework allows for non-equilibrium energy distributions to be considered, providing more accurate results, but calculations were more expensive since each level needs to be tracked during a simulation. Moreover, for high accuracy cross-sections and relaxation rates, complex quantum chemistry calculations need to be performed. Several approximate models have been proposed to avoid the lengthy calculation of exact potentials.

One such approximation is the forced harmonic oscillator (FHO) model. Based on the work of Kerner and Treanor [85,86], the model calculates collision probabilities for a harmonic oscillator acted upon by an external exponential force. The approximation has been used by Adamovich [87] for V-T, V-V, and V-V-T rate coefficients in N_2 and O_2 mixtures. Adamovich later extended the work to R-T and V-R-T interactions [88], and Boyd and Josyula showed the application of a high fidelity FHO model [89].

Anderson developed a state-to-state model based on the gap in energy between colliding particles and micro-reversibility [90]. Originally formulated for electronic energy, the model has been applied to quantized vibrational energy as well. For example, an adjusted version of the Anderson model has been shown by Josyula and Boyd in a discrete velocity framework [91].

Arguably, the most common approximation used in DSMC is the Larsen-Borgnakke model [92]. Developed as a phenomenological model to match available data for relaxation rates, the model is a simple superimposition of internal-translational energy exchange on top of an otherwise monatomic collision model [33]. The energy exchanges between modes ensure detailed balance by selection of post-collision energy levels from assumed equilibrium distributions of translational and internal energy, and inelastic collision rates are met by considering a fraction of all collisions as inelastic and the remaining collisions as elastic. The approach admits to being unrealistic from a physical

standpoint, but macroscopic properties can be properly modeled [2]. The model was originally applied to continuous rotation and vibration distributions [2], but more recent work by Koura [93], Boyd [94], and Bergemann [95] has shown applications to quantized rotation and vibration.

Despite the allure of approximate models, accurate state-to-state models have also been used for many calculations where collision cross-section data is available. For example, direct state-to-state computations for rotational levels in para-Hydrogen has been shown in DSMC by Willauer and Varghese [96], and results showed features of rotational energy level relaxations that approximate models failed to resolve. The advent of improved computational power has allowed recent work to give attention to rovibrational descriptions of internal energy as well. The models attempt to describe every coupled rotational and vibrational energy level in order to achieve correct rates of excitation and de-excitation due to molecular interactions. Examples include work at NASA Ames for N_2 [97–99] and the work of Esposito et al. [100] and Kim et al. [101] for H_2. These methods depend on accurate calculations of cross-section data that are currently severely limited to only a couple reactions such as $N_2 - N$ and H_2. However, work is currently being done to expand the database of state-to-state models.

Chapter 3

The Discrete Boltzmann Equation

The following chapter gives an introductory description of the velocity distribution function and its moments and properties. The scaling method used in this work is then described, followed by the discretization process. Next the scaled, discrete Boltzmann equation is presented. Finally, the Maxwellian equilibrium distribution and the the Bobylev-Krook-Wu distribution are presented as analytic solutions to the collision integral, and a set of 1D flow problems are discussed including normal shock waves and channel flow.

3.1 The Velocity Distribution Function

The velocity distribution function, $f(\vec{\eta})$, describes the statistical probability any molecule has of moving at any particular velocity, $\vec{\eta} = (\eta_x, \eta_y, \eta_z)$. This reflects the concept that molecules move in a chaotic nature at different speeds in different directions [1]. Accounting for the total number density, n, a density weighted velocity distribution function can be defined as:

$$\varphi(\vec{\eta}) = n \cdot f(\vec{\eta}) \tag{3.1}$$

For the sake of neatness, any further references to velocity will drop the over-arrow, and velocities are understood to be vectors representing three velocity components, $\eta = \vec{\eta} = (\eta_x, \eta_y, \eta_z)$.

3.2 Moments and Other Properties

Macroscopic quantities of interest can be calculated directly through integration of the distribution function, where dV_η is the volume element in velocity space. Defining a peculiar velocity as:

$$C_i = \eta_i - u_i \tag{3.2}$$

$$\text{And } C_i^2 = \sum_{i=x,y,z} (\eta_i - u_i)^2 \tag{3.3}$$

Number density (n), bulk velocity (u_i), temperature (T), heat flux (q_j), and viscous stress tensor (τ_{ij}) can all be directly related to the moments of the distribution function [1]:

$$n = \int_\eta \varphi(\eta) dV_\eta \tag{3.4a}$$

$$u_i = \frac{1}{n} \int_\eta \eta_i \varphi(\eta) dV_\eta \tag{3.4b}$$

$$T = \frac{2}{3k_b} \left(\frac{1}{2} m \overline{C_i^2} \right) = \frac{m}{3k_b n} \int_\eta C_i^2 \varphi(\eta) dV_\eta \tag{3.4c}$$

$$q_j = \frac{m}{2n} \int_\eta C_j C_i^2 \varphi(\eta) dV_\eta \tag{3.4d}$$

$$\tau_{ij} = -m \int_\eta C_i C_j \varphi(\eta) dV_\eta + p\delta_{ij} \tag{3.4e}$$

And pressure (p) can be directly related to number density and temperature with the ideal gas law as:

$$p = nk_bT = \frac{m}{3}\int_{\eta} C_i^2 \varphi(\eta) dV_\eta \tag{3.5}$$

Entropy (s) is a more complex term calculated as a function of the natural log of the velocity distribution as:

$$s = k_b N - k_b V \int_{\eta} \varphi(\eta) \ln\left(\frac{h^3}{m^3}\varphi(\hat{\eta})\right) dV_\eta \tag{3.6}$$

h is Planck's constant and N is the number of molecules in volume V for equation 3.6. A more in depth look at entropy can be found in [1]. Higher order moments may also be of interest, and the kth moment of the distribution, Q^k, can be written in a general form as:

$$Q^k = \frac{1}{n}\int_{\eta} |\eta_i - u_i|^k \varphi(\eta) dV_\eta \tag{3.7}$$

3.3 Collision Cross-Section

The likelihood of a scattering event is dependent on an effective area about the center of a particle called the collision cross-section, σ [1]. There are many potentials used to approximate collision interactions since complete information on the collision cross section is only readily available for a select few molecular interactions. Approximations include attraction/repulsion models such as the well known Lennard-Jones model [102], and inverse power-law based models such as hard spheres, variable hard spheres [103], and variable soft spheres [93,104]. In order to formulate a general description of σ we define the impact parameter, b, as the projected distance of closest approach, d as the distance between hard sphere molecular centers at the point of impact, χ as the scattering angle, and ϵ as the out-of-plane angle (not shown in Figure

3.1). b, d, and χ are related through equation 3.8, and using the geometry displayed, a differential cross section, $\frac{\partial\sigma}{\partial\Omega}$, is formulated for the solid angle $d\Omega$.

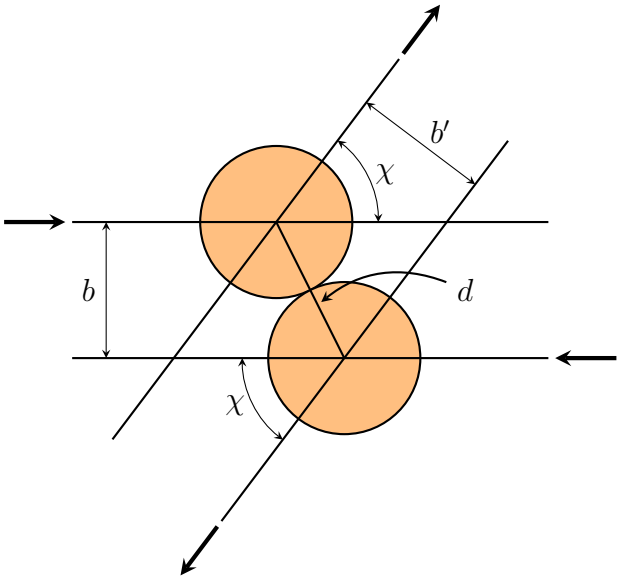

$$\chi = 2\cos^{-1}\left(\frac{b}{d}\right) \tag{3.8}$$

$$\frac{\partial\sigma}{\partial\Omega}d\Omega = bdbd\epsilon \tag{3.9}$$

Figure 3.1: Collision cross-section geometry

Where:

$$d\Omega = \sin\chi d\chi d\epsilon \tag{3.10}$$

So that:

$$\frac{\partial\sigma}{\partial\Omega} = \frac{b}{\sin\chi}\left|\frac{db}{d\chi}\right| \tag{3.11}$$

Integration of $\frac{\partial\sigma}{\partial\Omega}d\Omega$ over all possible scattering solid angles gives the total collision cross section, an easily calculable quantity for collision models with isotropic scattering.

$$\sigma_T = \int_0^{4\pi}\frac{\partial\sigma}{\partial\Omega}d\Omega = 2\pi\int_0^{\pi}\frac{\partial\sigma}{\partial\Omega}\sin(\chi)d\chi = 4\pi\cdot\frac{\partial\sigma}{\partial\Omega} \tag{3.12}$$

The mean collision rate, i.e. the average number of collisions per unit time, is obtained from the average value of the product of the cross-section and the relative velocity, g, as:

$$\nu = n\overline{\sigma_T g} \tag{3.13}$$

Further discussion of the cross section and collision rate can be found in Section 4.2, and a more complete analysis can be found in Vincenti and Kruger [1].

3.4 The Boltzmann Equation

First described by Ludwig Boltzmann in 1872 [105], the Boltzmann equation describes the behavior of molecules in a thermodynamic system not in thermodynamic equilibrium. Shown in the preferred form for this work by equation 3.14, the left-hand side contains differential terms describing molecular convection, and the right-hand side is an integration over distribution functions describing the results of molecular collisions.

$$\underbrace{\frac{\partial \varphi(\eta)}{\partial t}}_{\substack{\text{time} \\ \text{rate of} \\ \text{change}}} + \underbrace{\eta \frac{\partial \varphi(\eta)}{\partial x_i}}_{\substack{\text{convection} \\ \text{term}}} = \underbrace{\iiint_{\zeta} \int_{\Omega} [\varphi(\eta')\varphi(\zeta') - \varphi(\eta)\varphi(\zeta)] g \frac{\partial \sigma}{\partial \Omega} d\Omega \, dV_\zeta}_{\text{collision term}} \tag{3.14}$$

The effects of a body force term, $\vec{F}\frac{\partial \varphi(\eta)}{\partial \eta}$, typically located on the left hand side of the equation, are ignored because they are outside the scope of this work, and the differential cross section is replaced with a total cross section, σ_T, in subsequent presentations of the Boltzmann equation. Further information and analysis can be found in Vincenti & Kruger [1].

3.5 Scaling

Working with scaled variables can be convenient in many circumstances. The characteristic thermal speed is the most probable speed for a gas in equilibrium at a reference temperature, T_{ref}, with a reference molecular mass, m_{ref}, and is used to scale all relevant velocities. In this work, the value is defined as:

$$\eta_{ref} = \sqrt{\frac{2k_bT_{ref}}{m_{ref}}}. \tag{3.15}$$

A reference molecular diameter, d_{ref}, and a reference number density, n_{ref}, may also be set, and reference values can be calculated for stress, heat flux, and collision cross-section using the previously defined variables and the Boltzmann constant, k_b.

$$\tau_{ref} = 2n_{ref}k_bT_{ref}; \quad q_{ref} = \frac{m_{ref}}{n_{ref}}\eta_{ref}^3; \quad \sigma_{ref} = \pi d_{ref}^2 \tag{3.16}$$

All relevant variables in the Boltzmann equation can now be scaled by η_{ref}, equations 3.16, n_{ref}, and a characteristic length L:

$$\begin{gathered} \hat{t} \equiv t\frac{\eta_{ref}}{L}, \quad \hat{x} \equiv \frac{x}{L}, \quad \hat{\varphi} \equiv \varphi\frac{\eta_{ref}^3}{n_{ref}}, \quad \hat{\sigma}_T \equiv \frac{\sigma}{\sigma_{ref}} \\ \hat{g}, \hat{\eta}, \hat{\zeta} \equiv \frac{g, \eta, \zeta}{\eta_{ref}}, \quad \hat{u}_i \equiv \frac{u_i}{\eta_{ref}}, \quad \hat{q}_i \equiv \frac{q_i}{q_{ref}}, \quad \hat{\tau} \equiv \frac{\tau}{\tau_{ref}} \end{gathered} \tag{3.17}$$

When the scaling factors are applied to the Boltzmann equation, we can rewrite it as:

$$\frac{\partial\hat{\varphi}(\hat{\eta})}{\partial\hat{t}} + \hat{\eta}\frac{\partial\hat{\varphi}(\hat{\eta})}{\partial\hat{x}_i} = Ln_{ref}\sigma_{ref}\iiint_{\hat{\zeta}}[\hat{\varphi}(\hat{\eta}')\hat{\varphi}(\hat{\zeta}') - \hat{\varphi}(\hat{\eta})\hat{\varphi}(\hat{\zeta})]\hat{g}\hat{\sigma}_T\, dV_{\hat{\zeta}} \tag{3.18}$$

If we define a reference mean free path based on n_{ref} and σ_{ref}, and define the Knudsen number as the reference mean free path divided by the characteristic length:

$$\text{where } \lambda_{ref} = \frac{1}{n_{ref}\sigma_{ref}} \text{ then } Kn = \frac{\lambda_{ref}}{L}. \tag{3.19}$$

The scaled Boltzmann equation becomes:

$$\frac{\partial\hat{\varphi}(\hat{\eta})}{\partial\hat{t}} + \hat{\eta}\frac{\partial\hat{\varphi}(\hat{\eta})}{\partial\hat{x}_i} = \frac{1}{Kn}\iiint_{\hat{\zeta}}[\hat{\varphi}(\hat{\eta}')\hat{\varphi}(\hat{\zeta}') - \hat{\varphi}(\hat{\eta})\hat{\varphi}(\hat{\zeta})]\hat{g}\hat{\sigma}_T\, dV_{\hat{\zeta}} \tag{3.20}$$

For homogeneous relaxations and 1D shocks, the characteristic length, L, is typically defined as the reference mean free path of the gas. In these cases $Kn = 1$.

3.6 Discretization

The discrete velocity method is characterized by defining the velocity distribution function only at a finite set of discrete intervals in velocity space. This is advantageous since in the discrete framework only a limited number of velocities must be collided with each other. Defining $\hat{T}$ as the expected maximum kinetic temperature and $\hat{m}$ as the scaled molecular mas of the species (typically $\hat{m} = 1$ for single species flow), the velocity space for monatomic gases is truncated around a typical value of $\pm 2.8\sqrt{\hat{T}/\hat{m}}$, and the velocity domain is discretized by a scaled velocity, $\hat{\beta}$, that is typically less than or equal to $0.8\sqrt{\hat{T}/\hat{m}}$. The size of the velocity domain is chosen to accurately capture all relevant moments of the velocity distribution function, and the limits to grid spacing are enforced because discretization errors become very significant as the value of $\hat{\beta}$ begins to exceed $\sqrt{\hat{T}/\hat{m}}$ [5]. Once the velocity domain is

truncated and discretized, the number density value from the continuous function at each discrete velocity location is multiplied by the volume element, and the entire result is collapsed into a delta function on the grid point such that only a single velocity is represented by the entire spike. Figure 3.2 describes the discretization process, and Figure 3.3 illustrates the result on a 2D slice of the velocity domain.

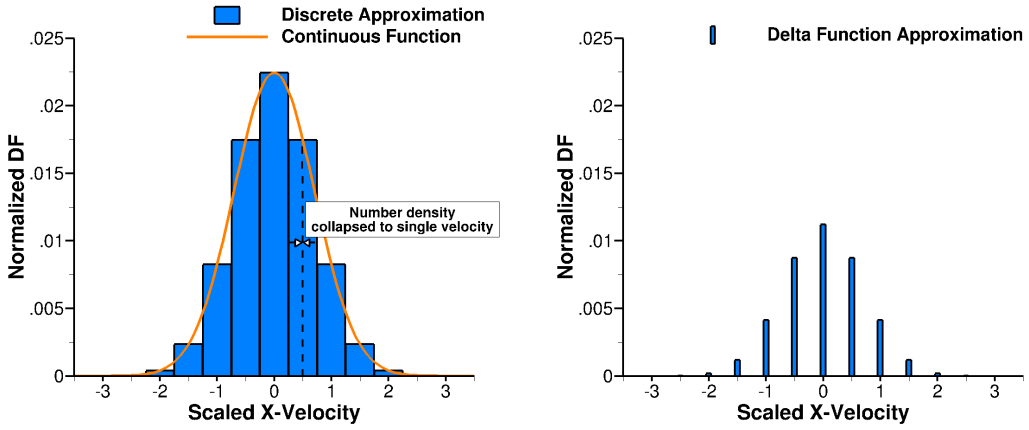

(a) (b)

Figure 3.2: (a) A continuous function is split into histogram elements with volume $\hat{\varphi}(\hat{\eta}) \cdot \hat{\beta}^3$. (b) Each volume element is collapsed into a delta function at a discrete velocity location.

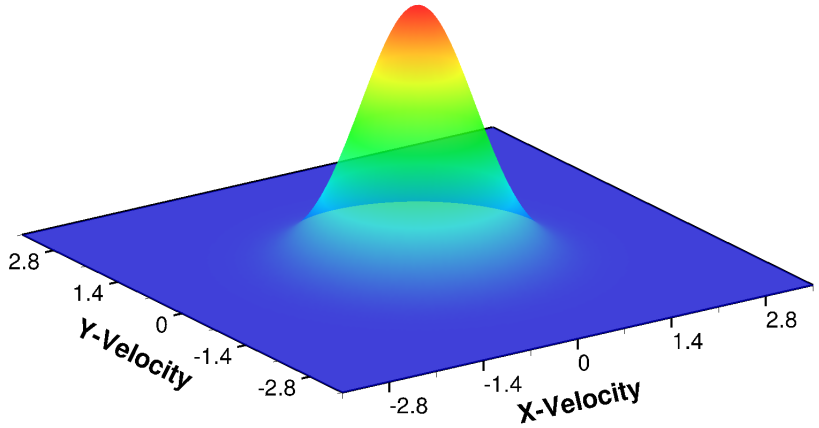

(a)

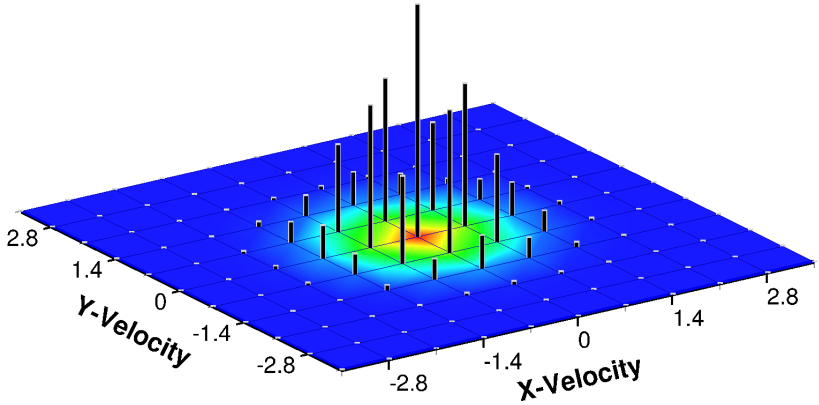

(b)

Figure 3.3: a) Example continuous distribution. b) Corresponding discrete distribution

A second option for calculating the magnitude of the delta functions would be to integrate the continuous function over each volume element for every discrete velocity location. However, in the variance reduced method (Section 4.1.2) a Maxwellian may need to be calculated every time step and the error functions needed for the integrations would become expensive. Furthermore, when the velocity distribution function is initialized in this manner,

there is no guarantee the error in moments higher than the 0th order will be less than when the distribution is initialized by the method initially presented. For now, it is sufficient to say that the 0th moment, the number density, is strictly enforced by multiplying the discrete initial distribution by $\hat{n}/\hat{n}_{calc}$ at every velocity location where $\hat{n}_{calc}$ is the number density after discretization calculated from equation 3.24a found in the following Section 3.7.

Using a discrete grid redefines the velocity distribution function to account for the entire volume element, $dV_{\hat{\zeta}}$, collapsed onto each discrete velocity. The volume element is equivalent to $\hat{\beta}^3$ on a uniform Cartesian grid, and the velocity distribution function becomes:

$$\hat{\varphi}(\hat{\eta}) = \hat{n} \cdot \hat{f}(\hat{\eta}) \cdot \hat{\beta}^3 \tag{3.21}$$

The collision integral can now be written as the summation over all discrete velocities, except those that are equal to each other since particles with like velocities would never collide.

$$\frac{\partial \hat{\varphi}(\hat{\eta})}{\partial \hat{t}} + \hat{\eta}\frac{\partial \hat{\varphi}(\hat{\eta})}{\partial \hat{x}_i} = \frac{1}{Kn}\sum_{\hat{\zeta}\neq\hat{\eta}}[\hat{\varphi}(\hat{\eta}')\hat{\varphi}(\hat{\zeta}') - \hat{\varphi}(\hat{\eta})\hat{\varphi}(\hat{\zeta})]\hat{g}\hat{\sigma}_T \tag{3.22}$$

In the current work, the Boltzmann equation is solved using an explicit, first order time scheme. While such a scheme is convenient, it is by no means the only possible way to approximate the derivative with respect to time. Higher order or implicit schemes might also be used, but would require further calculation and analysis. We thus represent equation 3.22 as:

$$\boxed{\frac{\hat{\varphi}^{n+1} - \hat{\varphi}^n}{\Delta \hat{t}} + \hat{\eta}\frac{\partial \hat{\varphi}(\hat{\eta})}{\partial \hat{x}_i} = \frac{1}{Kn}\sum_{\hat{\zeta}\neq\hat{\eta}}[\hat{\varphi}(\hat{\eta}')\hat{\varphi}(\hat{\zeta}') - \hat{\varphi}(\hat{\eta})\hat{\varphi}(\hat{\zeta})]\hat{g}\hat{\sigma}_T} \tag{3.23}$$

3.7 Scaling and Discretizing the Macroscopic Properties

The properties of the distribution function may also be scaled and written in discrete form. When discretized, integrations become Riemann sum integrations over every velocity class, and the various moments are:

$$\hat{n} = \sum_{\hat{\eta}} \hat{\varphi}(\hat{\eta}) \tag{3.24a}$$

$$\hat{u}_i = \frac{1}{\hat{n}} \sum_{\hat{\eta}} \hat{\eta}_i \hat{\varphi}(\hat{\eta}) \tag{3.24b}$$

$$\hat{T} = \frac{2\hat{m}}{3\hat{n}} \sum_{\hat{\eta}} \hat{C}_i^2 \hat{\varphi}(\hat{\eta}) \tag{3.24c}$$

$$\hat{p} = \frac{\hat{m}}{3} \sum_{\hat{\eta}} \hat{C}_i^2 \hat{\varphi}(\hat{\eta}) = \frac{1}{2} \hat{n}\, \hat{T} \tag{3.24d}$$

$$\hat{q}_j = \frac{\hat{m}}{2\hat{n}} \sum_{\hat{\eta}} \hat{C}_j \hat{C}_i^2 \hat{\varphi}(\hat{\eta}) \tag{3.24e}$$

$$\hat{\tau}_{ij} = -\hat{m} \sum_{\hat{\eta}} \hat{C}_i \hat{C}_j \hat{\varphi}(\hat{\eta}) + \hat{p}\delta_{ij} \tag{3.24f}$$

$$\hat{Q}^k = \frac{1}{\hat{n}} \sum_{\hat{\eta}} |\hat{\eta}_i - \hat{u}_i|^k \hat{\varphi}(\hat{\eta}) \tag{3.25}$$

Scaling the entropy is less obvious. For this work, the Boltzmann constant and reference number density are used as a scaling factor, and $\hat{B}$ is an additive constant which cancels when entropy differences are calculated.

$$\hat{s} = \hat{B} - \frac{1}{\hat{n}} \sum_{\hat{\eta}} \hat{\varphi}(\hat{\eta}) ln\left(\hat{\varphi}(\hat{\eta})\right) \tag{3.26}$$

3.8 Time Scales

There are two significant time scales in monatomic flows which will create constraints on the time step size: the collision time scale and the convective time scale. The convective time scale is determined by the speed of the fastest allowed particle and is constrained by the CFL number in explicit finite difference methods as:

$$\hat{t}_{conv} = \frac{\Delta\hat{x}}{|\hat{\eta}|_{max}} \tag{3.27}$$

The collision time determines the rate of change due to molecular interactions, and it is defined as the reciprocal of the collision frequency [2]. For hard sphere molecules in a Maxwellian function, the time scale can be further reduced since the cross-section is independent of the relative velocity and the average relative velocity can be approximated as proportional to the most probable thermal speed [2].

$$\hat{t}_{coll} = \frac{1}{\hat{n}\bar{\hat{\sigma}}\bar{\hat{g}}} = \frac{1}{\hat{n}\hat{d}^2\sqrt{2}\hat{\eta}_r} \tag{3.28}$$

Looking ahead to Section 4.2.3 where the variable hard sphere (VHS) model is introduced, a VHS time scale can be found from the VHS collision rate described by Bird [2] as:

$$\hat{t}_{coll} = \frac{1}{\hat{\nu}} = \left[2\hat{d}^2\hat{n}\sqrt{\frac{2\hat{T}_d}{\pi\hat{m}}}\left(\frac{\hat{T}}{\hat{T}_d}\right)^{1-\omega}\right]^{-1} \tag{3.29}$$

Where $\hat{T}_d$ is defined as the temperature used to calculate the species diameter. The VHS time scale cannot be exactly predetermined due to its dependence on the local temperature, but a conservative estimate can be made

from the maximum expected temperature in a gas simulation. Having estimated both values, the minimum between $\hat{t}_{conv}$ and $\hat{t}_{coll}$ is used to dictate the maximum allowed time step for the discrete velocity method.

3.9 The Maxwellian Distribution Function

The equilibrium velocity distribution function, formulated by Maxwell in 1860 [106], is a Gaussian distribution and the maximum entropy solution to the Boltzmann equation. It is the only function for which depleting collisions exactly cancel replenishing collisions [1]. The equation is formulated using the number density (n), kinetic temperature (T), and molecular mass (m) of the gas. The original function was formulated as a speed distribution but here the Maxwellian is presented as a velocity distribution as:

$$f^E(\eta) = \left(\frac{m}{2\pi k_b T}\right)^{3/2} e^{\frac{-C_i^2 m}{2k_b T}} \tag{3.30}$$

Where C_i^2 is defined by equation 3.3. The Maxwellian can be scaled by η_{ref}^3 and n_{ref}, and a density weighted delta function form, illustrated in Figure 3.4, is written as:

$$\hat{\varphi}^E(\hat{\eta}) = \hat{n} \cdot \hat{f}^E(\hat{\eta})\hat{\beta}^3 = \hat{n} \cdot \left(\frac{\hat{m}}{\pi \hat{T}}\right)^{3/2} e^{\frac{-\hat{C}_i^2 \hat{m}}{\hat{T}}} \hat{\beta}^3 \tag{3.31}$$

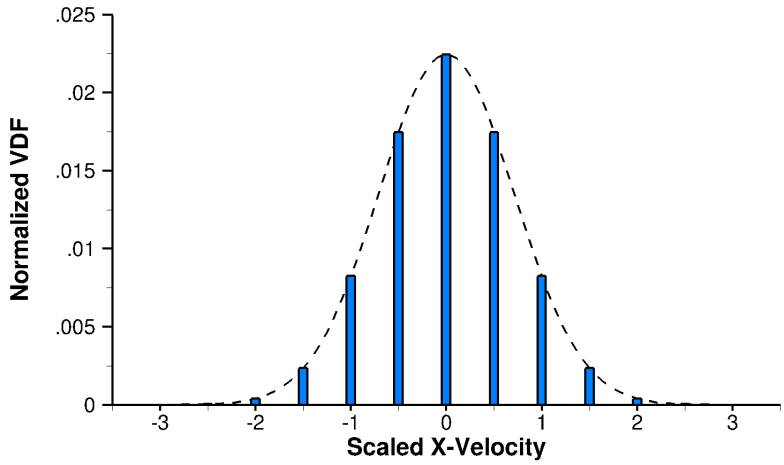

Figure 3.4: 1D slice of the discrete, truncated Maxwellian distribution function showing discrete delta functions and a continuous envelope (not to scale).

The Maxwellian is a common function used to initialize the domain in the discrete velocity method. However, errors occur in the moments during discretization since any discretization is an approximation. While these errors are small, a bigger issue may be that the discretized form of the Maxwellian is not the maximum entropy solution on the discrete velocity domain. This issue is further discussed in the results section of Chapter 4.

3.10 The Bobylev-Krook-Wu Solution

The only analytic solution known for the Boltzmann equation other than the Maxwellian was developed by Bobylev in 1975 [107] and independently by Krook and Wu in 1976 [108]. The solution describes the evolution over time of a distribution function shaped with a maximum located on a spherical shell in velocity space as illustrated by the 1D slice in Figure 3.5. The time-dependent analytic solution is obtained for a homogeneous problem (0D in space) for monatomic pseudo-Maxwell molecules with no body forces

as:

$$\hat{f}^{BKW}(\hat{\eta}) = \left(\frac{\hat{m}}{A\pi\hat{T}}\right)^{3/2} \cdot \frac{1}{2A} \cdot \left[5A - 3 + 2(1-A)\hat{\eta}^2 \frac{\hat{m}}{A\hat{T}}\right] \cdot e^{\frac{-\hat{\eta}^2\hat{m}}{A\hat{T}}} \qquad (3.32)$$

$$\text{where} \quad A = 1 - 0.4 \cdot e^{-\hat{t}/6}$$

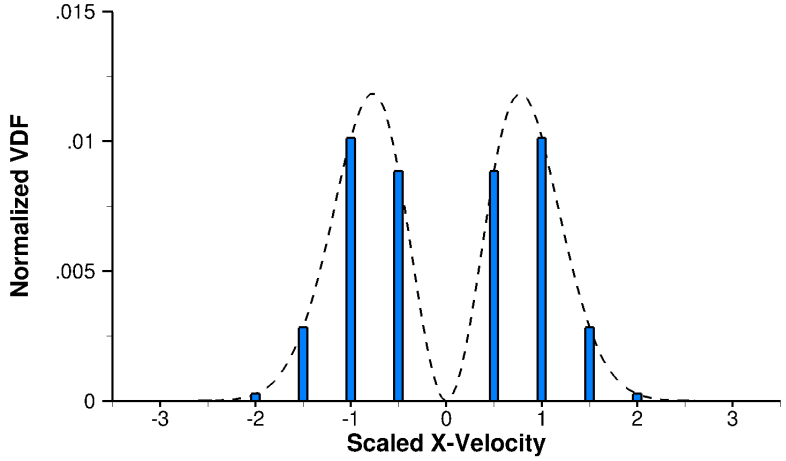

Figure 3.5: 1D slice of the discrete, truncated Bobylev-Krook-Wu distribution function showing discrete delta functions and a continuous envelope (not to scale) at $\hat{t} = 0$.

While the solution has no physical relevance, it has become an essential part of collision method verification for rarefied gas codes since the solution is independent of experimental data subject to errors. Comparisons of higher order moments of the exact solution and the discrete velocity method solution can be made to verify the total relaxation time to thermal equilibrium, the relaxation rate as a function of time, and the error in the higher order moments due to discretization of the velocity domain.

3.11 1D Shock Wave Theory

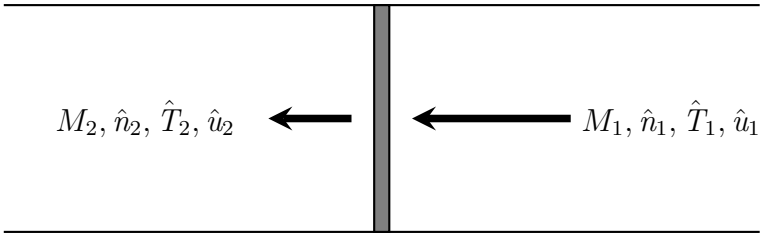

Figure 3.6: Stationary, 1D, normal shock.

Many simulated flows in 1D calculations are either stationary or moving normal shock waves. In continuum dynamics, the ratios between upstream and downstream macroscopic properties in a normal shock are described by the Rankine-Hugoniot conditions as functions of the ratio of specific heats, γ, and the upstream Mach number, M_1 [109] as:

$$\frac{\hat{n}_2}{\hat{n}_1} = \frac{(\gamma+1)M_1^2}{2+(\gamma-1)M_1^2} \tag{3.33}$$

$$\frac{\hat{T}_2}{\hat{T}_1} = \left[2+(\gamma-1)M_1^2\right] \cdot \frac{2\gamma M_1^2-(\gamma-1)}{(\gamma+1)^2 M_1^2} \tag{3.34}$$

$$\frac{\hat{p}_2}{\hat{p}_1} = 1 + \frac{2\gamma(M_1^2-1)}{\gamma+1} \tag{3.35}$$

Defining the scaled upstream speed of sound as $\hat{a}_1 = \sqrt{\gamma \hat{T}_1/2\hat{m}}$, the upstream Mach number for a stationary shock is $M_1 = \hat{u}_1/\hat{a}_1$ and the upstream Mach number for a travelling shock is $M_1 = (\hat{u}_s - \hat{u}_1)/\hat{a}_1$, where $\hat{u}_s$ is the travelling shock speed and $\hat{u}_1$ is the upstream bulk velocity normal to the shock. Shock speed can be found from the solution of [109]:

$$\hat{u}_s^2 - \frac{3-\gamma}{2}\hat{u}_1\hat{u}_s - \frac{1}{2}\left[\gamma+(\gamma-1)\hat{u}_1^2\right] = 0 \tag{3.36}$$

While continuum dynamics commonly approximate a shock as a sudden jump whose value is given by the Rankine-Hugoniot conditions, the reality is that shocks have a finite thickness typically defined by the density change divided by the maximum density gradient. However, the nature of molecular interactions drive the behavior of the changes in macroscopic properties, and thickness is often represented as a multiple of the upstream mean free path. A general definition of mean free path is given as a function of the average thermal speed and average collision cross section as [1]:

$$\lambda = \frac{\overline{c}}{n\overline{\sigma g}} \tag{3.37}$$

The hard sphere solution to equation 3.37 is easily found as [1]:

$$\lambda_{hs} = \frac{1}{\sqrt{2}n\sigma} \tag{3.38}$$

And Bird defines the mean free path for VHS molecules in DSMC as [2]:

$$\lambda_{vhs} = \frac{(T/T_{ref})^{\omega}}{(2-\omega)^{\omega}\Gamma(2-\omega)\sqrt{2}n\sigma_{ref}} \tag{3.39}$$

In comparison, recall the definition in equation 3.19 for the reference mean free path used to describe the characteristic length scale, L, for shocks and homogeneous relaxations in DVM:

$$\lambda_{ref} = \frac{1}{n_{ref}\pi d_{ref}^2} \tag{3.40}$$

Since a different value is used to scale the Boltzmann equation than is actually calculated for the mean free path, care must be taken when determining spatial grid spacing and when calculating the Knudsen number of a simulated flow. A scaled mean free path, λ/λ_{ref}, should be used for these calculations (relevant to information presented in Chapter 4).

3.12 Channel Flow

One of the more prominent applications for rarefied gas solvers is the simulation of flows in micro- and nano-channels. Standard test cases for these conditions include Couette and Fourier flows where either a velocity or temperature gradient is introduced between parallel plates. Solutions are known in the continuum and free-molecular limits, and good approximations have been made for the transition regime ($0.01 < Kn < 100$). Under these conditions a velocity slip and/or temperature jump occurs at the surface of the plates, and the magnitude of the slip can be estimated as a function of Knudsen number, Kn.

Couette Flow

Steady motion of two parallel walls separated by a fluid results in a Couette flow, and if the temperature of the two plates is equal, a continuum no-slip solution for the velocity profile can be found as a linear profile between the wall velocities [15]. Defining $\hat{u}_1$ and $\hat{u}_2$ as the speeds of the walls and L as the channel width, the flow velocity as a function of y is:

$$\hat{u} = \hat{u}_2 \cdot \frac{y}{L} - \hat{u}_1 \tag{3.41}$$

A free molecular solution when Kn becomes very large can also be found [15]. It is simply a constant velocity across the channel with a value of one half the difference between the wall velocities.

$$\hat{u} = \frac{\hat{u}_2 - \hat{u}_1}{2} \tag{3.42}$$

Finally, an approximate solution for transition flow ($0.01 < Kn < 100$) can be found by accounting for a slip velocity as $\hat{u}_s = \hat{\lambda}\frac{d\hat{u}}{d\hat{y}}$ [1]. For $Kn < 1$,

the slip velocity may be further approximated as $\hat{u}_s \propto Kn \cdot (\hat{u}_2 - \hat{u}_1)/2$ [110]. Adjusting equation 3.41 for the slip velocity gives:

$$\hat{u} = (\hat{u}_2 - \hat{u}_s)\frac{y}{L} - (\hat{u}_1 - \hat{u}_s) \tag{3.43}$$

In reality, near the wall the velocity is not a straight line but takes on a curved profile as seen in Figure 3.7. The region is called the Knudsen layer and typically has a distance into the channel on the order of a couple mean free paths [15]. This means that as the mean free path grows to be on the same order as the channel width ($Kn \sim 1$), the Knudsen layer disappears.

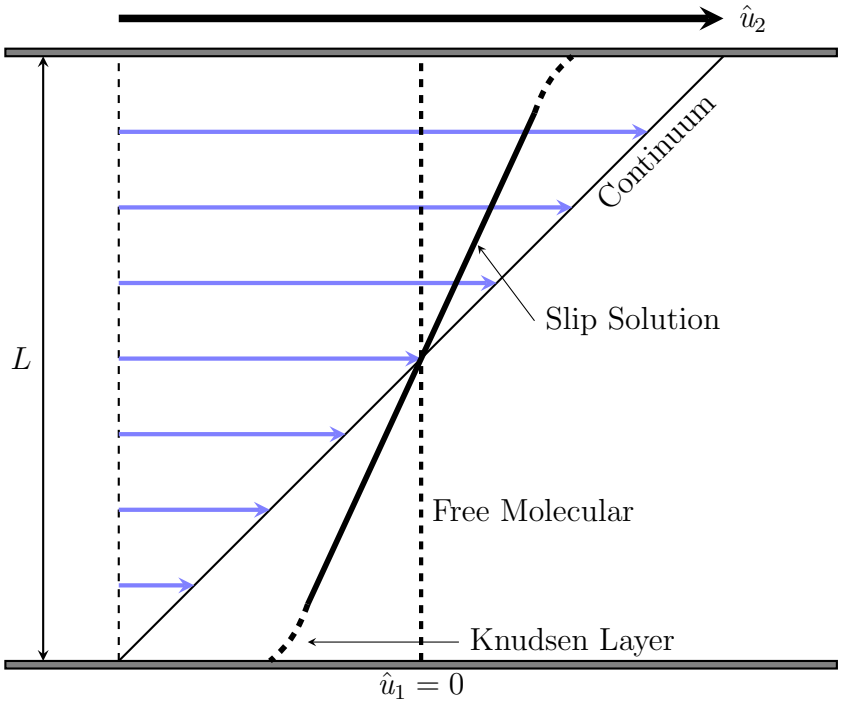

Figure 3.7: Couette flow schematic.

Fourier Flow

Two parallel walls with a temperature difference ($\hat{T}_1 \neq \hat{T}_2$) and no relative motion ($\hat{u}_1 = \hat{u}_2 = 0$) results in what is sometimes called a Fourier flow. Under these conditions, a steady state is reached from an arbitrary initial state after some time period in which molecules travel back and forth between the walls multiple times. For Knudsen numbers within the continuum limit, a steady state solution for temperature may be derived from Fourier's law [15]:

$$q_{cont} = -k\frac{\partial T}{\partial y} \tag{3.44}$$

As a linear function of y:

$$\hat{T}_{cont} = (\hat{T}_2 - \hat{T}_1) \cdot \frac{y}{L} + \hat{T}_1 \tag{3.45}$$

Where the solution has no bulk velocity and a uniform heat flux across the domain. In the free molecular limit, heat flux is calculated based on the number of molecules moving from a hot to cold surface, and the method assumes the effect of collisions between molecules to be negligible [15]. The solution is independent of the channel height, L, and and an analytic result can be found for Maxwell molecules if the reflection off the wall is assumed to be fully Maxwellian [15]. The result is:

$$\hat{T}_{FM} = \sqrt{\hat{T}_1 \cdot \hat{T}_2} \tag{3.46}$$

For the intermediate regimes, $0.01 < Kn < 10$, solutions should be compared to experimental or numerical results from previous studies [111–113] where the temperature profile takes on the shape shown in Figure 3.8. An approximation to the temperature profile can be obtained by combining

continuum and free molecular heat fluxes where the Knudsen number is used to weight the contribution of each model [113, 114].

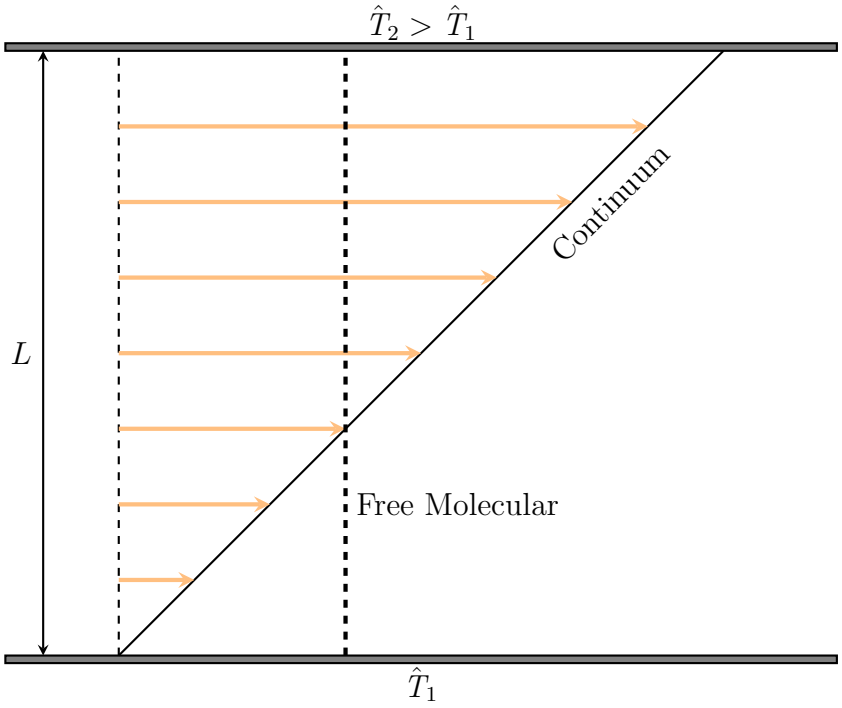

Figure 3.8: Fourier flow schematic.

Chapter 4

Implementation for Monatomic Gases

In this chapter, we discuss the discrete velocity method of solving the Boltzmann equation under the assumptions of a single monatomic species, uniform Cartesian velocity meshes, binary collisions, and no body forces. Most of this chapter will be restricted to collision cross-sections with isotropic scattering but the restriction will be lifted in Section 4.2 for the variable soft sphere collision model. Much of the research presented in this chapter was completed by A. Morris [31] and was the state of the discrete velocity method inherited at the start of this work. Table 4.1 indicates which sections of this chapter contain inherited work and which sections contain new developments. This discussion provides the background and context for improvements in the code that are the subject of subsequent chapters.

Table 4.1: Work inherited from previous research and current work for Chapter 4. Information under the "Section" heading refers to the location of the topic in the chapter, and information under "References" cites publications produced by the UT Austin research group pertaining to the relevant topic.

	Inherited Work	**Section**	**References**
•	Full Monte Carlo method	4.1.1	[5] [31]
•	Variance Reduction method	4.1.2	[6]
•	Conservative remapping	4.1.3	[30] [7]
•	Hard sphere and Pseudo-Maxwell models	4.2.1, 4.2.2	[5]
•	1st and 4th order finite difference	4.3	[28]
•	Specular wall, fixed property, and zero gradient boundaries	4.4.1, 4.4.2, 4.4.3	[115]

	Current Work	**Section**	**References**
•	Expanded stencil for out-of-domain remapping	4.1.3	N/A
•	Variable hard sphere and variable soft sphere models	4.2.3, 4.2.4	[115]
•	Diffuse wall and accommodated wall boundaries	4.4.1, 4.4.1	N/A

A time splitting method is implemented in the current work where the discretized equation is decomposed into convection and collision parts, the changes in the velocity distribution function due to each term is computed and applied, and the time step is progressed. The collision term is computed first as discussed in Section 4.1 and the velocity distribution function is updated. After completing the collision step, the convection term is computed using an explicit finite difference scheme as discussed in Section 4.3. See the flow chart in Figure 4.1 for the general structure of the DVM algorithm.

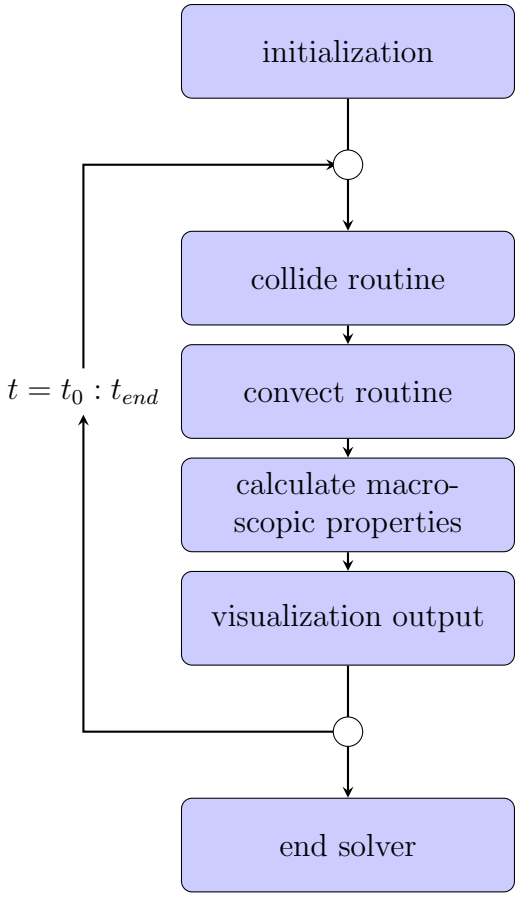

Figure 4.1: DVM flow chart.

4.1 Elastic Collision Theory

It is convenient to consider the collision integral as depleting and replenishing terms because depleting and replenishing collisions will be paired to enforce strict conservation of mass, momentum, and energy. The depletion term, equation 4.1c, involves the selection of colliding quasi-particle pairs and their removal from the velocity distribution function. The replenishment term, equation 4.1b, represents the relocation of the depleted quasi-particles to new velocity locations where they are added to the existing densities.

$$\left.\frac{\partial \hat{\varphi}}{\partial \hat{t}}\right|_{coll} = \hat{I}_{repl} - \hat{I}_{depl} \tag{4.1a}$$

$$\text{where } \hat{I}_{repl} = \sum_{\hat{\zeta}} \left[\hat{\varphi}(\hat{\eta}')\hat{\varphi}(\hat{\zeta}')\right] \cdot \hat{g}\hat{\sigma}_T \tag{4.1b}$$

$$\hat{I}_{depl} = -\sum_{\hat{\zeta}} \left[\hat{\varphi}(\hat{\eta})\hat{\varphi}(\hat{\zeta})\right] \cdot \hat{g}\hat{\sigma}_T \tag{4.1c}$$

Velocities $\hat{\eta}$ and $\hat{\zeta}$ are selected using on of a number of different deterministic or stochastic methods, and post-collision velocities $\hat{\eta}'$ and $\hat{\zeta}'$ are determined from $\hat{\eta}$ and $\hat{\zeta}$ from the dynamics of a collision. The entire structure of the DVM algorithm for solving the collision integral is given by the flow chart in Figure 4.2.

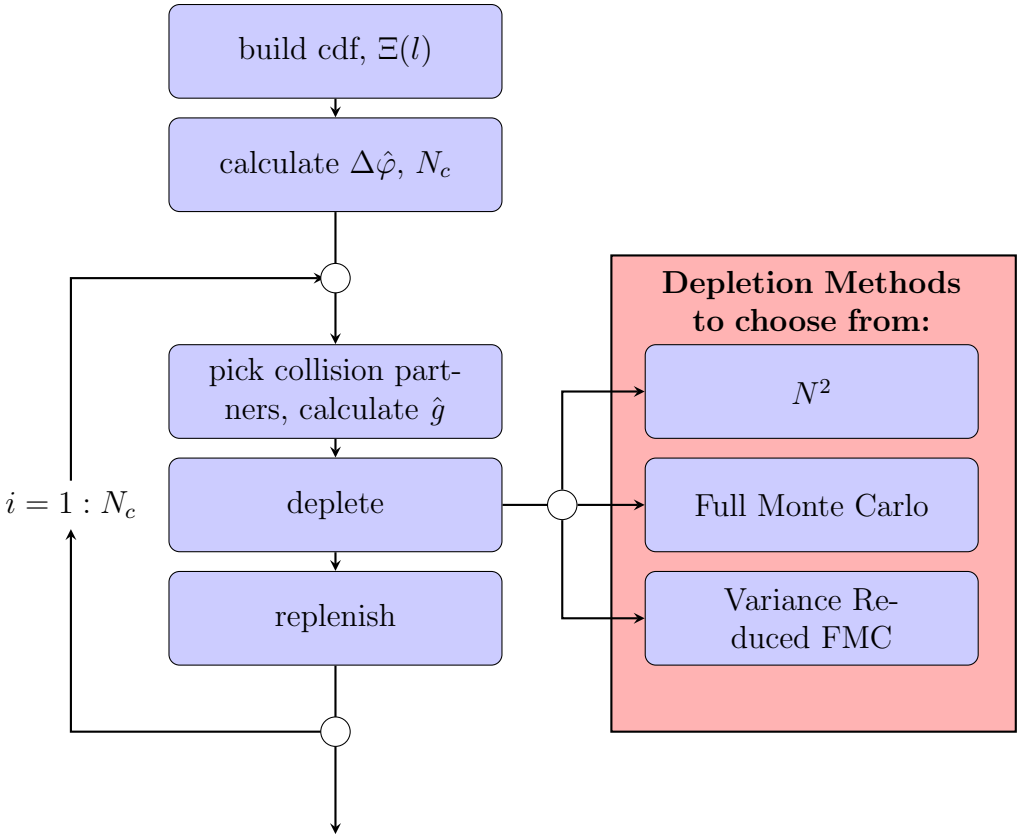

Figure 4.2: DVM flow chart for the collision routine

The most thorough method for solving the collision integral is to directly calculate the summations such that every velocity class is collided with every other velocity class. This method is called the N^2 method, named after the computational cost associated with it because as the number of points in velocity space, N_v, is increased the cost scales as N_v^2. The depletion part of the collision integral is solved in a deterministic manner where collisions are calculated over all possible velocities, and it should be noted that the depletion process produces no stochastic noise. However, because the replenishing points are chosen randomly, and at most a few velocity pairs are chosen for each depletion pair, the collision integral is only computed approximately even

with the N^2 method. A depletion of:

$$\Delta\hat{\varphi} = \frac{1}{2}\Delta\hat{t}\hat{\varphi}(\hat{\eta})\hat{\varphi}(\hat{\zeta}) \cdot \hat{g}\hat{\sigma}_T \tag{4.2}$$

is taken from each collision partner. The factor of $\frac{1}{2}$ is introduced to account for double counting if $\hat{\eta}$ and $\hat{\zeta}$ are drawn from the same distribution. It should be apparent that except for the coarsest of grids, the N^2 method is a prohibitively expensive operation since N is $O(10^1 \text{ to } 10^4)$.

4.1.1 Full Monte Carlo Depletion

Due to the N^2 method's high expense, a Monte Carlo based method is used instead. The method is a stochastic process where velocities are drawn randomly, weighted by the probability of each velocity class undergoing a collision. Once pairs are selected, the individual depletion quantities are calculated, and the contribution to the replenishing integral is computed by selecting a possible post-collision velocity pair and transferring the depletion to the pair's velocity locations. This is a pair-wise process where each depletion event is matched with a replenishment to ensure mass, momentum, and kinetic energy.

As mentioned, a pair of molecules must be selected to collide. The probability of a velocity $\hat{\eta}$ being selected out of all possible velocities is dependent on the magnitude of the distribution function at velocity $\hat{\eta}$ and the total density in the distribution [31].

$$P(\hat{\eta}|\hat{\zeta}) = \frac{|\hat{\varphi}(\hat{\eta})|}{\sum\limits_{\hat{\zeta}} |\hat{\varphi}(\hat{\zeta})|} \tag{4.3}$$

Collisions between molecules with identical velocities ($\hat{\eta} = \hat{\zeta}$) are allowed to be chosen but reduced to a null collision since two molecules with the

same velocity would never collide. To compute the probability of a particular velocity being drawn, a cumulative distribution function, Ξ, is constructed. All $\hat{\eta}$ locations are mapped onto a length N vector, and each $\Xi(l)$ is assigned the value of the sum of all previous $\hat{\varphi}$ values:

$$\Xi(l) = \sum_{m=1}^{l} \hat{\varphi}_k(m) \tag{4.4}$$

The mapping of velocity locations m and l is a function of the number of points in each Cartesian direction, N_x, N_y, N_x, and the velocity index of $\hat{\eta}$, (i, j, k).

$$l = (i - i_{min}) + (j - j_{min}) \cdot N_x + (k - k_{min}) \cdot N_x N_y \tag{4.5}$$

Where $(i_{min}, j_{min}, k_{min})$ are the minimum velocity indices, typically 0. The cumulative distribution eventually sums from $m = 1$ to $m = N_v$ where N_v is the total number of points in velocity space. As can be seen in Figure 4.3, if $\Xi(l)$ is plotted the larger values of $\hat{\varphi}$ create larger step sizes. If a random number, $0 \leq R_f \leq 1$, is drawn and multiplied by the maximum value of Ξ, the value of $R_f \cdot \Xi_{max}$ can be mapped back to a single l location through a binary search of Ξ. The random value is more likely to match a large step than a small step, and since each l index is associated with a unique velocity, the likelihood of a velocity being chosen as a collision partner is biased towards areas of the distribution function with larger density values.

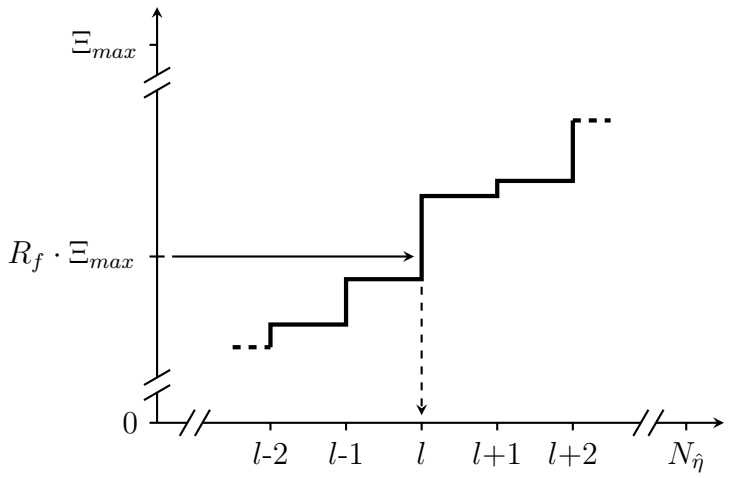

Figure 4.3: Example of a collision velocity selection from a cumulative distribution function.

Drawing from a cumulative distribution function, in comparison to an accept/reject scheme, reduces the number of random number draws because randomly sampled points are never rejected based on another random number draw. However, as the number of velocity locations increases for finer grids, the binary search to find l may become an expensive operation (cost is $O(log_2 N)$). Investigations into potential increases of efficiency, such as different structures for the relation between l and $\hat{\eta}$ such that the most probable velocities are centrally located, may become necessary.

One such method to reduce search times is the construction of a reference vector as the cumulative distribution is being built. The reference vector is an evenly spaced grid from 0 to Ξ_{max} whose elements consist of a range of l values to be searched when selecting a collision. Since the reference grid is evenly spaced with N_{bins} number of bins, it is a trivial operation to find the index value related to the random number draw.

$$int(R_f \cdot N_{bins}) \rightarrow \text{bin reference} \rightarrow [l_{start}, l_{end}] \tag{4.6}$$

Once a reference vector location has been determined, the cumulative distribution function only requires a search over the referenced l values.

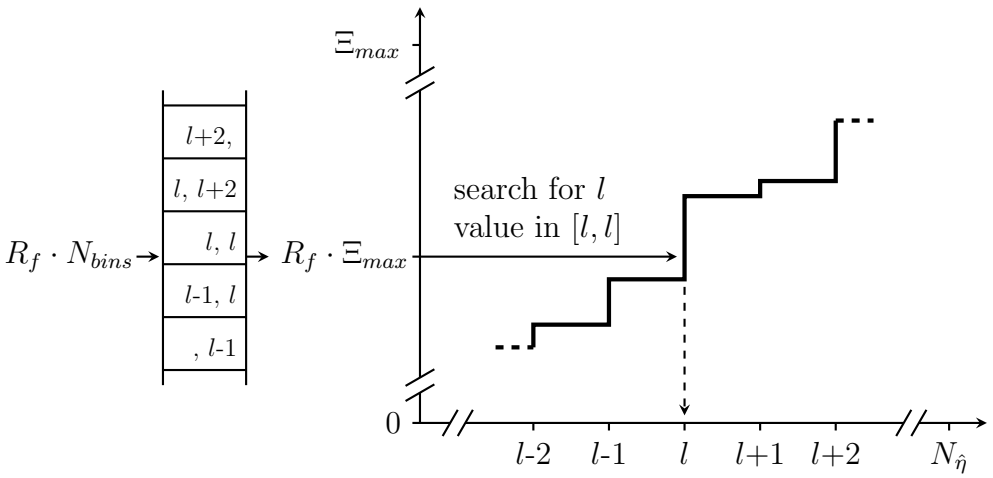

Figure 4.4: Example of a collision velocity selection from a cumulative distribution function with a reference vector.

The depletion at the chosen velocity locations is evaluated once a collision pair is selected. The depletion density is removed from the velocity distribution function, and the value is passed into the replenishing integral. Recall the depletion term in equation 4.1a, but suppose that the molecules are approximated as pseudo-Maxwell molecules, $\hat{g}\hat{\sigma}_T = 1$. The methodology for hard sphere and VHS collision models will be discussed is Section 4.2, but pseudo-Maxwell molecules will be assumed throughout for the current discussion. Hence:

$$\Delta\hat{\varphi}_{depl}(\hat{\eta}) = \frac{\Delta\hat{t}}{Kn} \cdot \hat{\varphi}(\hat{\eta}) \cdot \sum_{\hat{\zeta}} [\hat{\varphi}(\hat{\zeta})] \cdot 1 \tag{4.7}$$

A depletion number density may be calculated from equation 4.7 by summing over all $\hat{\eta}$ velocities and dividing by the total number of collisions in a time step, N_c. Note that for pseudo-Maxwell molecules the number density

depleted is the same for every collision regardless of available number density at the colliding pair locations (value of $\hat{\varphi}(\hat{\eta})$ and $\hat{\varphi}(\hat{\zeta})$).

$$\Delta\hat{\varphi} = \frac{\Delta\hat{t}\hat{n}^2}{2Kn \cdot N_c} \tag{4.8}$$

Since the velocities were selected from the same cumulative distribution function, Ξ, a factor of $\frac{1}{2}$ is included to prevent double counting. Appendix B shows proof the depletion step accounts for the correct total depletion per velocity location per time step. The number of simulated collisions in each time step is a function of a user specified constant C_{RMS}, the kinetic temperature of the gas, the reduced mass, and the velocity grid spacing. *nint* signifies rounding to the nearest integer, and the formula used to calculate N_c is:

$$N_c = nint\left(\frac{\Delta\hat{t} \cdot \hat{T}^{2/3}}{Kn \cdot C_{RMS}^2 \cdot \hat{m}_r^{3/2}\beta^3}\right) \tag{4.9}$$

C_{RMS} is proportional to the RMS noise in the distribution function at equilibrium, and the value is typically of $O(10^{-3})$ for most calculations [6]. A larger C_{RMS} value decreases the number of simulated collisions and increases the number density depletion per collision, therefore increasing the statistical noise due to collisions. A smaller C_{RMS} value increases the number of simulated collisions and decreases the number density depletion per collision, therefore decreasing the statistical noise due to collisions. A more in-depth analysis and discussion of the effects of C_{RMS} on the noise in a velocity distribution function can be found in the work of Morris [6].

There are two possible definitions for noise based on the properties of N_c. If the allow number of simulated collisions to be a function of the number density, noise in macroscopic density will reach the same average magnitude across the entire domain irrespective of local number density values. If the

number of collisions is not a function of number density, as in equation 4.9, the noise in number density is proportional to the local number density. The second option has been chosen throughout the rest of this work.

After choosing a velocity pair to collide, the depletion density is removed from each randomly selected velocity pair at the end of the depletion phase of a collision and sent to the replenishing subroutine. Equations 4.10 and Figure 4.5 show the process:

$$\hat{\varphi}^{t+\Delta t}(\hat{\eta}) = \hat{\varphi}^{t}(\hat{\eta}) - \Delta\hat{\varphi} \tag{4.10a}$$

$$\hat{\varphi}^{t+\Delta t}(\hat{\zeta}) = \hat{\varphi}^{t}(\hat{\zeta}) - \Delta\hat{\varphi} \tag{4.10b}$$

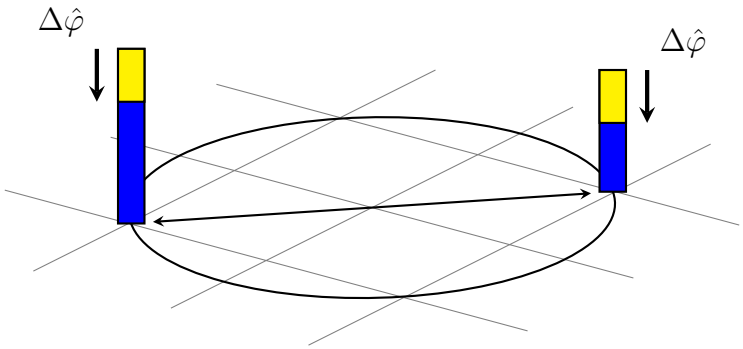

Figure 4.5: Depletion from two colliding velocity locations. The yellow portion of the spike is depleted from each delta-function and will be redistributed in the subsequent replenishing phase (Section 4.1.3)

4.1.2 Variance Reduction

Significant computational savings and reduction to statistical noise can be obtained when we recognize (i) the equilibrium distribution is the maximal entropy solution and (ii) many flows have large regions near or at equilibrium. The result of the first point is the following identity:

The net change in time in a discrete equilibrium distribution due to collisions between particles is zero.

The second point leads to the conclusion that operating on deviations from equilibrium alone could greatly reduce statistical error and the number of necessary simulated collisions due to the lesser density in the deviation distribution in comparison to the original velocity distribution.

In the variance reduction method [3], the distribution function is decomposed into an equilibrium Maxwellian function, $\hat{\varphi}^E$, and a deviation from the equilibrium function, $\hat{\varphi}^d$, such that $\hat{\varphi} = \hat{\varphi}^E + \hat{\varphi}^d$. The equilibrium Maxwellian, as defined by equation 3.30, is a function of the local density, temperature, and bulk velocity. Figure 4.6 shows how the deviation is calculated from the difference between $\hat{\varphi}$ and $\hat{\varphi}^E$. The net number density in the deviation is zero since $\hat{n}^E = \hat{n}$, and note that individual values of $\hat{\varphi}^d(\hat{\eta})$ can be either positive or negative.

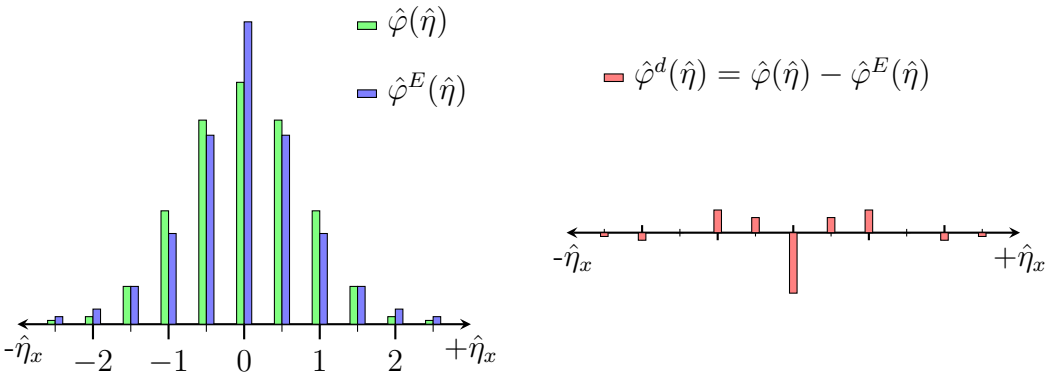

Figure 4.6: An example 1D slice a) of a velocity distribution overlaid with an equilibrium distribution and b) of the deviation distribution.

Applying the decomposition to the collision integral (equation 4.1a) results in four terms:

$$I_{coll}(\hat{\eta}) = \sum_{\hat{\zeta}} \Big[\big(\hat{\varphi}^E(\hat{\zeta}') + \hat{\varphi}^d(\hat{\zeta}')\big)\big(\hat{\varphi}^E(\hat{\eta}') + \hat{\varphi}^d(\hat{\eta}')\big) - \big(\hat{\varphi}^E(\hat{\zeta}) + \hat{\varphi}^d(\hat{\zeta})\big)\big(\hat{\varphi}^E(\hat{\eta}) + \hat{\varphi}^d(\hat{\eta})\big)\Big]$$

$$I_1 = \sum_{\hat{\zeta}} \Big[\hat{\varphi}^E(\hat{\zeta}')\hat{\varphi}^E(\hat{\eta}') - \hat{\varphi}^E(\hat{\zeta})\hat{\varphi}^E(\hat{\eta})\Big] = 0 \tag{4.11a}$$

$$I_2 = \sum_{\hat{\zeta}} \Big[\hat{\varphi}^d(\hat{\zeta}')\hat{\varphi}^E(\hat{\eta}') - \hat{\varphi}^d(\hat{\zeta})\hat{\varphi}^E(\hat{\eta})\Big] \tag{4.11b}$$

$$I_3 = \sum_{\hat{\zeta}} \Big[\hat{\varphi}^E(\hat{\zeta}')\hat{\varphi}^d(\hat{\eta}') - \hat{\varphi}^E(\hat{\zeta})\hat{\varphi}^d(\hat{\eta})\Big] \tag{4.11c}$$

$$I_4 = \sum_{\hat{\zeta}} \Big[\hat{\varphi}^d(\hat{\zeta}')\hat{\varphi}^d(\hat{\eta}') - \hat{\varphi}^d(\hat{\zeta})\hat{\varphi}^d(\hat{\eta})\Big] \tag{4.11d}$$

From the identity introduced above, the solution to term 4.11a can be set to zero, removing any need to simulate collisions between particles drawn from the equilibrium distribution. A large percentage of collisions will be of the equilibrium-equilibrium type in a region of the flow near equilibrium, and removing the need to simulate such collisions can greatly reduce computation time and provide solutions with greatly reduced statistical noise. Summations 4.11b-d are calculated separately with unique depletion and replenishment loops. However, the deviation-equilibrium terms (4.11b and 4.11c) may be calculated at the same time for a gas consisting of a single, monatomic species. Applying the reductions results in the following two collision integrals:

$$I_{coll} = 0 + I_2 + I_3 + I_4$$

$$I_{E-d} = I_2 + I_3 = 2 \cdot \sum_{\hat{\zeta}} \left[\hat{\varphi}^d(\hat{\zeta}') \hat{\varphi}^E(\hat{\eta}') - \hat{\varphi}^d(\hat{\zeta}) \hat{\varphi}^E(\hat{\eta}) \right] \tag{4.12a}$$

$$I_{d-d} = I_4 = \sum_{\hat{\zeta}} \left[\hat{\varphi}^d(\hat{\zeta}') \hat{\varphi}^d(\hat{\eta}') - \hat{\varphi}^d(\hat{\zeta}) \hat{\varphi}^d(\hat{\eta}) \right] \tag{4.12b}$$

Collision velocities are chosen using the picking algorithm described in Section 4.1.1, where the cumulative distribution has been formulated for both the equilibrium and deviation distributions. The deviation cumulative distribution, Ξ^d, is made from the magnitudes of the deviation values, and a second array is tracked containing the sign of each deviation.

$$\Xi^E(l) = \sum_{m=1}^{l} \hat{\varphi}^E(m) \tag{4.13a}$$

$$\Xi^d(l),\, s^d(l) = \sum_{m=1}^{l} \left| \hat{\varphi}^d(m) \right|,\, sgn(\hat{\varphi}^d(\hat{\eta})) \tag{4.13b}$$

$$\text{where } sgn\left(\hat{\varphi}^d(\hat{\eta})\right) = \begin{cases} 1, & \hat{\varphi}^d(\hat{\eta}) \geq 0 \\ -1, & \hat{\varphi}^d(\hat{\eta}) < 0 \end{cases}$$

As a flow approaches equilibrium, one of the more costly calculations is determining the appropriate equilibrium (Maxwellian) distribution for the decomposition of $\hat{\varphi}$ due to calculating the exponential in the formula (equation 3.31). To mitigate the cost of the procedure, a new equilibrium function is only calculated if the relevant properties ($\hat{n}$, $\hat{u}$, $\hat{T}$) change by a set amount, usually $O(0.1)$. E.g. if $|\hat{T}^{t+\Delta t} - \hat{T}^t| > 0.1$ then a new equilibrium is calculated. If not, deviations are found using the equilibrium velocity distribution from the previous time step.

One quasi-particle is drawn from the equilibrium, Ξ^E, and one from the deviation, Ξ^d, distribution for collisions used to solve the integral in equation

4.12a, and both quasi-particles are drawn from the deviation distribution for collisions used to solve the integral in equation 4.12b. The depletion per collision is a function of either the equilibrium density, $\hat{n}^E$, and the deviation density, $\hat{n}^d$, or just the deviation densities, the sign of the deviation terms selected, the size of the time step, and the number of simulated collisions.

$$\Delta\hat{\varphi}^{E-d} = \Delta\hat{t} \cdot \frac{sgn(\hat{\varphi}^d(\hat{\zeta})) \cdot \hat{n}^E \cdot \hat{n}^d}{Kn \cdot N_c^{E-d}} \tag{4.14a}$$

$$\Delta\hat{\varphi}^{d-d} = \Delta\hat{t} \cdot \frac{sgn(\hat{\varphi}^d(\hat{\eta})) \cdot sgn(\hat{\varphi}^d(\hat{\zeta})) \cdot \hat{n}^d \cdot \hat{n}^d}{2Kn \cdot N_c^{d-d}} \tag{4.14b}$$

Proof that equations 4.14 give the correct depletion per collision can be seen in Appendix B. The number of simulated collisions for each integral is chosen in the same way as the full Monte Carlo method (Section 4.1.1) except that a density ratio $\hat{n}^d/\hat{n}$ is included in the calculation to account for the reduction in density due to operating on the deviation.

$$N_c^{E-d} = nint\left(\frac{\Delta\hat{t} \cdot \left(\hat{n}^d/\hat{n}\right) \cdot \hat{T}^{2/3}}{Kn \cdot C_{RMS}^2 \cdot \beta^3}\right) \tag{4.15a}$$

$$N_c^{d-d} = nint\left(\frac{\Delta\hat{t} \cdot \left(\hat{n}^d/\hat{n}\right)^2 \cdot \hat{T}^{2/3}}{Kn \cdot C_{RMS}^2 \cdot \beta^3}\right) \tag{4.15b}$$

Note that the computational efficiency is directly proportional to the number of simulated collisions. Therefore, if the deviation increases to such an extent that:

$$\frac{\hat{n}^d}{\hat{n}} + \left(\frac{\hat{n}^d}{\hat{n}}\right)^2 > 1 \tag{4.16}$$

The number of collisions in the variance reduced method becomes larger than the standard full Monte Carlo method. This indicates that for highly non-equilibrium flows (where the magnitude of the deviation is at least $> 60\%$ of

the equilibrium) the standard full Monte Carlo version of the discrete velocity method would be more efficient than the variance reduced method. However, there may be significant overhead in determining the deviation density so basing collision method decisions on $\hat{n}^d$ alone may be a naive process if the overhead is not taken into account.

The remaining collision process is identical to the full Monte Carlo discussion seen in Section 4.1.1; once a point has been chosen, the depletion is removed (either as a negative or positive depletion) and the information is passed to the replenishing routine.

4.1.3 Replenishment

Once a colliding pair has been chosen and the correct amount depleted for the collision, the mass removed must be replenished back into the distribution in a manner that conserves mass, momentum, and energy. Aaron Morris proposed splitting each depletion into multiple replenishments [5], and looping over the replenishment process as the flow chart in Figure 4.7 indicates. Some small accuracy gains were made when going from $N_{repl} = 1$ to $N_{repl} = 2$, but the benefits rapidly stopped increasing for larger values of N_{repl}. Since even the gains achieved for $N_{repl} = 2$ were minor [5], the subsequent work will assume $N_{repl} = 1$ or $N_{repl} = 2$. The replenishment algorithm's structure is then:

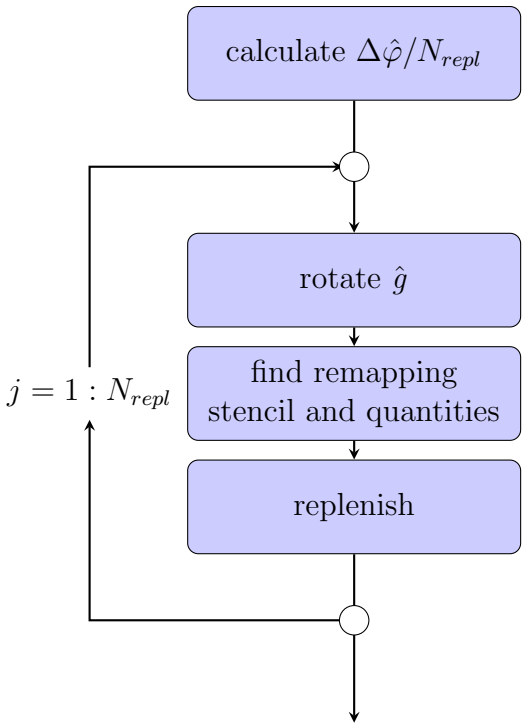

Figure 4.7: DVM flow chart for the replenishment routine

A relative velocity vector can be defined as $\hat{g} = |\hat{\eta} - \hat{\zeta}|$, where $\hat{\eta}$ and $\hat{\zeta}$ are the depletion velocity locations. The sphere made by rotating this vector about its center of mass results in the "collision sphere", or the range of energy conserving replenishment locations. In a collision with isotropic scattering, a random rotation of the relative velocity vector is used to determine the velocity locations for replenishment.

Shown in Figure 4.8, the relative velocity vector is rotated through two angles, the azimuth angle ϕ and the elevation angle θ. ϕ is drawn randomly from $0 \leq \phi \leq 2\pi$ and θ is drawn from $0 \leq \theta \leq \pi$. Computation time can be saved by randomly drawing θ from the sine and cosine functions as seen in equations 4.17b and 4.17c instead of drawing the angle and then calculating sine and cosine since the trigonometric functions are single valued on the

domain $(0, \pi)$.

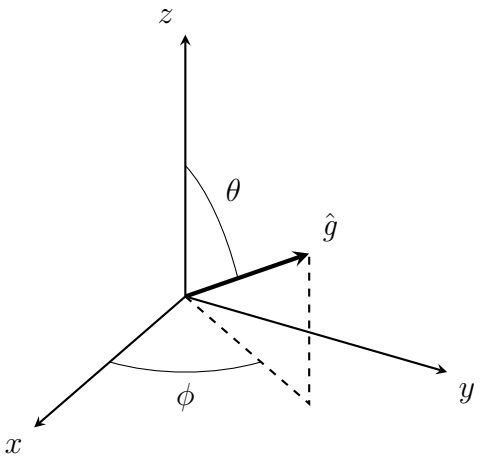

Figure 4.8: 3D Coordinate system.

$$\phi = 2\pi \cdot R_f \tag{4.17a}$$

$$cos(\theta) = 2 \cdot R_f - 1 \tag{4.17b}$$

$$sin(\theta) = \sqrt{1 - cos^2(\theta)} \tag{4.17c}$$

In equations 4.17, R_f is a random number from $0 \rightarrow 1$. Using the randomly selected angles, the x, y, z components of the post-collision relative velocity vector can be found from the transformation between Cartesian and spherical coordinates as:

$$\hat{g}'_x = \frac{1}{2}\hat{g} \cdot sin(\theta) \cdot cos(\phi) \tag{4.18a}$$

$$\hat{g}'_y = \frac{1}{2}\hat{g} \cdot sin(\theta) \cdot cos(\phi) \tag{4.18b}$$

$$\hat{g}'_z = \frac{1}{2}\hat{g} \cdot cos(\theta) \tag{4.18c}$$

Defining the center of mass of the collision as $\hat{V}_{com,x} = \frac{1}{2}(\hat{\eta}_x + \hat{\zeta}_x)$, $\hat{V}_{com,y} = \frac{1}{2}(\hat{\eta}_y + \hat{\zeta}_y)$, and $\hat{V}_{com,z} = \frac{1}{2}(\hat{\eta}_z + \hat{\zeta}_z)$, the post-collision velocity locations of the rotated relative velocity are found as:

$$\hat{\zeta}'_x = V_{com,x} - \hat{g}'_x \qquad \hat{\eta}'_x = V_{com,x} + \hat{g}'_x \tag{4.19a}$$

$$\hat{\zeta}'_y = V_{com,y} - \hat{g}'_y \qquad \hat{\eta}'_y = V_{com,y} + \hat{g}'_y \tag{4.19b}$$

$$\hat{\zeta}'_z = V_{com,z} - \hat{g}'_z \qquad \hat{\eta}'_z = V_{com,z} + \hat{g}'_z \tag{4.19c}$$

Figure 4.9 displays a 2D representation of the process used to determine replenishment locations. For isotropic scattering, all rotations are equally likely except one of 0°, which is disallowed as a null collision. Section 4.2.4 will discuss a case of anisotropic scattering.

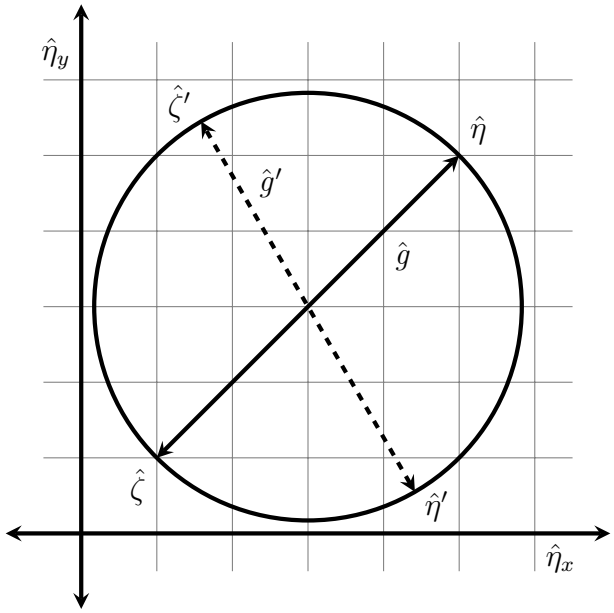

Figure 4.9: Monatomic collision sphere (2D slice) showing a rotation of the relative velocity vector ($\hat{g}$) to a pair of points off the velocity grid ($\hat{\eta}'$, $\hat{\zeta}'$).

Through a simple inspection of Figure 4.9 it can be seen that most replenishment locations do not lie on a node point on the velocity grid. In initial work by Tan [28] and Goldstein [29], a direct velocity matching procedure is used, where post-collision velocities were restricted to grid nodes. Possible rotations could be calculated for coarse grids but as the grid becomes finer and the number of possible post-collision velocity locations increases, such computations become expensive. Further difficulties will also become apparent when non-uniform velocity grids or inelastic collisions are introduced. A key innovation by Varghese [30] was the ability to independently map arbitrary velocities to grid nodes while conserving mass, momentum and energy. The mapping is done by creating a stencil of internal and external points ($o, ix, iy, iz, ex, ey, ez$ Figure 4.10), and the target velocity is mapped to these points using mass, momentum, and energy conservation laws.

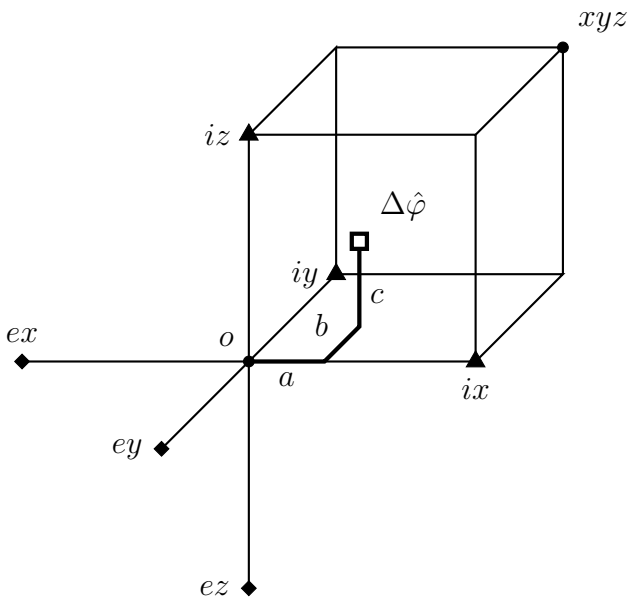

Figure 4.10: Remapping scheme stencil. a, b, and c are the xyz components of the distance between the replenishing mass, $\Delta\hat{\varphi}$, and the origin, o (the discrete velocity point nearest to a, b, c). Internal points, ix, iy, and iz reside on the frame surrounding $\Delta\hat{\varphi}$ while the external points, ex, ey, and ez lie outside the frame.

The origin, point o, is defined as the closest point on the velocity grid to the post-collision velocity location (the small square at location (a, b, c) in Figure 4.10). In the current method, the closest location is found through a search of each velocity component's values.

Exterior points, ex, ey, ez, are used in the stencil because if only surrounding points are used (e.g. point xyz instead of points ex, ey, ez), the system of conservation equations produces a singular matrix [30]. Since the conservation equations make a system of five equations, only one exterior point is actually needed. However, three are used for symmetry and to reduce the effect of negative values that will arise from satisfying the conservation equations. The density replenished to the external points is split evenly between

all three points, and the conservation equations for the 7 point stencil with the origin as a reference point are:

$$\begin{array}{c} \text{mass} \\ \text{x mom.} \\ \text{y mom.} \\ \text{z mom.} \\ \text{energy} \end{array} \begin{bmatrix} 1 & 1 & 1 & 1 & 3 \\ 0 & 1 & 0 & 0 & -1 \\ 0 & 0 & 1 & 0 & -1 \\ 0 & 0 & 0 & 1 & -1 \\ 0 & 1 & 1 & 1 & 3 \end{bmatrix} \begin{bmatrix} \Delta\hat{\varphi}_o \\ \Delta\hat{\varphi}_{ix} \\ \Delta\hat{\varphi}_{iy} \\ \Delta\hat{\varphi}_{iz} \\ \Delta\hat{\varphi}_{ext} \end{bmatrix} = \Delta\hat{\varphi} \cdot \begin{bmatrix} 1 \\ a \\ b \\ c \\ a^2+b^2+c^2 \end{bmatrix} \tag{4.20}$$

The conservation equations can be solved for the mass mapped to each stencil point. Note that the solution indicates the fraction of the replenishing mass, $\Delta\hat{\varphi}$, delivered to the external points ex, ey, ez will be negative in order to yield a net conservation of energy in the remapping. On a uniform grid, each stencil point is equidistant from the origin and the mapping equations reduce to:

$$\Delta\hat{\varphi}_o = \Delta\hat{\varphi}(1 - a^2 - b^2 - c^2) \tag{4.21a}$$

$$\Delta\hat{\varphi}_{ix} = \frac{\Delta\hat{\varphi}}{6}(a^2 + b^2 + c^2 + 5|a| - |b| - |c|) \tag{4.21b}$$

$$\Delta\hat{\varphi}_{iy} = \frac{\Delta\hat{\varphi}}{6}(a^2 + b^2 + c^2 + 5|b| - |a| - |c|) \tag{4.21c}$$

$$\Delta\hat{\varphi}_{iz} = \frac{\Delta\hat{\varphi}}{6}(a^2 + b^2 + c^2 + 5|c| - |a| - |b|) \tag{4.21d}$$

$$\Delta\hat{\varphi}_{ex} = \Delta\hat{\varphi}_{ey} = \Delta\hat{\varphi}_{ez} = \frac{\Delta\hat{\varphi}}{6}(a^2 + b^2 + c^2 - |a| - |b| - |c|) \tag{4.21e}$$

A more general form will be introduced in Section 5.2 when non-uniform velocity grids are discussed. A special case of the remapping scheme is if the post-collision velocity lies outside the velocity domain as seen in Figure 4.11a. Under these circumstances, one (point lies nearest a side), two (point lies nearest an edge), or all three (point lies nearest a corner) interior points may be unavailable for use in the standard remapping. An ulterior stencil is drawn

instead in Figure 4.11b with one or two exterior points behaving as interior points, and the density fractions must be recalculated from the conservation equations with the new stencil locations. If the closest point is a corner, not enough points are available and remapping cannot happen. The collision is nulled and a new post-collision location must be drawn instead.

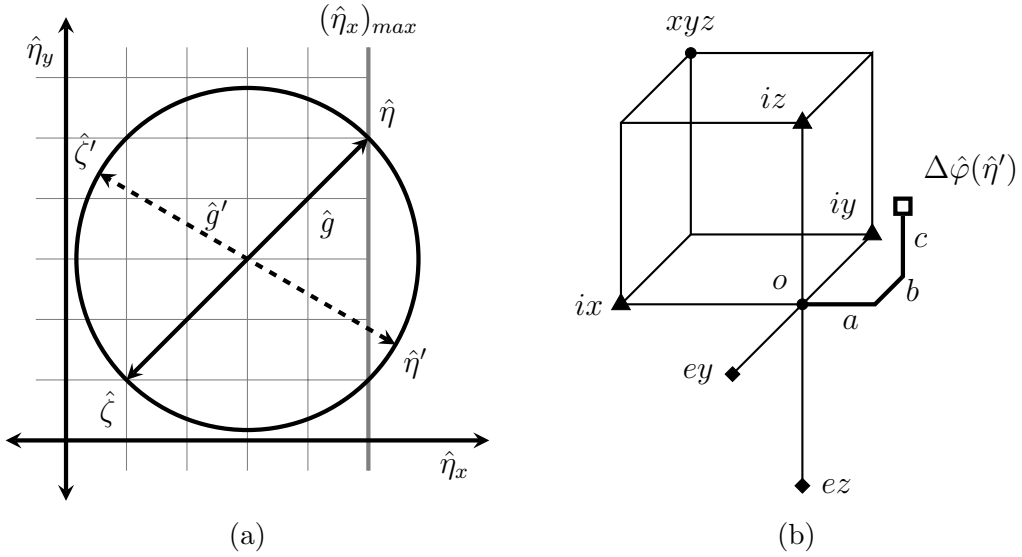

Figure 4.11: a) Monatomic collision sphere (2D slice) showing a rotation resulting in a post-collision velocity outside the velocity domain, $\hat{\eta}'$. b) Remapping scheme stencil with no available internal velocity in the x direction.

The conservation matrix corresponding to the stencil displayed in Figure 4.11b is defined as:

$$\begin{matrix}\text{mass}\\ \text{x mom.}\\ \text{y mom.}\\ \text{z mom.}\\ \text{energy}\end{matrix}\begin{bmatrix}1&1&1&1&2\\0&1&0&0&0\\0&0&1&0&-1\\0&0&0&1&-1\\0&1&1&1&2\end{bmatrix}\begin{bmatrix}\Delta\hat{\varphi}_o\\ \Delta\hat{\varphi}_{ix}\\ \Delta\hat{\varphi}_{iy}\\ \Delta\hat{\varphi}_{iz}\\ \Delta\hat{\varphi}_{ext}\end{bmatrix}=\Delta\hat{\varphi}\cdot\begin{bmatrix}1\\ a\\ b\\ c\\ a^2+b^2+c^2\end{bmatrix} \tag{4.22}$$

And the matrix is solved for the remapping densities:

$$\Delta\hat{\varphi}_o = \Delta\hat{\varphi}(1 - a^2 - b^2 - c^2) \tag{4.23a}$$

$$\Delta\hat{\varphi}_{ix} = \Delta\hat{\varphi} \cdot a \tag{4.23b}$$

$$\Delta\hat{\varphi}_{iy} = \frac{\Delta\hat{\varphi}}{4}(a^2 + b^2 + c^2 + 3|b| - |a| - |c|) \tag{4.23c}$$

$$\Delta\hat{\varphi}_{iz} = \frac{\Delta\hat{\varphi}}{4}(a^2 + b^2 + c^2 + 3|c| - |a| - |b|) \tag{4.23d}$$

$$\Delta\hat{\varphi}_{ey} = \Delta\hat{\varphi}_{ez} = \frac{\Delta\hat{\varphi}}{4}(a^2 + b^2 + c^2 - |a| - |b| - |c|) \tag{4.23e}$$

For post-collision velocities that lie outside the velocity grid domain, a more significant negative density is produced at the exterior points than for post-collision velocities that lie inside the velocity grid domain. This is because the post-collision velocity does not lie inside the stencil but outside, and both exterior points and interior points can have negative replenishment fractions. Furthermore, as the post-collision velocity gets farther outside the domain boundaries, the negative number density value increases. The negatives and consequent large positives at the origin may become large, especially for fine velocity grids, and the large errors can cause the solution to blow up over time as seen in Figure 4.13a. A simple mitigating technique that quiets the solution down to the levels seen in Figure 4.13b is to select interior stencil points from further away from the origin such that the distance between the edge of the velocity domain and the post-collision velocity location is less than the distance between the origin of the remapping stencil and the interior points. This is illustrated in Figure 4.12. A. Morris also presented the idea that only post-collision velocities that lie close to a grid point may be allowed [5]. This would decrease the diffusion of density due to remapping and may decrease error in higher order moments in the evaluation of the collision integral, but has not been implemented in the current method.

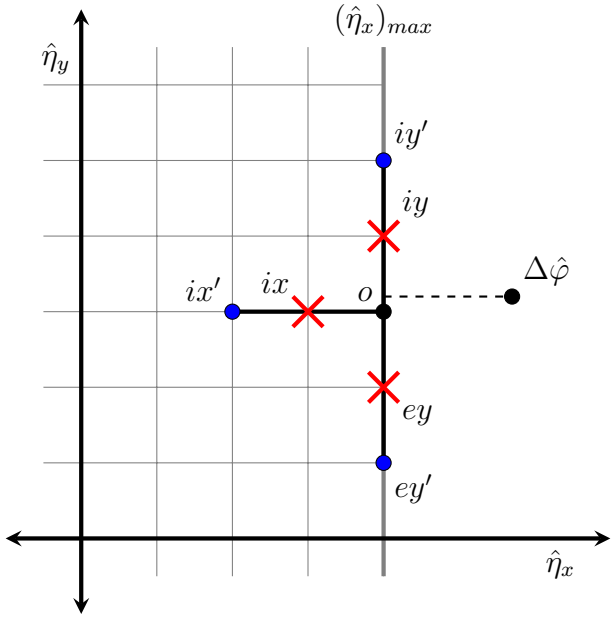

Figure 4.12: 2D schematic showing use of interior points whose distance from the origin is bounded by the distance from the edge of the domain to the post-collision velocity. Points ix, iy, ey are rejected in favor of points ix', iy', ey'.

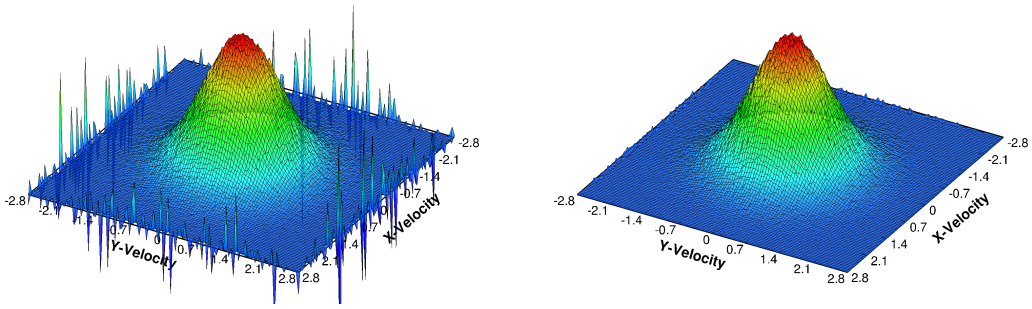

(a) (b)

Figure 4.13: Maxwellian distribution functions allowed to collide using (a) the closest neighbor edge remapping until blow up occurs at $\hat{t} = 1.2$ and (b) the expanded stencil remapping run without blow-up for a much longer time of $\hat{t} = 30$. The level of noise at the boundaries remains stable throughout the course of the simulation.

4.1.4 Negative Value of The Velocity Distribution Function

During the course of a simulation, values of the distribution function may become negative. A depletion can remove more number density than is currently available at a velocity class, negative density contributions from replenishment can push a velocity class to negative, or the sum of these effects over a time step can result in a negative value since an explicit time scheme is used (the algorithm does not have knowledge of the net result of all events until the end of the time step). Typically, the negative densities being discussed are very small, $O(10^{-4})$, and only produce a minor inconvenience to discrete velocity calculations, therefore only a couple changes need to be made to the method. The first change is the magnitude of negative values are taken when constructing the cumulative distribution function:

$$\Xi(l) = \sum_{m=1}^{l} |\hat{\varphi}(m)| \tag{4.24}$$

And if a point is chosen that contains a negative contribution in a collision, the sign of the point follows the depletion.

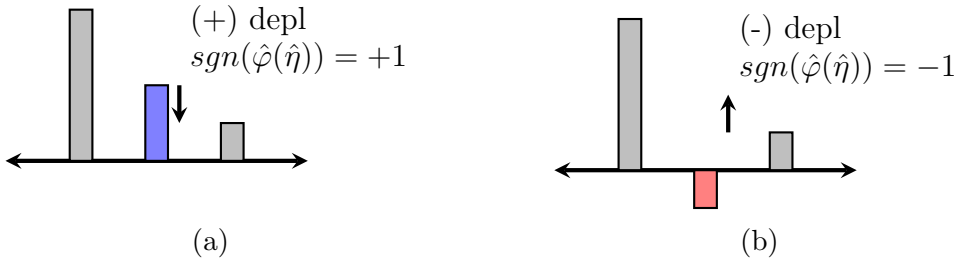

Figure 4.14: Effect of a depletion from (a) a positive distribution function value and (b) a negative distribution function value.

The number density depleted is multiplied by the signs found during collision velocity selection (Figure 4.14), and the total number density must be

adjusted for negative values of the velocity distribution function. The maximum value of the cumulative distribution function is the local number density ($\hat{n} = \hat{n}_{pos} + \hat{n}_{neg}$) adjusted for the magnitude of the negative contributions: $\Xi_{max} = \hat{n} - 2\hat{n}_{neg}$ where $\hat{n}_{neg} < 0$. Substituting the maximum value of the cumulative distribution function and the relevant signs into equation 4.8 gives:

$$\Delta\hat{\varphi}_{depl} = \Delta\hat{t}\frac{(\hat{n} - 2\hat{n}_{neg})^2}{2KnN_c} \cdot sgn(\hat{\varphi}(\hat{\eta})) \cdot sgn(\hat{\varphi}(\hat{\zeta})) \tag{4.25}$$

The negative values directly influence the calculation of entropy since the natural logarithm of a negative number is not defined. A. Morris presented four different approaches to calculating entropy [5] and in the current code, the magnitude of the distribution is used inside the logarithmic function.

$$\hat{s} = \hat{B} - \frac{1}{\hat{n}}\sum_{\hat{\eta}} |\hat{\varphi}(\hat{\eta})| \cdot \ln|\hat{\varphi}(\hat{\eta})| \tag{4.26}$$

4.2 Collision Cross-Section

There are several possible molecular models used to describe the total collision cross-section such as the hard sphere, variable hard sphere, variable soft sphere, and others. The primary model used in the current implementation of the discrete velocity method is the variable hard sphere (VHS) model.

4.2.1 Hard Sphere Model

The hard sphere model is simply explained by imagining two billiard balls colliding. They exert no force on each other until the instant they are in contact and then immediately after contact, they once again exert no force on each other. Every scattering angle (the angle between $\hat{g}$ and $\hat{g}'$), is equally likely, and can be chosen at random. This can be described mathematically

as the inverse power law with isotropic scattering when the power coefficient approaches infinity [1]. Therefore, the force is only effective when the distance between molecule centers is the radius of closest approach, d, and the total collision cross section can be found by solving equation 3.9 as:

$$\sigma_T = \int_0^{4\pi} \frac{1}{4} d^2 d\Omega = \pi d^2 \tag{4.27}$$

Scaling the cross section and substituting the scaled form into the Boltzmann equation results in a collision integral with linear dependence on $\hat{g}$.

$$\frac{\hat{\varphi}^{n+1} - \hat{\varphi}^n}{\Delta \hat{t}} + \hat{\eta} \frac{\partial \hat{\varphi}(\hat{\eta})}{\partial \hat{x}_i} = \frac{1}{Kn} \sum_{\hat{\zeta} \neq \hat{\eta}} [\hat{\varphi}(\hat{\eta}')\hat{\varphi}(\hat{\zeta}') - \hat{\varphi}(\hat{\eta})\hat{\varphi}(\hat{\zeta})] \hat{g} \hat{d}^2 \tag{4.28}$$

The hard sphere collision model is implemented in the discrete velocity method through a direct adjustment of the depletion factor, $\Delta\hat{\varphi}$. Unlike DSMC [2], the probability of a particular particle being chosen for a collision remains independent of the cross section. Instead, the number density depleted per collision is adjusted by $\hat{g}\hat{\sigma}_T$ after a collision is drawn:

$$\Delta\hat{\varphi}_{depl} = \Delta\hat{t} \cdot \frac{(\hat{n} - 2\hat{n}_{neg})^2}{KnN_c} \cdot sgn\left\{\hat{\varphi}(\hat{\eta}) \cdot \hat{\varphi}(\hat{\zeta})\right\} \cdot \hat{g}\hat{d}^2 \tag{4.29}$$

This means that, on the average, velocity locations at the wings of a distribution will have a greater depletion per collision than velocity locations near the center of the distribution. By removing the collision probability's dependence on cross section, any sort of acceptance-rejection scheme, and the related random number draw, is avoided and computational cost is reduced. The trade-off is the greater density drawn at the typically low-density wings of the distribution function. Larger density draws in the wings increases noise

in higher order moments and can lead to a greater chance of negative values in the distribution function. A kth order moment is dependent on $(\hat{\eta}_i - \hat{u}_i)^k$, therefore noise becomes more evident in the wings where $\hat{\eta}_i - \hat{u}_i$ is larger.

4.2.2 Pseudo-Maxwell Model

The Maxwell model is the limiting case for "soft" molecular models where collisions between particles are completely independent of the relative velocity, $\hat{g}$ [2], and a pseudo-Maxwell molecule is defined as a Maxwell molecule with isotropic scattering due to an angular cut-off. The discrete Boltzmann equation for pseudo-Maxwell molecules becomes:

$$\frac{\hat{\varphi}^{n+1} - \hat{\varphi}^n}{\Delta \hat{t}} + \hat{\eta} \frac{\partial \hat{\varphi}(\hat{\eta})}{\partial \hat{x}_i} = \frac{1}{Kn} \sum_{\hat{\zeta} \neq \hat{\eta}} [\hat{\varphi}(\hat{\eta}^{'}) \hat{\varphi}(\hat{\zeta}^{'}) - \hat{\varphi}(\hat{\eta}) \hat{\varphi}(\hat{\zeta})] \hat{d}^2 \tag{4.30}$$

Since depletions are not dependent on velocity location, the depletion per collision event is a constant. The Maxwell/pseudo-Maxwell model is very useful since the only analytic solution for the Boltzmann equation, the BKW solution [108, 116], is a homogeneous solution formulated for pseudo-Maxwell molecules.

4.2.3 The Variable Hard Sphere (VHS) Model

The hard sphere model fails to recognize that the collision cross-section should decrease as the relative speed increases since faster moving particles have less time for their forces to interact in a collision. The VHS model attempts to address the issue of velocity dependence by making the total cross section inversely proportional to the relative speed to some power [103]. Including a species specific coefficient gives a total collision cross-section of:

$$\sigma_T = \underbrace{\frac{\sigma_{ref}}{\Gamma(5/2-\omega)}\left(\frac{1}{\hat{m}_{red}}\right)^{1/2-\omega}}_{\sigma_{coeff}}\left(\frac{g^2}{g_{ref}^2}\right)^{1/2-\omega} \tag{4.31}$$

Here ω, the VHS coefficient, is defined for each individual molecular species with a value normally ranging from 0.5 to 1.0. At the lower limit, defining the coefficient equal to 0.5 simulates a hard sphere molecule, and at the higher limit, defining the coefficient equal to 1.0 simulates a pseudo-Maxwell molecule. Specific values for individual species can be found in Table A.1 in Appendix A under the column heading "Viscosity index". Substituting the VHS definition into the Boltzmann equation reduces the $\hat{g}\hat{\sigma}_T$ term to a single quantity.

$$\hat{g}\hat{\sigma}_T = \begin{cases} \sigma_{coeff} \cdot \hat{g}, & \omega = 0.5 \\ \sigma_{coeff} \cdot \hat{g}^{2-2\omega}, & 0.5 < \omega < 1.0 \\ \sigma_{coeff}, & \omega = 1.0 \end{cases} \tag{4.32}$$

The VHS collision model is implemented in the discrete velocity method through a direct adjustment of the depletion factor, $\Delta\hat{\varphi}$, in the same manner as the hard sphere model. The resulting depletion factor is:

$$\Delta\hat{\varphi}_{depl} = \Delta\hat{t} \cdot \frac{(\hat{n} - 2\hat{n}_{neg})^2}{2KnN_c} \cdot sgn\left\{\hat{\varphi}(\hat{\eta}) \cdot \hat{\varphi}(\hat{\zeta})\right\} \cdot \sigma_{coeff}\hat{g}^{2-2\omega} \tag{4.33}$$

4.2.4 The Variable Soft Sphere (VSS) Model

The Variable Soft Sphere (VSS) model uses the same adjustment to the cross-section as the VHS model, but it accounts for anisotropic scattering. The impact parameter is adjusted by an introduced parameter, α, to account for certain scattering angles being more likely than others [93, 104].

$$b = d\,\cos^{\alpha}(\chi/2) \tag{4.34}$$

Solving equation 4.34 for the scattering angle results in:

$$\cos(\chi) = 2\left(\frac{b}{d}\right)^{1/\alpha} - 1 \tag{4.35}$$

Which is used to determine the angle the relative velocity vector will be rotated through for post-collision velocity locations. Every value of $\cos(\chi)$ is equally likely when $\alpha = 1$, and the method then reduces to the VHS model. Values for α for different gas species can be found in Table A.1 in Appendix A.

The scattering angle is implemented in 3D velocity space through an azimuth angle ϕ, randomly chosen from the domain $[0,\ 2\pi]$ and an elevation angle θ such that $\chi = \theta$ in equation 4.35. The quantity (b/d) is a random number between 0 and 1 when VSS is implemented in the code. The post-collision relative velocity is then a rotation in spherical coordinates defined by ϕ and θ. $\hat{g}_x$, $\hat{g}_y$, and $\hat{g}_z$ are the directional components of the relative velocity, $\hat{g}$ [2], and the post-collision directional components, $\hat{g}'_x$, $\hat{g}'_y$, and $\hat{g}'_z$ are:

$$\hat{g}'_x = \frac{1}{2}\left[\hat{g}_x\,cos(\theta) + \frac{sin(\theta)\,[\hat{g}\,\hat{g}_y\,cos(\phi) - \hat{g}_z\,\hat{g}_x\,sin(\phi)]}{(\hat{g}_x^2 + \hat{g}_y^2)^{1/2}}\right] \tag{4.36a}$$

$$\hat{g}'_y = \frac{1}{2}\left[\hat{g}_y\,cos(\theta) - \frac{sin(\theta)\,[\hat{g}\,\hat{g}_x\,cos(\phi) + \hat{g}_z\,\hat{g}_y\,sin(\phi)]}{(\hat{g}_x^2 + \hat{g}_y^2)^{1/2}}\right] \tag{4.36b}$$

$$\hat{g}'_z = \frac{1}{2}\left[\hat{g}_z\,cos(\theta) + sin(\phi)sin(\theta)(\hat{g}_x^2 + \hat{g}_y^2)^{1/2}\right] \tag{4.36c}$$

4.2.5 Other Cross-Section Models

A variety of other collision cross-section models, such as Lennard-Jones or Coulombic, may be implemented in the discrete velocity method without

further difficulty. If a cross-section, σ, can be determined as a function of values found in the velocity distribution function (velocity location and number density), and if the probability of any particular scattering angle, θ, can be evaluated, the model may be implemented in the same manner as a VHS or VSS cross-section. Even very small rotations and very small number density values can be handled by the method since every potential rotation of the relative velocity vector is allowed and remapping strictly conserves mass, momentum, and energy. If the cross-section and scattering cannot be calculated as described, further analysis would be needed. It should also be noted that since the number of possible relative velocity magnitudes is a finite value for a discrete velocity framework, complicated functions of relative velocity may be pre-calculated to improve the efficiency of the method.

4.3 Convection

The convection operator, calculated after the collision operator has been completed, is solved using a finite difference scheme in the current method. First each boundary condition is solved, then the spatial elements are looped over, and for each spatial element, every velocity is looped over to find the change due to convection. The velocity distribution function is updated and the algorithm continues onto the next time step.

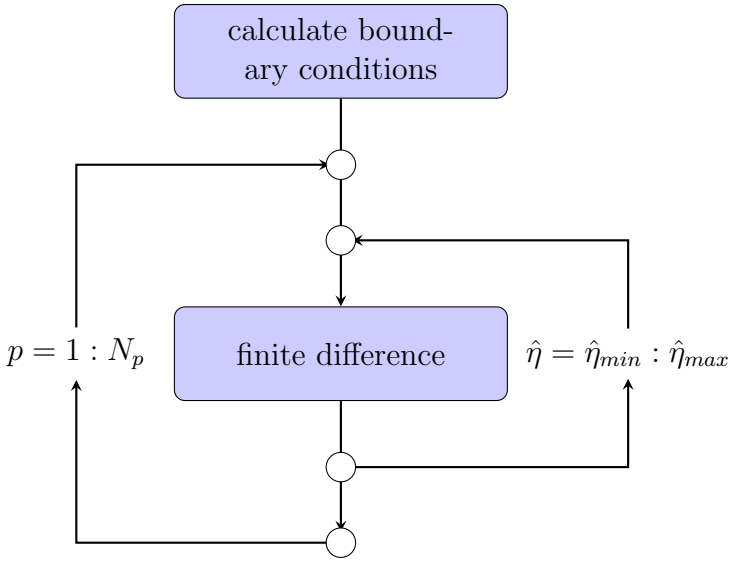

Figure 4.15: DVM flow chart for the convection routine

In an explicit time scheme, the collision integral can be considered a known, already calculated source term to the convection operator.

$$\Delta\hat{\varphi} = -\left(\Delta\hat{t}\hat{\eta}\frac{\partial\hat{\varphi}}{\partial\hat{x}}\right)_{conv} + \Delta\hat{t}\hat{I}_{coll} \tag{4.37}$$

Both a first order and fourth order finite difference scheme are currently implemented in the discrete velocity code to calculate the convection term. Defining the CFL number as $c = \hat{\eta}\frac{\Delta\hat{t}}{\Delta\hat{x}}$, the convection term is solved at each velocity location across all spatial elements. In the following formulas, p is the spatial index and t is the time. The current model assumes uniform spacing between the nodes in physical space, but this restriction can easily be lifted. The fourth order scheme developed by Tan [28] is:

$$\begin{aligned}\hat{\varphi}_p^{t+\Delta t}(\hat{\eta}) = \alpha_{-2}\cdot\hat{\varphi}_{p-2}^{t}(\hat{\eta}) + \alpha_{-1}\cdot\hat{\varphi}_{p-1}^{t}(\hat{\eta}) + \alpha_0\cdot\hat{\varphi}_{p}^{t}(\hat{\eta}) \\ + \alpha_1\cdot\hat{\varphi}_{p+1}^{t}(\hat{\eta}) + \alpha_2\cdot\hat{\varphi}_{p+2}^{t}(\hat{\eta})\end{aligned} \tag{4.38}$$

Where the coefficients are:

$$\begin{aligned}
\alpha_{\text{-}2} &= -c(1-c^2)(2+c)/24 \\
\alpha_{\text{-}2} &= c(1+c)(4-c^2)/6 \\
\alpha_0 &= (1-c^2)(4-c^2)/4 \\
\alpha_1 &= -c(1-c)(4-c^2)/6 \\
\alpha_2 &= c(1-c^2)(2-c)/24
\end{aligned} \tag{4.39}$$

The stability criterion for the 4th order central method described is $|c| < 1$. A first order, upwind scheme is applied at $p = 2$ and $p = p_{max} - 1$ in the fourth order model, or it can be applied across the entire domain instead if desired. The scheme is:

$$\hat{\varphi}_p^{t+\Delta t} = \hat{\varphi}_p^t - c \cdot \begin{cases} \hat{\varphi}_{p+1}^t(\hat{\eta}) - \hat{\varphi}_p^t(\hat{\eta}),\ \hat{\eta} < 0 \\ \hat{\varphi}_p^t(\hat{\eta}) - \hat{\varphi}_{p-1}^t(\hat{\eta}),\ \hat{\eta} > 0 \end{cases} \tag{4.40}$$

Where $p = 1$ and $p = p_{max}$ are solved through an application of the relevant boundary conditions.

4.4 Boundary Conditions

For monatomic gases, there are three boundary conditions available in the discrete velocity code: wall reflection, fixed properties (Dirichlet boundary), or zero gradients. Each boundary condition is applied before the convection step on points $p = 1$ and $p = p_{max}$.

4.4.1 Wall Reflection BCs

Reflection of a gas off a wall can satisfy either specular or diffuse boundary conditions or a combination of both in the current version of DVM. In order

to account for either reflection type, a ghost cell is defined outside the wall boundary (see Figure 4.16) and used to calculate a first order upwind finite difference scheme for particles leaving the wall (equation 4.41). The single ghost cell is located at $\Delta\hat{x}$ away from $p = 1$ ($p = p_{max}$) and the wall is assumed to reside at $\Delta\hat{x}/2$.

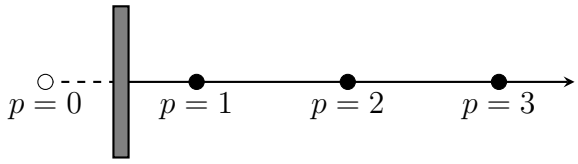

Figure 4.16: 1D spatial grid with a wall boundary and a single ghost cell ($p = 0$) at the left boundary.

The distribution function moving back into the domain at the ghost cell is found from the region of the distribution moving towards the wall at $p = 1$ ($p = p_{max}$ at the right boundary) and the rules governing reflection (discussed in the following sections). The newly calculated distribution is used in a first order upwind finite difference scheme to find the change due to convection from the ghost cell at $p = 1$ ($p = p_{max}$).

$$\hat{\varphi}_1' = \begin{cases} \hat{\varphi}_1 - |\hat{\eta}| \cdot (\hat{\varphi}_1 - \hat{\varphi}_2) & \hat{\eta}_x < 0 \\ \hat{\varphi}_1 & \hat{\eta}_x = 0 \\ \hat{\varphi}_1 - |\hat{\eta}| \cdot (\hat{\varphi}_1 - \hat{\varphi}_0) & \hat{\eta}_x > 0 \end{cases} \tag{4.41}$$

Specular Boundary

If a particle is specularly reflected from a wall, the normal component of the incoming particle velocity is reversed, while the tangential components of velocity are preserved. The momentum components are affected correspondingly. Figure 4.17a illustrates this process schematically and Figure 4.17b shows the post-reflection distribution function at a ghost cell.

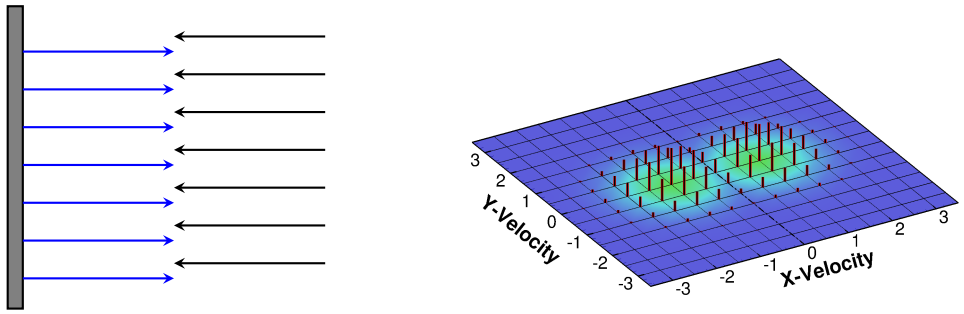

(a) (b)

Figure 4.17: a) Specular reflection. b) The distribution function at the ghost cell in specular reflection is the incoming distribution function at $p = 1$ reflected in the wall normal direction.

The reflected distribution at the ghost cell is found by taking the negative of the x-component of each incoming velocity then remapping the number density back to the grid at the reflected velocity location.

$$\hat{\varphi}_0(\hat{\eta}_x, \hat{\eta}_y, \hat{\eta}_z) = \hat{\varphi}_1(-\hat{\eta}_x, \hat{\eta}_y, \hat{\eta}_z) \tag{4.42}$$

The same remapping process discussed in Section 4.1.3 is used to ensure conservation of mass, momentum, and energy after a reflected velocity location has been identified. Since the incoming number density at each x-velocity location is equal to the outgoing number density at the reflected velocity and the reflected velocity's magnitude is equal to the incoming velocity's magnitude, the flux of number density across the boundary is conserved during the reflection.

Diffuse Boundary

The velocity of each particle after reflection is independent of the incoming velocity in diffuse reflection. Furthermore, the scattering of all particles results in a half Maxwellian at the wall velocity and temperature. Figure

4.18 shows the results of a diffuse reflection both schematically and with a distribution function at a ghost cell:

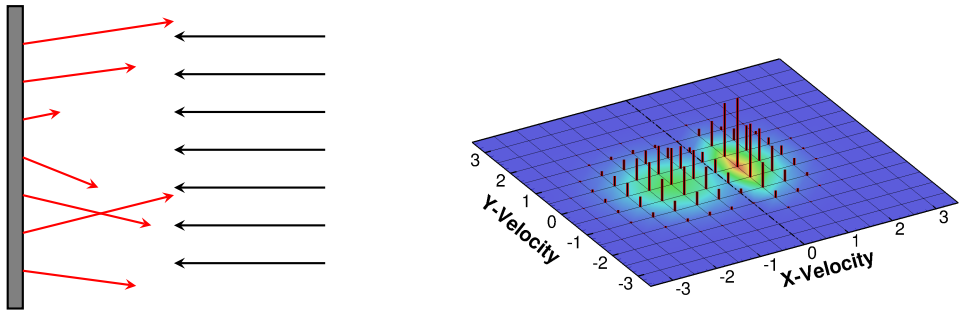

(a) (b)

Figure 4.18: a) Diffuse reflection. b) The distribution function at the ghost cell in diffuse reflection is the incoming flux from $p = 1$ outgoing as a half-Maxwellian with the wall velocity and temperature.

The reflected distribution at the ghost cell is found by first defining a Maxwellian with the wall velocity and temperature, $\hat{f}^{EQ}(\hat{T}_w, \hat{u}_w)$. The flux moving towards the wall at $p = 1$ ($p = p_{max}$) is calculated as:

$$\hat{\varphi}_0 = \hat{n}^* \cdot \hat{f}^{EQ}(\hat{T}_w, \hat{u}_w) \tag{4.43}$$

Where the ghost cell number density, $\hat{n}^*$, is found by matching the number density flux into the wall with the flux back into the domain for the ghost cell.

$$\hat{n}^* = \frac{\sum\limits_{\hat{\eta}_x<0} \hat{\eta}_x \hat{\varphi}_1}{\sum\limits_{\hat{\eta}_x>0} \hat{\eta}_x \hat{f}^{EQ}(\hat{T}_w, \hat{u}_w)} \tag{4.44}$$

Accommodated Boundary

First proposed by Maxwell [117], an accommodated boundary is a combination of specular and diffuse (Maxwell) reflection as shown in Figures 4.19a

and 4.19b. The purpose of the method is to be able to empirically match experimental data for different surfaces.

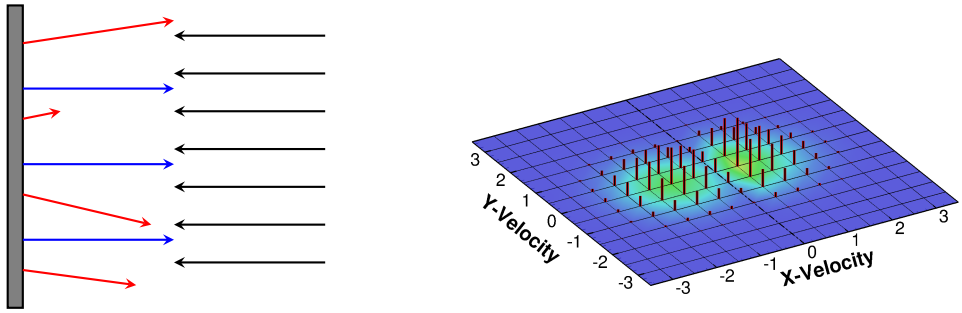

(a) (b)

Figure 4.19: a) Accommodated reflection. b) The distribution function at the ghost cell in accommodated reflection is part diffuse and part specular.

An accommodation coefficient, α, can be defined which controls the fraction of diffuse vs. specular reflection during the boundary calculation. A fully accommodated boundary ($\alpha = 1$) results in purely diffuse reflection, and $\alpha = 0$ results in purely specular reflection.

$$\hat{\varphi}_0 = \alpha \cdot \hat{\varphi}_0^{diffuse} + (1 - \alpha) \cdot \hat{\varphi}_0^{specular} \tag{4.45}$$

Note the number density flux over the boundary is conserved for the accommodated reflection since both diffuse and specular reflection models conserve the number density flux over the boundary individually.

4.4.2 Fixed Properties Boundary Condition

For a fixed properties boundary condition, a Maxwellian is initialized at the boundary every time step. The boundary condition is used for constant inflow where conditions within the domain do not affect conditions upstream of the domain. Denoting LW and RW to symbolize conditions at the left and right wall respectively, the new boundary distribution function becomes:

$$\hat{\varphi}_1(\hat{\eta}) = \hat{n}_{LW} \cdot \hat{f}^E(\hat{T}_{LW}, \hat{u}_{LW}, \hat{\eta}) \tag{4.46a}$$

$$\hat{\varphi}_N(\hat{\eta}) = \hat{n}_{RW} \cdot \hat{f}^E(\hat{T}_{RW}, \hat{u}_{RW}, \hat{\eta}) \tag{4.46b}$$

4.4.3 Zero Gradient Boundary Condition

The zero gradient boundary condition sets the boundary equivalent to the point adjacent to the boundary. This condition is useful for outflow where conditions outside the domain do not propagate into the domain. The boundary distribution functions become:

$$\hat{\varphi}_1(\hat{\eta}) = \hat{\varphi}_2(\hat{\eta}) \tag{4.47a}$$

$$\hat{\varphi}_N(\hat{\eta}) = \hat{\varphi}_{N-1}(\hat{\eta}) \tag{4.47b}$$

4.5 Results

The methods discussed in this chapter (4) have mostly been covered by A. Morris in sufficient detail [5–7, 31], but the effects of a variance reduced collision model are worth emphasizing as well as the physics/methods added in the current work.

4.5.1 BKW Relaxation

We first simulate a 0D relaxation problem to examine the variance reduced collision model and the effects of coarsening the velocity grid. A BKW test case is run with $\hat{n} = 1$, $\hat{T} = 1$, $\hat{m} = 1$, and $C_{RMS} = 0.004$ for the standard full Monte Carlo method (FMC) and the variance reduced method. A small grid spacing of $\hat{\beta} = 0.2$ is used with velocity bounds at $\hat{\eta} = \pm 3.2$. Since number density, velocity, and temperature are constant during the relaxation

process, the 4th and 6th moments as well as entropy are tracked and displayed in Figures 4.20a and 4.20b. The accuracy of the results of the standard FMC method and the variance reduction method are assessed by comparing to the analytic solution. Both collision models match the analytic solutions, and the differences in the 6th moment are plotted in Figure 4.21.

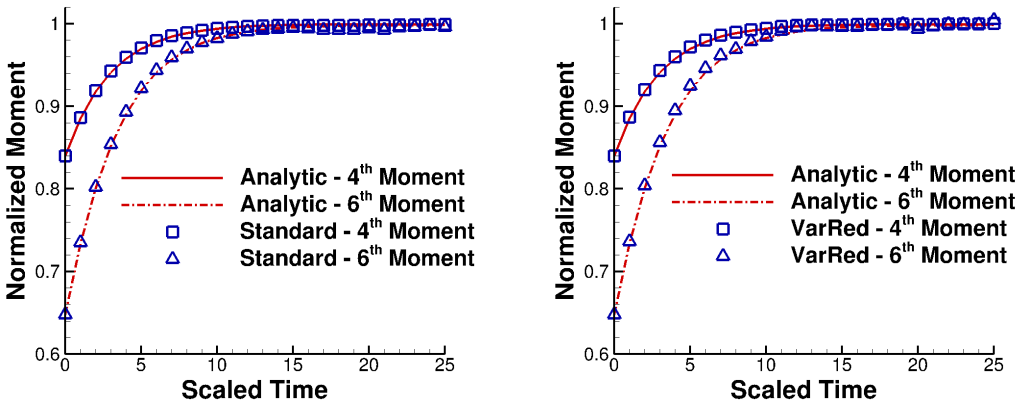

(a) (b)

Figure 4.20: Evolution of the moments for the BKW solution for (a) standard full Monte Carlo and (b) variance reduced methods.

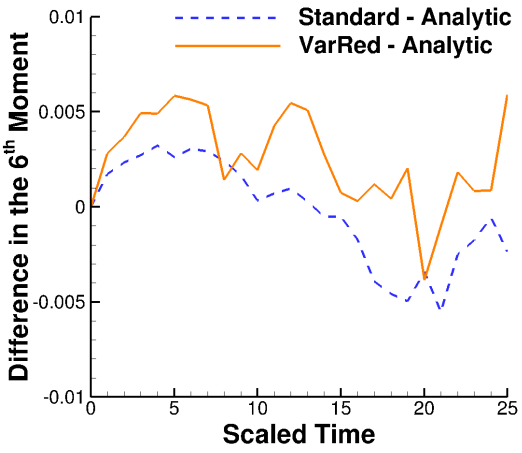

Figure 4.21: Difference between the DVM solution and analytic solution for standard full Monte Carlo and variance reduced collision models.

From the computation times shown in Table 4.2 it is immediately apparent that the variance reduced solution provides a much faster solution. Figure 4.22 illustrates the computational efficiency of the variance reduced method by plotting the number of simulated collisions per time step as the transient solution evolves in time towards equilibrium. The standard FMC method maintains a constant number of collisions during the entire simulation, but the number of collisions in the variance reduced method immediately falls at the start of the relaxation before nearing zero as the entropy reaches its maximum value. This shows how variance reduction can dramatically improve performance for near equilibrium flows.

Table 4.2: Computation time comparison for a BKW relaxation solved with standard full Monte Carlo and variance reduced models run to a scaled time of $\hat{t} = 30$.

Method	**total computation time**
Full Monte Carlo	153.98 s
Variance Reduced	6.99 s

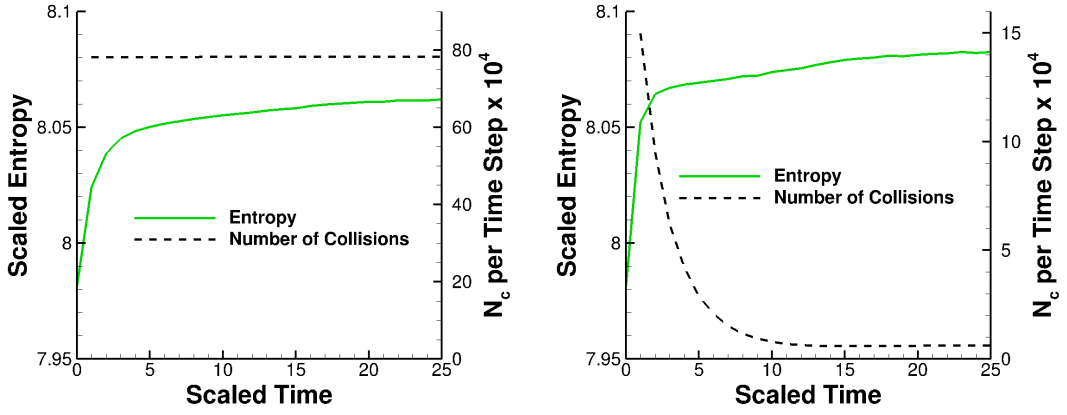

Figure 4.22: Evolution of entropy in comparison to the number of collisions. (a) Full Monte Carlo method: The number of simulated collisions remains constant throughout the simulation. (b) Variance Reduced method: As maximum entropy is reached, the number of collisions falls to zero.

In the above example, the final values of higher order moments are dependent on the discretization of the velocity grid. Figure 4.20 clearly shows good results for a fine grid with $\hat{\beta} = 0.2$. But coarse, uniform grids result in lower moment values at equilibrium than fine grids, and the steady state solution shows weak convergence to the expected equilibrium (discretized Maxwellian) solution as $\hat{\beta} \to 0$. This indicates that the Maxwellian may not be the exact equilibrium solution when discretized using the method discussed previously (Section 3.6). However, there is sufficient accuracy in the relevant macroscopic properties that the problem can be largely ignored, and only when higher order moments are necessary does the velocity grid need to be restricted to small $\hat{\beta}$ values. Furthermore, the issue largely disappears for the variance reduced method. The reason for this result is the variance reduced method assumes the discrete Maxwellian is the correct equilibrium distribution function and reduces the result of collisions between two particles drawn from the distribution to zero. Even if they might result in some small change due to

the discrete Maxwellian not being the exact equilibrium distribution function. The standard FMC and variance reduced BKW relaxations are re-run with $\hat{\beta} = 0.4$ and $\hat{\beta} = 0.64$ and displayed in Figure 4.23 to illustrate the divergence from the correct higher order moment solutions as grid spacing is increased. Notice that along with the divergence from the analytic solution in the standard FMC solution, both methods display increased noise as the grid spacing is increased (to be expected since N_c is a function of $1/\hat{\beta}^3$).

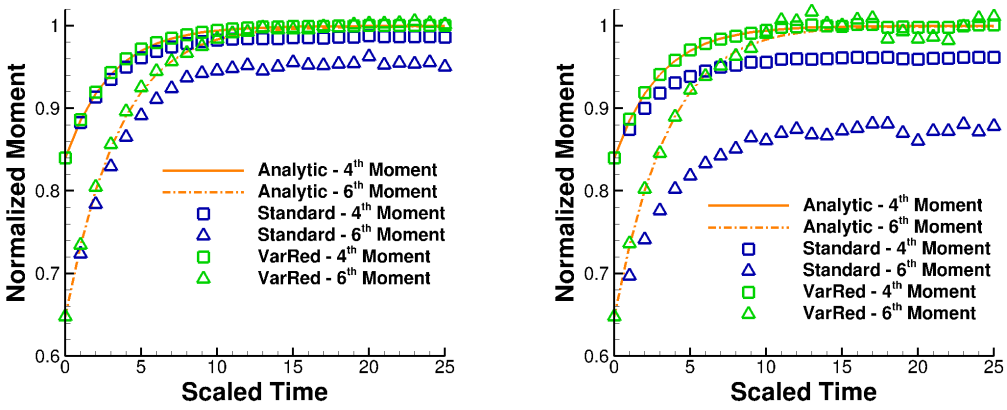

Figure 4.23: Evolution of the 4th and 6th moments for the BKW relaxation with coarse velocity grid spacing of (a) $\hat{\beta} = 0.4$ and (b) $\hat{\beta} = 0.64$.

4.5.2 Collision Cross-Section Models in a 1D Shock

A stationary, Mach 2 1D shock is simulated in argon with upstream conditions seen in Table 4.3. The same conditions are run for four different cross sections: pseudo-Maxwell, hard spheres, VHS, and VSS, and solutions are compared to DSMC solutions generated from Bird's code available on his website and described in his books [2, 45]. All DVM results were simulated using the variance reduced collision model and 1st order finite difference in space. The velocity domain was set with a grid spacing of $\hat{\beta} = 0.6$ and domain

boundaries at $\hat{\eta}_x = [-6.6, 5.4]$ and $\hat{\eta}_{y,z} = [-5.4, 5.4]$. The spatial domain spacing for all shocks is $\Delta x = 0.2\lambda_{ref}$ with 250 grid points, and the boundary condition at the left and right walls are a zero gradient boundary (Section 4.4.3) and a fixed property in-flow boundary (Section 4.4.2) respectively. A time step of $\Delta\hat{t} = 0.02$ gives a CFL number of $|\hat{\eta}|_{max}\frac{\Delta\hat{t}}{\Delta\hat{x}} = 0.66$, which ensures stability. C_{RMS} values of 0.003 are used for all DVM shocks, and DSMC shock are run until fully converged since only a comparison of shock profiles, not computation times, is being made. The shock solutions in Figure 4.24 show good agreement between the methods for each collision cross-section except for some minor differences. Most notably, the distance between density and temperature profiles in the hard sphere collision model are different for DVM and DSMC solutions, and the shock thickness for the VSS collision model for the DVM solution is slightly thinner than the DSMC solution.

Table 4.3: Argon, Mach 2, 1D shock conditions.

Property		**Upstream**	**Downstream**
n	$[1/m^3]$	1.0×10^{20}	2.3×10^{20}
u	$[m/s]$	645.357	282.0
T	$[K]$	300	623.0

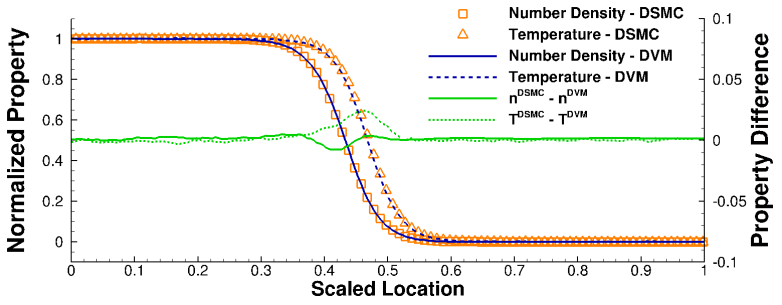

(a)

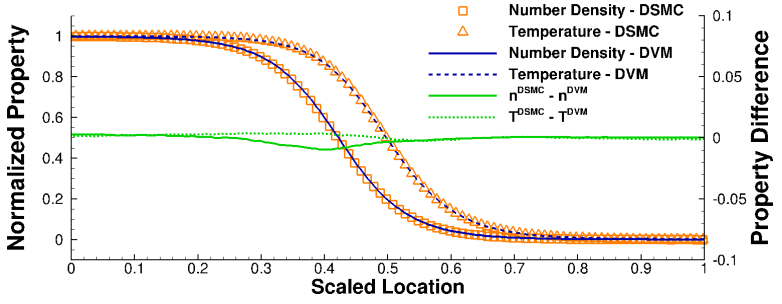

(b)

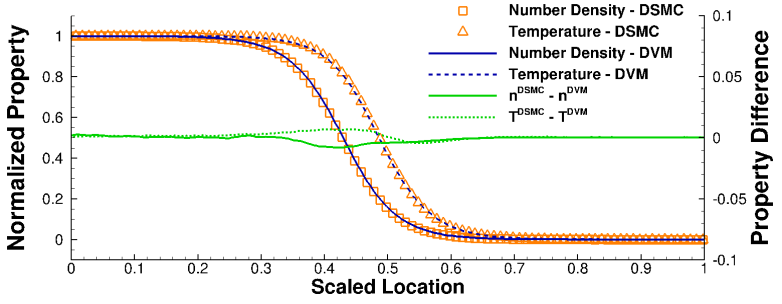

(c)

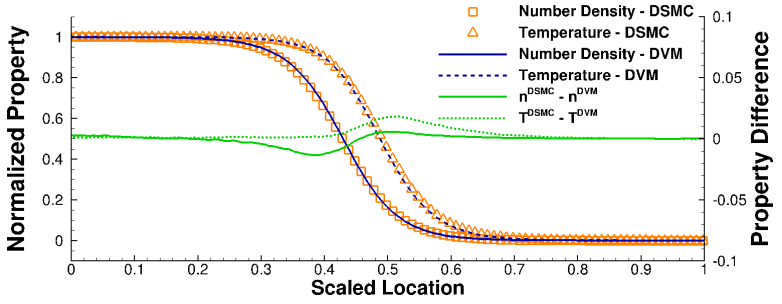

(d)

Figure 4.24: Argon, Mach 2, 1D shock profiles for (a) hard sphere, (b) pseudo-Maxwell, (c) VHS, and (d) VSS collision models.

In Figure 4.25, the number of simulated collisions is overlaid on the VHS shock profile from Figure 4.24 in order to illustrate how the variance reduction method focuses collisions on non-equilibrium regions of the flow while maintaining smooth, low cost solutions in the near-equilibrium regions. Notice the peak of the number of collisions aligns with the midpoint of the temperature profile, not the number density. This indicates the most significant non-equilibrium values of the velocity distribution functions across the spatial domain occur near the midpoint of the temperature profile.

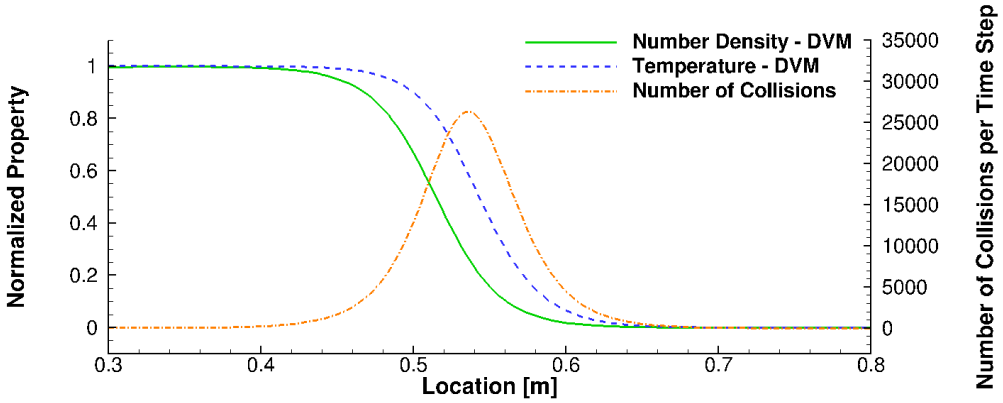

Figure 4.25: Number of collisions simulated using a variance reduced method in an argon, Mach 2, 1D shock.

4.5.3 Channel Flows

Diffuse boundary conditions and flows where $Kn \neq 1$ are tested using Couette flow and Fourier flow simulations. Figure 4.26 shows schematics for continuum channel flows.

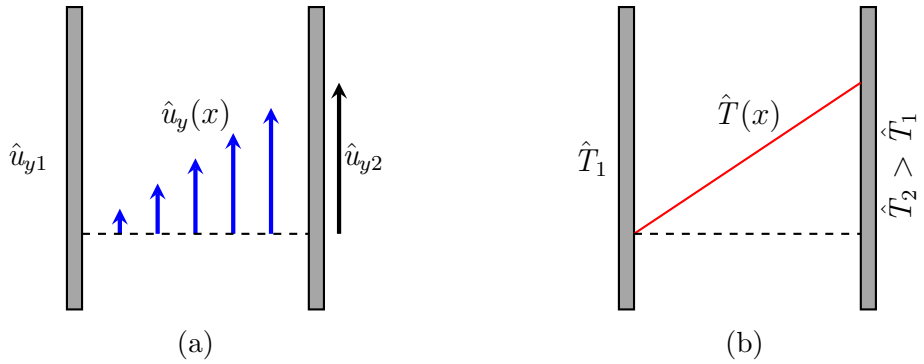

Figure 4.26: (a) Couette and (b) Fourier flow simulations.

Couette Flow

A Couette flow is run for a range of Knudsen numbers from 0.01 to 100. The gas is initially at rest between two plates 1 mm apart with equal temperatures ($T_1 = T_2$). The right wall is then instantaneously accelerated to 100 m/s, and the system is allowed to reach a steady-state solution. An Argon gas is used with a VHS collision model for the simulation. A velocity grid spacing of $\hat{\beta} = 0.5$ is used with velocity bounds at $\hat{\eta} = \pm 3.5$ for all five Knudsen numbers simulated, and the number of collisions is calculated using $C_{RMS} = 0.002$. Table 4.4 shows the flow conditions used for the simulation and Figure 4.27 shows comparisons of the steady-state solutions for y-velocity and temperature. Velocity solutions for the low and high Knudsen number cases approach the analytic solutions presented in Section 3.12, and temperature profiles in Figure 4.27b show a parabolic solution with a small temperature jump at the wall at low Knudsen numbers and a constant temperature profile with a large temperature jump at the wall for high Knudsen number. These solutions are consistent with DSMC, LBE, and numeric results [112, 118, 119].

Table 4.4: Flow conditions

Kn	n $[1/m^3]$	Δx $[mm]$	N_p	$\Delta\hat{t}$
0.01	1.830535×10^{23}	0.01	100	0.001
0.1	1.830535×10^{22}	0.02	50	0.002
1.0	1.830535×10^{21}	0.05	20	0.005
10.0	1.830535×10^{20}	0.05	20	0.005
100.0	1.830535×10^{19}	0.05	20	0.005

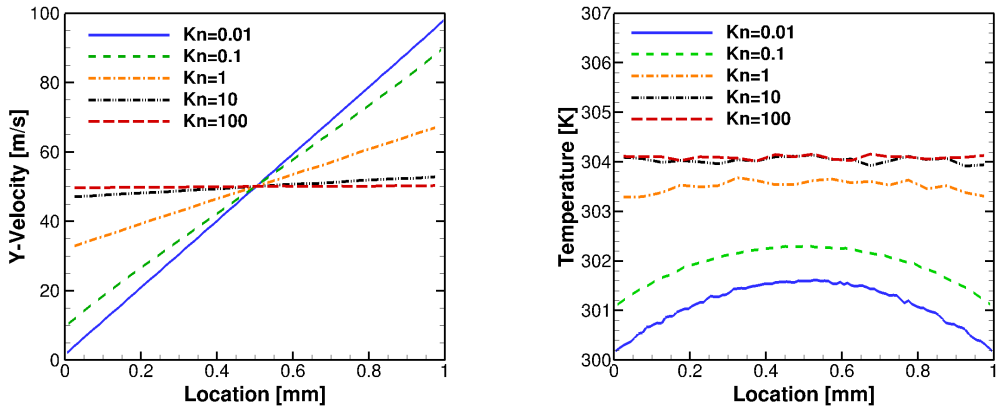

(a) (b)

Figure 4.27: Comparison of the effect of Knudsen number on steady-state (a) y-velocity and (b) temperature profiles in a Couette flow.

The time evolution of the $Kn = 0.1$ case is visualized as well in Figures 4.28 and 4.29. For this case, the number of collisions was calculated using $C_{RMS} = 0.001$. Y-velocity, temperature, and heat flux are plotted as the impulsively started flow develops in time. Relatively smooth transient solutions have been produced without ensemble averaging or a drastic increase in the number of simulated collisions per time step. In Figure 4.28b the difference between the final steady-state solution and an approximated linear slip solution is compared. Note that the deviations $O(0.1m/s)$ are small compared to the velocity and reflect the curvature seen in DSMC and model

solutions [112, 118, 119].

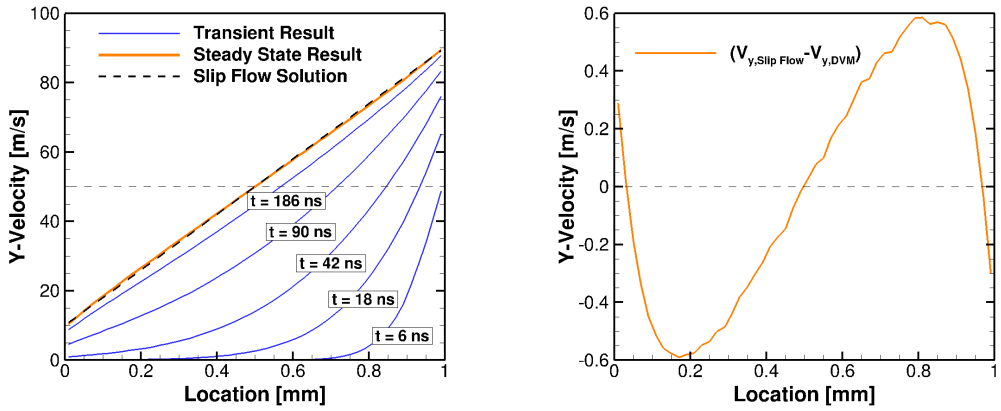

(a) (b)

Figure 4.28: (a) Evolution of y-velocity in a Couette flow for $Kn = 0.1$. (b) The difference between the steady solution and a linear slip line solution.

Figure 4.29 shows the transient solutions for temperature and heat flux. Both properties pulse across the domain, away from the moving wall, before reaching steady-state solutions which match results predicted by theory [15].

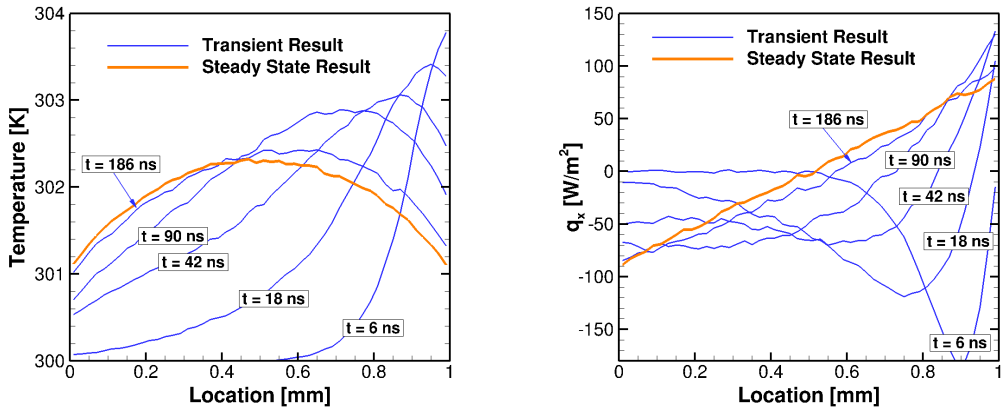

(a) (b)

Figure 4.29: Evolution of (a) temperature and (b) heat-flux in a Couette flow for $Kn = 0.1$.

Fourier Flow

A Fourier flow solution is run on the same spatial domain as the Couette flow solutions over the same range of Knudsen numbers (Table 4.4). The initial gas is pure Argon at rest with a temperature of $T = 300$K, and at the start of the simulation the right wall is instantaneously heated to 375K. There are $N = 16^3$ number of velocity grid nodes per spatial location with a velocity grid spacing of $\hat{\beta} = 0.467$ and a velocity domain of $\hat{\eta} = \pm 3.5$, and the number of simulated collisions is calculated with $C_{RMS} = 0.004$. Pseudo-Maxwell molecules were used in this simulation to match theoretical results presented in Section 3.12. Each simulation is allowed to run to a steady-state solution, and the results are shown in Figures 4.30 for temperature and heat flux. The solutions approach predicted analytic results at low and high Knudsen numbers, and intermediate temperature results display the temperature jump and profile curvature seen in DSMC and LBE solutions [111–113].

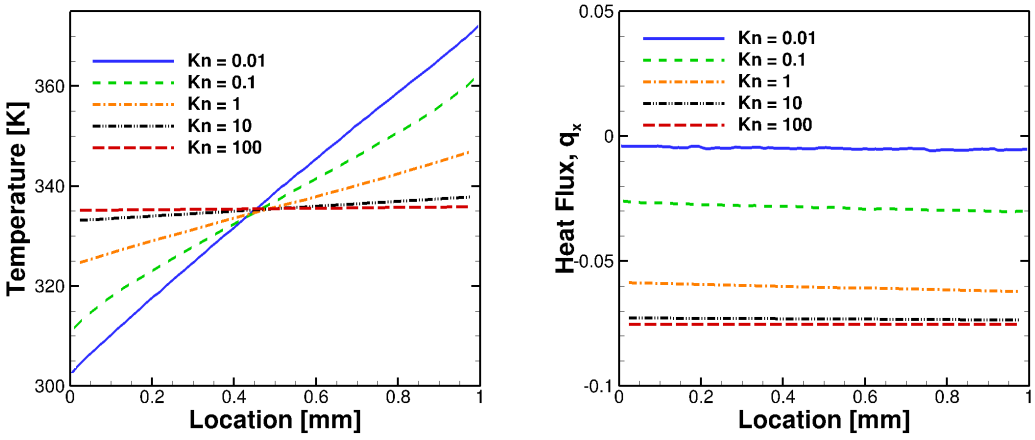

(a) (b)

Figure 4.30: Comparison of the effect of Knudsen number on steady-state (a) temperature and (b) heat flux profiles in a Fourier flow.

The time evolution of the $Kn = 0.1$ case is visualized as well in Figures 4.31. For this case the number of simulated collisions was calculated using $C_{RMS} = 0.002$. Temperature and density are plotted at progressive times, and the solutions show a wave created by the change in temperature bouncing between the two walls before coming to a final, steady solution. Note the smoothness of the transient solutions. Also note that the curvature of the steady-state solution matches trends seen in DSMC and other models [111–113].

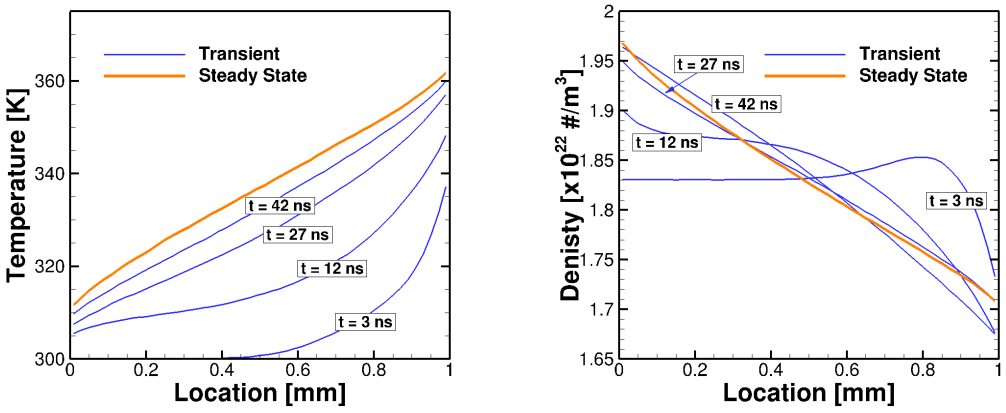

(a) (b)

Figure 4.31: Evolution of (a) temperature and (b) number density in a Fourier flow for $Kn = 0.1$

4.5.4 Expansion into a Vacuum

A final 1D flow is modeled as an analog of expansion into a vacuum. A domain is initialized with the two regions shown in Figure 4.32: a long section under a vacuum and a short section filled with Argon at $P = 100$ Pa and $T = 300$ K. The ratio between sections is 9:1.

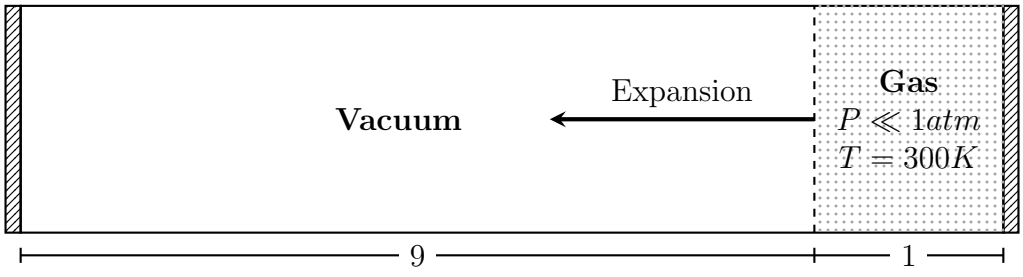

Figure 4.32: 1D expansion of argon into a vacuum.

A total of 1000 spatial grid points are used ($\Delta\hat{x} = 0.5$), a first order finite difference method is implemented, and the domain is capped by diffuse boundary conditions at each end. The velocity grid structure has a grid spacing

of $\hat{\beta} = 0.5$ with velocity bounds at $\hat{\eta} = \pm 3.5$, and the number of simulated collisions is calculated using $C_{RMS} = 0.004$. The density profiles in Figure 4.33a display the flow expanding into the vacuum section of the domain where high velocity particles travel in nearly collisionless flow towards the left wall followed by a larger density of slower moving particles. As particles begin to reach the left wall, they are reflected back forming a shock wave which travels upstream to the right. To the right of the initial contact surface an expansion wave travels upstream before reflecting off the right wall. The time it takes the first particle to reach the left wall is determined by the maximum velocity location on the velocity grid used for the simulation. Log plots of the number density profiles at various times in Figure 4.33b show accurate modeling of extremely small values (only limited by the computational precision of the machine used for the simulation) located at the front of the flow into the vacuum.

The ability to visualize very small density values is a potentially significant benefit of discrete velocity methods. The log plot of density also reveals the errors in the solution due to a discrete velocity approximation. As time progresses, high velocity particles separate from slower velocity particles, and due to the discrete nature of the velocity domain where no particles exist except at a finite set of velocities, "lumps" in the density distribution form. The errors could be mitigated by either increasing the number of velocity grid points or by increasing the order of the finite difference method.

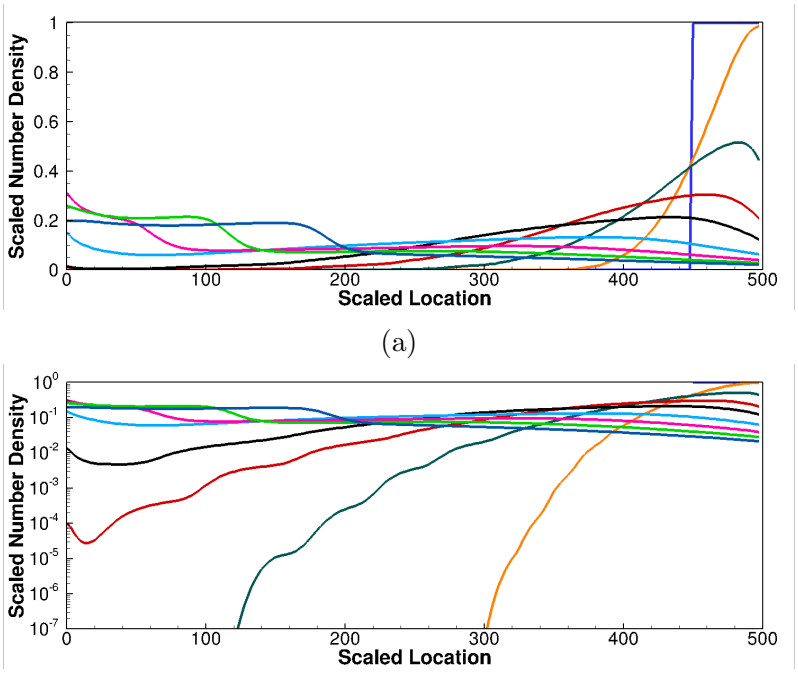

Figure 4.33: (a) Number density and (b) log number density profiles over time. The initial pressurized section is on the right of the profile.

The evolution of velocity in the x-direction presented in Figure 4.34 displays the same lumps discovered in the log plot of number density. Also, the maximum velocity of the discrete grid can be seen from the constant value leading the expansion, and maximum speed particles reach the wall when particles from the second fastest velocity class are significantly far behind.

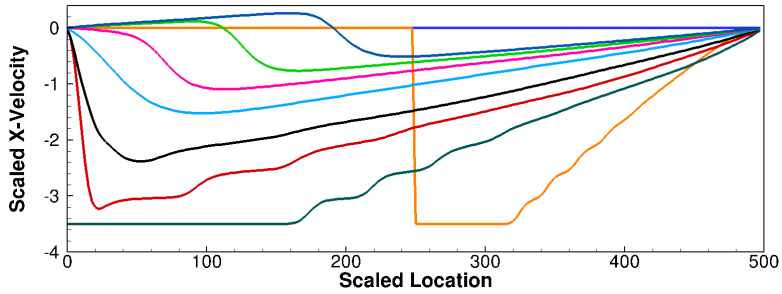

Figure 4.34: X-velocity profile over time.

As particles collide with the diffuse wall on the evacuated side of the domain, they impart a force on the wall. Initially only a very small number of particles with high velocities reach the domain boundary, but the method still manages to smoothly capture the imparted force on the diffuse wall. As a greater number density of particles with moderate velocity reach the wall, the force rapidly increases until a peak pressure is reached. The gas at the wall begins to equilibrate to the wall conditions, and the force in the wall drops to an equilibrium state.

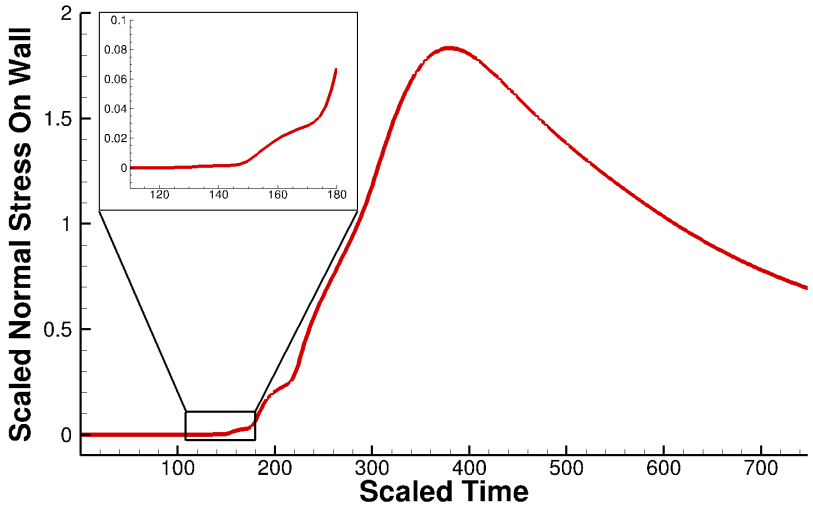

Figure 4.35: Force exerted on a diffuse wall due to particles.

4.6 Conclusions

In this chapter, a stochastic discrete velocity method for solving the Boltzmann equation was presented for a single, monatomic species defined on a uniform velocity grid. The majority of the work shown was completed by Morris, Varghese, and Goldstein [5,28,30,31], but several new additions to the method were made including: new collision cross-section models, diffuse and accommodated wall boundary conditions, Knudsen numbers not equal to 1, and a variety of improvements to stability and computational efficiency.

First, the computational differences between standard FMC and variance reduced collision models were displayed by a BKW relaxation. At the same time, the effect of grid spacing on higher order moments was investigated over several values of $\hat{\beta}$. It was seen that representing higher order moments accurately using the full Monte Carlo method required a grid spacing of $\hat{\beta} \leq 0.4$. However, accurately modeling high order moments is a rather stringent measure and most simulations only require accuracy up to the 2nd (temperature) or 3rd (heat flux) moment. Furthermore, the issue is mostly mitigated in the variance reduced method. Therefore a grid spacing of $\hat{\beta} \leq 0.8$ is generally acceptable. Next, good agreement was seen in a Mach 2, Argon, 1D shock for hard sphere, pseudo-Maxwell, VHS, and VSS cross-section models when compared with DSMC solutions. Diffuse boundary conditions and flow with $Kn \neq 1$ were demonstrated for basic Couette and Fourier flows across a range of Knudsen numbers. Accurate steady-state solutions were seen in several macroscopic properties, and clean transient solutions could also be visualized in both simulations. Expansion into a vacuum displayed the discrete velocity method's capabilities of handling very low density values and forces as well as vacuum conditions.

Chapter 5

Nonuniform Velocity Grids

Uniform Cartesian velocity grids work well for a large number of problems. However, for some common simulations such as highly non-equilibrium flows or flows with large gradients, uniform grids are unnecessarily expensive. For instance, in a high Mach number shock the upstream distribution is cold and fast but the downstream distribution is very hot and slower as shown in Figure 5.1. The downstream distribution requires a grid with a large domain and relatively coarse grid spacing but the upstream distribution requires a fine enough grid to fully resolve a narrow (cold) distribution. This means if we maintain the same grid throughout physical space the downstream grid will be overly resolved and the upstream grid will have too large of a domain (a lot of velocity space with no mass). In other simulations the conditions described may even occur at the same physical location over time; a moving shock would be a relevant example.

P. Clarke, P. Varghese, and D. Goldstein, A. Morris, P. Bauman, and D. Hegermiller, "A novel discrete velocity method for solving the Boltzmann equation including internal energy and variable grids in velocity space," in *Proceedings of the* 28th *International Symposium on Rarefied Gas Dynamics*, vol. 1501, (Zaragosa, Spain), p. 373, AIP Conference Proceedings, 2012.

P. Varghese and D. Goldstein supervised the project, A. Morris and D. Hegermiller collaborated on research ideas, and P. Bauman provided coding implementation support.

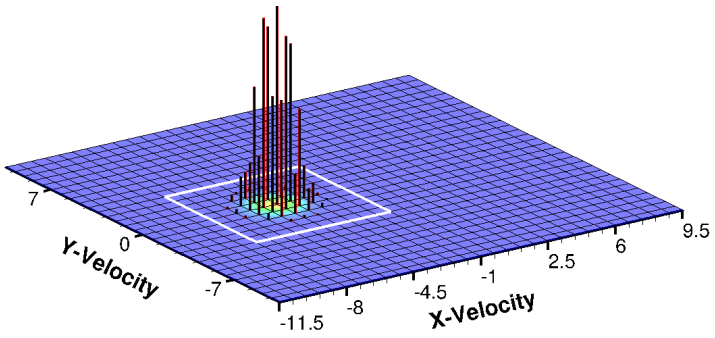

(a) Upstream distribution.

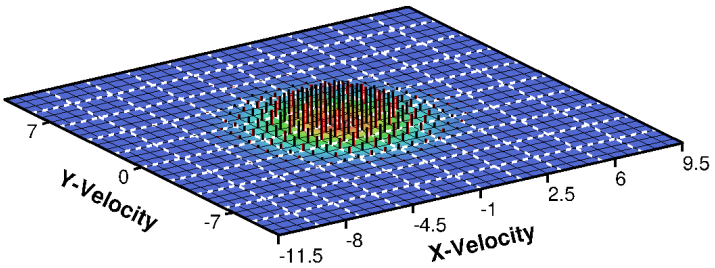

(b) Downstream distribution.

Figure 5.1: In a Mach 9 shock (a) a fine grid is necessary to resolve the cold upstream distribution. The white rectangle around the distribution shows the ideal domain bounds. (b) Downstream the distribution matches the domain size but is extremely over-refined. Dashed white lines show ideal grid spacing.

To combat the problem described, non-uniform Cartesian velocity grids were implemented in the discrete velocity method. Grid lines can be realigned as shown in Figure 5.2, but octree and other more complex types of grids, which would be even more efficient, are not implemented in the current version of the DVM code.

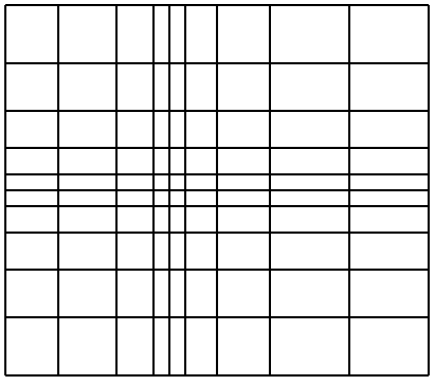

Figure 5.2: Example of a realigned velocity grid with points focused about a particular velocity.

The change from uniform velocity grid spacing to a nonuniform grid spacing requires both some basic and complicated changes to the DVM algorithm. In the monatomic version, the grid was normalized such that each node was located at an integer value [5]. Obviously, these normalizations can no longer be applied to uniform grid spacing because the distance between two adjacent points will not be constant. Along with removal of the normalization mentioned, delta function construction, collision quantities which are dependent on grid spacing, and the remapping scheme must all be revisited.

5.1 Definition of the Volume Element

Each grid spacing component $\hat{\beta}_{x,y,z}$ must be calculated in order to determine the initial distribution (equation 3.21) and equilibrium distributions for the variance reduced model (Section 4.1.2). Since the grid is now assumed to be non-uniform in nature, each velocity grid point in not necessarily equidistant from its nearest neighbors. Instead, each component of the volume element is calculated from the average distance between a velocity location and the adjacent points:

$$\beta_{x_i} = \frac{1}{2}|\hat{x}_i - \hat{x}_{i-1}| + \frac{1}{2}|\hat{x}_{i+1} - \hat{x}_i| \tag{5.1}$$

Since the grid spacing in each direction is no longer equal, the volume element $\hat{\beta}^3$ is expressed as $\hat{\beta}_x\hat{\beta}_y\hat{\beta}_z$ where the values of each component may be unique to each individual point on the velocity grid. Figure 5.3 shows a 2D representation of the volume element by the shaded (1) region.

Equation 5.1 cannot be applied to the edges of the domain since either $\hat{x}_{i-1}$ or $\hat{x}_{i+1}$ do not exist at the edge. Three options can be explored as seen in Figure 5.3. Since distribution functions generally follow an exponential relation where the wings fall to zero as the domain approaches infinity, extending the volume element outwards extensively (2) tends to overestimate the number density, but limiting the volume element to inside the domain boundaries (4) tends to underestimate the number density and higher order moments. Velocities at the domain boundaries tend to be large, and small errors in number density correspond to more significant errors in temperature and other higher order moments. Therefore (3) is currently implemented in the DVM code.

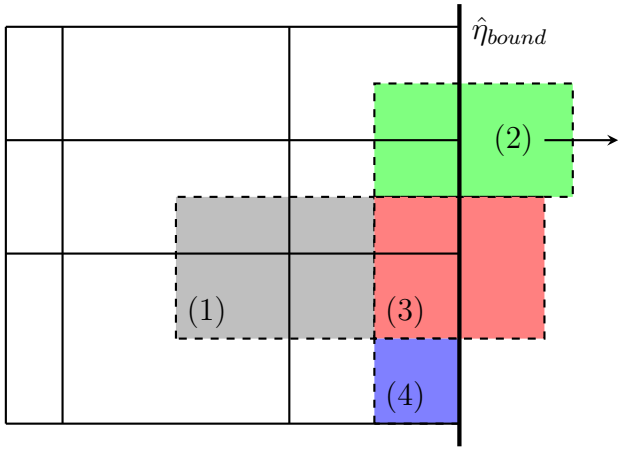

Figure 5.3: (1) Each point in the interior of the grid represents a set volume based on half the distance to the next closest point. Points on the edges: (2) the volume can extend an arbitrary distance out, (3) be double the volume that is in the interior, or (4) not include any exterior volume.

The new definition of the volume element is applied to the discretization process and the magnitude of the velocity distribution delta functions, described by equation 3.21, is rewritten as:

$$\hat{\varphi}(\hat{\eta}) = \hat{n} \cdot \hat{f}(\hat{\eta}) \cdot \hat{\beta}_x \hat{\beta}_y \hat{\beta}_z \tag{5.2}$$

Typically, the number of simulated collisions per time step is calculated as a function of the grid spacing (equation 4.9). However, the grid spacing is now non-uniform, and a new quantity must be used for finding N_c. Both the average grid spacing and the minimum grid spacing have been explored as possible options and each works best for particular distributions and corresponding grids. Use of minimum grid spacing is best when the majority of the density is located across the points with the finest resolution. However, if the density isn't concentrated at the finest resolution, more collisions than necessary to produce smooth solutions will be simulated. For situations with

minor changes in grid spacing or when density is spread throughout the fine and coarse resolutions of the domain, taking the average grid spacing works well. However, when density is concentrated at the finest resolutions, fewer collisions than necessary to produce smooth solutions will be simulated and statistical noise will be introduced into the result. The two options for N_c are:

$$N_c = nint\left(\frac{\Delta\hat{t}\cdot\hat{T}^{2/3}}{Kn\cdot C_{RMS}^2\cdot(\beta_x\beta_y\beta_z)_{avg}}\right) \tag{5.3a}$$

$$N_c = nint\left(\frac{\Delta\hat{t}\cdot\hat{T}^{2/3}}{Kn\cdot C_{RMS}^2\cdot(\beta_x\beta_y\beta_z)_{min}}\right) \tag{5.3b}$$

5.2 Non-Uniform Remapping

The interpolation scheme developed by Varghese [30] and presented in Section 4.1.3 must be generalized to account for a non-uniform grid. Mass, momentum, and energy conservation will be enforced as before, and the stencil will continue to have five to seven points: an origin point, three internal points on the frame around the point to be mapped back onto the grid, and one to three external points outside the frame. The non-uniform stencil is shown in Figure 5.4, and all stencil velocities are defined relative to the origin.

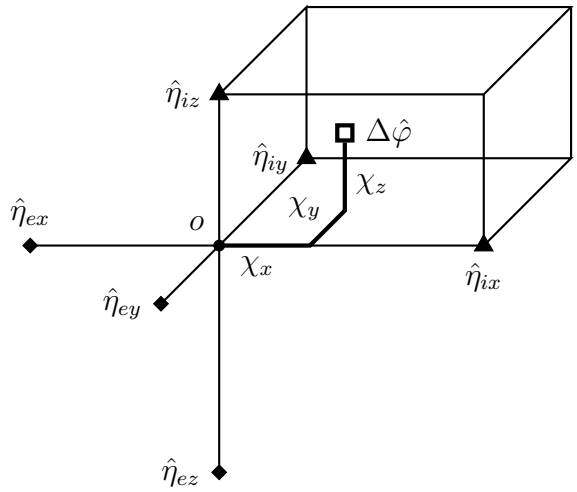

Figure 5.4: Remapping stencil for a non-uniform velocity grid. $\hat{\eta}_{ie,xyz}$ are the relative x, y, z velocity components of an internal/external stencil point, χ_{xyz} are the relative x, y, z velocity components of the off-grid replenishment location, and $\Delta\hat{\varphi}$ is the total replenishment number density.

Since three external points are being used where only a single point is necessary, density must be split between the points. There are three obvious ways to split the density: equal density at each point, equal momentum, or equal energy.

5.2.1 Equal Density Remapping

The first option is to distribute the density equally to each external point such that:

$$\Delta\hat{\varphi}_{ex} = \Delta\hat{\varphi}_{ey} = \Delta\hat{\varphi}_{ez} = \Delta\hat{\varphi}_{ext} \tag{5.4}$$

Using conservation of mass, momentum, and energy, and defining $\chi_x^2 + \chi_y^2 + \chi_z^2 = \chi^2$, a system of equations can be written:

$$\begin{bmatrix} 1 & 1 & 1 & 1 & 3 \\ 0 & \hat{\eta}_{ix} & 0 & 0 & \hat{\eta}_{ex} \\ 0 & 0 & \hat{\eta}_{iy} & 0 & \hat{\eta}_{ey} \\ 0 & 0 & 0 & \hat{\eta}_{iz} & \hat{\eta}_{ez} \\ 0 & \hat{\eta}_{ix}^2 & \hat{\eta}_{iy}^2 & \hat{\eta}_{iz}^2 & (\hat{\eta}_{ex}^2 + \hat{\eta}_{ey}^2 + \hat{\eta}_{ez}^2) \end{bmatrix} \begin{bmatrix} \Delta\hat{\varphi}_o \\ \Delta\hat{\varphi}_{ix} \\ \Delta\hat{\varphi}_{iy} \\ \Delta\hat{\varphi}_{iz} \\ \Delta\hat{\varphi}_{ext} \end{bmatrix} = \Delta\hat{\varphi} \cdot \begin{bmatrix} 1 \\ \chi_x \\ \chi_y \\ \chi_z \\ \chi^2 \end{bmatrix} \tag{5.5}$$

And the conservation equations are solved in Appendix C for the following remapping densities:

$$\Delta\hat{\varphi}_{ext} = \Delta\hat{\varphi} \cdot \frac{\sum_{k=xyz} [\chi_k(\chi_k - \hat{\eta}_{ik})]}{\sum_{k=xyz} [\hat{\eta}_{ek}(\hat{\eta}_{ek} - \hat{\eta}_{ik})]} \tag{5.6a}$$

$$\Delta\hat{\varphi}_{ik} = \frac{\chi_k \Delta\hat{\varphi} - \hat{\eta}_{ek}\Delta\hat{\varphi}_{ext}}{\hat{\eta}_{ik}}; \quad k = x, y, z \tag{5.6b}$$

$$\Delta\hat{\varphi}_o = \Delta\hat{\varphi} - \Delta\hat{\varphi}_{ix} - \Delta\hat{\varphi}_{iy} - \Delta\hat{\varphi}_{iz} - 3 \cdot \Delta\hat{\varphi}_{ext} \tag{5.6c}$$

Inspection of equation 5.6a reveals a singularity at $\hat{\eta}_{e,k} = 0$. When all three external velocity locations approach the origin of the remapping stencil as illustrated in Figure 5.5, a large negative density is created, and the negative density is offset by a large positive density created at the origin of the stencil. These densities can become large enough such that more density is being moved to the origin of the remapping stencil than was originally depleted from the pre-collision velocity locations.

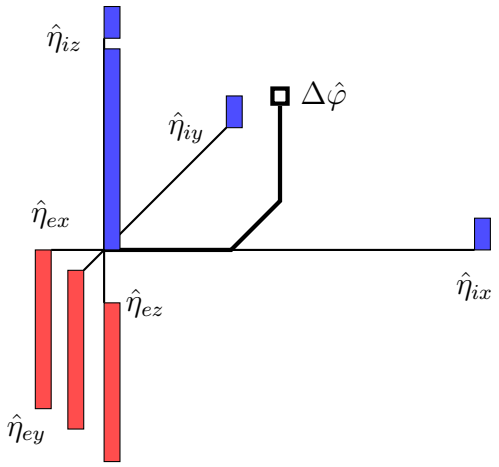

Figure 5.5: Remapping scheme result with equal mass sent to each external point and all three external points located near the origin.

5.2.2 Equal Momentum Remapping

In order to split the external mass between points based on equal momentum, we first define M as:

$$M \equiv |\hat{\eta}_{ex}|\Delta\hat{\varphi}_{ex} = |\hat{\eta}_{ey}|\Delta\hat{\varphi}_{ey} = |\hat{\eta}_{ez}|\Delta\hat{\varphi}_{ez} \tag{5.7}$$

Defining $\chi_x^2 + \chi_y^2 + \chi_z^2 = \chi^2$ and $\Delta\hat{\varphi}_{ex} + \Delta\hat{\varphi}_{ey} + \Delta\hat{\varphi}_{ez} = \Delta\hat{\varphi}_{ext,tot}$, the conservation equations become:

$$\begin{bmatrix} 1 & 1 & 1 & 1 & \Delta\hat{\varphi}_{ext,tot}/M \\ 0 & \hat{\eta}_{ix} & 0 & 0 & sgn(\hat{\eta}_{ex}) \\ 0 & 0 & \hat{\eta}_{iy} & 0 & sgn(\hat{\eta}_{ey}) \\ 0 & 0 & 0 & \hat{\eta}_{iz} & sgn(\hat{\eta}_{ez}) \\ 0 & \hat{\eta}_{ix}^2 & \hat{\eta}_{iy}^2 & \hat{\eta}_{iz}^2 & (|\hat{\eta}_{ex}| + |\hat{\eta}_{ey}| + |\hat{\eta}_{ez}|) \end{bmatrix} \begin{bmatrix} \Delta\hat{\varphi}_o \\ \Delta\hat{\varphi}_{ix} \\ \Delta\hat{\varphi}_{iy} \\ \Delta\hat{\varphi}_{iz} \\ M \end{bmatrix} = \Delta\hat{\varphi} \cdot \begin{bmatrix} 1 \\ \chi_x \\ \chi_y \\ \chi_z \\ \chi^2 \end{bmatrix} \tag{5.8}$$

And the conservation equations are solved in Appendix C for M as:

$$M = \frac{\Delta\hat{\varphi} \sum\limits_{k=xyz} [\chi_k(\chi_k - \hat{\eta}_{ik})]}{S} \tag{5.9}$$

Where the sum of the absolute values of the relative velocities is defined as $S = |\hat{\eta}_{ix}|+|\hat{\eta}_{iy}|+|\hat{\eta}_{iz}|+|\hat{\eta}_{ex}|+|\hat{\eta}_{ey}|+|\hat{\eta}_{ez}|$. With M determined, the remapping densities can be calculated as:

$$\Delta\hat{\varphi}_{ek} = \frac{M}{|\hat{\eta}_{ek}|}; \quad k = x, y, z \tag{5.10a}$$

$$\Delta\hat{\varphi}_{ik} = \frac{\chi_k \Delta\hat{\varphi} + M}{|\hat{\eta}_{ik}|}; \quad k = x, y, z \tag{5.10b}$$

$$\Delta\hat{\varphi}_o = \Delta\hat{\varphi} - \sum_{k=xyz} [\Delta\hat{\varphi}_{ik} + \Delta\hat{\varphi}_{ek}] \tag{5.10c}$$

In this case, a singularity occurs when any $\hat{\eta}_{ek} = 0$. Therefore, when any single external velocity location approaches the origin as in Figure 5.6, a large amount of negative density is created at the close proximity external point. The negative density is balanced by a large positive density at the origin in the same manner as the equal density case.

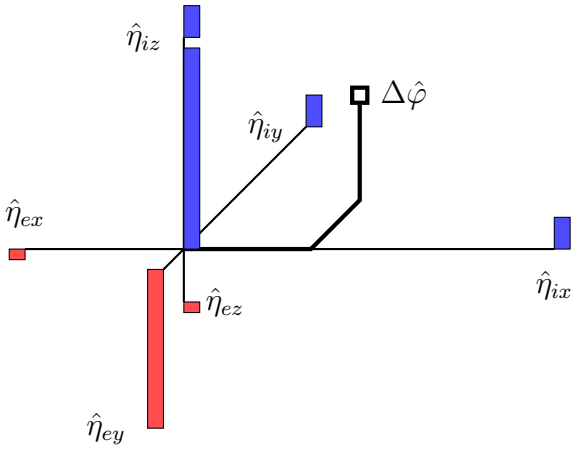

Figure 5.6: Remapping scheme result with equal momentum sent to each external point and one external point located near the origin.

5.2.3 Equal Energy Remapping

For equal kinetic energy at external interpolation points, E is defined as:

$$E \equiv \hat{\eta}_{ex}^2 \Delta\hat{\varphi}_{ex} = \hat{\eta}_{ey}^2 \Delta\hat{\varphi}_{ey} = \hat{\eta}_{ez}^2 \Delta\hat{\varphi}_{ez} \tag{5.11}$$

Defining $\chi_x^2 + \chi_y^2 + \chi_z^2 = \chi^2$ and $\Delta\hat{\varphi}_{ex} + \Delta\hat{\varphi}_{ey} + \Delta\hat{\varphi}_{ez} = \Delta\hat{\varphi}_{ext,tot}$, the conservation equations become:

$$\begin{bmatrix} 1 & 1 & 1 & 1 & \Delta\hat{\varphi}_{ext,tot}/E \\ 0 & \hat{\eta}_{ix} & 0 & 0 & 1/\hat{\eta}_{ex} \\ 0 & 0 & \hat{\eta}_{iy} & 0 & 1/\hat{\eta}_{ey} \\ 0 & 0 & 0 & \hat{\eta}_{iz} & 1/\hat{\eta}_{ez} \\ 0 & \hat{\eta}_{ix}^2 & \hat{\eta}_{iy}^2 & \hat{\eta}_{iz}^2 & 3 \end{bmatrix} \cdot \begin{bmatrix} \Delta\hat{\varphi}_o \\ \Delta\hat{\varphi}_{ix} \\ \Delta\hat{\varphi}_{iy} \\ \Delta\hat{\varphi}_{iz} \\ E \end{bmatrix} = \Delta\hat{\varphi} \cdot \begin{bmatrix} 1 \\ \chi_x \\ \chi_y \\ \chi_z \\ \chi^2 \end{bmatrix} \tag{5.12}$$

And the conservation equations are solved in Appendix C for E as:

$$E = \frac{\Delta\hat{\varphi} \sum\limits_{k=xyz} [\chi_k(\chi_k - \hat{\eta}_{ik})]}{3 - \sum\limits_{k=xyz} (\hat{\eta}_{ik}/\hat{\eta}_{ek})} \tag{5.13}$$

And the remapping densities can be calculated once E is determined as:

$$\Delta\hat{\varphi}_{ek} = \frac{E}{\hat{\eta}_{ek}^2}; \quad k = x, y, z \tag{5.14a}$$

$$\Delta\hat{\varphi}_{ik} = \frac{\chi_k \Delta\hat{\varphi} - E/\hat{\eta}_{ek}^2}{\hat{\eta}_{ik}}; \quad k = x, y, z \tag{5.14b}$$

$$\Delta\hat{\varphi}_o = \Delta\hat{\varphi} - \sum_{k=xyz} [\Delta\hat{\varphi}_{ik} + \Delta\hat{\varphi}_{ek}] \tag{5.14c}$$

The results in equations 5.14 produce large negatives in the limit of $\hat{\eta}_{ek} \to 0$, just like the equal momentum case. However, the large negative is

primarily balanced at the opposite internal points, $\hat{\eta}_{iy}$ in Figure 5.7, instead of the origin.

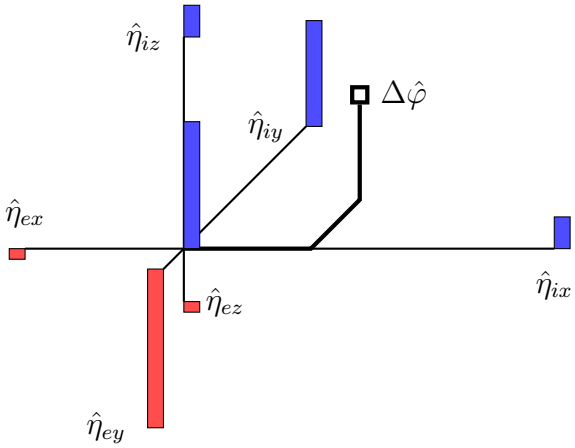

Figure 5.7: Remapping scheme result with equal energy sent to each external point and one external point located near the origin.

5.2.4 Selection of a Method

Inspecting the equations for each method reveals that using equal momentum or equal energy can result in excessively large negative and positive mass transfers to stencil locations when the external points become close to the origin with respect to the internal points ($\hat{\eta}_e/\hat{\eta}_i \rightarrow 0$). The large remapping fractions effect the distribution function by creating distortions near stretching locations that translate to errors in higher order moments. Equal mass splitting is the most robust of the three options, only creating large remapping fractions if all three external points move towards the origin together.

A conjecture is made that the distortions may be considered insignificant if the origin remapping fraction and the sum of external remapping fractions remain below 1. The curves in Figure 5.8 show the relation for $\hat{\eta}_e/\hat{\eta}_i$ in a worst case scenario where the post-collision velocity location is halfway

between the origin and each of the internal points. All three of the external points are moved towards the origin at the same rate, and equal mass splitting is implemented.

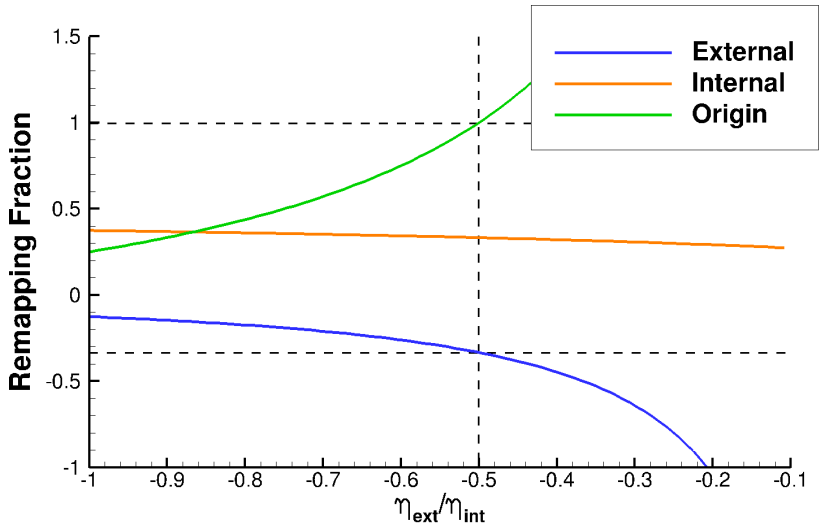

Figure 5.8: Relation between the closeness of external points to the origin with respect to internal points and the remapping fraction at each stencil location.

It can be seen that the requirements we have placed on the remapping fraction is met if $\hat{\eta}_e/\hat{\eta}_i > 0.5$. That is, only cell to cell stretching of a factor of two or less is allowed in velocity space.

5.3 Results

One of the biggest benefits of a non-uniform grid is maintaining the accuracy of a more refined uniform grid while matching the computational cost of a coarse uniform grid. A BKW distribution with macroscopic properties of $\hat{T} = 1$, $\hat{n} = 1$, and $\hat{m} = 1$ is defined on a non-uniform velocity grid and the relaxation is compared with relaxations of the same distribution defined on finely discretized and coarsely discretized uniform velocity grids. The properties of the velocity grid for all three cases are shown in Table 5.1. Note the

domain boundaries are the same, and the non-uniform grid shown in Figure 5.9a is defined with the same number of velocity points in each velocity direction as the coarse grid. Grid points are concentrated around the center of the distribution without making any major jumps in $\hat{\beta}$.

Table 5.1: Velocity grid properties.

Grid	$\hat{\eta}$ bounds	N_v	$\hat{\beta}_{min,max}$
Uniform Fine	$[-4.5,\ 4.5]$	19^3	0.5
Uniform Coarse	$[-4.5,\ 4.5]$	11^3	0.8
Nonuniform	$[-4.5,\ 4.5]$	11^3	$(0.4, 0.8)$

Using the evolution of the 4th and 6th moments to evaluate solution accuracy, Figure 5.9b shows that the solution using the non-uniform velocity space grid shows comparable accuracy to the solution on the fine grid while the solution on the coarse grid of the relaxation from initial to steady state ($\hat{t} = 2$) is significantly less accurate. The computational time to steady state for the non-uniform grid was slightly longer than the solution time for the coarse grid but much shorter than the solution time for the fine grid by a factor of almost 2.5. It should be noted that a grid that gives a systematic error of almost 20% in the computation of the 4th moment is inadequate for most practical purposes, so the slightly shorter computation time for the coarse grid relative to the non-uniform grid is not a significant advantage.

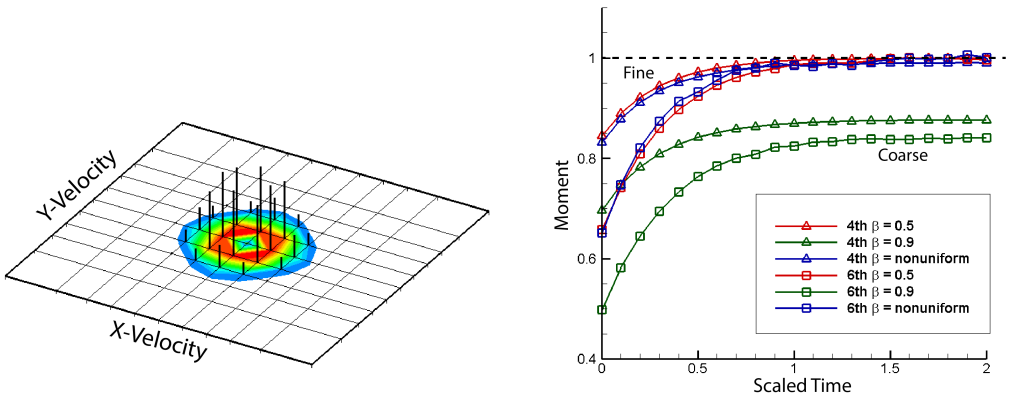

(a) (b)

Figure 5.9: a) Nonuniform velocity grid used for the grid comparison test. Grid points are squeezed towards the center of the distribution. b) 4th and 6th moments of velocity grids with small, large, and non-uniform grid spacing.

The results in Figure 5.9b show how non-uniform grids can be used to group points around high mass regions of the velocity distribution while maintaining a large domain. However, the locations for focusing fine and coarse grid resolutions may change based on the relevant quantities of interest and flow conditions, and the grid lines may also be grouped around a variety of different features of the distribution including high velocities or large gradients. The optimal parameter for determining velocity grid structure should be a focus of future work on the discrete velocity method, but is outside the current scope of this work.

A 1D shock at Mach 9 is run on the uniform grid shown in Figure 5.10a, and compared to the same shock simulated on the non-uniform grid shown in Figure 5.10b. The uniform grid spacing is equal to the finest region of the non-uniform velocity grid. The grid structure for both cases is displayed in Table 5.2, the spatial grid had a spacing of $\Delta\hat{x} = 0.4$ with 100 total spatial points, and the scaled time step was $\Delta\hat{t} = 0.01$. The Rankine-Hugoniot shock

conditions for the simulation are shown in Table 5.3.

Table 5.2: Velocity Grid Structure.

Grid Case	$\hat{\beta}^3_{avg}$	$\hat{\eta}_x$	$\hat{\eta}_{y,z}$	$N_x \cdot N_y \cdot N_z$
Uniform	0.343	[-17.4,13.4]	[-15.4,15.4]	45^3
Nonuniform	6.872	[-19.4,17.4]	[-14.8,14.8]	$21 \cdot 19 \cdot 19$

Table 5.3: Shock conditions.

Property		Upstream	Downstream
n	$[1/m^3]$	1.0×10^{20}	3.9×10^{20}
u	$[m/s]$	2904.11	752.5
T	$[K]$	300	7855.0

The density and temperature profiles in Figure 5.10 show good agreement between profiles simulated on the uniform and non-uniform velocity grids. Plots of differences show slight inconsistencies at the most downstream locations still within the shock structure, but these are relatively minor and the differences are balanced by computational gains subsequently discussed.

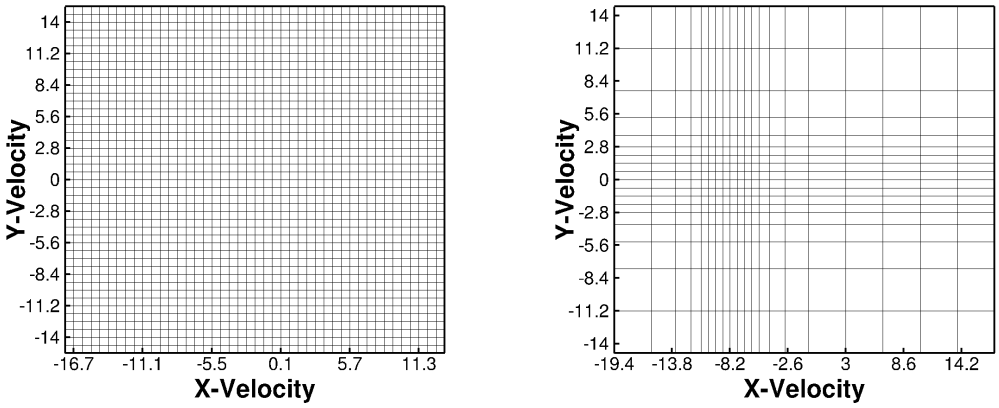

(a) (b)

Figure 5.10: a) Uniform and b) Non-uniform velocity grid used to simulate a Mach 9 shock.

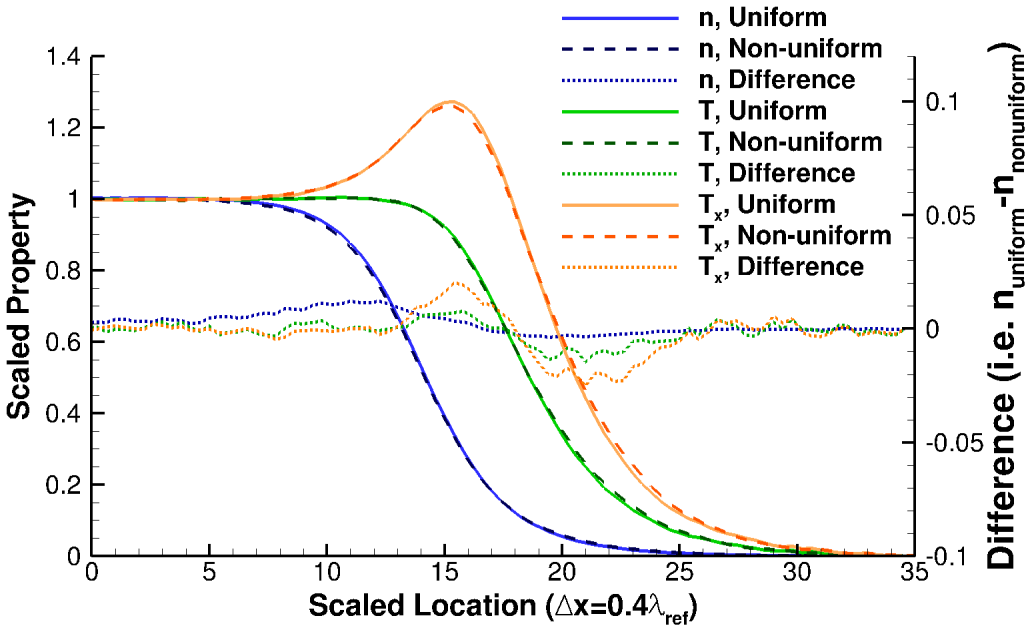

Figure 5.11: Argon, Mach 9, 1D shock profiles for a uniform and non-uniform velocity grid.

The density and temperature profiles computed using uniform and non-uniform velocity grids agree well, but the non-uniform grid calculations are much faster. The times shown in Table 5.4 are calculated over a 1000 time steps as the result evolves from the initial condition to the steady state solution.

Table 5.4: Computation time in seconds of the primary subroutines in a DVM calculation. Calculations were performed on a single thread of a 3.6 GHz Intel processor.

	Uniform	**Non-Uniform**	**Ratios**
N_c	91125	7581	12:1
$\hat{\beta}^3_{avg}$	0.343	6.872	1:20
Collisions	3299.97 s	574.24 s	6:1
- cdf calculation	824.94 s	79.82 s	10:1
Convection	140.38 s	9.57 s	15:1
Property Calculations	168.86 s	14.23 s	12:1
Total	3637.12 s	602.73 s	6:1

Note that the formula used to calculate the number of collisions per time step is a function of a user specified constant, temperature, molecular mass, non-equilibrium density, and average grid spacing, but not a direct function of the number of velocity grid points. Given the same values for each parameter, a grid with a much larger velocity domain (greater number of velocity grid points) will result in the same number of collisions as a smaller domain. The only increases in computational time in this case will be due to calculations of the cumulative distribution function, macroscopic properties, and convection term since each of these routines does directly depend on the number of velocity grid points. However, in the non-uniform case, the average velocity grid spacing is much larger. Therefore fewer simulated collisions are computed for the non-uniform grid calculation. However, notice that even though the ratio of average velocity volume element ($\hat{\beta}^3_{avg}$) is 1:20, the collision integral for the non-uniform grid is only 6 times faster than the uniform grid. This is

because of two reasons: the non-equilibrium density in the non-uniform grid case appears to be three times as large as in the uniform grid case, and the general remapping procedure is nearly twice as slow as the reduced, uniform remapping procedure. There is greater noise in the non-uniform result caused by the fewer simulated collisions (due to differences in average volume element size), which slows down the calculation. However, the non-uniform grid still maintains a significant speed-up despite these issues.

5.4 Conclusions

In this chapter, the discrete velocity method was extended from uniform to non-uniform grids in velocity space to take advantage of reductions in computational effort for a variety of flows, specifically for flows with large changes in velocity distribution width and position over time or space. A BKW relaxation was displayed for a fine, coarse, and non-uniform velocity grid to illustrate the effect of non-uniform grids on higher moments. Solutions generated on the non-uniform grid showed comparable accuracy to solutions generated on a fine grid and similar computation times to solutions generated on the coarse grid. A hypersonic Mach 9 shock was shown for a uniform and non-uniform grid. The number of velocity points in the non-uniform grid was 1/12 the number of points in the fine grid yet both solutions produced shock profiles which agreed. The results displayed how grids can be constructed from prior knowledge of flow conditions (cold, fast upstream and hot, slow downstream) in a manner which produces a decrease in computational effort without loss of accuracy. Non-uniform grids are currently restricted to stretching/compressing the gaps between grid lines, but more complex grids such as an octree structure may be beneficial for more accurately focusing effort at desirable locations.

Chapter 6

Multiple Species

Up to this point, the work described was restricted to a single monatomic species with variable hard sphere (VHS) cross-sections. However, accurate modeling of multi-species flow is essential as a step towards any realistic simulation. Therefore, in this chapter the single species restriction is lifted to allow for multiple, monatomic species of a wide range of mass and density ratios [120]. While gas mixtures with similar molecules have been shown for discrete velocity methods before [40, 121], simulations of gas mixtures with large molecular mass ratios or trace species have provided many difficulties. Such flows are usually restricted to linear (BGK) collision operators due to a lack of computational efficiency when operating on the large velocity domains required to model large molecular mass ratios. Operating on a momentum grid, instead of a velocity grid, extended the allowed molecular mass ratios in some methods, but excessively large ratios still required prohibitively large velocity domains [40]. In the following work, any benefit gained from a momentum description is made obsolete by the ability to completely uncouple each species' velocity grid from every other species' grid. This chapter also presents efficient solutions to flows with trace species which are significant to the gas physics, a process which can be troublesome in particle based methods

P. Clarke, P. Varghese, and D. Goldstein, "Discrete velocity computations with stochastic variance reduction of the Boltzmann eqation for gas mixtures," in *Proceedings of the* 29th *International Symposium on Rarefied Gas Dynamics*, vol. 1528, (Xi'an China), p. 1032, AIP Conference Proceedings, 2014.

P. Varghese and D. Goldstein supervised the project.

such as DSMC where noise may wash out changes in the properties of trace species. While developed for monatomic species, the methods discussed in this chapter hold true for the diatomic mixtures discussed in Chapter 8.

6.1 The Velocity Domain and Boltzmann Equation

Gas mixtures may be represented as a collection of independent velocity distribution functions, $\hat{\varphi}_A$, $\hat{\varphi}_B$, etc., and the mixture is defined as the sum of all distributions at a single spatial location. Since every species is stored independently, the velocity domain and grid resolution may be unique to each species and have the potential to vary greatly. Light species typically have much wider distributions than heavy species, so individual velocity domains allow for the removal of unnecessary velocity space from the heavy species' distribution (see Figure 6.1a), while light species can be stored on a grid with much wider spacing than the heavy species (see Figure 6.1b). The velocity domain for a species (A) is truncated at $\hat{\eta}_A = [-2.8(\hat{T}_A/\hat{m}_A)^{1/2} + \hat{u}_{min},\ 2.8(\hat{T}_A/\hat{m}_A)^{1/2} + \hat{u}_{min}]$ where $\hat{T}_A$ and $\hat{u}_A$ are suitably chosen as the global maximum temperature and the global maximum/minimum bulk velocity. Grid spacing is set as $\hat{\beta}_A = \hat{\beta}^*_A(\hat{T}_A/\hat{m}_A)^{1/2}$ where $\hat{T}_A$ is the global minimum temperature for species A, and $\hat{\beta}^*$ is determined by the user, typically in the range $0.2 \rightarrow 0.7$. These values are chosen consistent with the reasoning presented in Section 3.6 for a single species. Another benefit of individual velocity grids is that important species which require increased accuracy may be highly resolved in velocity space and unimportant species may be resolved with lower precision to save on both memory and computation time.

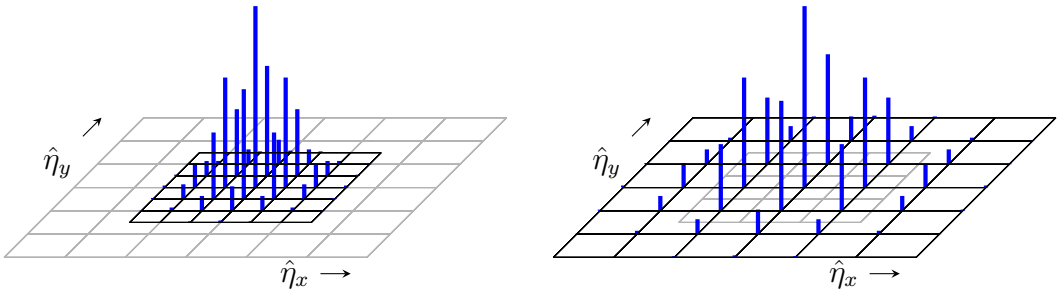

(a) (b)

Figure 6.1: 2D schematic of (a) high molecular mass and (b) low molecular mass Maxwellian distributions at the same number density and temperature. Note the wider grid spacing in (b) and the smaller domain in (a).

The multi-species, scaled, discrete, Boltzmann equation can be written using the the distributions from each independent species, $\hat{\varphi}_A$ and $\hat{\varphi}_B$, as:

$$\frac{\partial \hat{\varphi}_A}{\partial \hat{t}} + \hat{\eta}\frac{\partial \hat{\varphi}_A(\hat{\eta})}{\partial \hat{x}} = \sum_B \sum_{\hat{\zeta}} [\hat{\varphi}_A(\hat{\eta}')\hat{\varphi}_B(\hat{\zeta}') - \hat{\varphi}_A(\hat{\eta})\hat{\varphi}_B(\hat{\zeta})] \cdot \hat{g}\hat{\sigma}_T \tag{6.1}$$

Where every species is scaled by the same reference values during the scaling process, and "B" runs over all possible collision partners of species "A". If we define the value of the VHS coefficient for each species combination, ω_{AB}, as the average value of the VHS coefficients for the two separate species: $\omega_{AB} = \frac{1}{2}(\omega_A + \omega_B)$, a scaled VHS cross-section can be written as [2]:

$$\hat{\sigma}_T = \frac{\frac{1}{4}(\hat{d}_A + \hat{d}_B)^2}{\Gamma(5/2 - \omega_{AB})} \hat{m}_{red}^{1/2-\omega_{AB}} \cdot \hat{g}^{2-2\omega_{AB}} = \hat{\sigma}_{coeff}(A, B) \cdot \hat{g}^{2-2\omega_{AB}} \tag{6.2}$$

Where the hard sphere reference cross-section is defined as $\sigma_{ref} = \pi d_{ref}^2$, $\hat{m}_{red}$ is the scaled reduced mass, and $\hat{g}$ is the scaled relative velocity between colliding particles. This definition of cross-section is chosen to match Bird's VHS definition [2] since results are compared to DSMC solutions when possible. The multi-species VHS cross section is substituted into the Boltzmann

equation, resulting in collision probabilities being a function of relative velocity, reduced mass, and scaled molecular diameter. The final discrete Boltzmann equation for a mixture is:

$$\frac{\partial \hat{\varphi}_A}{\partial \hat{t}} + \hat{\eta}\frac{\partial \hat{\varphi}_A(\hat{\eta})}{\partial \hat{x}} = \sum_B \sum_{\hat{\zeta}} [\hat{\varphi}_A(\hat{\eta}')\hat{\varphi}_B(\hat{\zeta}') - \hat{\varphi}_A(\hat{\eta})\hat{\varphi}_B(\hat{\zeta})] \cdot \hat{\sigma}_{coeff}(A,B) \cdot \hat{g}^{2-2\omega_{AB}} \tag{6.3}$$

6.2 Mixture Properties

Mixture number density and mass density are defined as the sum of the individual species properties. The subscript s here stands for each species, and summations over s are run from $s = 1$ to N_s where N_s is the total number of species present in a gas mixture.

$$\hat{n}_{mix} = \sum_s \hat{n}_s \tag{6.4}$$

$$\hat{\rho}_{mix} = \sum_s \hat{m}_s \hat{n}_s \tag{6.5}$$

A mixture bulk velocity is defined as the mass average of the individual species' velocities as:

$$\hat{u}_{i,mix} = \frac{1}{\hat{\rho}_{mix}} \sum_s \hat{m}_s \hat{n}_s \hat{u}_{i,s} \tag{6.6}$$

Given the mass average velocity, a peculiar velocity is defined relative to $\hat{u}_{i,mix}$:

$$\hat{C}_i = \hat{\eta}_i - \hat{u}_{i,mix} \tag{6.7}$$

And the peculiar velocity is used to calculate higher order macroscopic properties of individual species in mixtures.

$$\hat{T}_s = \frac{3\hat{m}}{2\hat{n}} \sum_{\hat{\eta}} \hat{C}_i^2 \cdot \hat{\varphi}_s(\hat{\eta}) \tag{6.8}$$

$$\hat{q}_{s,j} = \frac{\hat{m}}{2\hat{n}} \sum_{\hat{\eta}} \hat{C}_j \hat{C}_i^2 \hat{\varphi}_s(\hat{\eta}) \tag{6.9}$$

$$\hat{\tau}_{s,ij} = -\hat{m} \sum_{\hat{\eta}} \hat{C}_i \hat{C}_j \hat{\varphi}_s(\hat{\eta}) + \hat{p}_s \delta_{ij} \tag{6.10}$$

It should be noted that species specific temperatures determined from a peculiar velocity defined by the species specific bulk velocity may still be used, specifically for the variance reduction collision method. A mixture temperature is calculated as a density average of the individual species temperatures.

$$\hat{T}_{mix} = \frac{1}{\hat{n}_{mix}} \sum_{s} \hat{n}_s \hat{T}_s \tag{6.11}$$

And mixture heat flux and stresses are the sum of the individual species heat fluxes and stresses.

$$\hat{q}_{mix} = \sum_{s} \hat{q}_s \tag{6.12}$$

$$\hat{\tau}_{mix} = \sum_{s} \hat{\tau}_s \tag{6.13}$$

6.3 Time stepping

The optimum time step for convection for species with a low molecular mass can be significantly shorter than for species with a high molecular mass since light species tend to have wider distribution functions that require larger velocity domains and thus more severe CFL restrictions.

$$|\hat{\eta}|_{max}^{light} > |\hat{\eta}|_{max}^{heavy} \Rightarrow \hat{t}_{conv}^{light} < \hat{t}_{conv}^{heavy} \tag{6.14}$$

The collision rate of species A for collisions with species B for VHS molecules is calculated from the species diameters, the temperature the diameters where calculated at, $\hat{T}_d$, the number density of species B, the mixture temperature, and the reduced mass of A and B as [2]:

$$\hat{\nu}_{AB} = \frac{2}{\sqrt{\pi}} \frac{(\hat{d}_A + \hat{d}_B)^2}{4} \hat{n}_B \sqrt{\frac{\hat{T}_d}{\hat{m}_{red}}} \left(\frac{\hat{T}_{mix}}{\hat{T}_d} \right)^{1-\omega_{AB}} \tag{6.15}$$

The collision time scale is defined as the reciprocal of the collision rate, and the value is calculated for every species combination (AA, AB, BA, BB, etc.) as:

$$\hat{t}_{coll,AB} = \frac{1}{\hat{\nu}_{AB}} \tag{6.16}$$

In the current method all relevant times scales in the flow are estimated a priori and the time step is chosen as a fraction of the shortest time scale.

$$\Delta\hat{t} \propto min\left(\hat{t}_{conv}^{A}, \hat{t}_{conv}^{B}, ..., \hat{t}_{coll}^{AA}, \hat{t}_{coll}^{AB}, \hat{T}_{coll}^{BA}, ... \right) \tag{6.17}$$

6.4 Full Monte Carlo

The discrete collision integral in equation 6.3 is decomposed into separate terms for each species combination as:

$$\begin{aligned}\left.\frac{\partial\hat{\varphi}_A}{\partial\hat{t}}\right|_{coll} &= \sum_{\hat{\zeta}}[\hat{\varphi}_A(\hat{\eta}')\hat{\varphi}_A(\hat{\zeta}') - \hat{\varphi}_A(\hat{\eta})\hat{\varphi}_A(\hat{\zeta})]\cdot\hat{\sigma}_{coeff}(A,A)\cdot\hat{g}^{2-2\omega_A} \\ &+ \sum_{\hat{\zeta}}[\hat{\varphi}_A(\hat{\eta}')\hat{\varphi}_B(\hat{\zeta}') - \hat{\varphi}_A(\hat{\eta})\hat{\varphi}_B(\hat{\zeta})]\cdot\hat{\sigma}_{coeff}(A,B)\cdot\hat{g}^{2-2\omega_{AB}} \\ &+ \sum_{\hat{\zeta}}[\hat{\varphi}_A(\hat{\eta}')\hat{\varphi}_C(\hat{\zeta}') - \hat{\varphi}_A(\hat{\eta})\hat{\varphi}_C(\hat{\zeta})]\cdot\hat{\sigma}_{coeff}(A,C)\cdot\hat{g}^{2-2\omega_{AC}} \\ &+ \quad ..... \text{ etc.}\end{aligned} \tag{6.18}$$

The terms are solved independently, and the final result of the collision integral is the sum of the changes due to collisions for every species combination. Some simplification can be obtained by associating a species combination with its reverse (A-B with B-A) since the terms are identical. However, the increase in computational effort still scales on $O(N_s^2)$ where N_s is the number of species.

In each collision integral from equation 6.18, the depletion per collision, $\Delta\hat{\varphi}^{AA}$ and $\Delta\hat{\varphi}^{AB}$, are derived in a similar manner as for a single species (Section 4.1.1) but with species dependent number densities. The resulting depletion quantities are:

$$\Delta\hat{\varphi}^{AA} = \Delta\hat{t}\cdot\frac{\hat{n}_A^2}{2Kn\cdot N_c^{AA}} \tag{6.19a}$$

$$\Delta\hat{\varphi}^{AB} = \Delta\hat{t}\cdot\frac{\hat{n}_A\cdot\hat{n}_B}{Kn\cdot N_c^{AB}} \tag{6.19b}$$

The number of simulated collisions per time step in equations 6.19 requires consideration of the appropriate adjustment for grid spacing since

two species can have vastly different values of $\hat{\beta}$. In this work, the number of simulated collisions, N_c^{AB}, is calculated as a function of the average volume element size and a user specified constant, C_{AB}

$$N_c^{AA} = nint\left(\frac{\Delta\hat{t}\cdot\hat{T}^{2/3}}{Kn\cdot C_{AA}^2\cdot\beta_A^3}\right) \tag{6.20a}$$

$$N_c^{AB} = nint\left(\frac{\Delta\hat{t}\cdot\hat{T}^{2/3}}{Kn\cdot C_{AB}^2\cdot\beta_{avg}^3}\right) \tag{6.20b}$$

The value of C_{AB} is specific to each collision integral term in equation 6.18 since every term is treated independently. The value is originally defined by Morris as proportional to the noise in the distribution function at equilibrium for a single, monatomic species (AA, BB, etc.) [6], but the proportionality of the constant is lost in multi-species flows due to unlike species collisions (AB, BA, etc.). The effect of C_{AB} on the RMS noise of an equilibrium distribution is investigated in Figure 6.2 for a mixture of two equal molecular mass species. Both species are initialized as a discrete Maxwellian at the same number density, temperature, and bulk velocity, and a standard full Monte Carlo method is used to compute the collision integral over 100 time steps. A "gold standard" solution is calculated by setting $C_{AA} = 0.0005$ and $C_{AB} = 0.0005$ and averaging the result over the 100 time steps. Next, the collision number for A-A type collisions is set to $C_{AA} = 0.004$, and a range of collision numbers, where $0.0005 \leq C_{AB} \leq 0.01$, is applied for A-B type collisions. The final time step of each calculation is used to calculate an RMS as:

$$RMS = \sqrt{\sum_{\hat{\eta}} \left(\hat{\varphi}_{GS}(\hat{\eta}) - \hat{\varphi}(\hat{\eta})\right)^2} \tag{6.21}$$

And the resulting values are displayed on a log-log plot of $1/C_{AB}^2$ vs RMS. The curve's trend indicates the expected increase in noise as the number of simulated collisions falls due to a higher C_{AB} value. Increasing the A-B type collision number such that $C_{AB} = C_{AA}$ resulted in nearly doubling the noise from the $C_{AB} \ll C_{AA}$ case. This indicates the noise from like and unlike species terms are roughly equivalent, and values of $C_{AB} \cong O(10^{-3})$ may be used as a guideline when determining an appropriate number of simulated collisions.

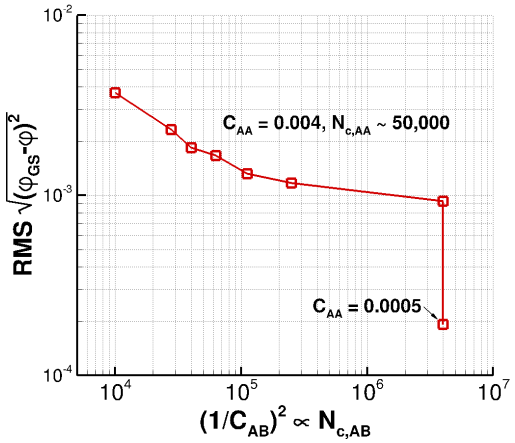

Figure 6.2: RMS noise in a two species gas due to a range of C_{AB} values.

One benefit of specific control over C_{AB} for each integral is that by raising or lowering the number of simulated collisions for a particular integral, computational effort can be focused on collisions between a specific combination of species. For instance, if there is a particularly energetic or reactive species in a mixture, a higher resolution may be desired for interactions involving that species. However, collisions among more stable or less energetic species could be modeled with fewer simulated collisions since the more interesting physics are not being driven by such interactions.

6.5 Variance Reduction

The identity stated in Section 4.1.2 can be extended for multi-species interactions as:

The net change in time in two discrete equilibrium distributions of different species due to collisions between particles of those distributions is zero if the species have the same kinetic temperature and bulk velocity.

Following the same method discussed previously in Section 4.1.2, any distribution function can be decomposed into equilibrium, $\hat{\varphi}^E$, and deviation from equilibrium, $\hat{\varphi}^d$, components such that $\hat{\varphi} = \hat{\varphi}^E + \hat{\varphi}^d$. The collision integral, I_c, for a single combination of species (A and B) can then be written as:

$$I_{coll}(\hat{\eta}) = I_{E-E} + I_{E-d} + I_{d-E} + I_{d-d} :$$

$$I_{E-E} = \sum_{\hat{\zeta}} [\hat{\varphi}_A^E(\hat{\eta}')\hat{\varphi}_B^E(\hat{\zeta}') - \hat{\varphi}_A^E(\hat{\eta})\hat{\varphi}_B^E(\hat{\zeta})]\hat{g}\hat{\sigma}_T = 0 \tag{6.22a}$$

$$I_{E-d} = \sum_{\hat{\zeta}} [\hat{\varphi}_A^E(\hat{\eta}')\hat{\varphi}_B^d(\hat{\zeta}') - \hat{\varphi}_A^E(\hat{\eta})\hat{\varphi}_B^d(\hat{\zeta})]\hat{g}\hat{\sigma}_T \tag{6.22b}$$

$$I_{d-E} = \sum_{\hat{\zeta}} [\hat{\varphi}_A^d(\hat{\eta}')\hat{\varphi}_B^E(\hat{\zeta}') - \hat{\varphi}_A^d(\hat{\eta})\hat{\varphi}_B^E(\hat{\zeta})]\hat{g}\hat{\sigma}_T \tag{6.22c}$$

$$I_{d-d} = \sum_{\hat{\zeta}} [\hat{\varphi}_A^d(\hat{\eta}')\hat{\varphi}_B^d(\hat{\zeta}') - \hat{\varphi}_A^d(\hat{\eta})\hat{\varphi}_B^d(\hat{\zeta})]\hat{g}\hat{\sigma}_T \tag{6.22d}$$

The first integral is identically zero because the total effect of all collisions drawn from two equilibrium distributions with equal mean velocity and temperature is identically zero. The second and third integrals are calculated separately when multiple species are introduced since $\hat{\varphi}_A^E(\hat{\eta}) \cdot \hat{\varphi}_B^d(\hat{\zeta}) \neq \hat{\varphi}_A^d(\hat{\zeta}) \cdot \hat{\varphi}_B^E(\hat{\eta})$. However, for like-species collision (A-A), the terms are equivalent and can be calculated within a single loop or separately.

Because every species combination is treated separately, a different equilibrium distribution can be chosen for each individual collision integral in equation 6.22. For like-species collisions (e.g. A-A), a single Maxwellian is used with the local species specific temperature, number density, and bulk velocity. (see equation 6.23a). For unlike-species collisions (e.g. A-B), a Maxwellian is formulated with the local number density and mass of the species but with the gas mixture bulk velocity and temperature based on that specific pair (AB) of two colliding species, (see equation 6.23b).

$$\hat{\varphi}_A^E(\hat{\eta})\big|_{A-A} = \hat{n}_A \left(\frac{\hat{m}_A}{\pi \hat{T}_A}\right)^{3/2} \exp\left(\frac{-\hat{m}_A(\hat{\eta} - \hat{u}_A)^2}{\hat{T}_A}\right) \tag{6.23a}$$

$$\hat{\varphi}_A^E(\hat{\eta})\big|_{A-B} = \hat{n}_A \left(\frac{\hat{m}_A}{\pi \hat{T}_{mix}}\right)^{3/2} \exp\left(\frac{-\hat{m}_A(\hat{\eta} - \hat{u}_{mix})^2}{\hat{T}_{mix}}\right) \tag{6.23b}$$

As each individual species distribution approaches Maxwellian, the number of like species collisions computed will be greatly reduced, but computations of collisions between unlike species will only be reduced as the entire mixture approaches global equilibrium. Figure 6.3 gives a schematic example of distribution function decompositions for like-species and unlike-species. The magnitude of the deviation distribution for unlike-species is larger since it reflects the distribution being both non-Maxwellian and out of equilibrium with species B.

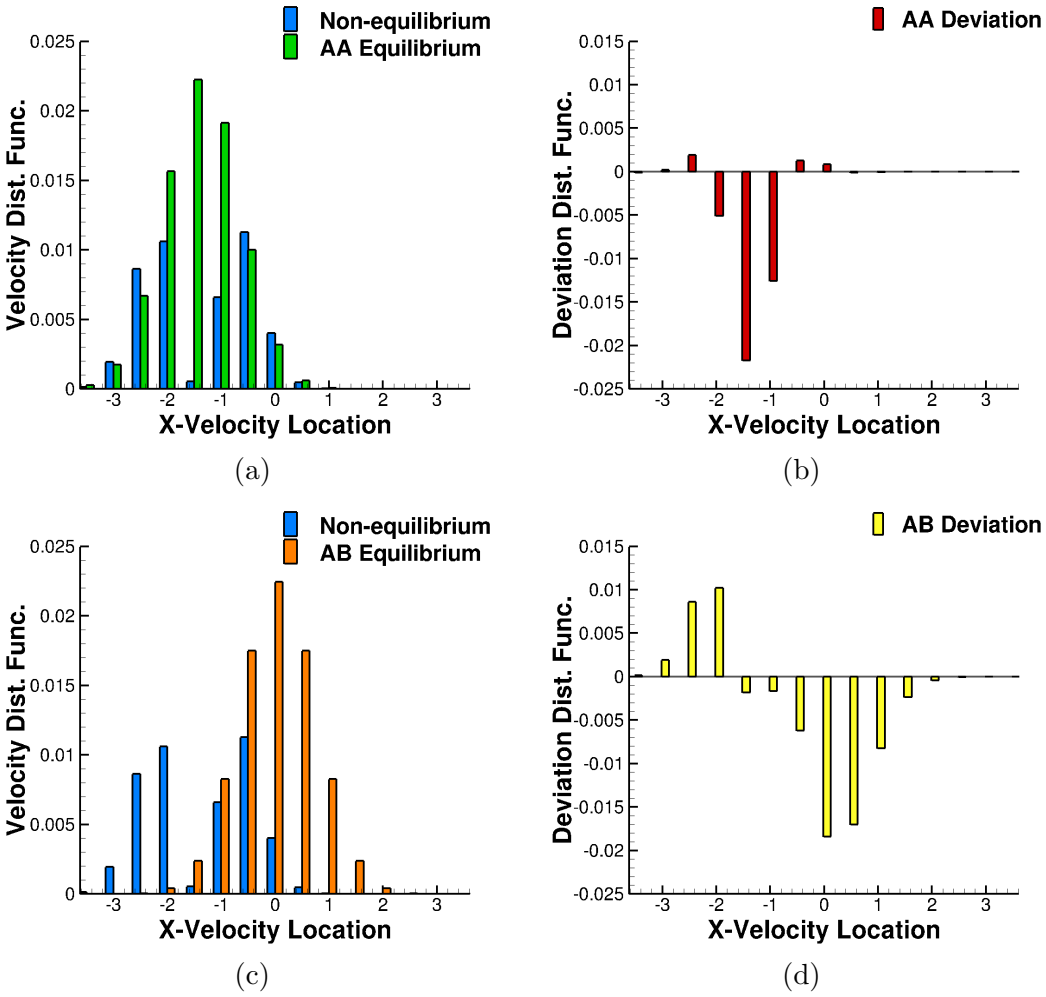

Figure 6.3: Schematic of the decomposition of a distribution for species A for collisions with itself (a,b) and species B (c,d). The schematic shows a highly non-equilibrium initial distribution and it assumes collisions with species B will drive the distribution towards a bulk velocity of $\hat{u} = 0$.

The net depletion rate is determined from the depleting term in equation 6.22, and the density depleted per collision is calculated by dividing the net depletion rate by the total number of simulated collisions (see equation 6.25), and if $A = B$, a factor of 1/2 would be included. The depletion at a single velocity location for pseudo-Maxwell molecules due to a single type A-B collision for each of the three variance reduction integrals is:

$$\Delta\hat{\varphi}_{AB}^{E-d}(\hat{\eta}) = \Delta\hat{t}\frac{sgn(\hat{\varphi}_B^d(\hat{\eta}))\hat{n}_A^E\hat{n}_B^d}{Kn\cdot N_c^{E-d}} \tag{6.24a}$$

$$\Delta\hat{\varphi}_{AB}^{d-E}(\hat{\eta}) = \Delta\hat{t}\frac{sgn(\hat{\varphi}_A^d(\hat{\eta}))\hat{n}_A^d\hat{n}_B^E}{Kn\cdot N_c^{d-E}} \tag{6.24b}$$

$$\Delta\hat{\varphi}_{AB}^{d-d}(\hat{\eta}) = \Delta\hat{t}\frac{sgn(\hat{\varphi}_A^d(\hat{\eta}))sgn(\hat{\varphi}_B^d(\hat{\eta}))\hat{n}_A^d\hat{n}_B^d}{Kn\cdot N_c^{d-d}} \tag{6.24c}$$

$$\text{where } sgn(x) = \begin{cases} +1, & x > 0 \\ -1, & x < 0 \end{cases}$$

The number of simulated collisions is adjusted for the deviation from equilibrium by multiplying by the ratio of deviation density, $\hat{n}^d = \sum|\hat{\varphi}^d|$, to the species density, $\hat{n}$. As $\hat{n}^d$ decreases, not only does the total depletion decrease, but the number of collisions decreases as well. The resulting formulas for calculating N_c for A-B type collisions are:

$$N_c^{E-d} = nint\left(\frac{\Delta\hat{t}\cdot\hat{T}^{1/3}}{Kn\cdot C_{AB}^2\hat{\beta}^3\hat{m}_{red}^{3/2}}\cdot\frac{\hat{n}_B^d}{\hat{n}_B}\right) \tag{6.25a}$$

$$N_c^{d-E} = nint\left(\frac{\Delta\hat{t}\cdot\hat{T}^{1/3}}{Kn\cdot C_{AB}^2\hat{\beta}^3\hat{m}_{red}^{3/2}}\cdot\frac{\hat{n}_A^d}{\hat{n}_A}\right) \tag{6.25b}$$

$$N_c^{d-d} = nint\left(\frac{\Delta\hat{t}\cdot\hat{T}^{1/3}}{Kn\cdot C_{AB}^2\hat{\beta}^3\hat{m}_{red}^{3/2}}\cdot\frac{\hat{n}_A^d\hat{n}_B^d}{\hat{n}_A\hat{n}_B}\right) \tag{6.25c}$$

6.6 Replenishment

Once a colliding pair has been chosen and the appropriate number density depleted for the collision, the mass removed must be replenished back into the distribution in a similar manner to the process described in Section 4.1.3. The spheres made by rotating the relative velocity vector, $\hat{g} = |\hat{\eta} - \hat{\zeta}|$, about its center of mass results in the "collision sphere" of each species, or the range of energy conserving replenishment locations for the collision, and the center of mass velocity is found from the mass fractions of each colliding species:

$$\begin{aligned} \hat{V}_{com,x} &= \frac{\hat{m}_A}{\hat{m}_A + \hat{m}_B}\hat{\eta}_x + \frac{\hat{m}_B}{\hat{m}_A + \hat{m}_B}\hat{\zeta}_x \\ \hat{V}_{com,y} &= \frac{\hat{m}_A}{\hat{m}_A + \hat{m}_B}\hat{\eta}_y + \frac{\hat{m}_B}{\hat{m}_A + \hat{m}_B}\hat{\zeta}_y \\ \hat{V}_{com,z} &= \frac{\hat{m}_A}{\hat{m}_A + \hat{m}_B}\hat{\eta}_z + \frac{\hat{m}_B}{\hat{m}_A + \hat{m}_B}\hat{\zeta}_z \end{aligned} \tag{6.26}$$

The velocity grids of the colliding species are overlapped in Figure 6.4 during the rotation to visualize post-collision values, but post-collision values are remapped to their species-specific grids. The replenishing number densities are mapped back to grid nodes using the scheme discussed in Section 4.1.3.

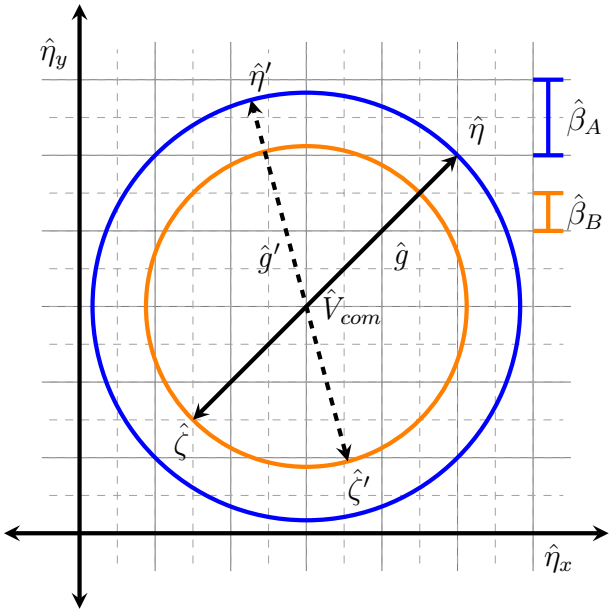

Figure 6.4: Multi-species energy collision sphere (2D slice) showing a rotation of the relative velocity vector ($\hat{g}$) about the center of mass velocity ($\hat{V}_{com}$) to a pair of points off the velocity grid ($\hat{\eta}'$, $\hat{\zeta}'$). $\hat{\eta}$ and $\hat{\zeta}$ lie on separate velocity grids: the solid lines show the grid for species A ($\hat{\eta}$) and the dashed lines show the grid for species B ($\hat{\zeta}$).

6.7 Results

Xe-He 1D Shock

The scheme described above has been used to simulate the canonical large mass ratio example of a xenon-helium 1D shock. The case is chosen because interesting experimental results with distinct shock profile features have been shown by Gmurczyk et al. [122] and DSMC solutions of the problem are easily read from Bird's DSMC book [2], making the results good for testing the accuracy of the method. A comparison between DSMC and the discrete velocity method is made for a Mach 3.9 shock in a gas mixture of 3% Xe by molar fraction. Shock properties can be seen in Table 6.1, and a VSS collision cross-section is used with values found in Appendix A. The convection step

uses a first order finite difference scheme and a scaled physical spacing of $\Delta\hat{x} = 0.4$. Using a time step of $\Delta\hat{t} = 0.002$, the CFL number at the maximum velocity, $\hat{\eta}_{max}\Delta\hat{t}/\Delta\hat{x} = 0.239$, is much smaller than the criterion necessary for stability. Velocity grid spacing and boundaries are shown in Table 6.2 for both species, and the collision number constants for every species combination was $C = 0.002$.

Table 6.1: Shock conditions.

Property		**Upstream**	**Downstream**
n_{Xe}	$[1/m^3]$	0.3x10^{18}	0.0973x10^{19}
n_{He}	$[1/m^3]$	9.7x10^{18}	3.145x10^{19}
u_{mix}	$[m/s]$	2740.457	845.183
T_{mix}	$[K]$	273.0	1591.377

Table 6.2: Velocity domain.

Species	$\hat{\eta}_x$	$\hat{\eta}_y$	$\hat{\eta}_z$	$\hat{\beta}$
Xe	$[-18.1, 3.9]$	$[-8.3, 8.3]$	$[-8.3, 8.3]$	0.69
He	$[-51.8, 43.0]$	$[-47.4, 47.4]$	$[-47.4, 47.4]$	3.95

Figure 6.5 shows instantaneous density ($\hat{\rho}$) and temperature ($\hat{T}$) profiles obtained from the discrete velocity solution compared to profiles obtained from Bird [2]. Good agreement can be seen between both methods, showing no loss of accuracy by using the variance reduced multi-species DVM code.

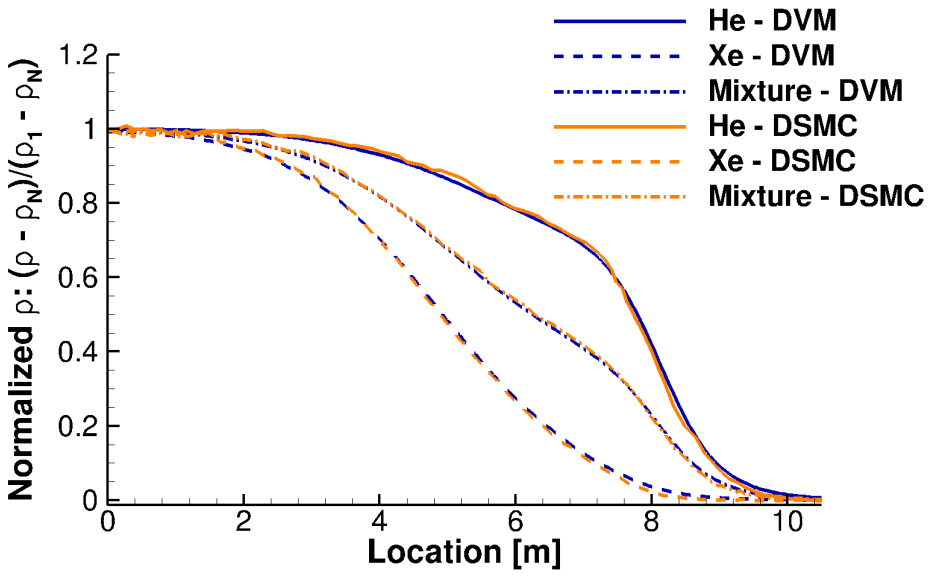

(a)

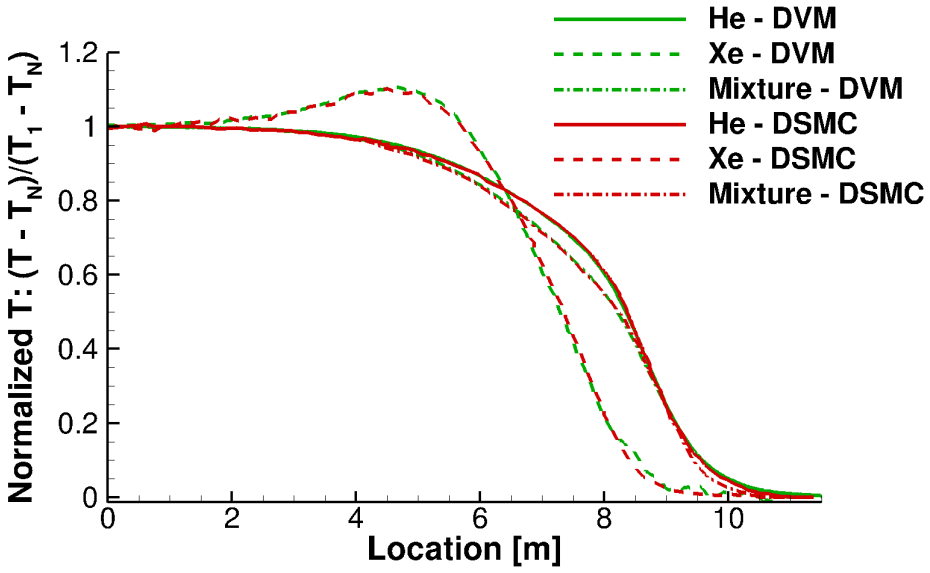

(b)

Figure 6.5: Xe-He, Mach 3.9, 1D shock profiles of (a) density and (b) temperature compared to DSMC solutions.

The number of collisions for Xe-Xe, Xe-He, and He-He species combinations was also investigated and the results are shown in Figure 6.6.

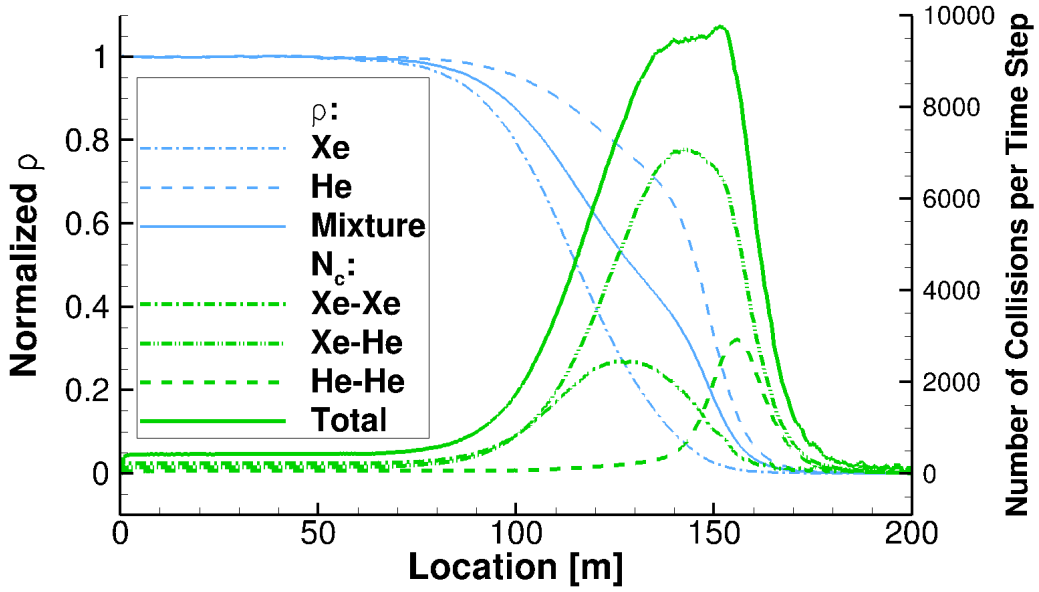

Figure 6.6: Xe-He, Mach 3.9, 1D shock profile showing the number of simulated collisions.

It can be seen that variance reduction greatly reduces the number of collisions in the upstream and downstream equilibrium sections of the shock profile, focusing computational effort on the important region of the simulation, i.e. the shock itself. As a result, large regions upstream and downstream of the shock can be accurately simulated without a large increase in effort, and the noise free solutions will be useful in future work when implementing hybrid continuum-rarefied solvers. Note the number of simulated collisions for He-He is on the same order as Xe-Xe despite the fact that the number density of He is nearly an order of magnitude higher. The observation illustrates how the method described allows for the appropriate number of Xe-Xe collisions necessary for a noise free solution without driving up the number of simulated He-He

collisions as well. The Xe-He collision number profile is wider than the Xe-Xe and He-He profiles, indicating that the individual species tend to approach near-Maxwellian distributions separately as they relax to an equilibrium state defined by macroscopic mixture properties downstream of the shock. Finally, note the peak number of simulated collisions, and therefore the largest non-equilibrium values, occurs early in the shock (near the maximum temperature gradient), not at the location of the maximum density gradient.

He Beam

A 0D simulation was run to demonstrate the treatment of a trace species with extreme importance to the flow physics. A velocity distribution is initialized representing a high speed (~ 44 km/s) beam of He colliding with cold Xe at 300 K. The He is present in a trace amount at a 1:1000 number density ratio with Xe. The entire density of He is initialized as a delta function at a single velocity ($\hat{T}_{He} = 0$) on a very coarse velocity grid with spacing of $\hat{\beta} = 16.0$ and domain boundaries at $\hat{\eta} = \pm 304.0$. For a more complex simulation, such a large number of grid points would be too expensive ($N = 39^3$), but a non-uniform grid could be devised that resolves the final distribution and also encloses the high velocities at early times [115]. The Xe is initialized as a Maxwellian on a velocity grid with spacing of $\hat{\beta} = 0.7$ and domain boundaries at $\hat{\eta} = \pm 4.9$. The grid is chosen to resolve the xenon velocity distribution function accurately at both the initial and final temperatures. A scaled time step of $\Delta\hat{t} = 5 \times 10^{-5}$ is used, and macroscopic data are written out every 1000 time steps. The mixture is relaxed without convection, allowing the He to heat the Xe to a final temperature of ~ 600 K. The coefficients used to calculate the number of simulated collisions are seen in Table 6.3.

Table 6.3: C_{AB} coefficient values.

Collision Type	C_{AB}
Xe-Xe	0.004
Xe-He	0.0004
He-He	0.004

At $\hat{t} = 0$ the helium distribution is a delta function with no temperature value and high velocity (Figure 6.7a). The helium very quickly scatters into a shell-like structure in velocity space, transferring kinetic energy from bulk velocity to temperature (Figure 6.7b). The temperature relaxes through further collisions with xenon particles, moving the shell inwards (Figure 6.7c) before finally reaching a Maxwellian distribution at equilibrium with the xenon species (Figure 6.7d).

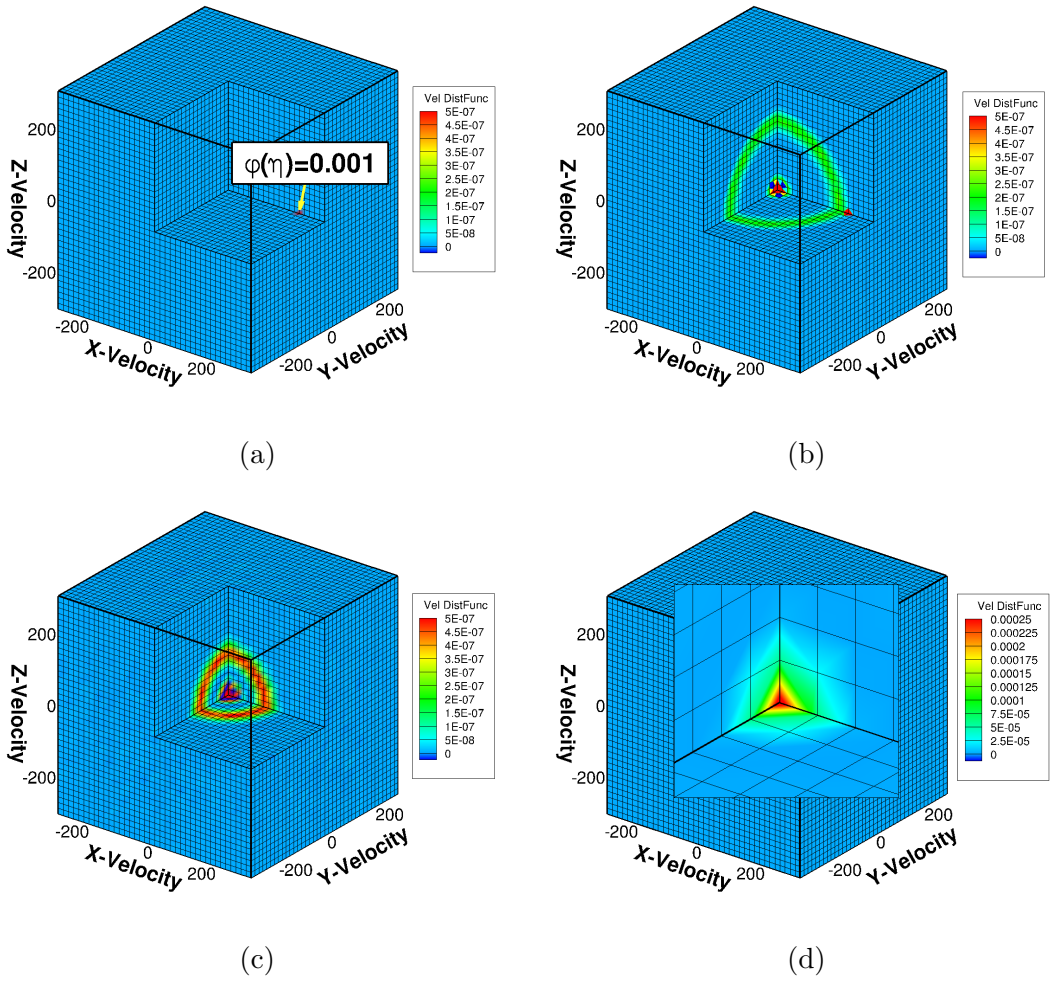

Figure 6.7: (a) Initial conditions for He are a single delta function at high velocity. (b) A shell forms with a radius equal to the distance between the delta function and the center of the distribution where the xenon initially lies. (c) The shell compresses as collisions between helium and xenon remove energy from the helium distribution. (d) The final solution for helium is a Maxwellian centered at the middle of the distribution as seen in the inset where the region near the velocity space origin is shown on an expanded scale. Note that the color scale for the inset in (d) is different from that used in (a)-(c) for display convenience.

The temperature variation of xenon can be seen in Figure 6.8 along with the number of simulated collisions per time step (N_c) used to compute each collision integral. At early times, the helium distribution function is highly non-equilibrium. In consequence, the deviation distribution for helium is large, but the number of simulated He-He type collisions is kept low due to the large velocity grid spacing and high C_{HeHe} value. In contrast, the xenon distribution relaxes very slowly and never deviates significantly from equilibrium. Therefore the number of simulated collisions for xenon remains very low throughout the simulation. The primary interaction for changes in macroscopic properties is collisions between helium and xenon. Therefore, the collision coefficient, C_{XeHe}, is chosen to be much smaller than the collision coefficient for other interactions, and a greater number of simulated collisions are used for computation of the Xe-He collision integral.

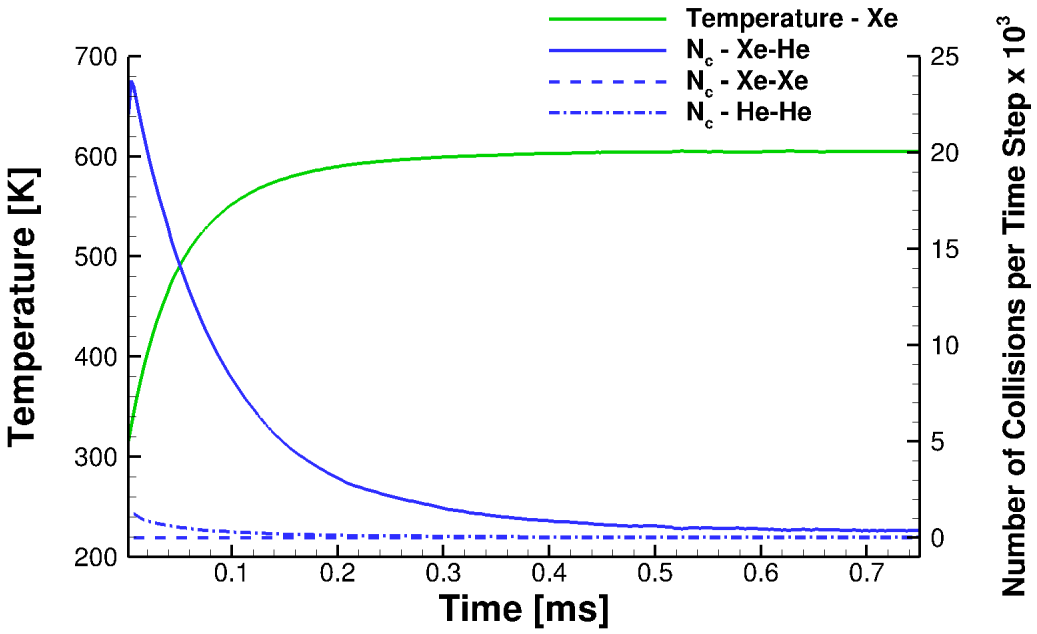

Figure 6.8: Temperature profile of xenon due to the effects of a helium beam and the number of simulated collisions for Xe-Xe, Xe-He, and He-He collision types

We choose a low C_{XeHe} to balance the relatively low n^d_{Xe} values at early times and keep the number of simulated Xe-He collisions used to compute the collision integral high enough to obtain an accurate computation. The collision coefficients for the Xe-Xe and He-He collision integrals do not need to be as low to obtain an accurate estimate. In the Xe-Xe case the distribution remains quite close to a Maxwellian so the integral is small and few collisions are needed. In the He-He case, helium's collisions with itself are relatively rare events and insignificant to the evolution of the macroscopic properties in comparison to Xe-He collisions. We emphasize that the collision coefficients were chosen to provide the accuracy necessary to resolve changes in the Xe velocity distribution and show a smooth variation of the resultant Xe temperature profile with time.

The He velocity distribution is computed on a much coarser grid and its collision integral is computed less accurately, so the resulting velocity distribution changes are computed at low resolution and the resulting temperature profile is much noisier at later times (see inset in Figure 6.9), because of stochastic fluctuations in the distribution function. If a smoother solution to the He profile were required, the C_{HeHe} value could be increased, focusing additional computational effort on the He-He collision type. The evolution of the helium's temperature and bulk velocity over initial times displayed in Figure 6.9 are calculated from the distribution functions in Figures 6.7.

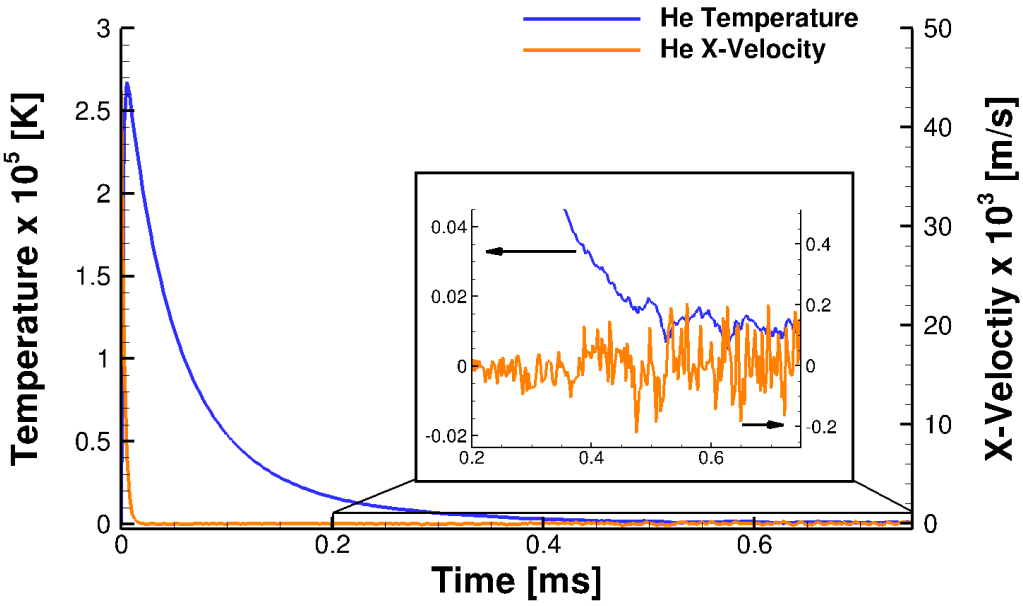

Figure 6.9: Heating of xenon by a helium beam. The velocity of the helium immediately drops as kinetic energy moves from bulk velocity to temperature. The helium temperature then relaxes towards equilibrium. Inset is expanded view of properties at later times showing noise associated with helium's macroscopic properties.

6.8 Conclusions

In this chapter, the discrete velocity scheme has been extended to gas mixtures with large mass ratios and/or trace species and I have shown how species-specific velocity grids, individual treatment of collisions for each species combination, and the variance reduction method can increase computational efficiency and allow for accurate simulations. The method was tested for accuracy through a 1D shock simulation of a Mach 3.91 shock with a 1:9 ratio of xenon to helium. Accurate profiles were obtained and inspection of the collision number at each spatial location revealed the multi-species variance reduction method focused effort (number of simulated collisions) on important regions of the shock. Also, the collision integral for the higher number density helium was approximated using a similar number of collisions as xenon, showing that the collision integral for the low-density species can be accurately computed with an adequate number of simulated collisions without driving up the number of simulated collisions for a denser species. The method was also tested with a 0D relaxation where a trace amount of helium moving at a high speed was collided with a xenon cloud. The mixture was allowed to relax toward equilibrium while ignoring the convection step in the Boltzmann equation, and the temperature profile for xenon was tracked. The number of simulated collisions used to approximate each collision integral was also investigated. It was shown how collisions important to describing the energy transfer to the Xe, specifically Xe-He collisions, can be run at a higher resolution while less important collisions, Xe-Xe and He-He, are run at a lower resolution. In standard particle methods if the effects of a trace species on a bulk species needed to be resolved, the number of collisions for the bulk species interactions with itself would also need to be increased proportionally.

Chapter 7

The Discrete Boltzmann Equation for Gases with Internal Energy

Up to this point, the discussion concerned monatomic particles without any form of internal structure. Such atoms only exist among the Noble gases (He, Ar, Ne, etc.), and it would be unusual to find mixtures made up solely of monatomic molecules in any real world problem. Instead, most molecules are polyatomic or diatomic molecules. Unlike monatomic atoms which can only undergo changes in translational and electronic energy, the bonds in polyatomic molecules give the molecule a moment of inertia to absorb rotational energy (Figure 7.1a), and can absorb vibrational energy (Figure 7.1b). Processes that change electronic energy will not be modeled in the following work, and all molecules will be assumed to reside in the electronic ground state.

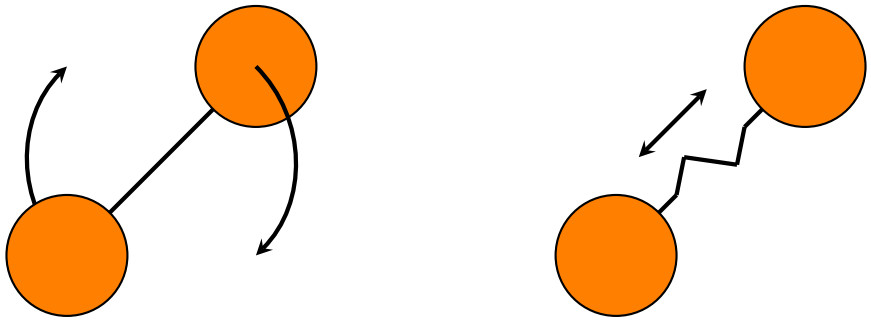

(a) (b)

Figure 7.1: (a) Rotation and (b) Vibration of a homonuclear diatomic molecule.

In this chapter, the internal energy distribution will be introduced,

a number of ways to account for the energy in each quantum level will be discussed, relaxation rates will be presented, and finally several approximations for calculating energy exchanges in inelastic collisions will be shown.

It is well known that molecules reside on a discrete set of internal energy levels [1]. Vibrational levels above the ground (0) level only begin to become significantly populated at the characteristic vibrational temperature (typically on the order of 10^3 K), and at lower temperatures, many models totally ignore vibrational effects. On the other hand, rotational energy levels are closer together, and the distribution may be considered excited at much lower temperatures. In fact, most common species have a rotational characteristic temperature on the order of 1-5 K (see Table A.3 of Appendix A). The levels are so closely packed together that at high temperatures, the rotational distribution is often approximated to be a continuous function. However, in this work, quantized distributions of both vibration and rotation will be described regardless of the local temperature (excluding the model described in Section 8.3). The vibrational and rotational distributions may have an equilibrium distribution over internal energy states given by the Boltzmann distribution as [1]:

$$f^E(i) = \frac{n_i}{n} = \frac{q_i e^{-\epsilon_i/k_b T}}{Q} \tag{7.1}$$

Here q_i is the degeneracy of level i (1 for vibration and $q_{ns}(2J+1)$ for rotation), ϵ_i is the energy in the level, and T is the temperature component associated with the energy mode being described. Q is the internal partition function, defined as the sum over every energy level.

$$Q = \sum_j q_j e^{\epsilon_j/k_b T} \tag{7.2}$$

7.1 The Dunham Equation and Decoupling Rotational and Vibrational Energy

In this work, diatomic molecules have $^1\sum$-ground electronic states, and the rotational and vibrational energy levels can be described using J, the rotational quantum number, ν, the vibrational quantum number, and q, the nuclear spin degeneracy of a molecule (further discussed in Section 7.2). The internal energy levels are commonly written in the field of molecular spectroscopy using the Dunham expansion where total energy is made up of a polynomial expression for both vibration and rotation as [123]:

$$\epsilon(\nu, J) = \sum_k \sum_m Y_{k,m}(\nu + \tfrac{1}{2})^k (J(J+1))^m \tag{7.3}$$

$Y_{k,m}$ are the Dunham coefficients which are equivalent to traditional spectroscopic constants (with some minor adjustments) [124]. The rotational constant, B_e, and the centrifugal distortion constant, -D_e, are equivalent to $Y_{0,1}$ and $Y_{0,2}$ respectively, and the harmonic wave number, ω_e, and the anharmonic correction, -$\omega_e x_e$, are equivalent to $Y_{1,0}$ and $Y_{2,0}$ respectively. Generally, the rotation only $Y_{0,1}$ and $Y_{0,2}$ terms, the vibration only $Y_{1,0}$ and $Y_{2,0}$ terms, and the coupling $Y_{1,1}$ and $Y_{1,2}$ terms are sufficient for reasonably accurate computations, and $Y_{0,0}$ represents a zero point energy above what is seen from the vibrational level equations (7.10 and 7.11). Since energy changes arising from changes in rotational state are typically much smaller than those resulting from changes in vibrational state, rotational energy states are put under the framework of being partitions of each vibrational level, and the resulting equation can be written as the sum of a vibration only term and a coupled rotation term [124]:

$$\begin{aligned}
\epsilon(\nu, J) &= G(\nu) + F_\nu(J) \\
G(\nu) &= Y_{1,0}(v + \tfrac{1}{2}) + Y_{2,0}(v + \tfrac{1}{2})^2 \\
F_\nu(J) &= Y_{0,1}[J(J+1)] + Y_{0,2}[J(J+1)]^2 \\
&\quad + Y_{1,1}(v + \tfrac{1}{2})[J(J+1)] + Y_{1,2}(v + \tfrac{1}{2})[J(J+1)]^2
\end{aligned} \tag{7.4}$$

When using a multi-temperature model to calculate population fractions, a temperature must be defined for each term. Typically, the vibrational temperature is used for the $G(\nu)$ term and the rotational temperature is used for the $F_\nu(J)$ term [124]. Defining the separate temperatures as T_r and T_v, the population density function $n_{\nu,J}/n$ is written as:

$$\frac{n_{\nu,J}}{n} = \frac{e^{-G(\nu)/kT_v} \cdot (2J+1)e^{-F_\nu(J)/kT_R}}{Q} \tag{7.5}$$

Where the partition function, $Q(T_r, T_v)$, is defined as:

$$Q(T_r, T_v) = \sum_\nu \left[e^{-G(\nu)/kT_v} \sum_J (2J+1)e^{-F_\nu(J)/kT_R} \right] \tag{7.6}$$

In this framework, the rotational partition function, $Q_r(\nu, T_r)$, is considered "vibration-prioritized" because each vibrational level is composed of a number of rotational partitions. However, our choice of decomposition was somewhat arbitrary. $\epsilon(\nu, J)$ can be rearranged in a "rotation-prioritized" framework (e.g. $G_J(\nu)$ and $F(J)$) where the coupled terms are split between each term as:

$$
\begin{aligned}
\epsilon(\nu, J) &= G_J(\nu) + F(J) \qquad (7.7)\\
G_J(\nu) &= Y_{1,0}(v+\tfrac{1}{2}) + Y_{2,0}(v+\tfrac{1}{2})^2 \\
&\quad + Y_{1,1}(v)[J(J+1)] + Y_{1,2}(v)[J(J+1)]^2 \\
F(J) &= Y_{0,1}[J(J+1)] + Y_{0,2}[J(J+1)]^2 \\
&\quad + Y_{1,1}(\tfrac{1}{2})[J(J+1)] + Y_{1,2}(\tfrac{1}{2})[J(J+1)]^2
\end{aligned}
$$

Under this framework each rotational level has a number of vibrational levels defined from the vibrational temperature and rotational level ($Q_v(J, T_v)$). The obvious differences between the two decompositions illustrate the error associated with the commonly accepted methods for describing internal energy distributions since all models are just approximations. Decoupling rotation and vibration improves computational efficiency, and removing the coupling terms (just assuming $Y_{1,1} = 0$ and $Y_{2,2} = 0$) from equation 7.3 does not increase error significantly in view of other approximations used for relaxation rates. The fully decoupled scheme is equivalent to describing the vibrational energy as an anharmonic oscillator and the rotational energy as a non-rigid rotor [124].

The non-rigid rotor is an extension of the rigid rotor model [1], and takes into account the stretching of molecular bonds as the rate of rotation increases [124]. The stretching is described with the second order term ($Y_{0,2}$) and decreases the energy needed to reach a higher energy level as can be seen by the increasing gap between rigid rotor and non-rigid rotor energy levels in Figure 7.2. The rotational energy levels expressed using Dunham coefficients and the equivalent spectroscopic constants are:

$$\epsilon_r(J) = Y_{0,1} \cdot J(J+1) + Y_{0,2} \cdot J^2(J+1)^2 \tag{7.8}$$

$$\epsilon_r(J) = B_e \cdot J(J+1) - D_e \cdot J^2(J+1)^2 \tag{7.9}$$

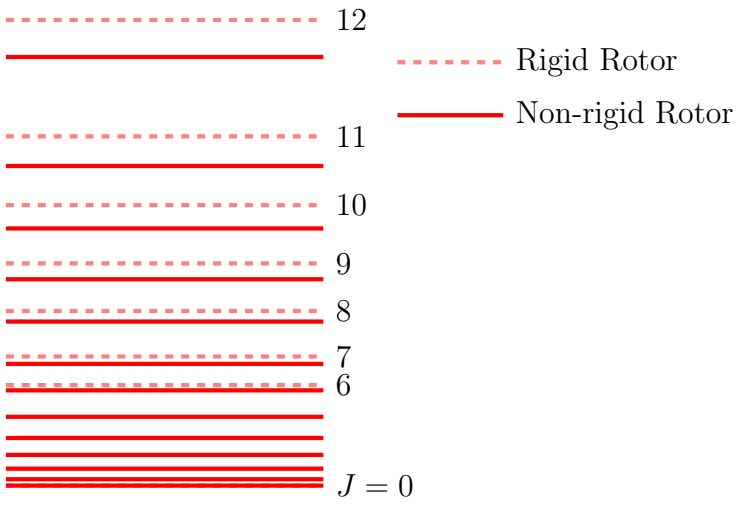

Figure 7.2: Rotational energy level spacing for a Rigid Rotor (dashed line) and a Non-rigid Rotor (solid line). $J = 0 \rightarrow 5$ are indistinguishable.

The nature of vibrational movement can be assumed to follow a simple harmonic oscillator (SHO), described with a first order term only, or an anharmonic oscillator (AHO) described by including a second order term. The AHO model results in the energy gap between successive energy levels decreasing, and reflects a nonlinear relationship between attractive force and molecular displacement for a vibrating molecule. The concept can be visualized by inspecting the potential well for a harmonic and an anharmonic model shown in Figure 7.3 [124]. The vibrational energy levels are expressed using Dunham coefficients and the equivalent spectroscopic constants as:

$$\epsilon'_v(\nu) = Y_{1,0}(\nu + \tfrac{1}{2}) + Y_{2,0}(\nu + \tfrac{1}{2})^2 \tag{7.10}$$

$$\epsilon'_v(\nu) = \omega_e(\nu + \tfrac{1}{2}) - \omega_e x_e(\nu + \tfrac{1}{2})^2 \tag{7.11}$$

Equation 7.11 can also be written with the ground level energy removed where $\omega_0 = \omega_e - 2\omega_e x_e$, and the resulting energy in each vibrational level becomes:

$$\epsilon_v(\nu) = \omega_0 \cdot \nu - \omega_e x_e \cdot \nu(\nu + 1) \tag{7.12}$$

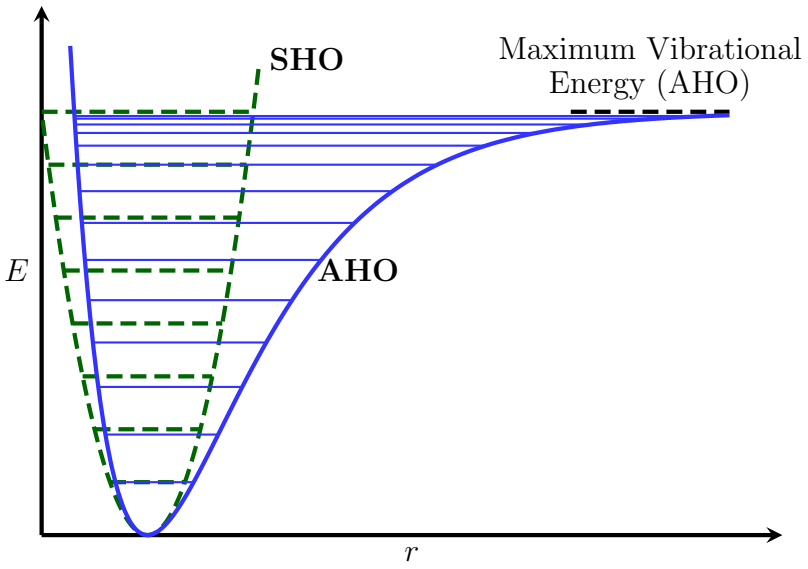

Figure 7.3: Vibrational energy level spacing in the potential well of a Simple Harmonic Oscillator (dashed parabola) and an Anharmonic Oscillator (solid line).

7.2 Nuclear Spin

The effect of nuclear spin must be considered when accurately modeling quantized rotational energy in a polyatomic molecule. For heteronuclear

molecules, the effects of spin can be neglected because the spin degeneracy, q, is constant for all levels [125]. Therefore, the constant can be factored out of the partition function calculation and canceled when calculating fractional populations as:

$$f_r(J) = \frac{q(2J+1)e^{-2\epsilon(J)/\hat{T}}}{q\sum_{j=0}^{N_J}(2j+1)e^{-2\epsilon(j)/\hat{T}}} = \frac{(2J+1)e^{-2\epsilon(J)/\hat{T}}}{\sum_{j=0}^{N_J}(2j+1)e^{-2\epsilon(j)/\hat{T}}} \tag{7.13}$$

However, nuclear spin cannot be neglected when modeling quantized rotational energy for homonuclear molecules because spin-symmetry affects the rotational energy states. Consider the case of a linear, diatomic molecule (e.g. N_2). Defining I as the moment of inertia, A rotation of 180° flips the nuclear positions of the two molecules, and even J values contribute $(I+1)(2I+1)$ nuclear spin degeneracy and odd J values contribute $I(2I+1)$ nuclear spin degeneracy [125]. The nuclear spin values for several diatomic molecules relevant to this work can be found in Table A.4 of Appendix A.

The partition function for a homonuclear molecule is defined with different nuclear spin degeneracy for odd and even states as:

$$Q_{rot} = \sum_{j=0,2,4,\ldots} q_{even}(2j+1)e^{-2\epsilon(j)/\hat{T}} + \sum_{j=1,3,5,\ldots} q_{odd}(2j+1)e^{-2\epsilon(j)/\hat{T}} \tag{7.14}$$

And the population density distribution is now dependent on the nuclear spin degeneracy of each individual rotational level.

$$f_r(J) = \frac{q_J(2J+1)e^{-2\epsilon(J)/\hat{T}}}{\sum_{j=0,2,4,\ldots} q_{even}(2j+1)e^{-2\epsilon(j)/\hat{T}} + \sum_{j=1,3,5,\ldots} q_{odd}(2j+1)e^{-2\epsilon(j)/\hat{T}}} \tag{7.15}$$

7.3 Scaling of Internal Energy Properties and Constants

Total energies are scaled by a reference translational energy, $E_{ref} = m_{ref}\hat{\eta}_{ref}^2$, as:

$$\hat{E}_i = \frac{E_i}{E_{ref}} \tag{7.16}$$

Where the index i indicates the energy mode (translational, rotational, etc.). Rotational and vibrational temperatures are scaled by the same reference temperature, T_{ref}, used in Section 3.5 to define the characteristic thermal speed and to scale the kinetic temperature:

$$\hat{T}_{r,v} = \frac{T_{r,v}}{T_{ref}} \tag{7.17}$$

Dunham coefficients and spectral constants are typically provided in units of cm^{-1}, and first must be converted to Joules through scaling by hc, Planck's constant and the speed of light in cm/s. The coefficient is then scaled by the reference translational energy:

$$Y_{ref}[cm^{-1}] = \frac{m_{ref}\eta_{ref}^2}{hc} = \frac{2k_bT_{ref}}{hc} = 1.39007[cm/K] \cdot T_{ref}[K] \tag{7.18}$$

$$\hat{Y}_{k,m} = \frac{Y_{k,m}}{Y_{ref}} \tag{7.19}$$

7.4 Internal Energy Form of The Distribution Function, Boltzmann Equation, and Collision Integral

If we assume the collision cross-section combined with the probability of a particular energy exchange takes the form: $\hat{\sigma}_T(\hat{g})P(\hat{g}, \nu\mu JK \rightarrow \hat{g}', \nu'\mu'J'K')$, the Boltzmann equation in its internal energy form is:

$$\frac{\partial\hat{\varphi}(\hat{\eta},\nu,J)}{\partial\hat{t}}+\hat{\eta}\frac{\partial\hat{\varphi}(\hat{\eta},\nu,J)}{\partial\hat{x}}= \tag{7.20}$$
$$\sum_{\mu}\sum_{K}\sum_{\hat{\zeta}}\Big[\underbrace{\frac{q'_J q'_K}{q_J q_K}\hat{\varphi}(\hat{\eta}',\nu',J')\hat{\varphi}(\hat{\zeta}',\mu',K')}_{replenishing}-\underbrace{\hat{\varphi}(\hat{\eta},\nu,J)\hat{\varphi}(\hat{\zeta},\mu,K)}_{depleting}\Big]$$
$$\cdot\,\hat{g}\hat{\sigma}_T(\hat{g})P(\hat{g},\nu\mu JK\rightarrow\hat{g}',\nu'\mu'J'K')$$

Where $\hat{\varphi}(\nu,J,\hat{\eta})$ is the density at every vibration and rotation internal energy level, ν, J, at every velocity location, $\hat{\eta}$. μ, K and $\hat{\zeta}$ are the energy level and velocity of the colliding partner and the post-collision values are $\nu', J', \hat{\eta}'$, and $\mu', K', \hat{\zeta}'$. The relative velocity between a colliding pair is defined as: $\hat{g}=|\hat{\eta}-\hat{\zeta}|$.

The distribution function can be rewritten as the product of the density at a single velocity class and a normalized matrix representing the distribution across vibrational and rotational energy levels for that velocity class. The subscript t denotes the total density for each velocity class, i.e. the number density value stored in a velocity distribution function at velocity $\hat{\eta}$.

$$\hat{\varphi}(\hat{\eta},\nu,J)=\hat{\varphi}_t(\hat{\eta})\cdot\hat{f}(\nu,J) \tag{7.21}$$

$$\text{where}\ \sum_{\nu,J}\hat{f}(\nu,J)=1 \tag{7.22}$$

The total equilibrium distribution is defined from the Maxwellian velocity distribution (equation 3.31) and the Boltzmann internal energy distribution (equation 7.5). It can be shown that the normalized energy density matrix for an equilibrium state is separable in ν and J if a decoupled description of rotational and vibrational energy is used ($f^E(\nu,J)=f_v^E(\nu)\cdot f_r^E(J)$), and the total equilibrium distribution is then written as:

$$\hat{\varphi}^E(\hat{\eta}, \nu, J) = \hat{\varphi}_t^E(\hat{\eta}) \cdot \hat{f}_v^E(\nu) \cdot \hat{f}_r^E(J) \tag{7.23}$$

An important assumption made in the current method is vibration and rotation distributions are separable at every velocity location outside equilibrium as well (this is particularly true near equilibrium).

$$\hat{\varphi}(\hat{\eta}, \nu, J) = \hat{\varphi}_t(\hat{\eta}) \cdot \hat{f}_v(\nu) \cdot \hat{f}_r(J) \tag{7.24}$$

Using the formulation in equation 7.24 The separated rotational and vibrational distributions shown in Figure 7.4 are unique to every velocity location, and the total rotational and vibrational distributions at a spatial location are found by taking the sum over every velocity location of the velocity dependent distributions.

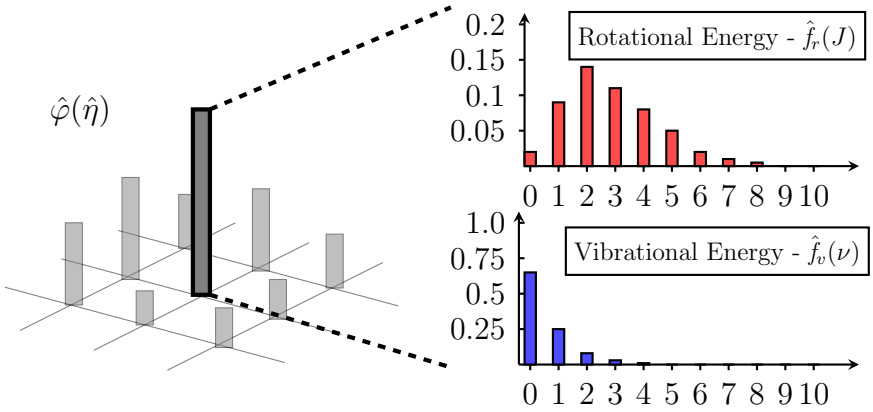

Figure 7.4: Scaled vibrational and rotational energy distributions at a single velocity location.

The distribution of internal energy may also be written using density weighted vibration and rotation distributions, $\hat{\psi} = \hat{\varphi}_t \cdot \hat{f}$, such that:

$$\hat{\varphi}_t(\hat{\eta}) = \sum_{\nu} \hat{\psi}_v(\nu) = \sum_{J} \hat{\psi}_r(J) \tag{7.25}$$

And the sum over all velocities is still the total density at each spatial location.

$$\hat{n} = \sum_{\hat{\eta}} \hat{\varphi}_t(\hat{\eta}) \tag{7.26}$$

7.5 Macroscopic Properties Related to Internal Energy

The total energy in either rotational or vibrational modes is the sum over all levels of the energy in each level.

$$\hat{E}_{rot} = \sum_{\hat{\eta}} \sum_{J} \hat{\psi}_r(J) \cdot \hat{\varepsilon}_r(J) \tag{7.27}$$

$$\hat{E}_{vib} = \sum_{\hat{\eta}} \sum_{\nu} \hat{\psi}_v(\nu) \cdot \hat{\varepsilon}_v(\nu) \tag{7.28}$$

With the introduction of rotational and vibrational energy, a rotational and vibrational temperature is also introduced, and the temperatures are calculated from the relation between energy and temperature at equilibrium. The commonly used analytic expressions are obtained under the assumptions of a simple harmonic oscillator, a rigid rotor, an infinite number of energy levels, and $\hat{T} >> \hat{\theta}_{rot}$ [1].

$$\hat{T}_r = 2 \cdot \hat{E}_{rot} \tag{7.29}$$

$$\hat{T}_v = \frac{\hat{\theta}_v}{ln\left(\frac{2 \cdot \hat{E}_v}{\hat{n}\hat{\theta}_v} + 1\right)} \tag{7.30}$$

However, in the discrete velocity method, the vibrational and rotational distributions have been truncated and both AHO and non-rigid rotor models

are often used. The analytic expressions (equations 7.29 and 7.30) do not hold for higher order models and break down at high temperatures due to the truncation of the internal energy distributions. A relation between equilibrium energy and temperature is formulated by running over an array of temperature values and calculating energy from a truncated Boltzmann distribution as:

$$\hat{E}_r = \sum_{J}^{N_J} f_r^E(J) \cdot \hat{\varepsilon}_r(J) \tag{7.31a}$$

$$\hat{E}_v = \sum_{\nu}^{N_\nu} f_v^E(\nu) \cdot \hat{\varepsilon}_v(\nu) \tag{7.31b}$$

A two part, piecewise continuous curve fit is matched to the resulting data where one function is used for low energies where the solution is close to the analytic expression and the other for high energies where truncation causes significant differences. The split between low and high energies is made at a somewhat arbitrary fraction of the maximum allowable energy (e.g. $E_{split} = \alpha\hat{\varepsilon}_{v,max}$ for vibration).

$$\hat{T} = \begin{cases} c_0 + c_1 \cdot \hat{E} + c_2 \cdot \hat{E}^2 + c_3 \cdot \hat{E}^3 + ... & \text{for } \hat{E} < \hat{E}_{split} \\ b_0 + b_1 \cdot \hat{E} + b_2 \cdot \hat{E}^2 + b_3 \cdot \hat{E}^3 + ... & \text{for } \hat{E} > \hat{E}_{split} \end{cases} \tag{7.32}$$

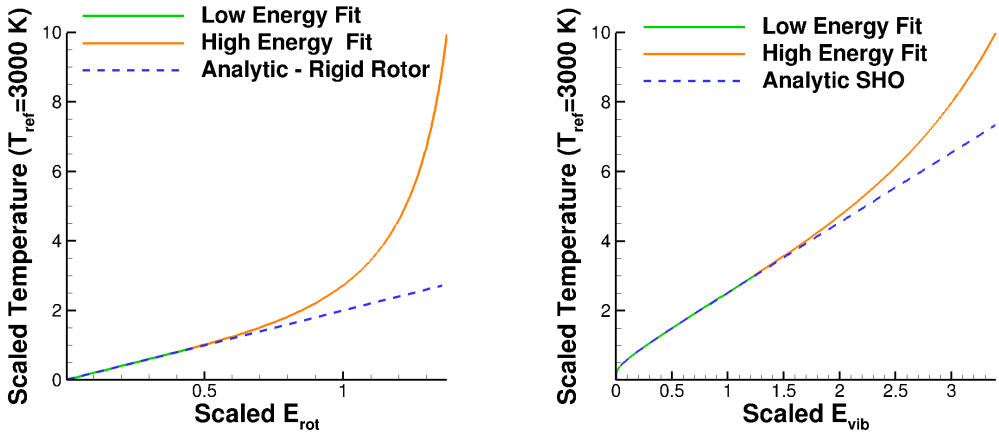

(a) (b)

Figure 7.5: Relation between total energy and temperature for a truncated (a) rotational and (b) vibrational distribution function at equilibrium.

A variable describing the effective vibrational degrees of freedom is defined for vibration to satisfy the relationship between energy and temperature at equilibrium. This quantity will be used when calculating the overall temperature.

$$\xi_v^* = \frac{4 \cdot \hat{E}_v}{\hat{T}_v} \tag{7.33}$$

7.6 Inelastic Interactions

The final section of this chapter is a discussion of methods for simulating inelastic collision events. In the present work, inelastic collisions exchange energy between translational and vibrational (V-T) or rotational (R-T) energy modes. Energy exchanges between all three modes (V-R-T), vibration only (V-V), and rotation only (R-R) are not currently accounted for in the DVM algorithm.

7.6.1 Relaxation Rates

The relaxation time of a gas species is the time required for the difference between the internal energy and the equilibrium energy, $E - E^E$, to fall to $1/e$ of its initial value [1]. Typically, the relaxation time may be written as the product of the collision time, τ_c, and a relaxation number, Z. In reality the relaxation number is a complicated function of microscopic properties, but is typically approximated as a function of kinetic temperature and modeled from experimental data. Furthermore, for small temperature ranges Z_r and Z_v can even be approximated as constants [2]. Parker's model [126], which is used in many CFD models, is implemented in the current work for rotational relaxation numbers as:

$$Z_R = \frac{Z_R^\infty}{1 + \left(\frac{\pi^3 T^*}{4T}\right)^{1/2} + \left(\frac{\pi^2}{4} + \pi\right)\left(\frac{T^*}{T}\right)} \tag{7.34}$$

The model depends on two constants, a reference temperature, T^*, and a reference relaxation number, Z_R^∞. Relevant constants can be found for a variety of polyatomic molecules in Appendix A. However, rotational non-equilibrium is neglected in applications of Parker's model due to the short rotational relaxation times in comparison to vibrational relaxation times [127]. This is despite evidence of its importance by Robben [128, 129], and work showing R-T and V-T relaxation times become comparable at high temperatures [130].

Millikan and White [131] derived a commonly used V-T relaxation number by fitting experimental results. The first term in equation 7.35 shows the original formulation as an exponential function of temperature divided by total pressure. However, the model breaks down at high temperatures, and a correction factor prescribed by Park [132] is applied (shown as the second term in equation 7.35).

$$Z_{v,AB} = \nu_{AB} \left[\underbrace{\frac{101325[Pa] \cdot e^{C_1 T_{mix}^{-1/3} + C_2}}{(n k_b T)_{mix}}}_{M\&W} + \underbrace{\frac{1}{\overline{c}\sigma_v n}}_{Park} \right] \tag{7.35}$$

$\overline{c}$ is the average molecular velocity, σ_v is a reference vibrational cross section, and ν_{AB} is the collision frequency between species A and species B. σ_v, ν_{AB}, C_1, and C_2 are calculated as:

$$\nu_{AB} = \frac{2}{\sqrt{\pi}} \frac{(\hat{d}_A + \hat{d}_B)^2}{4} \hat{n}_B \sqrt{\frac{\hat{T}_{diam}}{\hat{m}_{red}}} \left(\frac{\hat{T}_{mix}}{\hat{T}_{diam}} \right)^{1-\omega_{AB}} \tag{7.36}$$

$$\sigma_v = 10^{-20} [m^2] \tag{7.37}$$

$$C_1 = 1.16 \times 10^{-3} m_{red}^{1/2} \theta_{v,A}^{4/3} \tag{7.38}$$

$$C_2 = -1.74^{-5} m_{red}^{3/4} \theta_{v,A}^{4/3} - 18.42 \tag{7.39}$$

Bird provides a reduced, simplified form of Z_v using two species specific constants, C_3 and C_4, which can be found in his book [2].

$$Z_v = \left(\frac{C_3}{T^\omega} \right) e^{C_4 T^{-1/3}} \tag{7.40}$$

Defining P as the probability of an inelastic collision occurring out of the total number of collisions in a time step, it has been shown by [133,134] that the intuitive probability of $P = 1/Z$ is not accurate for the Larsen-Borgnakke model. As a solution, Haas *et al.* [135] showed the relaxation rate is adjusted by the translational and relevant internal degrees of freedom to account for the difference between macroscopic and microscopic quantities. The fraction of collisions between species A and species B treated as an inelastic collision is then:

$$P_r = \frac{\xi_{tr} + \xi_{rot}}{\xi_{tr}} \cdot \frac{1}{Z_r} \tag{7.41a}$$

$$P_v = \frac{\xi_{tr} + \xi_{vib}}{\xi_{tr}} \cdot \frac{1}{Z_v} \tag{7.41b}$$

Further adjustments to the probability in DSMC are made depending on the selection method for whether a molecule will undergo energy exchange of a particular mode. However, no further adjustments are needed in the models discussed in Chapter 8.

7.6.2 Landau-Teller Relaxation

One approximation of internal energy is to drop the quantum viewpoint and only operate on the total internal energy in a particular velocity class without any knowledge (or assumption) about the shape of the distribution [1].

Landau and Teller [81] and Jeans [136] put forward the theory for vibration and rotation respectively that the energy relaxation is described by the difference between the current internal energy, $\hat{E}_i(t)$ and an instantaneous equilibrium value, $\hat{E}^E(t)$.

$$\frac{d\hat{E}(t)}{dt} = -\frac{\left(\hat{E}_i(t) - \hat{E}^E(t)\right)}{\tau} \tag{7.42}$$

Where τ is a parameter called the *relaxation time*. In the original theory by Landau and Teller τ was a complex function of temperature and pressure, but the value can be approximated by the relaxation rate Z, presented in Section 7.6.1. The final equilibrium energy, $\hat{E}^E$, is assumed to be a function of kinetic temperature as:

$$\hat{E}^E = \hat{E}_i(\hat{T}_{kin}) = \frac{\xi_i}{4}\hat{T}_{kin} \tag{7.43}$$

While the continuous model requires a minimum amount of stored information, the method loses all information about any non-equilibrium structure of the internal energy distribution, only operating on the total energy value. The Landau-Teller model is also limited to moderate temperatures where $k_b T$ is much larger than $h\omega$ [1], but if T becomes too large the relaxation time, τ, becomes a more complicated function.

7.6.3 Larsen-Borgnakke Approximation

A common phenomenological model for calculating energy exchanges used in many DSMC models is the Larsen-Borgnakke model [2]. The model is formulated to relax energy modes towards equilibrium by drawing post-collision energy values from the combined translational and internal energy distributions. Correct relaxation rates are achieved by formulating collision numbers and selection probabilities to match empirical data.

Originally written for the simulation of energy transfers between translation and continuous rotation, the Larsen-Borgnakke method was extended to quantized rotation-translation [94] (with degenerate energy levels and nuclear spin) and quantized vibration-translation [95,136]. In the following discussion, quantized models will be assumed that do not allow for multiple relaxations, i.e. only a single molecule in a colliding pair exchanges either rotational or vibrational energy during an inelastic collision.

During an inelastic collision the post-collision level of each molecule is drawn from a distribution of a most probable energy levels given the total collision energy, where the total collision energy is the sum of the translational energy in the collision (equation 7.44) and the internal energy of one of the colliding particles (equation 7.45). In the following equations 7.44-7.47 "i" is the internal energy level of the colliding partner undergoing energy exchange (A).

$$\hat{E}_t = \frac{1}{2}\hat{m}_{red}\hat{g}^2 \tag{7.44}$$

$$\hat{E}_{int} = \frac{1}{2}\hat{m}_A\hat{\varepsilon}_{i,A} \tag{7.45}$$

$$\hat{E}_c = \hat{E}_t + \hat{E}_{int} \tag{7.46}$$

The probability distribution of a post-collision energy level, i', occurring is given as a function of the internal energy of the level, $\hat{E}_{int}(i')$, the degeneracy, $q_{i'}$, and the collision energy, $\hat{E}_c$, which is a constant during a single collision due to energy conservation [2].

$$F(i') \propto q_{i'}(\hat{E}_c - \hat{E}_{int}(i'))^{3/2-\omega} \tag{7.47}$$

The maximum of equation 7.47 gives the most probable post-collision energy level, i^*, and taking the ratio of $F(i')$ and $F(i^*)$ results in a probability distribution normalized such that the most probable level has a value of 1.

$$P(i') = \frac{q_{i'} \cdot (\hat{E}_c - \hat{E}_{int}(i'))^{3/2-\omega}}{q_{i^*} \cdot (\hat{E}_c - \hat{E}_{int}(i^*))^{3/2-\omega}} \tag{7.48}$$

The post-collision energy selection method is described below. The details of the derivations can be found in Appendix D.

Heteronuclear Larsen-Borgnakke

Rotational energy exchanges in heteronuclear molecules allow energy to be transferred from one energy level to any other available energy level. The first step is to find the maximum allowable energy level, J_{max}. The maximum

allowed level is the rotational level in which the maximum possible collision energy can be contained. For a rigid rotor model this means setting the collision energy, $\hat{E}_c$, equal to the rotational energy and then solving for J_{max}:

$$\hat{E}_c = \hat{B}_e \cdot J_{max}(J_{max}+1) \tag{7.49}$$

$$J_{max} = int\left\{\frac{1}{2}\left(-1+\sqrt{1+\frac{4\hat{E}_c}{\hat{B}_e}}\right)\right\} \tag{7.50}$$

And for a non-rigid rotor model the same process results in:

$$\hat{E}_c = \hat{B}_e \cdot J_{max}(J_{max}+1) - \hat{D}_e J_{max}^2(J_{max}+1)^2 \tag{7.51}$$

$$J_{max} = int\left\{\frac{1}{2}\left(-1+\sqrt{1-2\frac{\hat{B}_e}{\hat{D}_e}+\frac{2}{\hat{D}_e}\sqrt{\hat{B}_e^2-4\hat{E}_c\hat{D}_e}}\right)\right\} \tag{7.52}$$

For a rigid rotor, equation 7.47 can be written for rotation, and the most probable rotational level can be found from the maximum of the function, resulting in:

$$J^2 + J + \frac{3/2-\omega-2\frac{\hat{E}_c}{\hat{B}_e}}{8-4\omega} = 0 \tag{7.53}$$

Where solving for J gives:

$$J^* = nint\left\{\frac{1}{2}\left(-1+\sqrt{\frac{1+\frac{4\hat{E}_c}{\hat{B}_e}}{4-2\omega}}\right)\right\} \tag{7.54}$$

The most probable energy level for the rigid rotor is used as an approximation for the non-rigid rotor as well. The rigid rotor result is used for both

models because the non-rigid rotor requires a solution to a more complicated fourth order function, but the result is extremely close to the rigid rotor result. See Appendix D for a more in depth argument for the approximation. It is important to note that the probability of choosing a particular level does not change due to inaccuracies in the denominator of equation 7.48; rather the acceptance rate of all levels decreases proportionally and a greater number of random number draws will be used.

A post-collision energy level is selected by multiplying the maximum available energy level by a random fraction from 0 to 1 and finding the closest integer result.

$$J' = nint(R_f \cdot J_{max}) \tag{7.55}$$

The post-collision level is tested against the level probability using an acceptance rejection scheme. The probability of the chosen post-collision level in equation 7.48 is compared against a second random fraction, and if the random fraction is less than the probability, the post-collision level is accepted. If the random fraction is greater, a new post-collision level is drawn and the process is repeated.

Homonuclear Larsen-Borgnakke - Even Spin

If the particle undergoing energy exchange is a homonuclear molecule with an even pre-collision rotational energy level, only even post-collision energy levels are allowed. We redefine the energy level to be restricted to even values as:

$$J = 2j \quad j = 0, 1, 2, 3... \tag{7.56}$$

And substitute the definition into the general equations. The collision energy is equated to the maximum, even leveled rotational energy as:

$$\hat{E}_c = \hat{B}_e 2j_{max}(2j_{max}+1) \tag{7.57}$$

And solving equation 7.57 for j_{max} gives:

$$j_{max} = int\left\{\frac{1}{4}\left(-1+\sqrt{1+\frac{2\hat{E}_c}{\hat{B}_e}}\right)\right\} \tag{7.58}$$

For a non-rigid rotor, the collision energy equated to the maximum, even leveled rotational energy is:

$$\hat{E}_c = \hat{B}_e 2j_{max}(2j_{max}+1) - \hat{D}_e 4j_{max}^2(2j_{max}+1)^2 \tag{7.59}$$

And solving equation 7.59 for j_{max} gives:

$$j_{max} = int\left\{\frac{1}{4}\left(-1+\sqrt{1-2\frac{\hat{B}_e}{\hat{D}_e}+\frac{2}{\hat{D}_e}\sqrt{\hat{B}_e^2-4\hat{E}_c\hat{D}_e}}\right)\right\} \tag{7.60}$$

The most probable even energy level may also be found through a simple substitution of equation 7.56 into equation 7.50 as:

$$j^* = nint\left\{\frac{1}{4}\left(-1+\sqrt{\frac{1+4\hat{E}_c/\hat{B}_e}{4-2\omega}}\right)\right\} \tag{7.61}$$

Once a post-collision level has been chosen, the solution is converted back to J.

Homonuclear Larsen-Borgnakke - Odd Spin

If the particle undergoing energy exchange is a homonuclear molecule with an odd pre-collision rotational energy level, only odd post-collision energy levels are allowed. In a similar manner to Section 7.6.3, we redefine our definition of the energy level to be restricted to odd values as:

$$J = 2j + 1 \quad j = 0, 1, 2, 3... \tag{7.62}$$

And substitute the definition into the general equations. The collision energy is equated to the maximum, odd leveled rotational energy as:

$$\hat{E}_c = \hat{B}_e(2j_{max} + 1)(2j_{max} + 2) \tag{7.63}$$

And solving equation 7.63 for j_{max} gives:

$$j_{max} = int\left\{\frac{1}{4}\left(-3 + \sqrt{1 + \frac{2\hat{E}_c}{\hat{B}_e}}\right)\right\} \tag{7.64}$$

For a non-rigid rotor, the collision energy equated to the maximum, odd leveled rotational energy is:

$$\hat{E}_c = \hat{B}_e(2j_{max} + 1)(2j_{max} + 2) + \hat{D}_e(2j_{max} + 1)^2(2j_{max} + 2)^2 \tag{7.65}$$

And solving equation 7.65 for j_{max} gives:

$$j_{max} = int\left\{\frac{1}{4}\left(-3 + \sqrt{1 - 2\frac{\hat{B}_e}{\hat{D}_e} + \frac{2}{\hat{D}_e}\sqrt{\hat{B}_e^2 - 4\hat{E}_c\hat{D}_e}}\right)\right\} \tag{7.66}$$

Finally, the most probable odd energy level is:

$$j^* = nint\left\{\frac{1}{4}\left(-3+\sqrt{\frac{1+4\hat{E}_c/\hat{B}_e}{4-2\omega}}\right)\right\} \tag{7.67}$$

And once a post-collision level has been chosen, the solution is converted back to J.

Vibration

Vibrational energy transfers follow the same procedure as rotation. The maximum allowed vibrational level for a SHO model is:

$$\nu_{max} = int\left(\frac{E_c}{\hat{\omega}_0}\right) \tag{7.68}$$

$$\text{Where } \hat{E}_c = \hat{\omega}_0\nu \tag{7.69}$$

And the maximum allowed vibrational level for a AHO model is:

$$\nu_{max} = int\left(\frac{(\hat{\omega}_0 - \hat{\omega}_e\hat{\chi}_e) - \sqrt{B}}{2\hat{\omega}_e\hat{\chi}_e}\right) \tag{7.70}$$

$$\text{Where } \hat{E}_c = \hat{\omega}_0\nu - \hat{\omega}_e\hat{\chi}_e\nu(\nu+1) \tag{7.71}$$

$$\text{And } B = (\hat{\omega}_0 - \hat{\omega}_e\hat{\chi}_e) - 4\hat{\omega}_e\hat{\chi}_e\hat{E}_c \tag{7.72}$$

The most probable energy level in vibration is always the 0th level, $\nu^* = 0$, and equation 7.48 can be simplified as:

$$P(\nu') = \left(1 - \frac{\hat{E}(\nu')}{\hat{E}_c}\right)^{3/2-\omega} \tag{7.73}$$

7.6.4 Other Models

The Landau-Teller and Larsen-Borgnakke models are the energy exchange models implemented in Chapter 8. However, the choice to use these models was more a matter of convenience than anything else. A variety of other models may, and should, be implemented in the algorithm. Ideally, state-specific cross-sections can be found and used directly.

Chapter 8

Implementation for Gases with Internal Energy

Two different models for internal energy were implemented throughout the course of this work: A single valued rotational model where the total rotational energy is stored at each velocity location and a quantized rotation and vibration model where distribution functions for each internal energy mode are stored at each velocity. While the models are quite different, there are some overlaps in the methods for assuring accurate representation of the relaxation rates and conservation of mass, momentum, and total energy during replenishment. After discussing these overlapping concepts, each model will be discussed for both standard full Monte Carlo and variance reduced forms and a set of results will be presented for each model.

8.1 Depletion Splitting

The relaxation rates $Z_{r,A}$, $Z_{r,B}$, $Z_{v,A}$, and $Z_{v,B}$ are accounted for through a density splitting method where every collision is separated into five parts representing one elastic collision and four different inelastic collisions (two

P. Clarke, P. Varghese, and D. Goldstein, A. Morris, P. Bauman, and D. Hegermiller, "A novel discrete velocity method for solving the Boltzmann equation including internal energy and variable grids in velocity space," in *Proceedings of the* 28th *International Symposium on Rarefied Gas Dynamics*, vol. 1501, (Zaragosa, Spain), p. 373, AIP Conference Proceedings, 2012.

P. Varghese and D. Goldstein supervised the project, A. Morris and D. Hegermiller collaborated on research ideas, and P. Bauman provided coding implementation support.

for each particle in the colliding pair). Multiple relaxations are disallowed based on recommendations presented by Haas and Gimelshein [135, 137], and only one member of the colliding pair is allowed to either exchange energy between rotational and translational modes (R-T) or vibrational and translational modes (V-T) for each of the inelastic collisions. Note that energy transfers of rotation-vibration, rotation-rotation, and vibration-vibration are not allowed in the method, but future work should consider the effects of each of these processes since one or all of them may have significant effects on relaxation rates [89]. Under this framework, the number density depleted during a collision is separated into five individual pieces representing unique collision types:

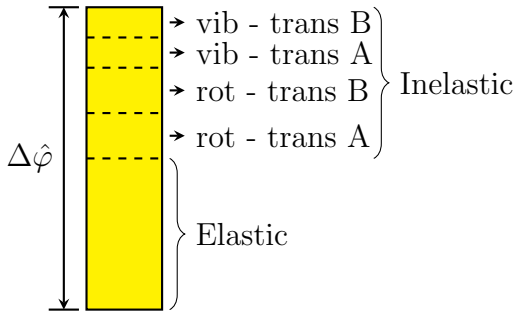

Figure 8.1: Total depletion ($\Delta\hat{\varphi}$) split into elastic and inelastic parts according to inelastic collision probabilities. Each inelastic part represents a change in a single mode (either rotation or vibration) of a single member of the colliding pair.

And the number density of each depletion segment is the product of the total number density and the probability of each collision type occurring.

$$\Delta\hat{\varphi}_{r,A} = P_{r,A}\Delta\hat{\varphi}_{depl} \tag{8.1a}$$

$$\Delta\hat{\varphi}_{r,B} = P_{r,B}\Delta\hat{\varphi}_{depl} \tag{8.1b}$$

$$\Delta\hat{\varphi}_{v,A} = P_{v,A}\Delta\hat{\varphi}_{depl} \tag{8.1c}$$

$$\Delta\hat{\varphi}_{v,B} = P_{v,B}\Delta\hat{\varphi}_{depl} \tag{8.1d}$$

$$\Delta\hat{\varphi}_{elastic} = \left(1 - P_{r,A} - P_{r,B} - P_{v,A} - P_{v,B}\right)\Delta\hat{\varphi}_{depl} \tag{8.1e}$$

The probabilities for an inelastic collision have been calculated from the equations in Section 7.6.3 for the Larsen-Borgnakke approach and as $1/Z_{r/t}$ for Landau-Teller-like methods, and the probability of an elastic collision is the remainder after removing each of the inelastic collision probabilities. Note that the use of the density splitting method as described restricts the sum of the inelastic probabilities to be less than one. The restriction may become important when considering an appropriate model for relaxation numbers. For instance, when the temperature drops below 100K, Parker's model calculates Z_r values less than 2 for diatomic Nitrogen, and the sum of the probabilities of an R-T inelastic collision between two N_2 particles may be greater than 1.

A single colliding velocity pair is chosen and used for all five of the depletion fractions, but the internal energy level selections, energy exchanges, and replenishing calculations are individually determined for each part. This results in multiple replenishment events per depletion and an increase in computational work per simulated collision in comparison to the DVM solution for monatomic atoms. However, the decrease in efficiency per collision is offset by avoiding an increase in the total number of simulated collisions necessary to produce smooth internal energy distributions. In most DSMC calculations, the relaxation rate is met by allowing a collision to either be elastic or inelastic based on an accept/reject comparison to the relaxation numbers, Z_r and Z_v.

On the average, a V-T inelastic collision will occur once every Z_v number of collisions, and a R-T inelastic collision will occur once every Z_r number of collisions. However, if a relaxation number is large (like Z_v for low temperatures) the method may produce noisy solutions because the entire internal energy relaxation each time step is spread over only a couple (or fewer) collisions. The typical solution to the problem in DSMC is to increase the number of simulated molecules until the number of collisions is much larger than Z_r or Z_v. In contrast, the depletion splitting method spreads the energy exchange across every collision, and smooth solutions are produced without an increase in the number of simulated collisions.

However, for low Z values, the benefits of depletion splitting start to disappear. Future work may find it beneficial to formulate a hybrid method where modes with low Z are treated with an accept/reject scheme and modes with high Z are treated by a depletion splitting scheme. E.g. if Z_r is very low and Z_v is high, the depletion is split into three parts: two inelastic fractions for V-T collisions and one fraction which can either be elastic or R-T inelastic depending on an accept/reject decision.

8.2 Replenishment

After a depletion has been performed according to the models discussed in the upcoming Sections 8.3 and 8.4, an energy exchange, $\Delta\hat{E}$, is calculated between the translational and internal energies in the collision from an appropriate energy exchange model. The change in internal energy can be positive or negative and is associated with an equal and opposite change in translational energy. The change in translational energy is written as:

$$\Delta\hat{E}_{tr} = -\Delta\hat{E}_{int} = \frac{1}{2}\hat{m}_r(\hat{g})^2 - \frac{1}{2}\hat{m}_r(\hat{g}')^2 \tag{8.2}$$

Where $\hat{g}'$ is a new relative post-collision speed. Reorganizing equation 8.2 gives:

$$\hat{g}' = \sqrt{\hat{g}^2 - \frac{2\Delta \hat{E}_{int}}{\hat{m}_r}} \tag{8.3}$$

The relative velocity vector $\hat{g}$ is replaced with $\hat{g}'$ (appropriately aligned with the center of mass velocity of the collision pair, $\hat{V}_{com}$), and replenishing velocities are chosen by rotating the new relative velocity vector about $\hat{V}_{com}$ to find the post-collision velocities $\hat{\eta}'$ and $\hat{\zeta}'$ as can be seen in Figure 8.2. The rotation of the relative velocity vector is performed according to one of the collision cross-section models presented in Section 4.1.3, and remapping onto the grid is done according to the mass, momentum, and kinetic energy conservative scheme from Section 4.1.3. Internal energy follows the replenishing number densities during the remapping process. If some fraction of the replenishment, $f_i \Delta\hat{\varphi}$, is sent to a stencil location the same fraction of internal energy, $f_i \hat{E}_{int}$, is sent to the stencil location.

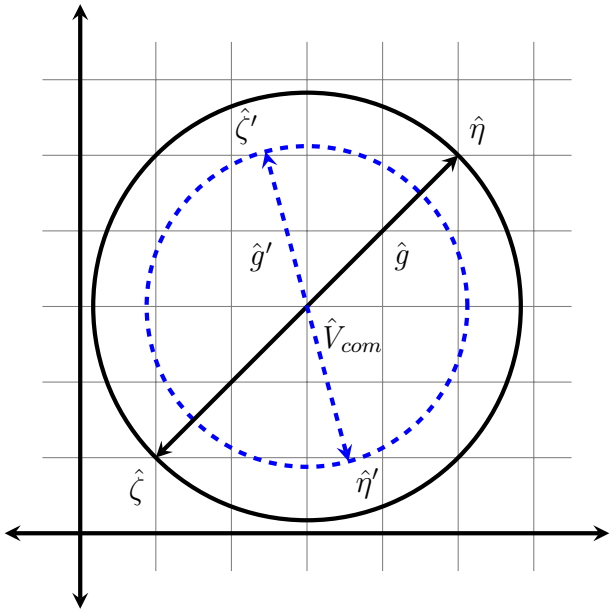

Figure 8.2: 2D representation of the energy exchange collision sphere between 2 diatomic (or 1 diatomic and 1 monatomic) particles having the same mass. The dashed lines represents a collision which loses relative translational energy.

8.3 Single Valued Rotational Energy

The first model chosen to describe rotational energy states is basic, with room for expansion to a more detailed description of internal energy. The model is only intended to represent the total internal energy and the transfer between rotational and translational energy with minimal additional computational effort. With these requirements in mind, only a single rotational energy value is stored at each grid location of the velocity distribution function. The value, $\hat{E}_r(\hat{\eta})$, represents the total rotational energy of all molecules at that particular velocity, and an average rotational energy per unit number density, $\hat{\varepsilon}_r(\hat{\eta})$, can be calculated from $\hat{E}_r(\hat{\eta})$ and $\hat{\varphi}(\hat{\eta})$.

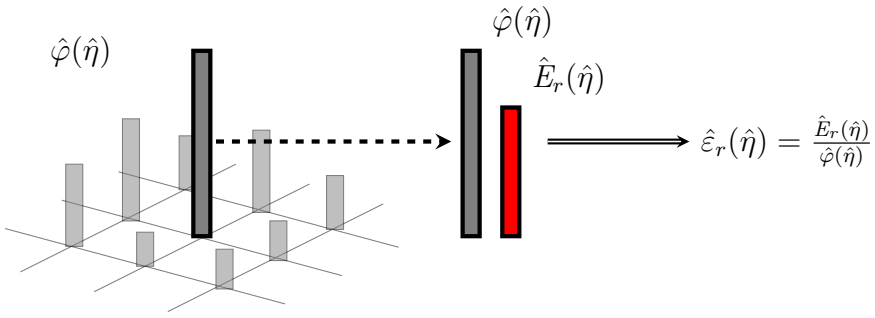

Figure 8.3: Rotational energy stored as a single value at each velocity location.

The single valued rotational model has no knowledge of the underlying distribution of number density across rotational energy levels. The non-equilibrium nature of rotational energy may only be judged by comparing the values of $\hat{\varepsilon}_{rot}$ at every velocity location (at equilibrium, the values should be the same) and from the difference between the kinetic temperature and the rotational temperature. Since distributions are not known, the rotational temperature is calculated with an analytic solution based on the rotational degrees of freedom, ξ_{rot}, total rotational energy, and number density:

$$\hat{T}_{rot} = \frac{4}{\hat{n}\xi_{rot}} \cdot \sum_{\hat{\eta}} \hat{E}_{rot}(\hat{\eta}) \tag{8.4}$$

Note: $\xi_{rot} = 2$ for linear molecules (including diatomics) and $\xi_{rot} = 3$ for non-linear polyatomic molecules. In the single valued rotational model, the rotational energy at each velocity location is initialized by determining the total energy at each velocity location as a function of scaled rotational temperature, rotational degrees of freedom, ξ_{rot}, and the local value of the velocity distribution function as:

$$\hat{E}_r(\hat{\eta}) = \hat{\varepsilon}_{r,init} \cdot \hat{\varphi}(\hat{\eta}) = \frac{\xi_r}{4} \hat{T}_{r,init} \cdot \hat{\varphi}(\hat{\eta}) \tag{8.5}$$

8.3.1 Full Monte Carlo Depletion

Depletion selection, calculating depletion quantities, and determining the number of simulated collisions are exactly the same as in the monatomic method for the standard full Monte Carlo case described in Section 4.1.1. The quantity of rotational energy depleted, $\Delta\hat{E}_{depl}$, is equal to the rotational energy per unit number density at the collision location, $\hat{\varepsilon}_r(\hat{\eta})$, multiplied by the depletion amount, $\Delta\hat{\varphi}$:

$$\Delta\hat{E}_{depl}(\hat{\eta}) = \Delta\hat{\varphi} \cdot \hat{\varepsilon}_r(\hat{\eta}) \tag{8.6}$$

And the depletion density and energy are removed from the colliding velocity locations after choosing each colliding velocity pair (Figure 8.4). Note that since vibrational energy was not modeled, the depletion is only split into three parts: elastic, inelastic R-T$_A$, and inelastic R-T$_B$. The total energy is split into parts using the same fractions as the number density depletion.

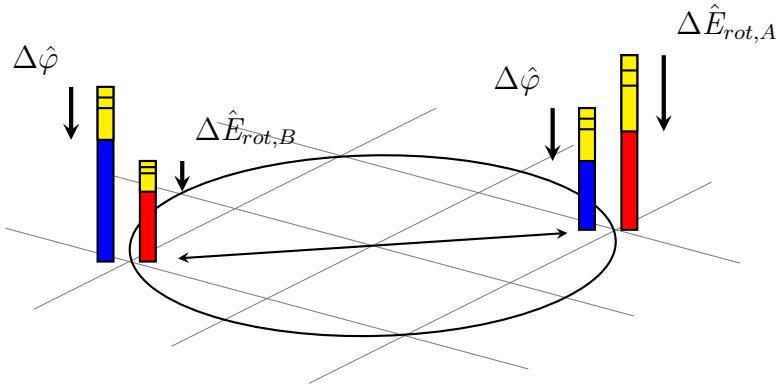

Figure 8.4: Proportional depletion is made from both density and average rotational energy distributions. There are three depletion fractions per simulated collision representing one elastic and two R-T inelastic collisions.

8.3.2 Variance Reduced Depletion

As in previous discussions (Sections 4.1.2 and 6.5), constructing a variance reduction technique starts with an identity describing the nature of collisions between particles drawn from equilibrium distributions.

The net change in time is zero in a distribution in total (thermal and rotational) equilibrium due to collisions with particles drawn from itself or another equilibrium distribution at the same temperature (kinetic and rotation) and bulk velocity.

The decomposition of $\hat{\varphi}$ into equilibrium and deviation parts is made in the same manner as first presented in Section 4.1.2, but the equilibrium distribution is calculated from an equilibrium temperature defined as a function of kinetic and rotational temperatures.

$$\hat{T}_{eq} = \frac{3}{3+\xi_{rot}}\hat{T}_{tr} + \frac{\xi_{rot}}{3+\xi_{rot}}\hat{T}_{rot} \tag{8.7}$$

Using the equilibrium temperature to calculate the equilibrium distribution means the decomposition of $\hat{\varphi}$ will always result in a deviation if $\hat{T}_{kin} \neq \hat{T}_{rot}$ or if the velocity distribution function is not a Maxwellian function. However, the method does not account for rotational non-equilibrium. If $\hat{T}_{kin} = \hat{T}_{rot}$ and $\hat{\varphi}$ is a Maxwellian but the rotational energy is spread across the velocity distribution function in a non-equilibrium manner, the method described will not recognize the presence of the non-equilibrium. The number of simulated collisions will be zero, and the method will fail to equilibrate rotational energy across the velocity domain.

Figure 8.5 shows an example of a decomposition of a Maxwellian function where $\hat{T}_{rot} = 0 \neq \hat{T}_{kin}$. In the decomposition, if $\hat{\varphi}^d \to 0$, $\hat{\varepsilon}_r^d(\hat{\eta})$ can approach infinity. While picking the problem location for a collision is rare because the probability of selecting a low density point is small, such a large

number may become problematic since $\Delta\hat{E}_{depl}$ is calculated from the average rotational energy and the (constant) depletion quantity, $\Delta\hat{\varphi}$. When the low density (and high $\hat{\varepsilon}_r^d$) point is chosen, an extremely large rotational energy will be depleted, causing a drastic increase in noise and eventual blow-up of a simulation. The problem is mitigated by limiting $\Delta\hat{E}_{depl}$ to the total energy available at the velocity location, $\hat{\varepsilon}(\hat{\eta})\cdot\hat{\varphi}(\hat{\eta})$. Therefore, the depletion will have a much smaller rotational energy per unit number density than the depleting velocity location originally contained, and the rotational energy at the point will be completely removed.

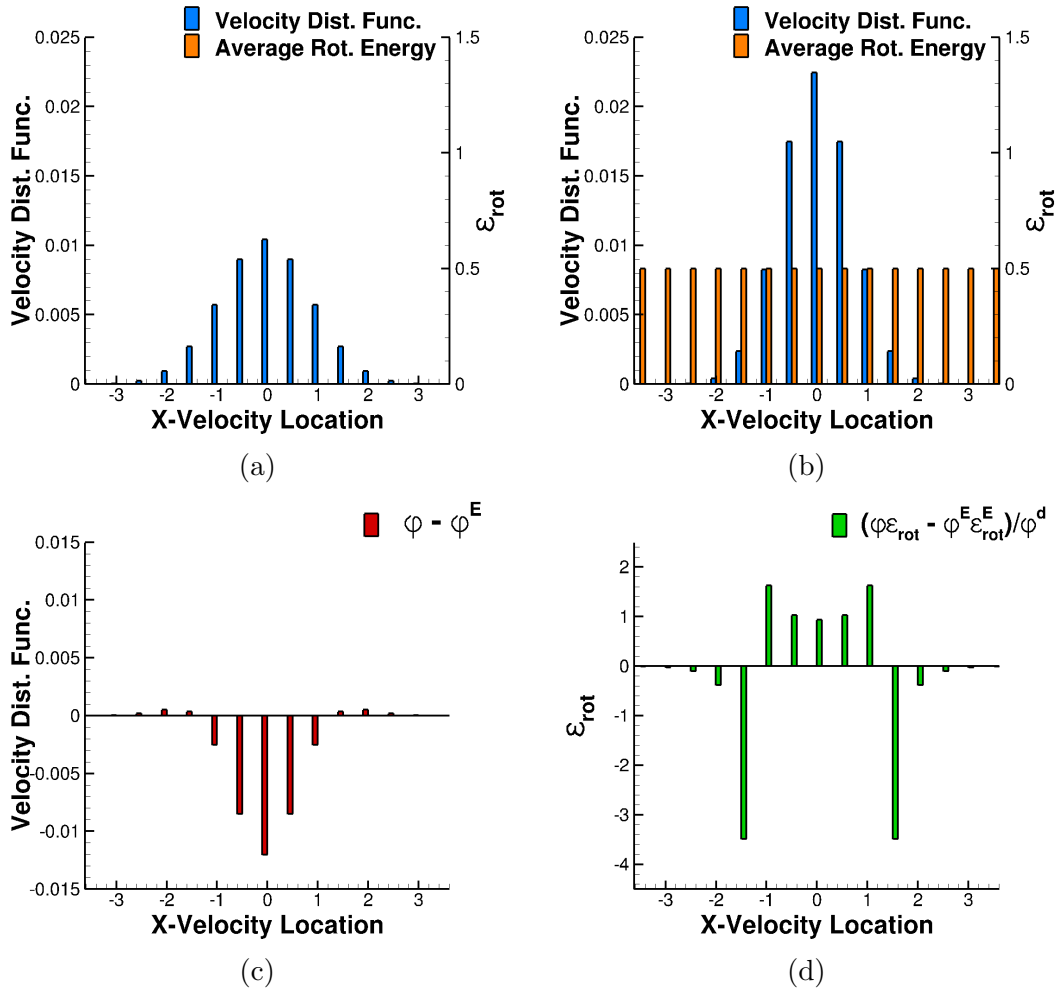

Figure 8.5: (a) A schematic non-equilibrium distribution with zero rotational energy is decomposed using a (b) equilibrium distribution where $\hat{T}_{kin} = \hat{T}_{rot} = \hat{T}_{eq}$. The deviation between (a) and (b) is shown for the (c) velocity distribution function and (d) the rotational energy per unit number density distribution function.

After determining the deviation distribution functions as depicted in Figure 8.5, cumulative distribution functions are constructed from the deviation and equilibrium parts, and collision partners are selected following the methods discussed in Section 4.1.1. The number of simulated collisions drawn is calculated in the same manner as that for a simple mixture of monatomic species under variance reduction (equations 6.25). After drawing a colliding pair, the number density depleted from the velocity locations of the collision partners is:

$$\Delta\hat{\varphi}^{d-E}_{depl} = \Delta\hat{t} \cdot \frac{sgn(\hat{\varphi}^{d}_{A}(\hat{\eta})) \cdot \hat{n}^{d}_{A}\hat{n}^{E}_{B}}{Kn \cdot N_c^{d-d}} \tag{8.8a}$$

$$\Delta\hat{\varphi}^{E-d}_{depl} = \Delta\hat{t} \cdot \frac{sgn(\hat{\varphi}^{d}_{B}(\hat{\zeta})) \cdot \hat{n}^{E}_{A}\hat{n}^{d}_{B}}{Kn \cdot N_c^{d-d}} \tag{8.8b}$$

$$\Delta\hat{\varphi}^{d-d}_{depl} = \Delta\hat{t} \cdot \frac{sgn(\hat{\varphi}^{d}_{A}(\hat{\eta})) \cdot sgn(\hat{\varphi}^{d}_{B}(\hat{\zeta})) \cdot \hat{n}^{d}_{A}\hat{n}^{d}_{B}}{Kn \cdot N_c^{d-d}} \tag{8.8c}$$

And the rotational energy depleted during each collision event is a product of the rotational energy per unit number density at the depleting velocity location and the depletion per collision described by equations 8.8.

$$\Delta\hat{E}^{E-d}(\hat{\eta})\Big|_{E} = \Delta\hat{\varphi}^{E-d} \cdot \hat{\varepsilon}^{E}_{r}(\hat{\eta}) = \Delta\hat{\varphi}^{E-d} \cdot \frac{\xi_r}{4}\hat{T}_{eq} \tag{8.9a}$$

$$\Delta\hat{E}^{E-d}(\hat{\eta})\Big|_{d} = \Delta\hat{\varphi}^{E-d} \cdot \hat{\varepsilon}^{d}_{r}(\hat{\eta}) = \Delta\hat{\varphi}^{E-d} \cdot \frac{\hat{E}_r(\hat{\eta}) - \hat{E}^{E}_{r}(\hat{\eta})}{\hat{\varphi}^{d}(\hat{\eta})} \tag{8.9b}$$

$$\Delta\hat{E}^{d-d}(\hat{\eta}) = \Delta\hat{\varphi}^{d-d} \cdot \hat{\varepsilon}^{d}_{r}(\hat{\eta}) = \Delta\hat{\varphi}^{d-d} \cdot \frac{\hat{E}_r(\hat{\eta}) - \hat{E}^{E}_{r}(\hat{\eta})}{\hat{\varphi}^{d}(\hat{\eta})} \tag{8.9c}$$

After a depletion number density and energy have been calculated for each colliding partner, the quantities are removed from the appropriate (either equilibrium or deviation) distribution functions.

8.3.3 Rotation-Translation Energy Exchange

Once a depletion event has been determined, an energy exchange is calculated for the inelastic parts of the collision. Since only a total rotational energy is being stored at each velocity location, a Landau-Teller-like relaxation (Section 7.6.2) based on the Jeans equation for rotational energy exchange is used to calculate changes in rotational and translational energy. In a more traditional formulation, a factor of $1/Z_r$ would be included, but the relaxation rate, Z_r, has already been accounted for by the depletion splitting technique from Section 8.1 and does not appear in equation 8.10. The resulting equation for a change in rotational energy is:

$$\Delta \hat{E}_r = \Delta \hat{t} \cdot \frac{\hat{E}^* - \hat{E}_r}{\hat{\tau}_c} \tag{8.10}$$

Where τ_c is the scaled collision time and the equilibrium energy, $\hat{E}^*$, can be defined as the collision translational energy adjusted by the rotational degrees of freedom:

$$\hat{E}^* = \Delta\hat{\varphi} \cdot \frac{\xi_{rot}}{4} \cdot \hat{T}_{coll} = \Delta\hat{\varphi} \cdot \frac{\xi_{rot}}{4} \cdot \frac{2}{3}\hat{m}_r \hat{g}^2 \tag{8.11}$$

$\hat{E}_r$ is defined as the rotational energy of the colliding quasi-particle which is undergoing an energy exchange between rotational and translational modes (labeled as A).

$$\hat{E}_{r,A} = \Delta\hat{\varphi} \cdot \hat{m}_A \cdot \hat{\varepsilon}_A \tag{8.12}$$

The change in energy during an inelastic collision is calculated from substituting equations 8.11 and 8.12 into equation 8.10, and the resulting change is sent into the replenishing routine described in Section 8.2.

8.3.4 Replenishment Adjustments

There is a slight adjustment for the single valued rotation model to the remapping scheme presented in Section 5.2. At the external points, a negative quantity is replenished, and there is the potential for a velocity location to develop a non-zero total rotational energy and a net zero number density or a negative total rotational energy and a positive number density. To avoid this, a value of rotational energy proportional to the net change in number density is depleted at the external points (equation 8.13a). The energy removed from the external points is added to the rotational energy depleted during the collision, and the sum is replenished to the internal points and the origin in proportion to the number density changes (equations 8.13b and 8.13c).

$$\Delta\hat{E}_{r,ej} = \frac{\hat{\varphi}_{ej} + f_{ej}\Delta\hat{\varphi}}{\hat{\varphi}_{e,j}}\hat{E}_{r,ej} - \hat{E}_{r,ej} \tag{8.13a}$$

$$\Delta\hat{E}_{r,ij} = \frac{f_{ij}}{f_o + f_{ix} + f_{iy} + f_{iz}}(\Delta\hat{E}_r + \hat{E}_{r,ex} + \hat{E}_{r,ey} + \hat{E}_{r,ez}) \tag{8.13b}$$

$$\Delta\hat{E}_{r,o} = \frac{f_o}{f_o + f_{i,x} + f_{i,y} + f_{i,z}}(\Delta\hat{E}_r + \hat{E}_{r,ex} + \hat{E}_{r,ey} + \hat{E}_{r,ez}) \tag{8.13c}$$

where $j = x, y, z$. This correction is minor and still exactly conserves mass, momentum, and energy, but it does cause a slight diffusion of rotational energy across velocity space.

8.3.5 Results

A homogeneous relaxation of N_2 is used to verify the collision integral for the representation of rotational energy by a single value at each point in velocity space. The distribution is initialized with a scaled kinetic temperature of $\hat{T}_{kin} = 1.6667$ and no rotational energy, $\hat{T}_{rot} = 0$. The rotational relaxation rate was approximated as a constant $Z_r = 5$, and the velocity grid is uniformly

spaced with $\hat{\beta} = 0.4$ and the domain boundary is located at $\hat{\eta} = \pm 4.0$. The simulation is run for 300 time steps of $\Delta\hat{t} = 0.1$, and the solution is compared against an exponential relaxation suitably integrated for the Jeans equation as:

$$\hat{T}_r(\hat{t}) = [\hat{T}_r(0) - \hat{T}(\infty)] \cdot e^{\frac{-\hat{t}}{\hat{\tau}_c Z_r}(1+\frac{\xi_r}{\xi_t})} + \hat{T}(\infty) \tag{8.14}$$

The results in Figure 8.6 show good agreement including a final rotational temperature of 299.85K and a final translational temperature of 300.06K.

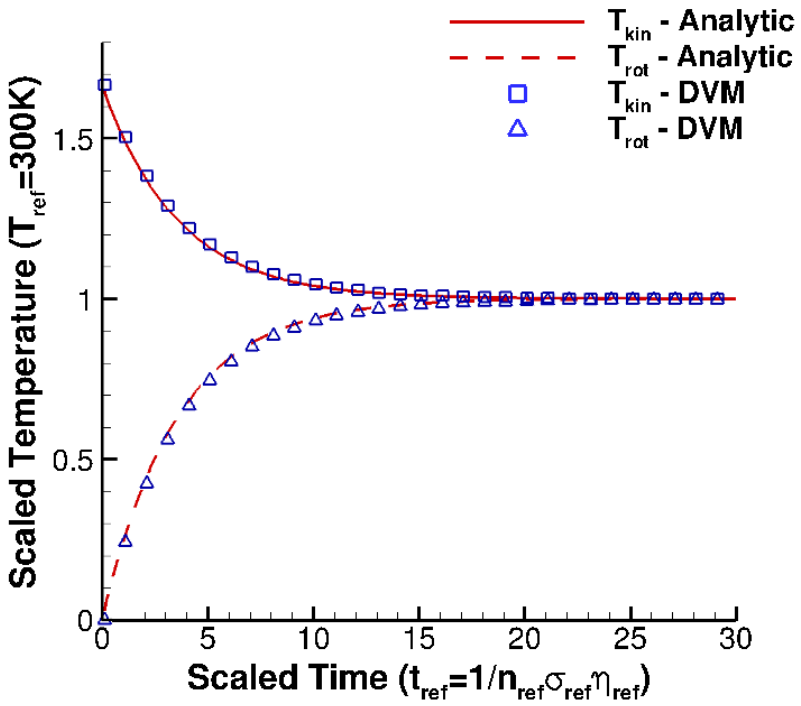

Figure 8.6: Rotational temperature relaxation for N_2 over time.

The velocity distribution function is visualized in Figure 8.7. As energy is transferred from translational to rotational modes, the velocity distribution cools, creating a thinner but taller distribution that retains a Maxwellian shape

throughout the process. The total rotational energy in Figure 8.8a shows a steady increase in energy corresponding to the cooling of the velocity distribution function. When rotational energy per unit mass is plotted in Figure 8.8b, the energy distribution shows a slight rise at the center of the domain in comparison to the wings, but increases fairly evenly over time as energy is transferred to rotational modes. The majority of the collisions occur between quasi-particles of lower velocity since density is higher at the lower velocities, and the high velocity values are noisy and lag slightly behind during the relaxation as a result.

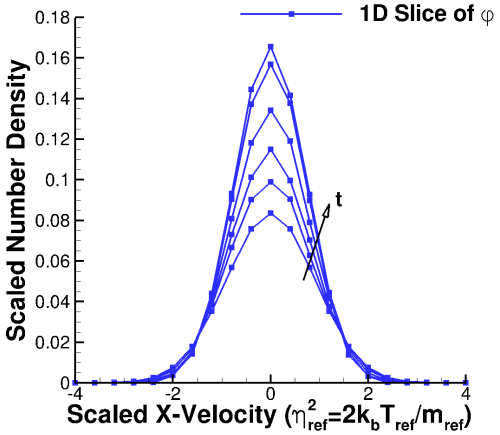

Figure 8.7: A 1D slice of the velocity distribution function over time during a homogeneous relaxation with single valued rotation.

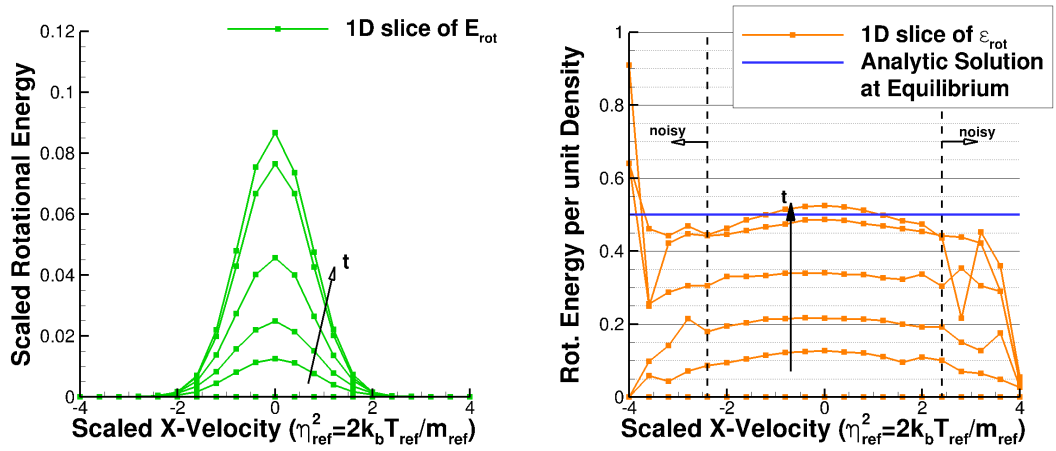

(a) (b)

Figure 8.8: (a) A 1D slice of the total rotational energy distribution relaxation. (b) A 1D slice of the rotational energy per unit density distribution relaxation.

In a second example, diatomic Nitrogen (N_2) is used to simulate a Mach 2.6 normal shock. The shock was initialized with upstream conditions shown in Table 8.1 and compared to an equivalent DSMC solution. The DVM spatial domain consisted of 60 points with $\Delta\hat{x} = 0.2$, and the velocity domain had grid spacing of $\hat{\beta} = 0.7$ and domain bounds at $\hat{\eta} = \pm 4.2$. A constant $Z_r = 5$ was implemented for DSMC and DVM methods. The DSMC solution was run until fully converged with a smooth solution, and the results were plotted against the DVM shock profiles. Good agreement can be seen between the two methods in Figure 8.9 except a slightly thicker temperature profile in the DVM solution and a higher peak kinetic temperature in the DSMC solution. The differences described may arise from differences between the Larsen-Borgnakke method used in DSMC and the Landau-Teller based method used for the DVM calculation.

Table 8.1: Shock conditions.

Property		Upstream	Downstream
M		2	0.577
n	$[1/m^3]$	1.0×10^{20}	2.67×10^{20}
u	$[m/s]$	706.4	264.7
T	$[K]$	300	506

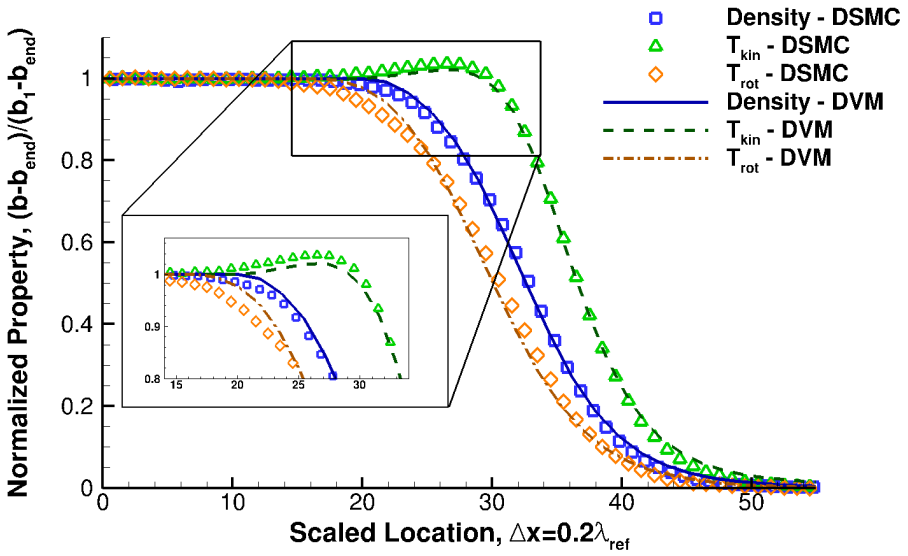

Figure 8.9: Comparison of DSMC and DVM produced normalized density and temperature profiles for a Mach 2, 1D, N_2 shock. The inset is an expanded view of the peak of the profile where differences are greatest.

8.4 Quantized Internal Energy

The second model described in this chapter permits quantized rotation and vibration. Quantized rotation is a more accurate model than the single valued model presented in Section 8.3 because non-equilibrium rotation effects are considered and very cold flows where the rotation distribution is

no longer continuous can be simulated. Because vibrational energy levels are more widely spaced than rotational levels, a continuous distribution cannot easily be assumed, and a quantized model should generally be used. The form of the Boltzmann equation used in conjunction with quantized energy levels was presented in Section 7.4 in equation 7.20, and the structure of the equation closely resembles a multi-species equation where each internal energy level is treated as a separate species.

8.4.1 Full Monte Carlo Depletion

The density depleted at a particular vibrational and rotational level at a single velocity is represented by the depleting term of the collision integral. The probability of an energy exchange between levels, $P(g, \nu\mu JK \rightarrow g', \nu'\mu' J' K')$, is accounted for at the end of the depletion process through a Larsen-Borgnakke based method in the current version of the DVM algorithm, and the depleting term without P is:

$$\left.\frac{\Delta\hat{\varphi}(\nu, J, \hat{\eta})}{\Delta\hat{t}}\right|_{depl} = -\sum_{\mu=0}^{N_v}\sum_{K=0}^{N_r}\sum_{\hat{\zeta}}\hat{\varphi}_A(\nu, J, \hat{\eta})\hat{\varphi}_B(\iota, K, \hat{\zeta})\hat{g}\hat{\sigma}_T \tag{8.15}$$

Collision pair velocities for diatomic/polyatomic molecules are chosen in the same manner as monatomic molecules. A cumulative distribution, Ξ, is built from the number density at each velocity location, and a random number draw is used to pick a velocity. The density depleted at the chosen locations is adjusted by the collision cross section, $\hat{g}\hat{\sigma}_T$, and the depletion number density per collision is the same as in equation 6.19 of Section 6.4. If $A = B$, a factor of $1/2$ is included in:

$$\Delta\hat{\varphi}_{depl} = \frac{\Delta\hat{t}\cdot\hat{n}_A\cdot\hat{n}_B}{KnN_c} \tag{8.16}$$

After choosing colliding velocity locations and applying the depletion splitting method discussed in Section 8.1, elastic and inelastic depletion events are performed. Defining $\hat{\psi}_i$ as the internal energy distribution at a single velocity location, normalized internal energy arrays, $\vec{f}_r$ and $\vec{f}_v$, are defined such that the sum over the magnitude of all levels is 1.

$$\vec{f}_r = \frac{\hat{\vec{\psi}}_r}{\sum_J |\hat{\psi}_r(J)|}; \qquad \vec{f}_v = \frac{\hat{\vec{\psi}}_v}{\sum_\nu |\hat{\psi}_v(\nu)|} \tag{8.17}$$

Depletion Step for an Elastic Collision

Depletion quantities for elastic collisions are drawn from every vibrational and rotational energy level in proportion to their current internal energy distributions as seen in Figure 8.10. In this manner, a potentially large depletion (elastic collisions are generally more significant than inelastic collisions) is not focused on a single energy level, and the noise in internal energy caused by the elastic collision event is kept to a minimum. The depleting arrays using this methodology are:

$$\begin{aligned} \Delta\hat{\psi}_r(J) &= \Delta\hat{\varphi} \cdot \hat{f}_r(J) \\ \Delta\hat{\psi}_v(\nu) &= \Delta\hat{\varphi} \cdot \hat{f}_v(\nu) \end{aligned} \tag{8.18}$$

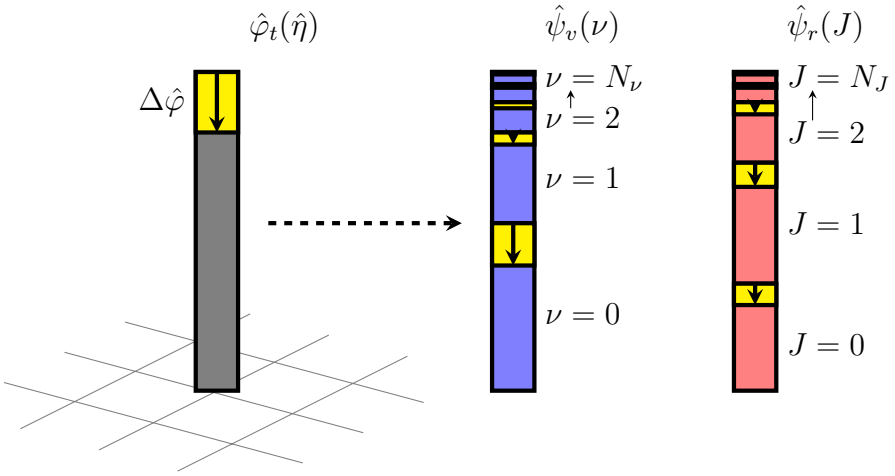

Figure 8.10: Elastic depletion from a single velocity location. The total depletion is taken proportionally from every vibrational level and proportionally from every rotational level.

Depletion Step for an Rotation-Translation Inelastic Collision

An inelastic collision which transfers energy between rotational and translational modes draws from a single rotational energy level, J, and a single vibrational energy level, ν as seen in Figure 8.11. A single rotational level is chosen because if multiple levels were drawn, each level would need to undergo its own energy exchange and each would need its own unique replenishment calculation. This would become prohibitively expensive because the number of rotational levels is typically large. A single vibrational level or an array of vibrational levels could be used, but a single level is chosen in the current work for two reasons: To decrease the computational cost of the calculation (the amount of data moved from one point to another) and to remain consistent with the variance reduced model discussed in Section 8.4.2, below, which benefits from a single level being used. The resulting depletion quantities from a chosen ν and J are:

$$\Delta\hat{\psi}_r(J) = \Delta\hat{\varphi}; \qquad \Delta\hat{\psi}_v(\nu) = \Delta\hat{\varphi} \tag{8.19}$$

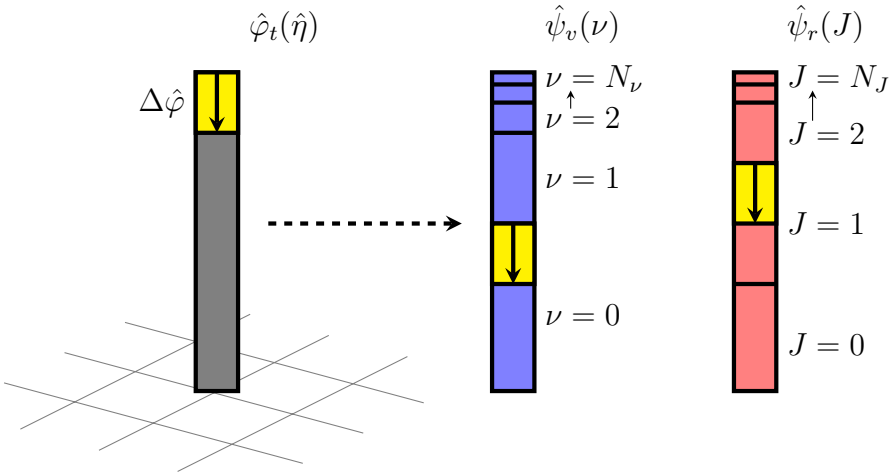

Figure 8.11: Inelastic depletion from a single velocity location. The total depletion is taken from a single vibrational level and a single rotational level.

Depletion Step for a Vibration-Translation Inelastic Collision

Inelastic collisions which transfer energy between vibrational and translational modes are depleted in the same manner as R-T collisions, and the depletion quantities at the chosen levels, ν and J, are the same as equation 8.19.

One result of the current methodology where single energy levels are used for inelastic collisions and a constant (adjusted for $\hat{g}\hat{\sigma}_T(\hat{g})$) density is depleted is the energy level densities become capped with a minimum value of $\Delta\hat{\varphi}_{r/v} \cdot (\hat{g}\hat{\sigma}_T(\hat{g}))_{min}$. Values can only change by the amount depleted or replenished since single collisions are not being spread between multiple energy levels. If a depletion pushes the density of an internal energy distribution below zero, the negative density fraction is allowed and the absolute value of

the negative is taken under consideration when calculating the probability of picking that energy level during a later collision ($P(J) = |\hat{f}_r(J)|/\sum|\hat{f}_r(J)|$). If an internal energy level with a negative number density value is subsequently chosen for a R-T or V-T collision, the sign associated with the depletion from that level is the sign of the distribution function of the energy mode undergoing an energy transfer: $sgn(\hat{f}_r(J))$ for R-T and $sgn(\hat{f}_v(\nu))$ for V-T.

8.4.2 Variance Reduced Model for Quantized Internal Energy

The identity which leads to variance reduction in a quantized model is the same as in the single valued rotation case (Section 8.3.2) except vibrational energy is now included.

The net change in time is zero in a distribution in total (thermal and internal) equilibrium due to collisions with particles drawn from itself or another equilibrium distribution at the same temperature (kinetic, rotation, and vibration) and bulk velocity.

The equilibrium functions in the current work are defined with a single equilibrium temperature, $\hat{T}_{eq}$. If the same equilibrium temperature is not used for all energy modes, inelastic collisions between particles drawn from the "equilibrium" distributions will result in a net change in the velocity distribution, and the corresponding contributions to the collision integral cannot be ignored. Equation 8.20 shows the calculation of equilibrium temperature as a function of the degrees of freedom, ξ, where ξ_v^* is the effective number of degrees of freedom in vibration as presented in equation 7.29.

$$\hat{T}_{eq} = \frac{\xi_t}{\xi_t + \xi_r + \xi_v^*}\hat{T}_t + \frac{\xi_r}{\xi_t + \xi_r + \xi_v^*}\hat{T}_r + \frac{\xi_v^*}{\xi_t + \xi_r + \xi_v^*}\hat{T}_v \tag{8.20}$$

The calculated equilibrium function necessary for the conditions of the identity to be met is a Maxwellian distribution calculated at the equilibrium

temperature with the species' density and bulk velocity. The associated rotational and vibrational density fractions are calculated as Boltzmann distributions at the same equilibrium temperature.

$$\hat{\varphi}^E \left(\hat{n}, \hat{u}_i, \hat{T}_{eq}, \hat{\eta};\ \hat{\psi}_r^E(\hat{T}_{eq}, J);\ \hat{\psi}_v^E(\hat{T}_{eq}, \nu) \right) \tag{8.21}$$

Decomposition of the Distribution Function

The main task in formulating a variance reduced collision model is to implement a decomposition of both the vibration and rotation distributions so that the equilibrium function described can be isolated. In this work, each energy distribution function is independently decomposed into equilibrium, $\hat{\psi}_i^E$, and deviation, $\hat{\psi}_i^d$, parts as:

$$\hat{\vec{\psi}}_r = \hat{\vec{\psi}}_r^E + \hat{\vec{\psi}}_r^d \tag{8.22a}$$

$$\hat{\vec{\psi}}_v = \hat{\vec{\psi}}_v^E + \hat{\vec{\psi}}_v^d \tag{8.22b}$$

Where the sum over all rotational levels in 8.22a or the sum over all vibrational levels in 8.22b is equivalent to:

$$\hat{\varphi} = \hat{\varphi}^E + \hat{\varphi}^d \tag{8.23}$$

Note that the equilibrium distributions in both the rotational and vibrational cases are dependent on the equilibrium (Maxwellian) velocity distribution value at each velocity location. Therefore, even if the internal energy distributions are Boltzmann distributions, a deviation will still occur if the velocity distribution is not Maxwellian. The reverse condition of an equilibrium Maxwellian velocity distribution with non-Boltzmann internal energy

distributions will also result in a deviation. Figure 8.12 illustrates example decompositions of a vibrational distribution under these two conditions.

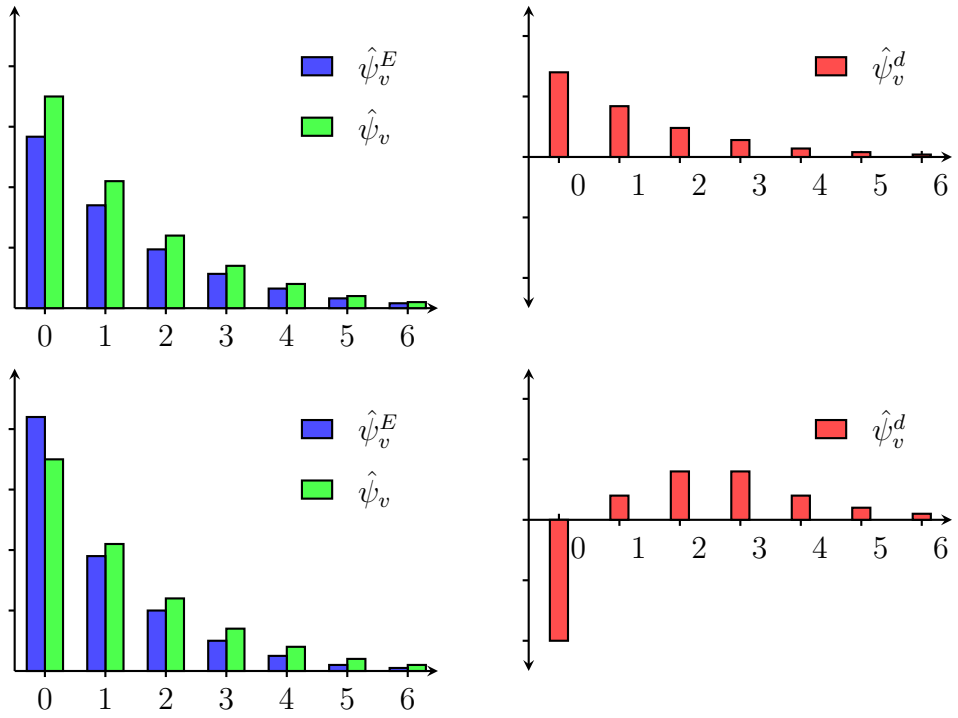

Figure 8.12: Example decompositions of the vibrational distribution function. The top shows a decomposition where vibration is in equilibrium but the velocity distribution function is out of equilibrium ($\sum \hat{\psi}_v \neq \sum \hat{\psi}_v^E$, but both are Boltzmann distributions). The bottom shows a decomposition where the velocity distribution function is in equilibrium but vibration is out of equilibrium ($\sum \hat{\psi}_v \neq \sum \hat{\psi}_v^E$, but $\hat{\psi}_v$ is not a Boltzmann distribution). In this case, $\sum \hat{\psi}_v^d = 0$. A general case can also be imagined where both are out of equilibrium as well.

The decomposition leads to several different definitions of density quantities used in the following work. As already mentioned, the sum over the equilibrium internal energy functions at each velocity location is equal to the equilibrium density (equation 8.24), and the sum over the deviation internal energy functions at each velocity location is equal to the deviation from equi-

librium of the velocity distribution function, $\hat{\varphi}_t^d$ (equation 8.25).

$$\hat{\varphi}_t^E = \sum_{\nu} \hat{\psi}_v^E(\nu) = \sum_{J} \hat{\psi}_r^E(J) \tag{8.24}$$

$$\hat{\varphi}_t^d = \sum_{\nu} \hat{\psi}_v^d(\nu) = \sum_{J} \hat{\psi}_r^d(J) \tag{8.25}$$

The sum of the magnitudes of each deviation internal energy distribution results in the absolute deviation of rotation, $\hat{\varphi}_r^d$, and the absolute deviation of vibration, $\hat{\varphi}_v^d$.

$$\hat{\varphi}_v^d = \sum_{\nu} \left| \hat{\psi}_v^d(\nu) \right| \tag{8.26a}$$

$$\hat{\varphi}_r^d = \sum_{J} \left| \hat{\psi}_r^d(J) \right| \tag{8.26b}$$

Finally, the sum of the rotational and vibrational absolute deviation densities will be defined as:

$$\hat{\varphi}_{rv}^d = \hat{\varphi}_r^d + \hat{\varphi}_v^d \tag{8.27}$$

And the sum over all velocities for equation 8.27 is given by the symbol $\hat{n}_{rv}^d$. If the decomposition from equation 8.23 is substituted into the Boltzmann equation, the collision integral is decomposed into four terms:

$$I_{AB}^{E-E} = \tag{8.28a}$$
$$\sum_{\hat{\zeta},K,\iota} \left[\hat{\varphi}_A^E(\hat{\eta}', J', \nu') \hat{\varphi}_B^E(\hat{\zeta}', K', \iota') - \hat{\varphi}_A^E(\hat{\eta}, J, \nu) \hat{\varphi}_B^E(\hat{\zeta}, K, \iota) \right]$$
$$\cdot \hat{g} \hat{\sigma}_T(\hat{g}) \cdot P(\hat{g}, \nu\iota JK \rightarrow \hat{g}', \nu'\iota' J'K') = \mathbf{0}$$

$$I_{AB}^{E-d} = \tag{8.28b}$$
$$\sum_{\hat{\zeta},K,\iota} \left[\hat{\varphi}_A^E(\hat{\eta}', J', \nu') \hat{\varphi}_B^d(\hat{\zeta}', K', \iota') - \hat{\varphi}_A^E(\hat{\eta}, J, \nu) \hat{\varphi}_B^d(\hat{\zeta}, K, \iota) \right]$$
$$\cdot \hat{g} \hat{\sigma}_T(\hat{g}) \cdot P(\hat{g}, \nu\iota JK \rightarrow \hat{g}', \nu'\iota' J'K')$$

$$I_{AB}^{d-E} = \tag{8.28c}$$
$$\sum_{\hat{\zeta},K,\iota} \left[\hat{\varphi}_A^d(\hat{\eta}', J', \nu') \hat{\varphi}_B^E(\hat{\zeta}', K', \iota') - \hat{\varphi}_A^d(\hat{\eta}, J, \nu) \hat{\varphi}_B^E(\hat{\zeta}, K, \iota) \right]$$
$$\cdot \hat{g} \hat{\sigma}_T(\hat{g}) \cdot P(\hat{g}, \nu\iota JK \rightarrow \hat{g}', \nu'\iota' J'K')$$

$$I_{AB}^{d-d} = \tag{8.28d}$$
$$\sum_{\hat{\zeta},K,\iota} \left[\hat{\varphi}_A^d(\hat{\eta}', J', \nu') \hat{\varphi}_B^d(\hat{\zeta}', K', \iota') - \hat{\varphi}_A^d(\hat{\eta}, J, \nu) \hat{\varphi}_B^d(\hat{\zeta}, K, \iota) \right]$$
$$\cdot \hat{g} \hat{\sigma}_T(\hat{g}) \cdot P(\hat{g}, \nu\iota JK \rightarrow \hat{g}', \nu'\iota' J'K')$$

Each integral term can be evaluated independently, and the resulting changes to the distribution function are summed at the end of the time step. According to the identity presented at the start of Section 8.4.2, the equilibrium term may be set to zero. This term is dominant in near equilibrium flows, and its removal yields significant savings in the number of simulated collisions necessary to achieve a solution. In equations 8.28 ν and ι are vibrational energy levels, J and K are rotational energy levels, $\hat{\eta}$ and $\hat{\zeta}$ are velocity locations, $\hat{g}$ is the relative velocity, post-collision variables are primed, and P is the probability of a particular energy exchange occurring.

Depletion Step for Elastic and Inelastic Collisions

The equilibrium density, $\hat{\varphi}^E$, and the total deviation density, $\hat{\varphi}^d_{rv}$, are used to build equilibrium and deviation cumulative distribution functions respectively as:

$$\Xi^E(l) = \sum_{\hat{\eta}=0}^{l} \hat{\varphi}^E(\hat{\eta}) \tag{8.29a}$$

$$\Xi^d(l) = \sum_{\hat{\eta}=0}^{l} \hat{\varphi}^d_{rv}(\hat{\eta}) \tag{8.29b}$$

And the same methods discussed in Section 4.1.1 are used to draw collision partners, which results in the probability of a single velocity, $\hat{\eta}$, being selected from either the equilibrium or deviation distributions to be:

$$P\left(\hat{\varphi}^E(\hat{\eta})\right) = \frac{\hat{\varphi}^E(\hat{\eta})}{\hat{n}^E} \tag{8.30a}$$

$$P\left(\hat{\varphi}^d(\hat{\eta})\right) = \frac{\hat{\varphi}^d_r(\hat{\eta}) + \hat{\varphi}^d_v(\hat{\eta})}{\hat{n}^d_{rv}} \tag{8.30b}$$

Where $\hat{n}^E = \hat{n}$ and $\hat{n}^d_{rv}$ can simply be found from the final value of the cumulative deviation distribution function, $\hat{n}^d_{rv} = \Xi^d(N)$. The number density depleted per simulated collision in a time step for each of the three variance reduction integrals shown in equations 8.28 can be found as a function of $\hat{n}^E$ and/or $\hat{n}^d_{rv}$, the time step, the Knudsen number, the relative velocity, and the collision cross-section. Note a factor of 1/2 would be present in equations 8.31 if $A = B$.

$$\Delta\hat{\varphi}^{E-d} = \frac{\Delta\hat{t} \cdot \hat{n}_A^E \cdot \hat{n}_{rv,B}^d}{Kn \cdot N_c^{E-d}} \cdot \hat{g}\hat{\sigma}_T \tag{8.31a}$$

$$\Delta\hat{\varphi}^{d-E} = \frac{\Delta\hat{t} \cdot \hat{n}_{rv,A}^d \cdot \hat{n}_B^E}{Kn \cdot N_c^{d-E}} \cdot \hat{g}\hat{\sigma}_T \tag{8.31b}$$

$$\Delta\hat{\varphi}^{d-d} = \frac{\Delta\hat{t} \cdot \hat{n}_{rv,A}^d \cdot \hat{n}_{rv,B}^d}{Kn \cdot N_c^{d-d}} \cdot \hat{g}\hat{\sigma}_T \tag{8.31c}$$

The number of collisions simulated in a single time step for each term also matches the form for multi-species, monatomic variance reduction. However, note that since $\hat{n}_{rv}^d$ is the sum of rotational and vibrational deviations, a factor of two is included. The temperature, $\hat{T}_{kin}$, is the average kinetic temperature of species A and B.

$$N_c^{E-d} = nint\left(\frac{\Delta\hat{t} \cdot \hat{T}_{kin}^{2/3}}{Kn \cdot C_{AB}^2 \cdot \beta_{avg}^3} \cdot \frac{\hat{n}_{rv,B}^d}{2\hat{n}_B}\right) \tag{8.32a}$$

$$N_c^{d-E} = nint\left(\frac{\Delta\hat{t} \cdot \hat{T}_{kin}^{2/3}}{Kn \cdot C_{AB}^2 \cdot \beta_{avg}^3} \cdot \frac{\hat{n}_{rv,A}^d}{2\hat{n}_A}\right) \tag{8.32b}$$

$$N_c^{d-d} = nint\left(\frac{\Delta\hat{t} \cdot \hat{T}_{kin}^{2/3}}{Kn \cdot C_{AB}^2 \cdot \beta_{avg}^3} \cdot \frac{\hat{n}_{rv,A}^d}{2\hat{n}_A} \cdot \frac{\hat{n}_{rv,B}^d}{2\hat{n}_B}\right) \tag{8.32c}$$

After choosing a collision pair, the next step in developing a depletion process for the variance reduced method is building a deviation distribution for both rotation and vibration. The equilibrium distributions are defined as normalized Boltzmann distributions, and the deviation distributions are normalized by the absolute deviation densities, $\hat{\varphi}_v^d$ and $\hat{\varphi}_r^d$.

$$\vec{f}_v^E = \frac{\hat{\vec{\psi}}_v^E}{\hat{\varphi}_t^E}; \qquad \vec{f}_r^E = \frac{\hat{\vec{\psi}}_r^E}{\hat{\varphi}_t^E} \tag{8.33}$$

$$\vec{f}_v^d = \frac{\hat{\vec{\psi}}_v^d}{\hat{\varphi}_v^d}; \qquad \vec{f}_r^d = \frac{\hat{\vec{\psi}}_r^d}{\hat{\varphi}_r^d}$$

And the summation over each normalized array results in:

$$\sum_{\nu} \hat{f}_v^E(\nu) = 1; \qquad \sum_{\nu} \hat{f}_v^d(\nu) = \frac{\hat{\varphi}_t^d}{\hat{\varphi}_v^d} \tag{8.34}$$
$$\sum_{J} \hat{f}_r^E(J) = 1; \qquad \sum_{J} \hat{f}_r^d(J) = \frac{\hat{\varphi}_t^d}{\hat{\varphi}_r^d}$$

Depletion quantities are taken from all rotational and vibrational levels of both collision partners in an elastic collision, and from all levels for the collision partner not undergoing changes in internal energy during an inelastic collision. A requirement is that the sum over all levels in the rotational and vibrational depletion arrays are equivalent to each other, which is not the case for $\vec{f}_r^d$ and $\vec{f}_v^d$ as shown by equation 8.34. To meet this requirement, the depletion arrays are rewritten as:

$$\vec{F}_r = \frac{\hat{\vec{\psi}}_r^d}{\hat{\varphi}_{rv}^d} \tag{8.35a}$$

$$\vec{F}_v = \frac{\hat{\vec{\psi}}_v^d}{\hat{\varphi}_{rv}^d} \tag{8.35b}$$

The sums over every rotational and vibrational energy level in equations 8.35a and 8.35b are equal to each other, and the value represents the fraction of $\Delta\hat{\varphi}$ depleted due to the sum of positive and negative values. The fraction is given the symbol D in equation 8.36, and the product of D from each collision partner is used to determine the total number density depleted from the velocity distribution function during a collision. For a deviation array:

$$D \equiv \sum_{J} F_r(J) = \sum_{\nu} F_v(\nu) = \frac{\hat{\varphi}_t^d}{\hat{\varphi}_{rv}^d} \tag{8.36}$$

Equations 8.37 and 8.38 show the changes in rotation, vibration, and the velocity distribution function during an elastic collision between two particles drawn from the deviation distribution. Depletion quantities are drawn from every energy level in proportion to the rotational and vibrational depletion distributions and adjusted by the D value of the colliding partner.

Particle A:

$$\hat{\psi}'_{r,A} = \hat{\psi}_{r,A} - \Delta\hat{\varphi}_{depl} \cdot \vec{F}_{r,A} \cdot D_B \tag{8.37a}$$

$$\hat{\psi}'_{v,A} = \hat{\psi}_{v,A} - \Delta\hat{\varphi}_{depl} \cdot \vec{F}_{v,A} \cdot D_B \tag{8.37b}$$

$$\hat{\varphi}'_A(\hat{\eta}) = \hat{\varphi}_A(\hat{\eta}) - \Delta\hat{\varphi}_{depl} \cdot D_A \cdot D_B \tag{8.37c}$$

Particle B:

$$\hat{\psi}'_{r,B} = \hat{\psi}_{r,B} - \Delta\hat{\varphi}_{depl} \cdot \vec{F}_{r,B} \cdot D_A \tag{8.38a}$$

$$\hat{\psi}'_{v,B} = \hat{\psi}_{v,B} - \Delta\hat{\varphi}_{depl} \cdot \vec{F}_{v,B} \cdot D_A \tag{8.38b}$$

$$\hat{\varphi}'_B(\hat{\zeta}) = \hat{\varphi}_B(\hat{\zeta}) - \Delta\hat{\varphi}_{depl} \cdot D_B \cdot D_A \tag{8.38c}$$

If either particle was drawn from an equilibrium distribution the depletion arrays would be $\vec{F}_r = \vec{f}_r^{\,E}$ and $\vec{F}_v = \vec{f}_v^{\,E}$, and the related D value would be $+1$. Equations 8.30, 8.31, and 8.35 are used in Appendix B to prove that the formulas provided in equation 8.37 and 8.38 result in the correct depletion per time step at every velocity location for elastic collisions.

During an inelastic collision a single rotational level and a single vibrational level are drawn for the particle undergoing energy exchange, and the full rotational and vibrational arrays are used in the same manner as an elastic collision for the particle not undergoing energy exchange. Since $\Delta\hat{\varphi}$ has been determined from the sum of rotational and vibrational deviations (n^d_{rv}), an adjustment to the amount depleted from a single level is made. The levels are chosen from $\vec{f}_r^{\,d}$ and $\vec{f}_v^{\,d}$ from equation 8.33 with probability:

$$P(\hat{\psi}_r(J)) = \frac{\left|\hat{\psi}_r^d(J)\right|}{\hat{\varphi}_r^d} \tag{8.39a}$$

$$P(\hat{\psi}_v(\nu)) = \frac{\left|\hat{\psi}_v^d(\nu)\right|}{\hat{\varphi}_v^d} \tag{8.39b}$$

And the depletion number density is multiplied by the factor $C_r = \hat{\varphi}_r^d/\hat{\varphi}_{rv}^d$ or $C_v = \hat{\varphi}_v^d/\hat{\varphi}_{rv}^d$ to match the required depletion per time step for rotation-translation energy exchanges or vibration-translation energy exchanges respectively (shown in Appendix B). Having determined the rotational and vibrational levels involved in the depletion, the signs of each level, s_J and s_ν, are determined.

$$s_J = sign\left(f_r(J)\right) \tag{8.40a}$$

$$s_\nu = sign\left(f_r(\nu)\right) \tag{8.40b}$$

The contribution to the sign of the depletion from the collision partner undergoing energy exchange is only the sign of the changing mode (s_J for an R-T collision and s_ν for a V-T collision). The contribution to the sign of the depletion from the collision partner not undergoing energy exchange is reflected in the sign of D.

The depletion event described by equations 8.41 and 8.42 represents a rotation-translation for particle A for the deviation-deviation type integral (equation 8.28d). The entire depletion adjusted by D_B is taken from the chosen internal energy levels in particle A, and the depletion is taken from every internal energy level in particle B in proportion to the depletion arrays. If the energy exchange is being applied to particle B, switching the subscripts A and B gives the correct depletion process, and if the depletion is for an

equilibrium-deviation (or deviation-equilibrium) type integral, $\vec{F}_r$ and $\vec{F}_v$ are the equilibrium arrays $\vec{f}_r^E$ and $\vec{f}_v^E$, $D = 1$, and $A = 1$ for the particle drawn from the equilibrium distribution.

Particle A:

$$\hat{\psi}'_{r,A}(J) = \hat{\psi}_{r,A}(J) - \Delta\hat{\varphi}_{depl} \cdot s_{J,A} \cdot C_{r,A} \cdot D_B \tag{8.41a}$$

$$\hat{\psi}'_{v,A}(\nu) = \hat{\psi}_{v,A}(\nu) - \Delta\hat{\varphi}_{depl} \cdot s_{J,A} \cdot C_{r,A} \cdot D_B \tag{8.41b}$$

$$\hat{\varphi}'_A(\hat{\eta}) = \hat{\varphi}_A(\hat{\eta}) - \Delta\hat{\varphi}_{depl} \cdot s_{J,A} \cdot C_{r,A} \cdot D_B \tag{8.41c}$$

Particle B:

$$\hat{\psi}'_{r,B} = \hat{\psi}_{r,B} - \Delta\hat{\varphi}_{depl} \cdot s_{J,A} \cdot C_{r,A} \cdot \vec{F}_{r,B} \tag{8.42a}$$

$$\hat{\psi}'_{v,B} = \hat{\psi}_{v,B} - \Delta\hat{\varphi}_{depl} \cdot s_{J,A} \cdot C_{r,A} \cdot \vec{F}_{v,B} \tag{8.42b}$$

$$\hat{\varphi}'_B(\hat{\zeta}) = \hat{\varphi}_B(\hat{\zeta}) - \Delta\hat{\varphi}_{depl} \cdot s_{J,A} \cdot C_{r,A} \cdot D_B \tag{8.42c}$$

A vibration-translation energy exchange for particle A for the deviation-deviation type integral is similar to rotation-translation except the sign used is the sign of the vibrational level, not the rotational level.

Particle A:

$$\hat{\psi}'_{r,A}(J) = \hat{\psi}_{r,A}(J) - \Delta\hat{\varphi}_{depl} \cdot s_{\nu,A} \cdot C_{v,A} \cdot D_B \tag{8.43a}$$

$$\hat{\psi}'_{v,A}(\nu) = \hat{\psi}_{v,A}(\nu) - \Delta\hat{\varphi}_{depl} \cdot s_{\nu,A} \cdot C_{v,A} \cdot D_B \tag{8.43b}$$

$$\hat{\varphi}'_A(\hat{\eta}) = \hat{\varphi}_A(\hat{\eta}) - \Delta\hat{\varphi}_{depl} \cdot s_{\nu,A} \cdot C_{v,A} \cdot D_B \tag{8.43c}$$

Particle B:

$$\hat{\psi}'_{r,B} = \hat{\psi}_{r,B} - \Delta\hat{\varphi}_{depl} \cdot s_{\nu,A} \cdot C_{v,A} \cdot \vec{F}_{r,B} \tag{8.44a}$$

$$\hat{\psi}'_{v,B} = \hat{\psi}_{v,B} - \Delta\hat{\varphi}_{depl} \cdot s_{\nu,A} \cdot C_{v,A} \cdot \vec{F}_{v,B} \tag{8.44b}$$

$$\hat{\varphi}'_B(\hat{\zeta}) = \hat{\varphi}_B(\hat{\zeta}) - \Delta\hat{\varphi}_{depl} \cdot s_{\nu,A} \cdot C_{v,A} \cdot D_B \tag{8.44c}$$

Appendix B shows proof the formulas given in equations 8.41-8.44 match the correct depletion per time step for every velocity location.

Inspection of the depletion from the velocity distribution function shows that if the distribution is already in thermal equilibrium but out of equilibrium in rotation or vibration, depletion events only reflect the movement of internal energy information due to collisions, and they will not affect the velocity distribution function since D would be zero.

8.4.3 Energy Exchanges

Energy exchanges in the quantized model are calculated using the Larsen-Borgnakke model formulated for quantized rotational and vibrational energy as shown in Section 7.6.3. An energy exchange is calculated for either rotation or vibration depending on the inelastic collision type, and the relative velocity, $\hat{g}$, is adjusted to conserve total energy. The replenishment process proceeds in the manner described in Section 8.2, and the entire depletion-exchange-replenishment process is repeated for every simulated collision.

8.4.4 Results

A series of results is run to verify the standard full Monte Carlo (FMC) and variance reduced collision models, energy level descriptions (non-rigid rotor, rigid rotor, SHO, and AHO), and investigate the number of modeled energy levels. Finally, a 1D shock at Mach 12 of cold N_2 is simulated to illustrate the information the DVM code can produce using the models described.

Verification using a Homogeneous Relaxation

Three test cases using N_2 are run for verification of the quantized method for the standard FMC method and the variance reduced method.

Each case is a homogeneous relaxation with the initial internal temperature set to 1/3 the initial kinetic temperature, and a comparison is made to analytic solutions of the Jeans and Landau-Teller equations or DSMC solutions. All three simulations were run on a velocity grid of $N = 15^3$ number of nodes, grid spacing of $\hat{\beta} = 0.5$, velocity domain boundaries of $\hat{\eta} = \pm 3.5$, and the number of simulated collisions was calculated with the coefficient $C_{N_2} = 0.004$. The scaled time step used in each simulation was $\Delta\hat{t} = 0.5$, slightly less than the mean collision time, $\hat{t}_c = 0.595$. In the first case only rotation is allowed to excite, a low reference temperature of 300K is used, and a constant rotational relaxation rate of $Z_r = 5$ was implemented.

Solutions are found using a pseudo-Maxwell molecules since an exact solution to Jeans equation can be found without numerical integration to be:

$$\hat{T}_r(\hat{t}) = [\hat{T}_r(0) - \hat{T}(\infty)] \cdot e^{\frac{-\hat{t}}{\hat{\tau}_c Z_r}(1+\frac{\xi_r}{\xi_t})} + \hat{T}(\infty) \tag{8.45}$$

Where $\hat{T}_v$, ξ_v^*, and Z_v are used in place of $\hat{T}_r$, ξ_r, and Z_r for an analytic solution to the Landau-Teller equation. Figure 8.13a compares the DVM solutions for full Monte Carlo and variance reduction against a analytic solution when a rigid rotor approximation is used to describe rotational energy levels. The difference between the kinetic temperature of each result and the analytic solution shown in Figure 8.13b displays that the DVM solutions agree to within 1% of the analytic solution at their worst.

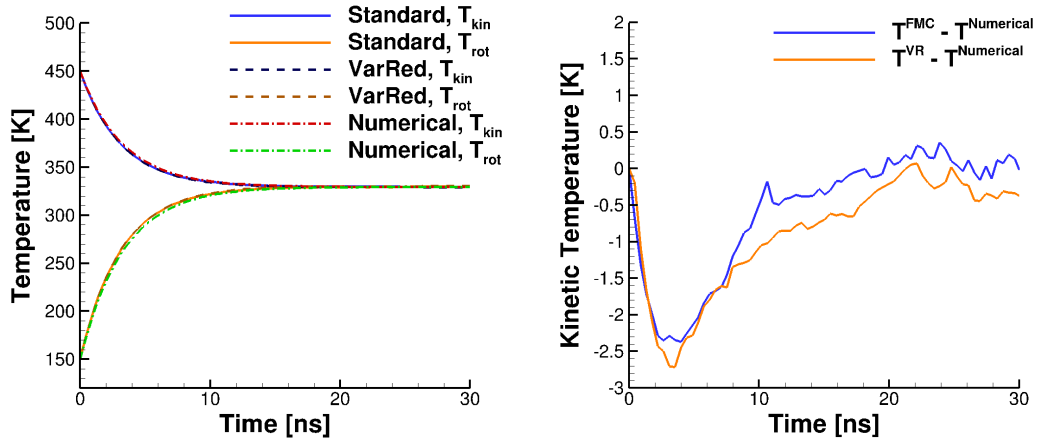

(a) (b)

Figure 8.13: (a) Comparison of full Monte Carlo and variance reduced models during homogeneous rotation-only relaxation of N_2 and (b) the differences between the kinetic temperatures of the solutions of each model and a analytic solution.

Figure 8.14a shows the final rotational distribution ($t = 30ns$) for the standard FMC, rigid rotor case whose solution is displayed in Figure 8.13a. The shape of the rotational distribution and nuclear spin effects are accurately represented, but the evolution of the rotational density fractions is most easily visualized when normalized by the degeneracy and plotted on a log scale for the y-axis. All future internal energy distributions will be shown in this manner. The rotational relaxation displayed in Figure 8.14b shows the same trends seen in DSMC solutions using a Larsen-Borgnakke energy exchange model [138]. Note that in the DVM solution, a smooth final answer is achieved up to density fractions $O(10^{-9})$.

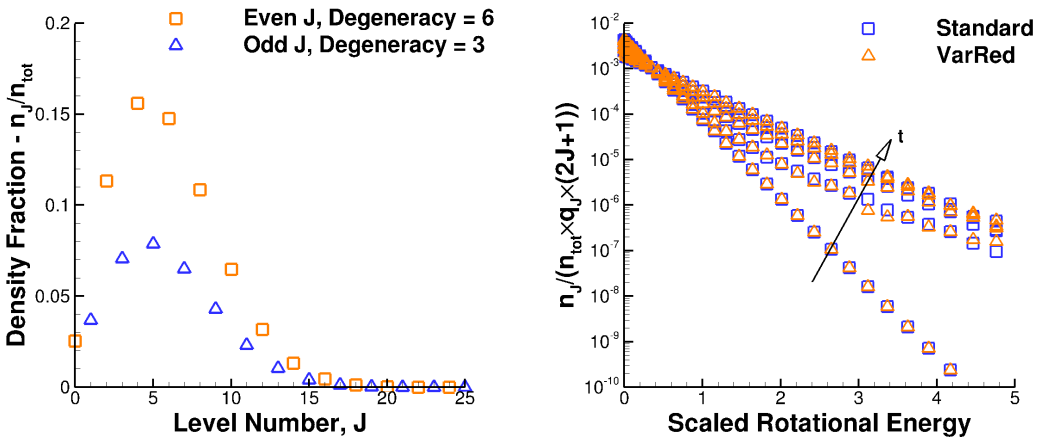

(a) (b)

Figure 8.14: (a) Final rotational distribution for the rigid rotor case in Figure 8.13a showing differences in even/odd levels due to nuclear spin. (b) Normalized rotational distribution during rotation-only relaxation of N_2. A comparison is made between full Monte Carlo and variance reduced Monte Carlo for the rigid rotor model.

The rigid rotor and non-rigid rotor models for a variance reduced collision integral evaluation are investigated in Figure 8.15a. The non-rigid rotor relaxation has a slightly faster relaxation rate due to higher energy levels being closer than the rigid rotor model.

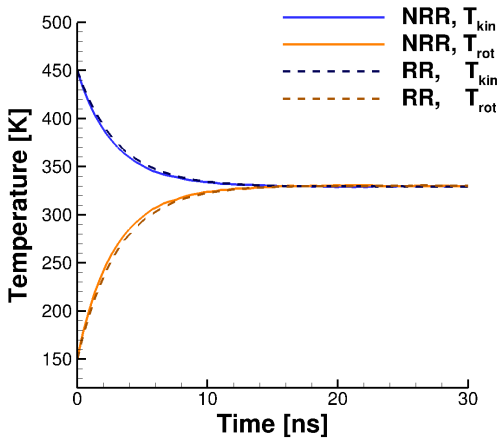

(a)

Figure 8.15: (a) Comparison of rigid rotor and non-rigid rotor models both using variance reduction and (b) the corresponding differences in kinetic temperature with a analytic solution.

In the second case, only vibration is allowed to excite, a high reference temperature of 10000K is used, and a constant vibrational relaxation rate of $Z_v = 50$ was implemented. This relaxation rate is not realistic, but the simulation was only used for verification of the model. Figures 8.16a and 8.16b display temperature relaxations and differences for the full Monte Carlo, variance reduced, and analytic solutions when using a simple harmonic oscillator approximation to describe vibrational energy levels. The point of largest difference in Figure 8.16b is 0.5% of the kinetic temperature.

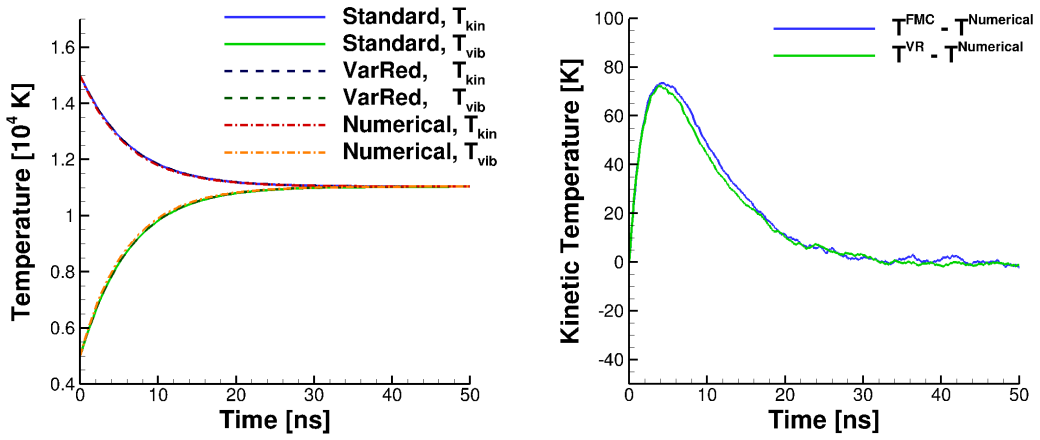

(a) (b)

Figure 8.16: (a) Comparison of the full Monte Carlo and variance reduced models during homogeneous vibration-only relaxation of N_2 and (b) the differences between the kinetic temperature of the solution for each collision model and a analytic solution. A simple harmonic oscillator is used.

Figure 8.17 shows that the relaxation of the vibrational levels follows the expected trends seen in other Larsen-Borgnakke based simulations [89]. It is especially important to recognize that high level vibration states are cleanly resolved to $O(10^{-6})$ in the DVM solution since high level vibration states are important to many chemical reactions. The high resolution of these states is a feature of DVM that is expected to be exploited in future work.

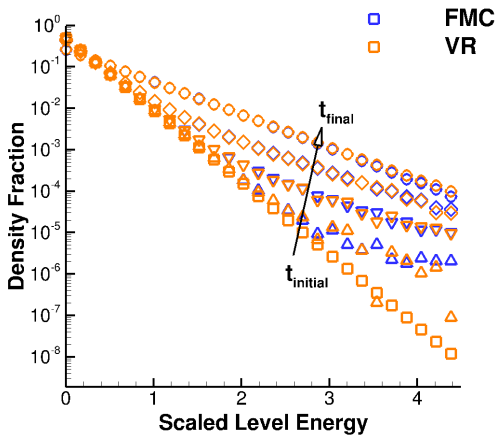

Figure 8.17: Normalized vibrational distribution during vibration-only relaxation of N_2. A comparison is made between full Monte Carlo and variance reduced Monte Carlo for the SHO model.

SHO and AHO approximations for a variance reduced model are compared in Figure 8.18a. While the time to full relaxation is comparable, the SHO and AHO models reach a different final equilibrium temperature. The difference can be explained by inspecting the effective vibrational degrees of freedom for each, and Figure 8.18b displays the value of the the effective vibrational degrees of freedom through the relaxation for each model. Notice the higher final value of the AHO model, indicating a greater number of available degrees of freedom for energy transfers in the AHO distribution.

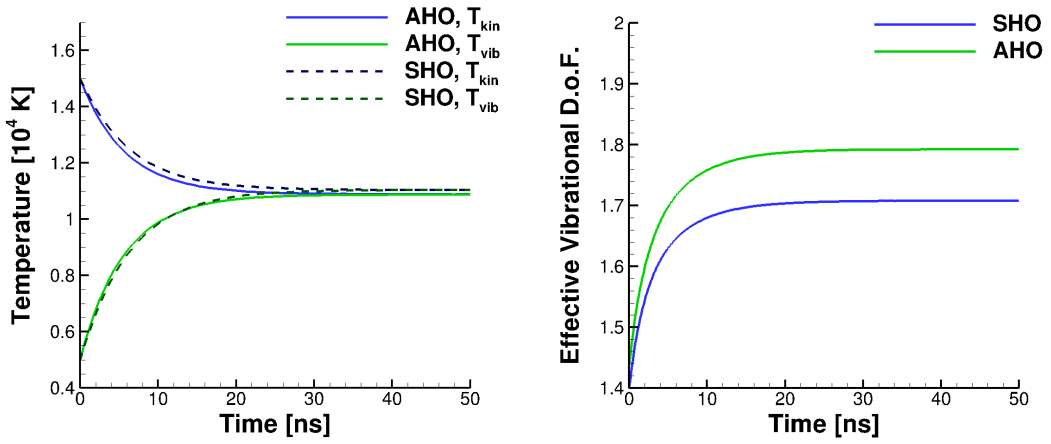

(a) (b)

Figure 8.18: (c) Comparison of simple harmonic and anharmonic oscillator models and (d) the corresponding effective vibrational degrees of freedom over time.

The final verification case allows both rotational and vibrational excitation with a reference temperature of 3000K, a constant relaxation rate of $Z_r = 5$, and a constant vibrational relaxation rate of $Z_v = 50$. The variance reduced method and DSMC solutions are compared in Figure 8.19a using the rigid rotor and SHO models for rotation and vibration respectively, and a closer inspection of the differences in Figure 8.19b shows good agreement in the solutions except for small differences in the gradient of the relaxation and the value rotational temperature. The point of largest difference is at the peak of the rotational temperature curve, where the DVM solution achieves a higher temperature.

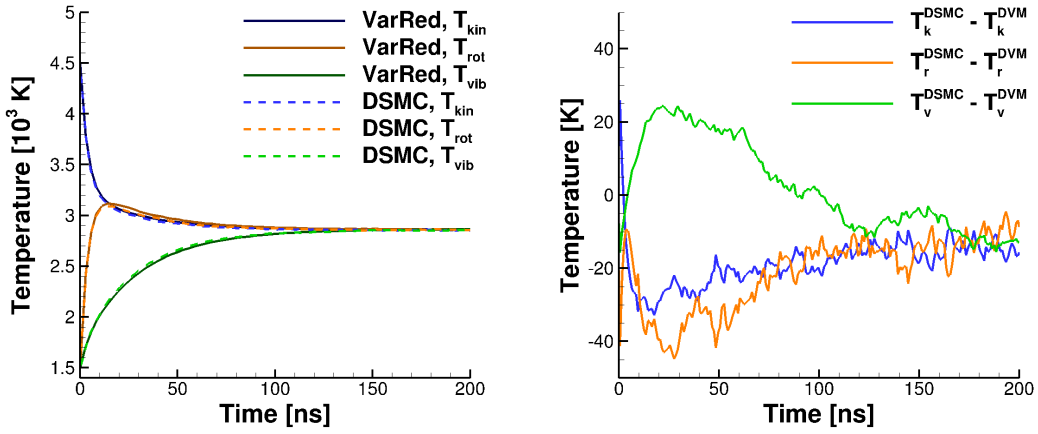

(a) (b)

Figure 8.19: (a) Comparison of full Monte Carlo and variance reduced models during homogeneous relaxation of N_2 and (b) the differences between the solutions. Rigid rotor and simple harmonic oscillator approximations are used.

The computation times for standard FMC (not shown in Figure 8.19a), variance reduced, and DSMC solutions are shown in Table 8.2.

Table 8.2: Comparison of computation times for various methods for homogeneous relaxation of N_2.

Method	**Computation Time** [s]
Standard FMC	284.20
• Rotational array computations	94.17
• Vibrational array computations	29.76
Variance Reduced	82.60
• Rotational array computations	27.81
• Vibrational array computations	8.95
DSMC	121.06

While specific statements about efficiency are difficult to make due to a lack of optimization in both DVM and DSMC codes, general statements can be made. The variance reduced model shows improvement over the standard

FMC model, but the computational gains are not nearly as impressive as for the monatomic variance reduced model. Recall that in the monatomic case (Section 4.5), standard FMC had computation times 10-20x as long as the variance reduced model. When both rotational and vibrational energy are included however, those gains drop to ∼3.5x. DSMC computation times appear slower than variance reduced DVM for this specific homogeneous relaxation, but there is no indication that the trend would or would not hold for all conditions. However, a more in depth analysis reveals nearly 45% of computational effort in DVM is spent on manipulation of rotational and vibrational distribution arrays. This is due to the large number of internal (primarily rotational) energy levels. If the number of levels simulated by the discrete velocity method is reduced through some approximation such as level grouping, a significant increase in computational efficiency should be seen. However, optimization of the description of internal energy is outside the scope of this work and will be reserved for future investigations.

1D Shock at Mach 12 for N_2

The structure of internal energy distributions can be viewed at various locations in a shock profile in the discrete velocity method without additional effort. Such investigations may be important when calculating physical phenomena which are dependent on the internal energy distributions such as chemical reactions. The way these physical phenomena propagate through a flow may depend on differences between low and high speed particles, and the capability of modeling smooth internal energy distributions at every velocity location would become an important feature of the discrete velocity method.

A Mach 12 N_2 shock at a very low upstream temperature of 10K is used for this investigation. The low temperature removes vibrational energy from consideration, allowing the focus of the simulation to be on rotational energy.

The DVM results were simulated using a 1st order finite difference method in space with $\Delta x = 0.2$, 240 spatial grid points, and the boundary conditions at the left and right walls were a zero gradient boundary (Section 4.4.3) and a fixed property boundary (Section 4.4.2) respectively. The velocity domain was set with grid spacing of $\hat{\beta} = 0.3$, domain boundaries at $\hat{\eta}_x = [-5, 4]$ and $\hat{\eta}_{y,z} = [-4.5, 4.5]$, and the number of simulated collisions was calculated with $C_{AB} = 0.004$. Finally, a constant rotational relaxation number of $Z_r = 5$ was used. The simulation was run until it had reached a steady state solution with upstream and downstream properties as shown in Table 8.3, and the shock profiles show the expected structures and compare well to DSMC solutions. Figure 8.20 show profiles of scaled density, kinetic temperature, and rotational temperature.

Table 8.3: 1D shock conditions based on Rankine-Hugoniot calculations.

Property		**Upstream**	**Downstream**
M		12	0.385
n	$[1/m^3]$	5.0×10^{19}	2.90×10^{20}
u	$[m/s]$	773.72	133.55
T	$[K]$	10.0	289.4

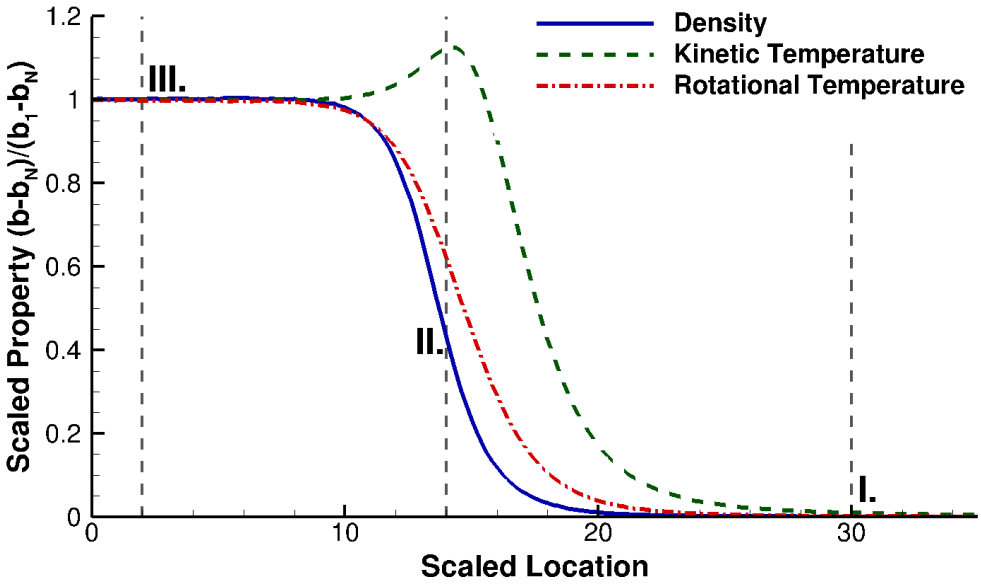

Figure 8.20: Normalized density and temperature profiles of a cold Mach 12 N_2 shock with downstream (I), upstream (III), and mid-shock (II) positions marked.

Three different spatial locations can be inspected to investigate how the rotational distribution changes as a function of location in the shock. The points chosen are upstream (I), at the shock midpoint (II), and downstream (III). Rotational distributions shown are summations over all velocity locations. Upstream of the shock shows a cold, fast velocity distribution function (Figure 8.21a) with a low energy rotational distribution also at equilibrium (Figure 8.21b). Downstream of the shock one finds a hot, slow velocity distribution function (Figure 8.22a) with an energetic rotational distribution in the form of an equilibrium Boltzmann distribution (Figure 8.22b). The shock midpoint show a "peanut" shaped velocity distribution function (Figure 8.23a) made up of components from the upstream and downstream distributions. The rotational distribution also seems to reflect both upstream and downstream

components (Figure 8.23b). Low energy rotational levels align with a slope similar to upstream conditions and high energy rotational levels align with a slope similar to downstream conditions.

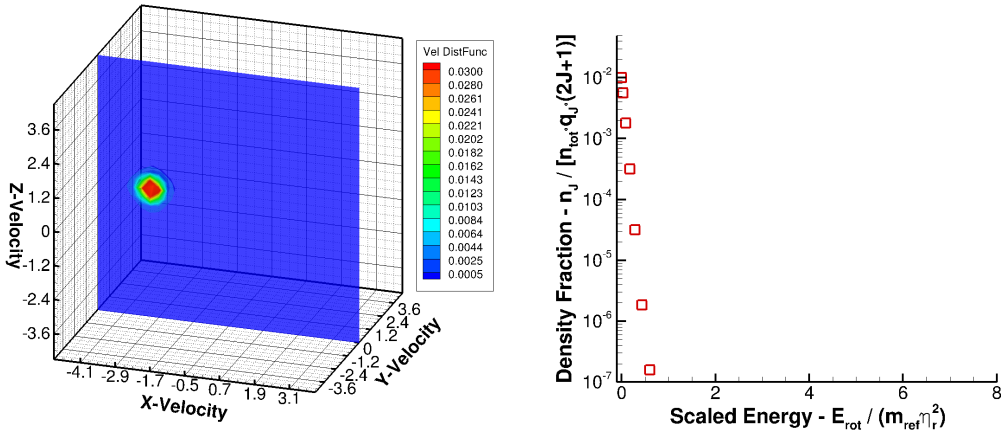

(a) (b)

Figure 8.21: Upstream of the shock (location III in Figure 8.20) (a) velocity distribution function and the (b) total rotational distribution. Flow is moving in the -x direction.

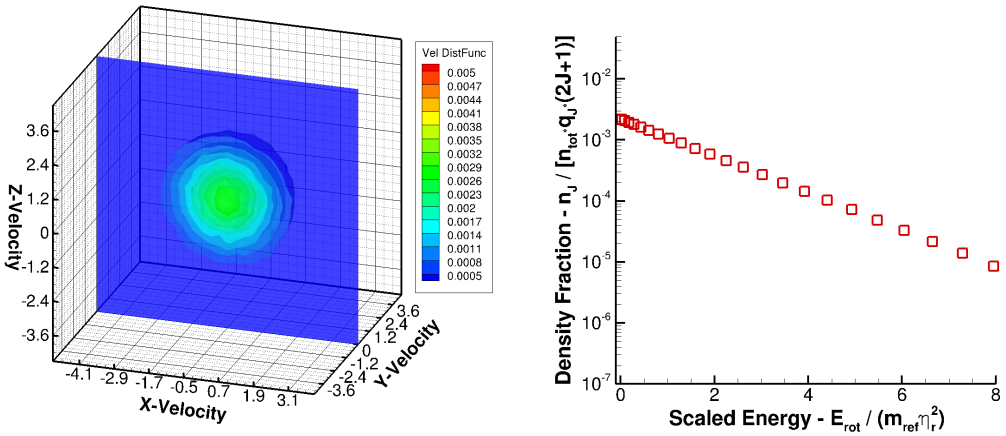

(a) (b)

Figure 8.22: Downstream of the shock (location I in Figure 8.20) (a) velocity distribution function and the (b) total rotational distribution. Flow is moving in the -x direction.

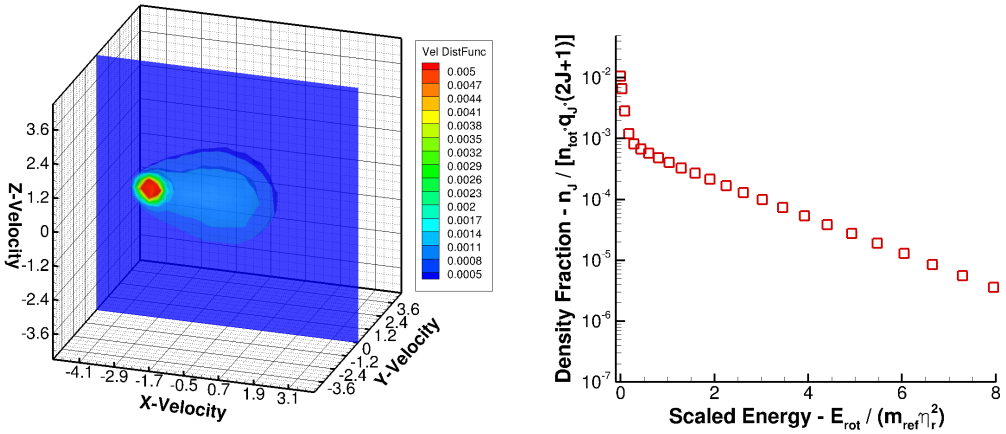

(a) (b)

Figure 8.23: Mid-shock (location II in Figure 8.20) (a) velocity distribution function and the (b) total rotational distribution. Flow is moving in the -x direction.

A more in-depth look at the shock midpoint in Figure 8.24 shows variations in the rotational distribution as a function of velocity location. Seven velocity locations are chosen: 3 located in the cold fast region of the velocity distribution function (A, B, and C), 3 located in the hot fast region (G, F, and E), and 1 in the neck between the two regions (D).

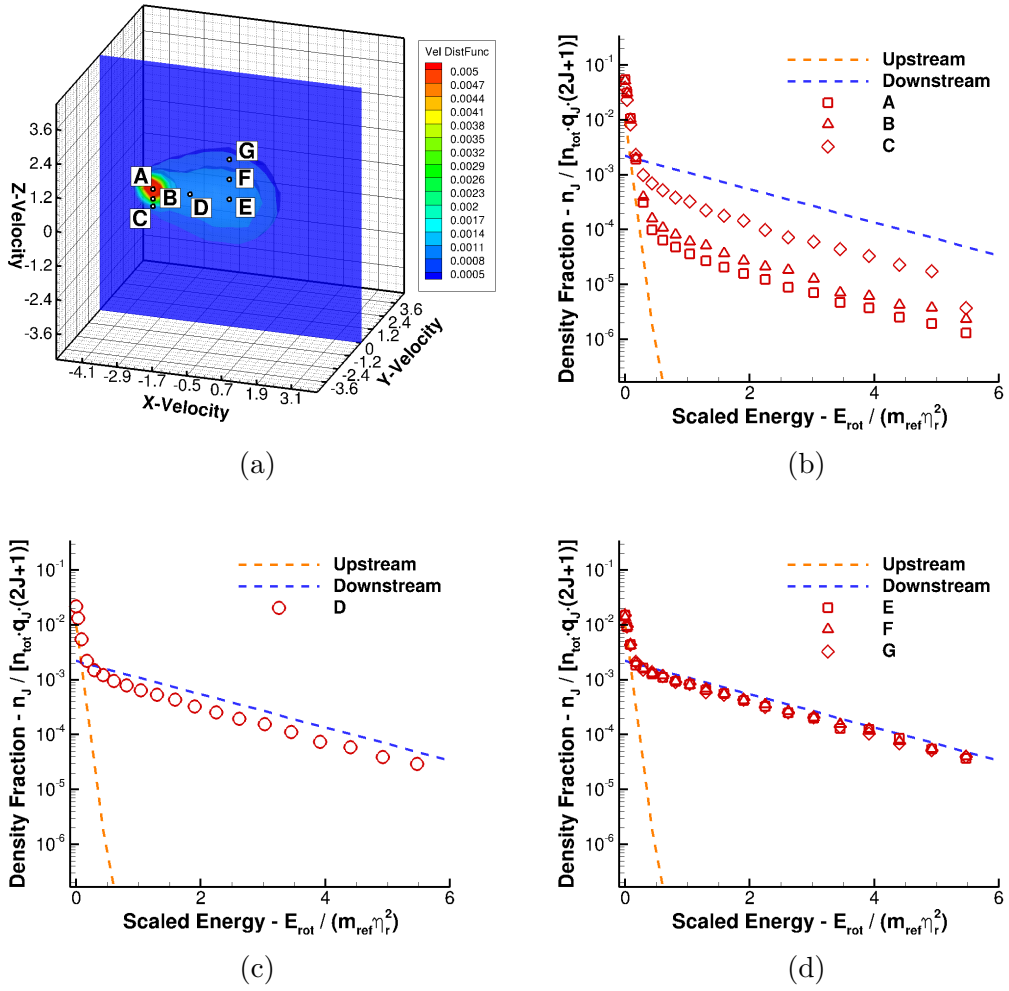

Figure 8.24: (a) Mid-shock velocity distribution function marked with velocity locations sampled for velocity dependent rotational distribution functions. (b) Sampled locations A-C, located in the cold, fast region of the velocity distribution. (c) Sampled location D, located in the middle part of the velocity distribution. (d) Sampled locations E-G, located in the hot, slow region of the velocity distribution.

Inspection of the rotational distributions at each point shows a wide range of distributions with similar shape in log space but orders of magnitude difference in density fraction value. All of the curves appear to be split into two distinct regions: a steeply sloped segment at low energies representative of a cold gas and a shallow sloped segment at higher energies representative of a hot gas. The distributions from upstream and downstream have been included in each of the figures, and it can be seen the rotational level populations appear to be a loose combination of the slopes of the upstream and downstream distributions with a curvature at the joint of the two lines. In Figure 8.24b, rotational distributions further from the center of the cold region of the velocity distribution function have a shorter steeply sloped segment than rotational distributions closer to the center. Meanwhile, points in the hot region of the velocity distribution function all have very similar rotational distributions despite their proximity to the center of the hot region. Note that while the results shown were for rotational distributions, a higher temperature shock with excited vibrational states could easily be imagined, and it is expected that vibrational distributions would follow similar trends to the rotational distributions for such a case.

A DSMC solution was not produced for the preceding simulation since only the capability of producing rotational distributions at particular velocity locations in DVM was of interest. Performing such an investigation with DSMC would require the available code to be rewritten to sample molecules at particular velocities, and in order to produce smooth distributions, either a very large number of simulated molecules would be required or rotational distributions would need to be built from an average over many time steps. Either way, it would be a very expensive operation.

8.5 Conclusions

In the preceding two chapters, the internal energy form of the Boltzmann equation was introduced as the Wang-Chang-Uhlenbeck equation, various energy exchange methods were discussed including Landau-Teller based models and the Larsen-Borgnakke model, and several energy level models were introduced including single valued rotation and quantized vibration and rotation. Furthermore, both full Monte Carlo and Variance Reduction collision models were developed for each energy level model. The methods were tested for a variety of different homogeneous relaxations and 1D shocks.

While fast solutions could be produced by the single value rotation formulation, it comes at the cost of removing information on the non-equilibrium nature of the rotational distribution. The single valued formulation also presented difficulties when the number density approached zero at a particular velocity location while the rotational energy stayed present. The combination of both issues led to the single value formulation for rotational energy to be discarded in favor of the quantized model.

A 1D shock was used to illustrate the capability of the discrete velocity method to visualize internal energy distributions at various spatial locations and for various velocity locations. The flexibility shown by the DVM code in accurately describing the distributions at these locations is an important feature of the method.

The largest concern for the quantized formulation is the relatively high cost of simulating the large number of levels that are populated at high temperatures. Future research should investigate methods for reduction in the rotational energy description with the purpose of decreasing the computational cost of simulations at high temperatures.

Chapter 9

Conclusions

In this chapter a summary will be made of the completed work, the range of inputs/variables needed by the algorithm will be discussed, an examination of the limits of the method will be made, and considerations for future work will be presented.

9.1 Summary

This work is focused on the development of a discrete velocity model for solving the Boltzmann equation with the capability to simulate a wide range of flow conditions. A variety of extensions to the method were implemented with a focus on either expanding physical models or increasing the computational efficiency of the algorithm, allowing for more complex flow conditions.

The basis of this work was inherited from A. Morris's Masters thesis research [5]. The original work was a simple method limited to a single, monatomic species interacting as pseudo-Maxwell molecules, and the velocity distribution function was approximated on a uniformly spaced velocity grid. The collision integral was solved with a variance reduced Monte Carlo model [6, 31], and post-collision molecules where mapped back onto the grid using a mass, momentum, and energy conservative scheme [7] first developed by Varghese [30].

The basic premise behind the discrete velocity method is characterized by defining the velocity distribution function only at discrete intervals

in velocity space. Each velocity location is assigned a variable weight quasi-particle which changes magnitude due to collisions or convection. Limiting the number of discrete velocities is advantageous by decreasing the number of quasi-particles stored in memory and restricting the number of possible velocity pairs in a collision event. Furthermore, the number of simulated collisions can be manipulated up or down to increase resolution of the velocity distribution function or decrease computational effort since the quasi-particles have no fixed mass value and the density involved in each collision is a floating point variable. The discretized velocity distribution function is then used as the framework for solving the full Boltzmann equation in an efficient and accurate manner. The equation is split into convection (left hand side) and collision (right hand side) parts, each is solved in sequence, and time is advanced.

Solving the collision integral is done through selecting a simulated collision weighted by the number density at each velocity location, depleting the appropriate number density adjusted by the total collision cross-section and relative velocity, determining a post-collision replenishing location, returning the number density in a manner which conserves mass, momentum, and energy, and finally repeating the process until a total number of simulated collisions has been reached. The number of simulated collisions is chosen to obtain a desired level of computational efficiency and stochastic noise, and the density depleted per collision is determined from the total depletion indicated by the collision term in the Boltzmann equation divided by the number of simulated collisions. Convection is performed using a finite difference method appropriate to the flow parameters and desired accuracy.

A variety of extensions to the method were implemented with a focus on either expanding physical models or increasing the computational efficiency of the algorithm, allowing for more complex flow conditions. Each extension was first implemented then tested against either known analytic solutions,

experimental trends, or another accepted computational method. Alongside a variety of minor improvements, the discrete velocity method presented in this PhD work includes the following major additions:

- Variable hard sphere (VHS) and variable soft sphere (VSS) collision models were implemented to model the collision cross-section of molecules. In both models, the probability of a collision occurring is adjusted by multiplying the depletion density by $\hat{g}\hat{\sigma}_T(\hat{g})$. VHS maintains isotropic scattering, but VSS has anisotropic scatting and requires further calculations when rotating the relative velocity vector during a collision. Results showed good agreement between the DVM algorithm and DSMC for 1D shock profiles using variable hard sphere, variable soft sphere, hard sphere, and pseudo-Maxwell molecules.

- A variety of new boundary conditions were added including diffuse and accommodated wall reflection. These additions were demonstrated using both Couette and Fourier channel flows. A range of Knudsen numbers showed property profiles which matched results from DSMC, LBE, and model solutions. A final result showed expansion into a vacuum capped by a diffuse wall. The simulation illustrated accurate modeling of very small property values and vacuum conditions.

- Using simple realignment of grid lines, non-uniform velocity grids were implemented with the intention of focusing computational effort in a more efficient manner. A Mach 9 shock displayed how simulations with large gradients in flow properties (velocity and temperature) through either space or time can be solved more efficiently using non-uniform grids.

- The method was extended to include gas mixtures. A major focus of this work was on mixtures with large number density or mass ratios.

Two flow conditions were used to test the validity of the improvement. A Mach 3.9 shock where the flow consisted of 3% Xe by molar fraction in a Xe-He mixture showed good agreement with a DSMC solution. A 0D relaxation where a trace amount of high speed He was mixed with stationary, room temperature Xe demonstrated the method's capability of modeling trace species with high importance to the flow.

- The final improvement to the discrete velocity method was the implementation of a quantized internal energy model where full rotational and vibrational distributions are stored and updated during elastic and inelastic collisions. Energy exchanges are calculated using a Larsen-Borgnakke scheme in the current work. Verification of full Monte Carlo and variance reduced methods was made comparing a homogeneous relaxation with numerical solutions of Jeans and Landau-Teller equations. A cold Mach 12 N_2 shock was simulated to illustrate DVM's ability to produce detailed information about the internal energy distributions easily and smoothly.

- Variance reduced formulations were associated with each of the preceding bullet points. Variance reduction methods reduce stochastic noise and the number of simulated collisions, especially in near-equilibrium flows. Results showed significant improvement for monatomic flows and flows with internal energy. However, the latter did not show as drastic an improvement as the former. Furthermore, it should be noted that for highly non-equilibrium flows variance reduction may actually be slower than the full Monte Carlo method.

Each of the improvements discussed above allow for more complex, more accurate, or a wider range of flow simulations by either expanding the physical complexity of the model or providing more efficient computations.

These are significant building blocks in the development of a complete model which can be considered competitive with other flow solvers across a wide range of conditions.

9.2 Future Work

The DVM code has a number of major improvements to its physical models that must be made before a complex, realistic flow simulation can be performed. Improvements may also be made to the code itself that will allow for more efficient solutions.

- *Complex 2D and 3D geometries with non-perpendicular boundaries*: The current method has been restricted to homogeneous relaxations and 1D flows, and expansion to more complex geometry will allow for a much greater range of realistic flow simulations. The work may either focus on integrating the DVM code with a third party flow solver or the development of a DVM-specific flow solver.

- *Parallelization*: There is significant room for increases in computational speed by including multi-threading and/or multi-processor elements to the DVM code. The DVM algorithm would allow significant benefits if parallelized since the collision integral is solved independently at each spatial location in an explicit manner.

- *Oct-tree and other more complex velocity grids*: Non-uniform velocity grids where implemented, but they were restricted to simply stretching or shrinking the grid spacing at each point. Oct-tree or other complex grids could further reduce the number of points being modeled and reduce the amount of memory needed to store velocity grids and cumulative distribution functions. Memory reductions will allow for a greater number of spatial points and more complex geometries.

- *Adaptable Velocity Grids*: The introduction of adaptable velocity grids would help mitigate many of the issues due to large gradients in the distribution function and transient solutions. Velocity grid nodes could be focused on regions of the velocity distribution function with high number density, large gradients, or one of a variety of other measures. The adaptability could be done temporally or spatially, but in either case methods would need to be developed to handle convection between differently defined velocity grids.

- *Body forces*: Gravity, electromagnetic fields, and fictitious forces (centrifugal forces, etc) all have influences on molecules in many real world flows. Accurate modeling of these forces would greatly increase the range of available conditions.

- *Chemistry, ionization, electronic energy*: Molecular interactions go beyond simple elastic and inelastic collisions. Chemistry, ionization, and exchanges of electronic energy all effect the outcomes of many real world problems, and accurate modeling of this would be highly beneficial for the future of the method.

Along with the major subject areas, there are several improvements to the current method that should be made to improve the accuracy of the modeled processes or increase computational efficiency.

- *Polyatomic molecules with multiple vibrational modes*: In the current method, different vibrational modes would be treated as different species. Formulating an efficient and accurate method to account for different modes will be essential when modeling species such as CO_2 or H_2O.

- *State-to-state (improved) cross-section models*: As discussed previously, improved cross-section models would provide more accurate solutions not subject to the assumptions and inaccuracies of Larsen-Borgnakke.

- *Reduced energy level descriptions*: The current rotational and vibrational descriptions model every energy level up to a maximum cut-off value. Implementing an approximation where a reduced number of levels are used could greatly increase the computational speed of the code. These approximations would be used when exact representations of the internal energy distributions are unnecessary.

- *Spatial and temporal adaptability*: Changing the spatial grid spacing or temporal spacing as a simulation progresses could improve the efficiency of the DVM code.

Appendices

Appendix A

Gas Properties

The properties used in this work are based on data in Chapman and Cowling [14]. Diameters in Table A.1 are calculated for a VHS model at $T_d = 273$ K.

Table A.1: Molecular properties at 1 atm and 273 K.

Molecule	**mass** $\times 10^{-27}$ **[kg]**	**diameter** $\times 10^{-10}$ **[m]**	**viscosity index,** ω	α
He	6.65	2.33	0.657	1.26
Ar	66.3	4.17	0.811	1.40
Xe	218	5.74	0.85	1.44
H_2	3.34	2.92	0.67	1.35
N_2	46.5	4.17	0.738	1.36
O_2	53.12	4.07	0.773	1.40

The characteristic temperatures of rotation, vibration, and dissociation for several diatomic molecules are presented in Table A.2 [2].

Table A.2: Characteristic temperatures.

Molecule	Θ_r	Θ_v	Θ_d
H_2	85.4	6159	52000
N_2	2.88	3371	113500
O_2	2.07	2256	59500

Table A.3 shows the spectroscopic constants and the para-/ortho- nuclear spin statistical weights for several diatomic species used in this work. Spectroscopic constants were pulled from [124], and spin statistical weights can be found in [125].

Table A.3: Spectroscopic constants and nuclear spin statistical weights.

Molecule	ω_e	-$\omega_e\chi_e$	B_e	-D_e	q_{even}	q_{odd}
H_2	4401.213	121.336	60.8530	1.6×10^{-2}	1	3
N_2	2358.57	14.324	1.99824	5.8×10^{-6}	6	3
O_2	1580.161	11.9513	1.44562	4.8×10^{-6}	0	1

Table A.4 shows constants used to evaluate the rotational relaxation according to Parker's model [126] and constants used to evaluate the vibrational relaxation according to Bird [2] for N_2 and O_2.

Table A.4: Constants for rotational and vibrational relaxation rate calculations.

Molecule	Z_∞	T^*	$C_{v,1}$	$C_{v,2}$
N_2	15.7	80.0	9.1	220.0
O_2	14.4	90.0	56.5	153.5

Appendix B

Evaluation of the Depletion Integral Term

Direct (N^2) computation of the collision integral is a prohibitively expensive operation so a statistical (Monte Carlo based) method is formulated instead.

B.1 Monatomic Full Monte Carlo

The depletion in a single time step due to collisions between velocity class $\hat{\eta}$ and velocity class $\hat{\zeta}$ can be directly determined from the discrete Boltzmann equation as:

$$\Delta\hat{\varphi}_{depl,AB}(\hat{\eta},\hat{\zeta}) = \frac{\Delta\hat{t}}{Kn}\cdot\hat{\varphi}_A(\hat{\eta})\cdot\hat{\varphi}_B(\hat{\zeta})\cdot\hat{g}\hat{\sigma}_T(\hat{g}) \tag{B.1}$$

In the statistical representation of the collision integral, colliding velocity pairs are chosen by a random draw from the cumulative distribution function. The depletion per collision, here called C, is chosen to be a function of the absolute number density, $\hat{n}-2\hat{n}_{neg}$, the signs of the colliding partners, the Knudsen number, the time step, and the relative velocity, $\hat{g}\hat{\sigma}_T(\hat{g})$.

$$\begin{aligned} C =& \Delta\hat{t}\cdot\hat{g}\hat{\sigma}_T(\hat{g})\cdot \\ & \left[\frac{(\hat{n}_A-2\hat{n}_{A,neg})\cdot(\hat{n}_B-2\hat{n}_{B,neg})\cdot sgn(\hat{\varphi}_A(\hat{\eta}))\cdot sgn(\hat{\varphi}_B(\hat{\zeta}))}{Kn\cdot N_c}\right] \end{aligned} \tag{B.2}$$

Given this depletion per collision, the total depletion due to collisions between particles with velocity classes $\hat{\eta}$ and $\hat{\zeta}$ in a single time step is given as the product of the depletion per collision, the number of simulated collisions, and the individual probabilities of $\hat{\varphi}_A(\hat{\eta})$ and $\hat{\varphi}_B(\hat{\zeta})$ being chosen for a collision.

$$\Delta\hat{\varphi}_{depl,AB}(\hat{\eta},\hat{\zeta}) = N_c \cdot P(\hat{\varphi}_A(\hat{\eta})) \cdot P(\hat{\varphi}_B(\hat{\zeta})) \cdot C \tag{B.3}$$

Where the probability of any single velocity class being chosen for a collision is the magnitude of the velocity distribution function at the velocity class over the absolute magnitude of all values of the velocity distribution function. If $\sum \hat{\varphi}(\hat{\zeta}) = \hat{n}$, then the sum over the absolute values is $\hat{n} - 2\hat{n}_{neg}$ where $\hat{n}_{neg} = \sum_{\ominus} \hat{\varphi}(\hat{\zeta})$ is the total negative number density in the velocity distribution function.

$$P(\hat{\varphi}(\hat{\eta})) = \frac{|\hat{\varphi}(\hat{\eta})|}{\sum_{\hat{\zeta}} |\hat{\varphi}(\hat{\zeta})|} = \frac{\hat{\varphi}(\hat{\eta}) \cdot sgn(\hat{\varphi}(\hat{\eta}))}{\hat{n} - 2\hat{n}_{neg}} \tag{B.4}$$

Equation B.4 is then substituted into equation B.3.

$$\begin{aligned} &\Delta\hat{\varphi}_{depl,AB}(\hat{\eta},\hat{\zeta}) = \\ &\Delta\hat{t} \cdot N_c \cdot \frac{\hat{\varphi}_A(\hat{\eta}) \cdot sgn(\hat{\varphi}_A(\hat{\eta}))}{\hat{n}_A - 2\hat{n}_{A,neg}} \cdot \frac{\hat{\varphi}_B(\hat{\zeta}) \cdot sgn(\hat{\varphi}_B(\hat{\zeta}))}{\hat{n}_B - 2\hat{n}_{B,neg}} \cdot \hat{g}\hat{\sigma}_T(\hat{g}) \cdot \\ &\left[\frac{(\hat{n}_A - 2\hat{n}_{A,neg}) \cdot (\hat{n}_B - 2\hat{n}_{B,neg}) \cdot sgn(\hat{\varphi}_A(\hat{\eta})) \cdot sgn(\hat{\varphi}_B(\hat{\zeta}))}{Kn \cdot N_c}\right] \end{aligned} \tag{B.5}$$

Finally, reducing equation B.5 results in the depletion in a single time step due to simulated collisions using the discrete velocity method; a function equivalent to equation B.1.

$$\boxed{\Delta\hat{\varphi}_{depl,AB}(\hat{\eta},\hat{\zeta}) = \frac{\Delta\hat{t}}{Kn} \cdot \hat{\varphi}_A(\hat{\eta}) \cdot \hat{\varphi}_B(\hat{\zeta}) \cdot \hat{g}\hat{\sigma}_T(\hat{g})} \tag{B.6}$$

The proof shown is for collisions between two unlike species using a full Monte Carlo method. If written for like species, a factor of 2 must be included in equation B.5 to account for double counting, and a factor of 1/2 is included in equation B.2.

For the variance reduced model, the proof also holds for each collision integral (equilibrium-deviation and deviation-deviation) by substituting $\hat{n} - 2\hat{n}_{neg} = \hat{n}^d$ and recognizing $\sum |\hat{\varphi}^d(\hat{\zeta})| = \hat{n}^d$ for the deviation array, and

substituting $\hat{n} - 2\hat{n}_{neg} = \hat{n}^E$ and recognizing $\sum |\hat{\varphi}^E(\hat{\zeta})| = \hat{n}^E$ for the equilibrium array.

B.2 Diatomic Variance Reduction

The statistical method for evaluation of the collision integral with quantized rotational and vibrational energy follows the structure seen above in Appendix B.1. The version of the method presented is for a variance reduced, deviation-deviation, collision term between unlike species, and the probability $P(\hat{g}, JK\nu\iota \rightarrow \hat{g}', J'K'\nu'\iota')$ is accounted for during replenishment except for a VHS component, $\hat{\sigma}_T(\hat{g})$.

Elastic Collisions

The depletion in a single time step due to elastic collisions between velocity class $\hat{\eta}$ and velocity class $\hat{\zeta}$ can be directly determined as:

$$\Delta\hat{\varphi}^{d-d}_{AB}(\hat{\eta}, \hat{\zeta})\Big|_{depl} = \frac{\Delta\hat{t}}{Kn} \cdot \hat{\varphi}^d_A(\hat{\eta}) \cdot \hat{\varphi}^d_B(\hat{\zeta}) \cdot \hat{g}\hat{\sigma}_T(\hat{g}) \cdot P_{elastic} \tag{B.7}$$

Where $P_{elastic}$ is the probability of a collision being elastic, and it is a function of the inelastic relaxation numbers and the degrees of freedom of each mode. As presented in Section 8.4.2, the depletion per collision is assumed to be a function of the sum of rotational and vibrational deviation densities, and is adjusted by the depletion splitting process to be:

$$C = \Delta\hat{t} \cdot \hat{g}\hat{\sigma}_T(\hat{g}) \cdot \left[\frac{\hat{n}^d_{rv,A} \cdot \hat{n}^d_{rv,B}}{Kn \cdot N_c}\right] \cdot P_{elastic} \tag{B.8}$$

And a final depletion for an individual collision is adjusted by D_A and D_B, the ratio between the deviation in the velocity distribution function and the total absolute density in the internal energy distributions ($\hat{\varphi}^d_{rv}$ is defined by equation 8.27).

$$C' = C \cdot D_A \cdot D_B = C \cdot \frac{\hat{\varphi}^d_A(\hat{\eta})}{\hat{\varphi}^d_{rv,A}(\hat{\eta})} \cdot \frac{\hat{\varphi}^d_B(\hat{\zeta})}{\hat{\varphi}^d_{rv,B}(\hat{\zeta})} \tag{B.9}$$

The total depletion due to collisions between deviation particles with velocity classes $\hat{\eta}$ and $\hat{\zeta}$ in a single time step is calculated from the probabilities of $\hat{\eta}$ and $\hat{\zeta}$ being chosen for a collision as:

$$\Delta\hat{\varphi}_{AB}^{d-d}(\hat{\eta},\hat{\zeta})\Big|_{depl} = N_c \cdot P(\hat{\varphi}_A^d(\hat{\eta})) \cdot P(\hat{\varphi}_B^d(\hat{\zeta})) \cdot C' \tag{B.10}$$

Where the probability of $\hat{\eta}$ being chosen is:

$$P(\hat{\varphi}_A^d(\hat{\eta})) = \frac{\hat{\varphi}_{rv,A}^d(\hat{\eta})}{\sum\limits_{\hat{\zeta}} \hat{\varphi}_{rv,A}^d(\hat{\zeta})} = \frac{\hat{\varphi}_{rv,A}^d(\hat{\eta})}{\hat{n}_{rv,A}^d} \tag{B.11}$$

Equations B.8 and B.10 are then substituted into equation B.11 to get:

$$\begin{aligned}\Delta\hat{\varphi}_{AB}^{d-d}\,(\hat{\eta},\hat{\zeta})\Big|_{depl} =& \Delta\hat{t} \cdot N_c \cdot \left[\frac{\hat{n}_{rv,A}^d \cdot \hat{n}_{rv,B}^d}{Kn \cdot N_c}\right] \cdot \hat{g}\hat{\sigma}_T(\hat{g}) \cdot P_{elastic} \cdot \\ & \frac{\hat{\varphi}_{rv,A}^d(\hat{\eta})}{\hat{n}_{rv,A}^d} \cdot \frac{\hat{\varphi}_{rv,B}^d(\hat{\zeta})}{\hat{n}_{rv,B}^d} \cdot \frac{\hat{\varphi}_A^d(\hat{\eta})}{\hat{\varphi}_{rv,A}^d(\hat{\eta})} \cdot \frac{\hat{\varphi}_B^d(\hat{\zeta})}{\hat{\varphi}_{rv,B}^d(\hat{\zeta})}\end{aligned} \tag{B.12}$$

Which can be reduced to equation B.7, showing the statistical model accurately represents the depletion per time step at each velocity location for elastic collisions.

Inelastic Collisions for R-T Energy Exchange

The total depletion over every rotational level due to inelastic collisions between $\hat{\eta}$ and $\hat{\zeta}$ can be directly determined as:

$$\Delta\hat{\varphi}_{AB}^{d-d}(\hat{\eta},\hat{\zeta})\Big|_{depl} = \frac{\Delta\hat{t}}{Kn} \cdot \hat{\varphi}_A^d(\hat{\eta}) \cdot \hat{\varphi}_B^d(\hat{\zeta}) \cdot \hat{g}\hat{\sigma}_T(\hat{g}) \cdot P(Z_{r,A}) \tag{B.13}$$

The depletion at a single rotational level due to inelastic collisions which exchange energy between rotational and translational modes must be accurately modeled using the statistical method if relaxation rates are to be matched. The depletion value is directly evaluated as:

$$\Delta\hat{\varphi}_{AB}^{d-d}(J,\hat{\zeta})\Big|_{depl} = \frac{\Delta\hat{t}}{Kn}\cdot\hat{\psi}_{A}^{d}(J)\cdot\hat{\varphi}_{B}^{d}(\hat{\zeta})\cdot\hat{g}\hat{\sigma}_{T}(\hat{g})\cdot P(Z_{r,A}) \tag{B.14}$$

For a single R-T inelastic collision, the depletion per collision, C, is the same as in Appendix B.2 above, but the adjustment on each individual collision has a contribution of D from the particle not undergoing energy exchange and a contribution of A_r from the particle undergoing an R-T energy exchange (the ratio between the rotational deviation and the total absolute deviation in rotational and vibrational distributions combined).

$$C' = C\cdot A_r\cdot D_B = C\cdot\frac{\hat{\varphi}_{r}^{d}(\hat{\eta})}{\hat{\varphi}_{rv,A}^{d}(\hat{\eta})}\cdot\frac{\hat{\varphi}_{B}^{d}(\hat{\zeta})}{\hat{\varphi}_{rv,B}(\hat{\zeta})} \tag{B.15}$$

The total depletion due to collisions between a deviation particle with a velocity class of $\hat{\eta}$ and rotational level J and a deviation particle with a velocity class of $\hat{\zeta}$ in a single time step is dependent on each velocity class being chosen and the probability of a particular rotational level being chosen:

$$\Delta\hat{\varphi}_{AB}^{d-d}(J,\hat{\zeta})\Big|_{depl} = N_c\cdot P(\hat{\varphi}_{A}^{d}(\hat{\eta}))\cdot P(\hat{\psi}_{r}^{d}(J))\cdot P(\hat{\varphi}_{B}^{d}(\hat{\zeta}))\cdot C' \tag{B.16}$$

Where the probability of any single velocity class being chosen is:

$$P(\hat{\varphi}_{A}^{d}(\hat{\eta})) = \frac{\hat{\varphi}_{rv,A}^{d}(\hat{\eta})}{\sum\limits_{\hat{\zeta}}\hat{\varphi}_{rv,A}^{d}(\hat{\zeta})} = \frac{\hat{\varphi}_{rv,A}^{d}(\hat{\eta})}{\hat{n}_{rv,A}^{d}} \tag{B.17}$$

And the probability of a rotational level J being chosen is:

$$P(\hat{\psi}_{r}^{d}(J)) = \frac{|\hat{\psi}_{r}^{d}(J)|}{\sum\limits_{J}|\hat{\psi}_{r}^{d}(J)|} = \frac{|\hat{\psi}_{r}^{d}(J)|}{\hat{\varphi}_{r}^{d}(\hat{\eta})}\Bigg|_{\hat{\eta}} \tag{B.18}$$

Equations B.15, B.17, and B.18 are substituted into equation B.16:

$$\Delta\hat{\varphi}_{AB}^{d-d}\left(\hat{\eta},\hat{\zeta}\right)\Big|_{depl} = \Delta\hat{t}\cdot N_c\cdot\left[\frac{\hat{n}_{rv,A}^{d}\cdot\hat{n}_{rv,B}^{d}}{Kn\cdot N_c}\right]\cdot\hat{g}\hat{\sigma}_T(\hat{g})\cdot \tag{B.19}$$
$$\frac{\hat{\varphi}_{rv,A}^{d}(\hat{\eta})}{\hat{n}_{rv,A}^{d}}\cdot\frac{|\hat{\psi}_{r}^{d}(J)|}{\hat{\varphi}_{r}^{d}(\hat{\eta})}\cdot\frac{\hat{\varphi}_{rv,B}^{d}(\hat{\zeta})}{\hat{n}_{rv,B}^{d}}\cdot\frac{\hat{\varphi}_{r}^{d}(\hat{\eta})}{\hat{\varphi}_{rv,A}^{d}(\hat{\eta})}\cdot\frac{\hat{\varphi}_{B}^{d}(\hat{\zeta})}{\hat{\varphi}_{rv,B}^{d}(\hat{\zeta})}$$

Which reduces to equation B.14, and when equation B.19 is summed over every J level, equation B.13 returned.

Appendix C

Non-Uniform Remapping

All derivations of the general remapping scheme begin from mass, momentum, and energy conservation along with a chosen relation between external points. The system of equations is then solved for post-collision fractions. Reference Figure 5.4 for the remapping stencil used in the following calculations.

C.1 Equal Density

The conservation equations for the case where equal density is mapped to each external point are:

$$f_0 + f_{i1} + f_{i2} + f_{i3} + 3f_{ext} = f_{\text{off}} \tag{C.1a}$$
$$\hat{\eta}_{i1} f_{i1} + \hat{\eta}_{e1} f_{ext} = \chi_1 f_{\text{off}} \tag{C.1b}$$
$$\hat{\eta}_{i2} f_{i2} + \hat{\eta}_{e2} f_{ext} = \chi_2 f_{\text{off}} \tag{C.1c}$$
$$\hat{\eta}_{i3} f_{i3} + \hat{\eta}_{e3} f_{ext} = \chi_3 f_{\text{off}} \tag{C.1d}$$
$$\hat{\eta}_{i1}^2 f_{i1} + \hat{\eta}_{i2}^2 f_{i2} + \hat{\eta}_{i3}^2 f_{i3} + (\hat{\eta}_{e1}^2 + \hat{\eta}_{e2}^2 + \hat{\eta}_{e3}^2) f_{ext} = (\chi_1^2 + \chi_2^2 + \chi_3^2) f_{\text{off}} \tag{C.1e}$$

First, the momentum equations can be rearranged as:

$$f_j = \frac{\chi_j f_{\text{off}} - \hat{\eta}_{ej} f_{ext}}{\hat{\eta}_{ij}}; \;\; j \in 1, 2, 3 \tag{C.2}$$

Substituted into equation C.1e:

$$\hat{\eta}_{i1}^2 \left(\frac{\chi_1 f_{\text{off}} - \hat{\eta}_{e1} f_{ext}}{\hat{\eta}_{i1}} \right) + \hat{\eta}_{i2}^2 \left(\frac{\chi_2 f_{\text{off}} - \hat{\eta}_{e2} f_{ext}}{\hat{\eta}_{i2}} \right) + \hat{\eta}_{i3}^2 \left(\frac{\chi_3 f_{\text{off}} - \hat{\eta}_{e3} f_{ext}}{\hat{\eta}_{i3}} \right) + (\hat{\eta}_{e1}^2 + \hat{\eta}_{e2}^2 + \hat{\eta}_{e3}^2) f_{ext} = (\chi_1^2 + \chi_2^2 + \chi_3^2) f_{\text{off}}$$

Reduced:

$$\begin{aligned}(\hat{\eta}_{e1}^2 + \hat{\eta}_{e2}^2 + \hat{\eta}_{e3}^2 - \hat{\eta}_{i1}\hat{\eta}_{e1} - \hat{\eta}_{i2}\hat{\eta}_{e2} - \hat{\eta}_{i3}\hat{\eta}_{e3})f_{ext} \\ = (\chi_1^2 + \chi_2^2 + \chi_3^2 - \chi_1\hat{\eta}_{i1} - \chi_2\hat{\eta}_{i2} - \chi_3\hat{\eta}_{i3})f_{\text{off}}\end{aligned}$$

And solved for f_{ext} as:

$$f_{ext} = \frac{f_{\text{off}} \sum_{j=1}^{3} [\chi_j(\chi_j - \hat{\eta}_{ij})]}{\sum_{j=1}^{3} [\hat{\eta}_{ej}(\hat{\eta}_{ej} - \hat{\eta}_{ij})]} \tag{C.3}$$

Since χ_j is always less than $\hat{\eta}_{ij}$ and $\hat{\eta}_{ij}$ is the opposite sign as $\hat{\eta}_{ej}$, it can be observed that f_{ext} will always be negative. f_{ij} may be found from equation C.2 now that f_{ext} has been defined, and the density mapped to the origin is simply:

$$f_o = f_{\text{off}} - f_{i1} - f_{i2} - f_{i3} - 3f_{ext} \tag{C.4}$$

C.2 Equal Momentum

A second option is to map equal momentum to each external point such that:

$$|\hat{\eta}_{e1}|f_{e1} = |\hat{\eta}_{e2}|f_{e2} = |\hat{\eta}_{e3}|f_{e3} \equiv M \tag{C.5}$$

The conservation equations under this condition become:

$$f_0 + f_{i1} + f_{i2} + f_{i3} + f_{e1} + f_{e2} + f_{e3} = f_{\text{off}} \tag{C.6a}$$

$$\hat{\eta}_{i1}f_{i1} + sgn(\hat{\eta}_{e1})M = \chi_1 f_{\text{off}} \tag{C.6b}$$

$$\hat{\eta}_{i2}f_{i2} + sgn(\hat{\eta}_{e2})M = \chi_2 f_{\text{off}} \tag{C.6c}$$

$$\hat{\eta}_{i3}f_{i3} + sgn(\hat{\eta}_{e3})M = \chi_3 f_{\text{off}} \tag{C.6d}$$

$$\hat{\eta}_{i1}^2 f_{i1} + \hat{\eta}_{i2}^2 f_{i2} + \hat{\eta}_{i3}^2 f_{i3} + (|\hat{\eta}_{e1}| + |\hat{\eta}_{e2}| + |\hat{\eta}_{e3}|)M = (\chi_1^2 + \chi_2^2 + \chi_3^2)f_{\text{off}} \tag{C.6e}$$

The momentum equations can be solved in terms of M as:

$$f_{ij} = \frac{\chi_j f_{\text{off}} - sgn(\hat{\eta}_{ej})M}{\hat{\eta}_{ij}}; \quad j \in 1,2,3 \tag{C.7}$$

And substituted into equation C.6e:

$$\begin{aligned}(\chi_1^2+\chi_2^2+\chi_3^2)f_{\text{off}} = & \\ & (sgn(\hat{\eta}_{e1})\hat{\eta}_{e1} + sgn(\hat{\eta}_{e2})\hat{\eta}_{e2} + sgn(\hat{\eta}_{e3})\hat{\eta}_{e3})M \\ & + \hat{\eta}_{i1}^2\left(\frac{\chi_1 f_{\text{off}} - sgn(\hat{\eta}_{e1})M}{\hat{\eta}_{i1}}\right) + \hat{\eta}_{i2}^2\left(\frac{\chi_2 f_{\text{off}} - sgn(\hat{\eta}_{e2})M}{\hat{\eta}_{i2}}\right) \\ & + \hat{\eta}_{i3}^2\left(\frac{\chi_3 f_{\text{off}} - sgn(\hat{\eta}_{e3})M}{\hat{\eta}_{i3}}\right)\end{aligned} \tag{C.8}$$

And recognizing $sgn(\eta_{ij}) = -sgn(\eta_{ej})$, the expression is reduced to:

$$\begin{aligned}(|\hat{\eta}_{i1}| + |\hat{\eta}_{i2}| + |\hat{\eta}_{i3}| + |\hat{\eta}_{e1}| + |\hat{\eta}_{e2}| + |\hat{\eta}_{e3}|)M & \\ = (\chi_1^2 - \chi_1\hat{\eta}_{i1} + \chi_2^2 - \chi_2\hat{\eta}_{i2} + \chi_3^2 - \chi_3\hat{\eta}_{i3})f_{\text{off}} &\end{aligned}$$

And finally M can be found as:

$$M = \frac{f_{\text{off}}\sum_{j=1}^{3}[\chi_j(\chi_j - \hat{\eta}_{ij})]}{\sum_{j=1}^{3}[|\eta_{ij}| + |\eta_{ej}|]} \tag{C.9}$$

With M defined, formulas for f_{ij}, f_o, and f_{ej} can be found as:

$$f_{ij} = \frac{\chi_j f_{\text{off}} + M}{|\hat{\eta}_{ij}|} \tag{C.10}$$

$$f_{ej} = \frac{M}{|\hat{\eta}_{ej}|} \tag{C.11}$$

$$f_o = f_{\text{off}} - \sum_{j=1}^{3}[f_{ij} + f_{ej}] \tag{C.12}$$

If the equation for M is inspected with the knowledge that $\hat{\eta}_{ij}$ will always have a greater magnitude and the same sign as χ_i, it can be seen that M will always be negative. This implies that the mass moved to the external points will always be negative as well.

C.3 Equal Energy

A final option is to map equal energy to each external point such that:

$$\hat{\eta}_{e1}^2 f_{e1} = \hat{\eta}_{e2}^2 f_{e2} = \hat{\eta}_{e3}^2 f_{e3} \equiv E \tag{C.13}$$

And the conservation equations under this condition become:

$$f_0 + f_{i1} + f_{i2} + f_{i3} + f_{e1} + f_{e2} + f_{e3} = f_{\text{off}} \tag{C.14a}$$

$$\hat{\eta}_{i1} f_{i1} + \frac{E}{\hat{\eta}_{e1}} = \chi_1 f_{\text{off}} \tag{C.14b}$$

$$\hat{\eta}_{i2} f_{i2} + \frac{E}{\hat{\eta}_{e2}} = \chi_2 f_{\text{off}} \tag{C.14c}$$

$$\hat{\eta}_{i3} f_{i3} + \frac{E}{\hat{\eta}_{e3}} = \chi_3 f_{\text{off}} \tag{C.14d}$$

$$\hat{\eta}_{i1}^2 f_{i1} + \hat{\eta}_{i2}^2 f_{i2} + \hat{\eta}_{i3}^2 f_{i3} + 3E = (\chi_1^2 + \chi_2^2 + \chi_3^2) f_{\text{off}} \tag{C.14e}$$

Rearranging momentum equations results in:

$$f_{ij} = \frac{\chi_j f_{\text{off}}}{\hat{\eta}_{ij}} - \frac{E}{\hat{\eta}_{ij}\hat{\eta}_{ej}}; \;\; j \in 1, 2, 3 \tag{C.15}$$

And equation C.15 can be substituted into equation C.14e:

$$-\hat{\eta}_{i1}\frac{E}{\hat{\eta}_{e1}} - \hat{\eta}_{i2}\frac{E}{\hat{\eta}_{e2}} - \hat{\eta}_{i3}\frac{E}{\hat{\eta}_{e3}} + 3E = (\chi_1^2 + \chi_2^2 + \chi_3^2 - \hat{\eta}_{i1}\chi_1 - \hat{\eta}_{i2}\chi_2 - \hat{\eta}_{i3}\chi_3) f_{\text{off}} \tag{C.16}$$

And reduced to:

$$E = \frac{f_{\text{off}} \sum_{j=1}^{3} [\chi_j (\chi_j - \hat{\eta}_{ij})]}{3 - \sum_{j=1}^{3} (\frac{\hat{\eta}_{ij}}{\hat{\eta}_{ej}})} \tag{C.17}$$

The origin, internal and external points can then be calculated as:

$$f_{ij} = \frac{1}{\hat{\eta}_{ij}} (\chi_j f_{\text{off}} - \frac{E}{\hat{\eta}_{ej}}) \tag{C.18}$$

$$f_{ej} = \frac{E}{\hat{\eta}_{ej}} \tag{C.19}$$

$$f_o = f_{\text{off}} - \sum_{j=1}^{3} (f_{ij} + f_{ej}) \tag{C.20}$$

Appendix D

Larsen-Borgnakke for Quantized Rotation

A quantized Larsen-Borgnakke model was originally formulated by Boyd in [94], and the most probable rotational level for both a rigid rotor and non-rigid rotor are re-derived here. The most probable rotational level is used to normalize the level probability equation (equation 7.48) in Larsen-Borgnakke energy exchange models. The most probable energy level is found from the combined rotation and translation distribution, $F(J)$, such that:

$$F(J) \propto (2J+1)(\hat{E}_c - \hat{E}_r(J))^{3/2-\omega} \tag{D.1}$$

By taking the derivative with respect to j (not J because in homonuclear molecules a substitution of J=f(j) is made):

$$\begin{aligned}\frac{\partial}{\partial j}F(J) = &\left[\frac{\partial}{\partial j}(2J+1)\right](\hat{E}_c - \hat{E}_r(J))^{3/2-\omega} \\ &+ (2J+1)(3/2-\omega)(\hat{E}_c - \hat{E}_r(J))^{1/2-\omega}\left[-\frac{\partial}{\partial j}\hat{E}_r(J)\right]\end{aligned} \tag{D.2}$$

And setting the result equal to 0:

$$2\left[\frac{\partial J}{\partial j}\right](\hat{E}_c - \hat{E}_r(J)) - (2J+1)(3/2-\omega)\left[\frac{\partial}{\partial J}\hat{E}_r(J)\frac{\partial J}{\partial j}\right] = 0 \tag{D.3}$$

Making a substitution of $a = 3/2 - \omega$ for convenience, and dividing each side by $\frac{\partial J}{\partial j}$ results in:

$$2(\hat{E}_c - \hat{E}_r(J)) - a \cdot (2J+1)\left[\frac{\partial}{\partial J}\hat{E}_r(J)\right] = 0 \tag{D.4}$$

Equation D.4 can be used for either rigid rotor or non-rigid rotor models through a substitution for $\hat{E}_r(J)$.

Rigid Rotor

The energy in each J level for a rigid rotor is:

$$\hat{E}_r(J) = B_e \cdot J(J+1) \tag{D.5}$$

And substituting equation D.5 into equation D.4 results in:

$$2\left[\hat{E}_c - B_e \cdot J(J+1)\right] - a \cdot (2J+1) \cdot B_e \cdot (2J+1) = 0 \tag{D.6}$$

The function can be divided by B_e:

$$2\left[\frac{\hat{E}_c}{B_e} - J(J+1)\right] - a \cdot (2J+1) \cdot (2J+1) = 0 \tag{D.7}$$

And rearranged into:

$$J^2 + J + \frac{a - 2\frac{\hat{E}_c}{B_e}}{2+4a} = 0 \tag{D.8}$$

Solving the formula for J gives:

$$J = nint\left\{\frac{1}{2}\left(-1 + \sqrt{\frac{1+\frac{4\hat{E}_c}{B_e}}{4-2\omega}}\right)\right\} \tag{D.9}$$

Non-Rigid Rotor

The energy in each J level for a non-rigid rotor is:

$$\hat{E}_r(J) = B_e \cdot J(J+1) - D_e \cdot J^2(J+1)^2 \tag{D.10}$$

And substituting equation D.10 into equation D.4 results in:

$$\begin{aligned} &2\left[\hat{E}_c - B_e \cdot J(J+1) + D_e \cdot J^2(J+1)^2\right] \\ &- a \cdot (2J+1)\left[B_e \cdot (2J+1) - D_e \cdot (4J^3 + 6J^2 + 2J)\right] = 0 \end{aligned} \tag{D.11}$$

Rearranging equation D.11 into a 4th order polynomial expression give:

$$\begin{aligned} &J^4(-8aD_e - 2D_e) + J^3(-16aD_e - 4D_e) \\ &\quad + J^2(4aB_e + 2B_e - 10aD_e - 2D_e) \\ &\quad + J(4aB_e + 2B_e - 2aDe) + (aB_e - 2\hat{E}_c) = 0 \end{aligned} \tag{D.12}$$

And making a substitution of $C = \frac{D_e}{B_e}$ results in a final formula:

$$\begin{aligned} &J^4C(8a + 2) + J^3C(16a + 4) + J^2(10aC + 2C - 4a - 2) \\ &\quad + J(2aC - 4a - 2) + (2\frac{\hat{E}_c}{B_e} - a) = 0 \end{aligned} \tag{D.13}$$

That can be solved for J as:

$$J = nint\left\{\frac{1}{2B} \cdot \left(\sqrt{B \cdot A} - B\right)\right\} \tag{D.14}$$

$$\begin{aligned} \text{Where} \quad A &= 4\sqrt{a^2(\frac{C^2}{4} + C + 1) - \frac{\hat{E}_c}{B_e}B + a + \frac{1}{4}} \\ &\quad + C(2a + 1) + 4a + 2 \\ \text{And} \qquad B &= C \cdot (4a + 1) \end{aligned}$$

The final expression for the most probable non-rigid rotor level is a complicated function requiring multiple square root calculations. However, it can be seen that the solutions for the rigid rotor and non-rigid rotor are very similar when calculated in Figure D.1 as function of E_c/B_e. The differences never exceed half a rotational level. Therefore, in the quantized Larsen-Borgnakke model implemented in this work, the rigid rotor solution is used for both rigid rotor and non-rigid rotor formulations.

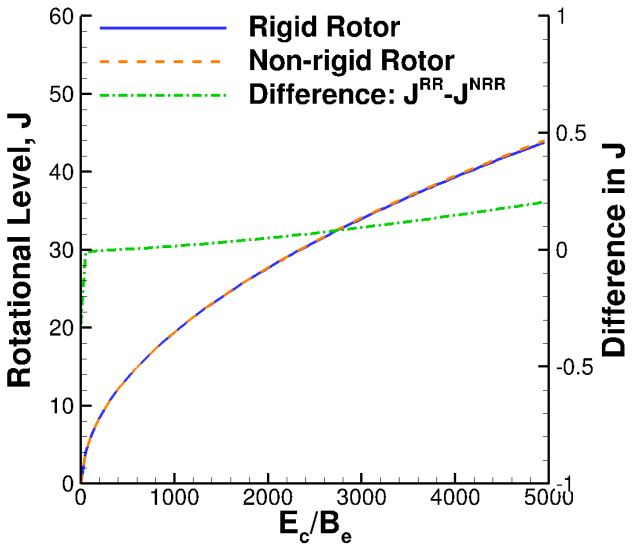

Figure D.1: Comparison of the most probable rotational level for rigid rotor and non-rigid rotor models.

Bibliography

[1] W. Vincenti and C. Kruger, *Introduction to Physical Gas Dynamics*. Malabar, FL: Krieger Publishing Company, 1965.

[2] G. Bird, *Molecular Gas Dynamics and the Direct Simulation of Gas Flows*, vol. 42 of *Oxford Engineering Science*. New York: Oxford University Press Inc., 1994.

[3] L. Baker and N. Hadjiconstantinou, "Variance reduction for Monte Carlo solutions of the Boltzmann equation," *Physics of Fluids*, vol. 17, no. 5, pp. 051703–1–4, 2005.

[4] T. Homolle and N. Hadjiconstantinou, "A low-variance deviational simulation Monte Carlo for the Boltzmann equation," *Journal of Computational Physics*, vol. 226, pp. 2341–2358, 2007.

[5] A. Morris, "Investigation of a discrete velocity Monte Carlo Boltzmann equation solver," Master's thesis, The University of Texas at Austin, 2009.

[6] A. Morris, P. Varghese, and D. Goldstein, "Variance reduction of a discrete velocity gas," in *Proceedings of the 27th International Symposium on Rarefied Gas Dynamics*, vol. 1333, (Pacific Grove, CA), pp. 952–957, AIP Conference Proceedings, 2010.

[7] A. Morris, P. Varghese, and D. Goldstein, "Improvement of a discrete velocity boltzmann equation solver with arbitrary post-collision velocities," in *Proceedings of the 27th International Symposium on Rarefied Gas Dynamics*, vol. 1084, (Pacific Grove, CA), pp. 458–463, AIP Conference Proceedings, 2010.

[8] C. Cercignani, *The Boltzmann equation and its application*. Berlin: Springer-Verlag, 1988.

[9] H. Grad, "On the kinetic theory of rarefied gases," *Comm. Pure and Appl. Math.*, vol. 25, pp. 331–407, 1949.

[10] P. Bhatnagar, E. Gross, and M. Krook, "A model for collision processes in gases. i. small amplitude processes in charged and neutral one-component systems," *Physical Review*, vol. 94, no. 3, pp. 511–525, 1954.

[11] E. Shakhov, "Kinetic model equations and numerical results," in *Rarefied Gas Dynamics* (H. Oguchi, ed.), pp. 137–148, Tokyo: University of Tokyo Press, 1984.

[12] B. Segal, "Shock-wave structure using nonlinear model boltzmann equation," *Physics of Fluids*, vol. 15, pp. 1233–1247, 1972.

[13] C. Cercignani, *Theory and Application of the Boltzmann Equation*. New York: Elsevier, 1975.

[14] S. Chapman and T. Cowling, *The Mathematical Theory of Non-Uniform Gases*. New York, NY: Cambridge University Press, third ed., 1970.

[15] C. Cercignani, *Rarefied Gas Dynamics, From Basic Concepts to Actual Calculations*. New York, NY: Cambridge University Press, 2000.

[16] L. Mieussens and H. Struchtrup, "Numerical comparison of bhatnagar-gross-krook models with proper prandtl number," *Physics of Fluids*, vol. 16, no. 8, pp. 2797–2813, 2004.

[17] L. Holway, "New statistical models for kinetic theory: methods of construction," *Physics of Fluids*, vol. 9, pp. 1958–1673, 1966.

[18] M. Krook, "On the solution of equations of transfer," *Astrophysical Journal*, vol. 122, pp. 488–497, 1955.

[19] E. Gross, "Recent investigations of the boltzmann equation," in *Proceedings for the 1st International Symposium on Rarefied Gas Dynamics* (F. Devienne, ed.), (New York, NY), pp. 139–150, Pergamon Press, Inc, 1960.

[20] J. Broadwell, "Study of rarefied shear flow by the discrete velocity method," *Journal of Fluid Mechanics*, vol. 19, pp. 401–414, 1964.

[21] J. Broadwell, "Shock structure in a simple discrete velocity gas," *Physics of Fluids*, vol. 7, pp. 1243–1247, 1964.

[22] S. Yen, "Numerical solution of the nonlinear Boltzmann equation for nonequilibrium gas flow problems," *Annual Review of Fluid Mechanics*, vol. 16, pp. 67–97, 1984.

[23] A. Nordsieck and B. Hicks, "Monte Carlo evaluation of the Boltzmann collision integral," in *Proceedings of the 5th International Symposium on Rarefied Gas Dynamics* (C. Brundin, ed.), vol. 1, pp. 695–710, AIP Conference Proceedings, 1966.

[24] V. Aristov and F. Tcheremissine, "The kinetic numerical method for rarefied and continuum gas flows," in *Rarefied Gas Dynamics* (e. a. Belotserkovskii, ed.), vol. 1, pp. 269–276, New York, NY: Plenum Press, 1985.

[25] Z. Tan, Y. Chen, P. Varghese, and J. Howell, "New numerical strategy to evaluate the collision integral of the boltzmann equation," in *Proceeding of the 16th International Symposium on Rarefied Gas Dynamics*, (Pasadena, CA), pp. 359–373, AIAA, 1988.

[26] T. Inamuro and B. Sturtevant, "Numerical study of discrete-velocity gases," *Physics of Fluids A*, vol. 2, no. 12, pp. 2196–2203, 1990.

[27] D. Goldstein, B. Sturtevant, and J. Broadwell, "Investigations of the motion of discrete-velocity gases," in *Proceedings of the 16th International Symposium on Rarefied Gas Dynamics*, (Pasadena, CA), pp. 100–117, AIAA, 1988.

[28] Z. Tan and P. Varghese, "The $\Delta-\epsilon$ method for the Boltzmann equation," *Journal of Computational Physics*, vol. 110, no. 2, pp. 327–340, 1994.

[29] D. Goldstein, "Discrete-velocity collision dynamics for polyatomic molecules," *Physics of Fluids*, vol. 4, no. 8, pp. 1831–1839, 1992.

[30] P. Varghese, "Arbitrary post-collision velocities in a discrete velocity scheme for the Boltzmann equation," in *Proceedings of the 25th International Symposium on Rarefied Gas Dynamics*, (St. Petersburg, Russia), AIP Conference Proceedings, 2006.

[31] A. Morris, P. Varghese, and D. Goldstein, "Monte Carlo solution of the Boltzmann equation via a discrete velocity model," *Journal of Computational Physics*, vol. 230, pp. 1256–1280, 2011.

[32] D. Hegermiller, "A new method to incorporate internal energy into a discrete velocity monte carlo boltzmann equation solver," Master's thesis, The University of Texas at Austin, 2011.

[33] D. Pullin, "Kinetic models for polyatomic molecules with phenomenological energy exchange," *Physics of Fluids*, vol. 21, no. 2, pp. 209–216, 1978.

[34] F. Tcheremissine, "Direct numerical solution of the boltzmann equation," in *Proceedings of the 24th International Symposium on Rarefied Gas Dynamics*, (Monopoli, Italy), AIP Conference Proceedings, 2004.

[35] V. Aristov and F. Tcheremissine, "Conservative splitting method for solving the boltzmann equation," *Computational Mathematics and Mathematical Physics*, vol. 20, pp. 208–225, 1980.

[36] V. Aristov and F. Tcheremissine, "Shock wave structure in a monatomic gas in the case of power-law interaction potentials," *Fluid Dyn.*, vol. 17, pp. 964–968, 1982.

[37] F. Tcheremissine, "Solution to the Boltzmann kinetic equation for high speed flows," *Computational Mathematics and Mathematical Physics*, vol. 46, no. 2, pp. 315–329, 2006.

[38] F. Tcheremissine, "Solution of the Boltzmann kinetic equation for low speed flows," *Transport Theory and Statistical Physics*, vol. 37, pp. 564–575, 2008.

[39] V. Kolobov, R. Arslanbekov, V. Aristov, A. Frolova, and S. Zabelok, "Unified solver for rarefied and continuum flows with adaptive mesh and algorithm refinement," *Journal of Computational Physics*, vol. 223, pp. 589–608, 2007.

[40] O. Dodulad and F. Tcheremissine, "Multipoint conservative projection method for computing the boltzmann collision integral for gas mixtures," in *Proceedings of the 28th International Symposium on Rarefied Gas Dynamics*, vol. 1501, (Zaragosa, Spain), pp. 302–309, AIP Conference Proceedings, 2012.

[41] F. Tcheremissine, "Method for solving the boltzmann kinetic equation for polyatomic gases," *Computational Mathematics and Mathematical Physics*, vol. 52, no. 2, pp. 252–268, 2012.

[42] V. Aristov, *Direct Methods for Solving the Boltzmann Equation and Study of Nonequilibrium Flows*. Boston, MA: Kluwer Academic Publishers, 2001.

[43] K. Nanbu, "Direct simulation scheme derived from the boltzmann equation. i. monocomponent gases," *Journal of the Physical Society of Japan*, vol. 49, no. 5, pp. 2042–2049, 1980.

[44] H. Babovsky and H. Neunzert, "On a simulation scheme for the boltzmann equation," *Mathematical Methods in the Applied Sciences*, vol. 8, no. 1, pp. 223–233, 1986.

[45] G. Bird, *The DSMC Method*. Sydney, Australia: CreateSpace Independent Publishing Platform, 2013.

[46] D. Hash and H. Hassan, "Two-dimensional coupling issues of hybrid dsmc/navier-stokes solvers," *AIAA*, pp. 97–2507, 1997.

[47] M. Ivanov, A. Kashakovsky, S. Gimelshein, and G. Markelov, "SMILE system for 2D/3D DSMC," in *Proceedings of the 25th International Symposium on Rarefied Gas Dynamics*, (St. Petersburg, Russia), AIP Conference Proceedings, 2006.

[48] M. Ivanov and S. Gimelshein, "Computational hypersonic rarefied flows," *Annual Review of Fluid Mechanics*, vol. 30, pp. 469–505, 1998.

[49] G. Radtke, N. Hadjiconstantinou, and W. Wagner, "Low-noise monte carlo simulation of the variable hard sphere gas," *Physics of Fluids*, vol. 23, no. 3, 2011.

[50] J. Chun and D. Koch, "A direct simulation of monte carlo method for rarefied gas flows in the limit of small mach number," *Physics of Fluids*, vol. 17, p. 107107, 2005.

[51] H. Al-Mohssen and N. Hadjiconstantinou, "Low-variance direct monte carlo simulations using importance weights," *ESAIM*, vol. 44, pp. 1069–1083, 2010.

[52] N. Hadjiconstantinou, G. Radtke, and L. Baker, "On variance reduced simulations of the boltzmann transport equation for small-scale heat transfer applications," *Journal of Heat Transfer*, vol. 132, p. 112401, 2010.

[53] U. Frisch, B. Hasslacher, and Y. Pomeau, "Lattice-gas automata for the navier-stokes equation," *Physical Review Letters*, vol. 56, no. 14, pp. 1505–1508, 1986.

[54] S. Succi, *The Lattice Boltzmann Equation for Fluid Dynamics and Beyond*. Numerical Mathematics and Scientific Computation, Oxford University Press Inc., 2001.

[55] G. McNamara and G. Zanetti, "Use of the boltzmann equation to simulate lattice-gas automata," *Physical Review Letters*, vol. 61, no. 20, pp. 2332–2335, 1988.

[56] F. Higuera and J. Jimenez, "Boltzmann approach to lattice gas simulations," *Europhys. Lett.*, vol. 9, p. 663, 1989.

[57] F. Higuera, "Lattice gas simulation based on the boltzmann equation," in *Discrete Kinetic Theory, Lattice Gas Dynamics and Foundations of Hydrodynamics* (R. Monaco, ed.), p. 162, Singapore: World Scientific, 1989.

[58] F. Higuera, S. Succi, and R. Benzi, "Lattice gas dynamics with enhanced collisions," *Europhys. Lett.*, vol. 9, p. 345, 1989.

[59] A. Bobylev, "The method of the fourier transform in the theory of the boltzmann equation for maxwell molecules," *Dokl. Akad. Nauk SSSR*, vol. 225, no. 6, pp. 1041–1044, 1975. in Russian.

[60] A. Bobylev, "The theory of nonlinear spatially uniform boltzmann equation for maxwell molecules," *Soviet Sci. Rev. Sect. C Math. Phys. rev.*, vol. 7, 1988.

[61] L. Pareschi and B. Perthame, "A fourier spectral method for homogeneous boltzmann equations," *Transport Theory and Statistical Physics*, vol. 25, pp. 369–382, 1996.

[62] A. Bobylev and S. Rjasanow, "Fast deterministic method of solving the boltzmann equation for hard spheres," *European Journal of Mechanics B Fluids*, vol. 18, pp. 869–887, 1999.

[63] F. Filbet, C. Mouhot, and L. Pareschi, "Solving the boltzmann equation in $Nlog_2N^*$," *SIAM Journal of Scientific Computing*, vol. 28, no. 3, pp. 1029–1053, 2006.

[64] I. Gamba and S. Tharkabhushanam, "Spectral-lagrangian methods for collisional models of non-equilibrium statistical states," *Journal of Computational Physics*, vol. 228, no. 6, pp. 2012–2036, 2009.

[65] J. Haack and I. Gamba, "Conservative deterministic spectral boltzmann-poisson solver near the landau limit," in *Proceedings of the 28th International Symposium on Rarefied Gas Dynamics*, (Zaragosa, Spain), AIP Conference Proceedings, 2012.

[66] A. Heintz, P. Kowalczyk, and R. Grzhibovskis, "Fast numerical method for the Boltzmann equation on non-uniform grids," *Journal of Computational Physics*, vol. 227, pp. 6681–6695, 2008.

[67] A. Alekseenko and E. Josyula, "Deterministic solution of the Boltzmann equation using discontinuous Galerkin discretizations in velocity space," *Journal of Computational Physics*, 2013.

[68] A. Munafo, J. Haack, I. Gamba, and T. Magin, "A spectral-lagrangian boltzmann solver for a multi-energy level gas," *Journal of Computational Physics*, vol. 264, pp. 152–176, 2014.

[69] J. Haack and I. Gamba, "A conservative spectral method for the boltzmann equation with anisotropic scattering and the grazing collisions limit," *Journal of Computational Physics*, vol. 270, pp. 40–57, 2013.

[70] C. W. Chang and G. Uhlenbeck, "Transport phenomena in polyatomic gases," Tech. Rep. CM-681, University of Michigan, Ann Arbor, MI, July 1951.

[71] S. Dellacherie, "On the wang chang-uhlenbeck equation," *Discrete Continuous Dynamical Systems - Series B*, vol. 3, pp. 229–253, 2003.

[72] L. Waldmann, "Transporterscheinungen in gasen von mittlerem druck," *Handbuch der Physik*, vol. 12, pp. 295–514, 1958.

[73] R. Snider, "Quantum-mechanical modified boltzmann equation for degenerate internal states," *Journal of Chemical Physics*, vol. 32, p. 1051, 1960.

[74] J. Appleton and K. Bray, "The conservation equations for a non-equilibrium plasma," *Journal of Fluid Mechanics*, vol. 20, no. 4, pp. 659–672, 1964.

[75] C. Park, "Assessment of two-temperature kinetic model for ionizing air," *Journal of Thermophysics and Heat Transfer*, vol. 3, no. 3, pp. 233–244, 1989.

[76] C. Park, "The limits of two-temperature model," in *AIAA Paper 2012-911. 48th AIAA Aerospace Sciences Meeting including the New Horizons Forum and Aerospace Exposition*, (Orlando, FL), 2010.

[77] C. Park, *Nonequilibrium Hypersonic Aerothermodynamics*. New York, NY: John Wiley & Sons, 1990.

[78] P. Gnoffo, "Planetary-entry gas dynamics," *Annual Review in Fluid Mechanics*, vol. 31, pp. 459–494, 1999.

[79] G. Candler and R. MacCormack, "Computation of weakly ionized hypersonic flows in thermochemical nonequilibrium," *Journal of Thermophysics and Heat Transfer*, vol. 5, no. 3, pp. 266–273, 1991.

[80] P. Gnoffo, R. Gupta, and J. Shinn, "Conservation equations and physical models for hypersonic air flows in thermal and chemical nonequilibrium," Tech. Rep. 2867, NASA Technical Paper, Langley Research Center, Hampton, VA, February 1989.

[81] L. Landau and E. Teller, "Theory of sound dispersion," *Phys. Z. Sowjetunion*, vol. 10, no. 1, pp. 34–43, 1936. in German.

[82] M. Capitelli, C. Ferreira, B. Gordiets, and A. Osipov, *Plasma Kinetics in Atmospheric Gases*. New York, NY: Springer, 2000.

[83] S. Losev, "Two temperature chemical kinetics in gas dynamics," in *AIAA Fluid Dynamics Conference*, (Orlando, FL), pp. 1996–2026, 1996.

[84] A. Bultel, B. Cheron, A. Bourdon, O. Motapon, and I. Schneider, "Collisional-radiative model in air for earth re-entry problems," *Physics of Plasmas*, vol. 13, no. 4, p. 043502, 2006.

[85] C. Treanor, "Vibrational energy transfer in high energy collisions," *Journal of Chemical Physics*, vol. 43, no. 2, pp. 532–538, 1965.

[86] E. Kerner, "Note on the forced and damped oscillator in quantum mechanics," *Canadian Journal of Physics*, vol. 36, no. 3, pp. 371–377, 1958.

[87] I. Adamovich, S. Macheret, J. Rich, and C. Treanor, "Vibrational energy transfer rates using a forced harmonic oscillator model," *Journal of Thermophysics and Heat Transfer*, vol. 12, no. 1, pp. 57–65, 1998.

[88] I. Adamovich, "Three-dimensional analytic model of coupled vibrational-rotational-translational energy transfer in diatomic molecule collisions," in *AIAA SciTech: 52nd Aerospace Sciences Meeting*, (National Harbor, Maryland), American Institute of Aeronautics and Astronautics, 2014.

[89] I. Boyd and E. Josyula, "State resolved vibrational relaxation modeling for strongly nonequilibrium flows," *Physics of Fluids*, vol. 23, no. 5, p. 057101, 2011.

[90] J. Anderson, J. Foch, M. Shaw, R. Stern, and B. Wu, "Statistical theory of electronic energy relaxation," in *RGD: Proceedings of the 15th International Symposium on Rarefied Gas Dynamics*, (Grado, Italy), 1986.

[91] E. Josyula, C. Suchyta, I. Boyd, and P. Vedula, "Internal energy relaxation in shock wave structure," *Physics of Fluids*, vol. 25, p. 126102, 2013.

[92] C. Borgnakke and P. Larsen, "Statistical collision model for monte carlo simulation of polyatomic gas mixture," *Journal of Computational Physics*, vol. 18, pp. 405–420, 1975.

[93] K. Koura, "Statistical inelastic crosssection model for the monte carlo simulation of molecules with discrete internal energy," *Physics of Fluids A*, vol. 4, pp. 1782–1788, 1992.

[94] I. Boyd, "Relaxation of discrete rotational energy distributions using a monte carlo method," *Physics of Fluids*, vol. 5, pp. 2278–2286, 1993.

[95] F. Bergemann and I. Boyd, "New discrete vibrational energy model for the direct simulation monte carlo method," in *RGD: Proceedings of the 18th International Symposium on Rarefied Gas Dynamics*, (Vancouver, Canada), pp. 174–183, AIAA, 1992.

[96] D. Willauer and P. Varghese, "Direct simulation of rotational relaxation using state-to-state cross sections," *Journal of Thermophysics and Heat Transfer*, vol. 7, pp. 49–54, 1993.

[97] R. Jaffe, D. Schwenke, G. Chaban, and W. Huo, "Vibrational and rotational excitation and relaxation of nitrogen from accurate theoretical calculations," in *46th AIAA Aerospace Sciences Meeting and Exhibit*, (Reno, NV), p. 1208, AIAA, 2008.

[98] R. Jaffe, D. Schwenke, and G. Chaban, "Theoretical analysis of N_2 collisional dissociation and rotation-vibration energy transfer," in *47th AIAA Aerospace Sciences Meeting and Exhibit*, (Orlando, FL), p. 1569, AIAA, 2009.

[99] G. Chaban, R. Jaffe, D. Schwenke, and W. Huo, "Dissociation cross-sections and rate coefficients for nitrogen from accurate theoretical calculations," in *46th AIAA Aerospace Sciences Meeting and Exhibit*, (Reno, NV), p. 1209, AIAA, 2008.

[100] F. Esposito, C. Gorse, and M. Capitelli, "Quasi-classical dynamics calculations and state-selected rare coefficients for $H + H_2(v, j) \rightarrow 3H$ processes: application to the global dissociation rate under thermal equilibrium conditions," *Chemical Physics Letters*, vol. 303, no. 5, 1999.

[101] J. Kim, O. Kwon, and C. Park, "Master equation study and nonequilibrium chemical reactions for $H + H$ and $He + H_2$," *Journal of Thermophysics and Heat Transfer*, vol. 23, no. 3, pp. 443–453, 2009.

[102] J. Lennard-Jones *Cohesion. Proceedings of the Physical Society*, vol. 43, pp. 461–482, 1931.

[103] G. Bird, "Monte-carlo simulation in an engineering context," in *Proceedings of the 12th International Symposium on Rarefied Gas Dynamics*, (Charlottesville, VA), pp. 174–183, AIAA, 1981.

[104] K. Koura and H. Matsumoto, "Variable soft sphere molecular model for inverse-power-law or lennard-jones potential," *Physics of Fluids A*, vol. 3, no. 10, pp. 2459–2465, 1991.

[105] L. Boltzmann, "Weitere studien uver das warmegleichgewicht unter gasmolekulen," *Wiener Berichte*, vol. 66, pp. 275–370, 1872.

[106] J. Maxwell, "Illustrations of the dynamical theory of gases," *Philosophical Magazine, 4th Series*, vol. 19, pp. 19–32, 1860.

[107] A. Bobylev, "Exact solution of the Boltzmann equation," *(Russian) Dokl. Akad. Nauk SSSR*, vol. 25, pp. 1296–1299, 1975.

[108] M. Krook and T. T. Wu, "Exact solutions of the Boltzmann equation," *Physics of Fluids*, vol. 20, no. 10, pp. 1589–1595, 1977.

[109] J. Anderson, *Modern Compressible Flow*. New York, NY: McGraw-Hill, third ed., 2003.

[110] W. Marques, G. Kremer, and F. Sharipov, "Couette flow with slip and jump boundary conditions," *Continuum Mech. Thermodyn.*, vol. 12, pp. 379–386, 2000.

[111] P. Lopez and Y. Bayazitoglu, "An extended thermal lattice boltzmann model for transition flow," *International Journal of Heat and Mass Transfer*, vol. 65, pp. 374–380, 2013.

[112] M. Gallis, J. Torczynski, and D. Rader, "Normal solutions of the boltzmann equation for highly nonequilibrium fourier flow and couette flow," *Physics of Fluids*, vol. 18, p. 017104, 2006.

[113] M. Calvert and J. Baker, "Thermal conductivity and gaseous microscale transport," *Journal of Thermophysics and Heat Transfer*, vol. 12, no. 2, pp. 138–145, 1998.

[114] G. Springer, "Heat transfer in rarefied gases," in *Advances in Heat Transfer* (T. I. Jr. and J. Hartnett, eds.), vol. 7, pp. 163–218, New York, NY: Academic Press, 1971.

[115] P. Clarke, P. Varghese, and D. Goldstein, "A novel discrete velocity method for solving the Boltzmann equation including internal energy and variable grids in velocity space," in *Proceedings of the 28th International Symposium on Rarefied Gas Dynamics*, vol. 1501, (Zaragosa, Spain), p. 373, AIP Conference Proceedings, 2012.

[116] A. Bobylev and C. Cercignani, "Exact eternal solutions of the Boltzmann equation," *Journal of Statistical Physics*, vol. 106, no. 5/6, pp. 1019–1038, 2002.

[117] J. Maxwell, "On stresses in rarefied gases arising from inequalities of temperature," *Proceedings of the Royal Society of London*, vol. 27, pp. 304–308, 1878.

[118] V. Sofonea and R. Sekerka, "Diffuse-reflection boundary conditions for a thermal lattice boltzmann model in two dimensions: Evidence of temperature jump and slip velocity in microchannels," *Physical Review*, vol. 71, p. 066709, 2005.

[119] N. Singh, A. Gavasane, and A. Agrawal, "Analytical solution of plane couette flow in the transition regime and comparison with direct simulation monte carlo data," *Computers and Fluids*, vol. 97, pp. 177–187, 2014.

[120] P. Clarke, P. Varghese, and D. Goldstein, "Discrete velocity computations with stochastic variance reduction of the Boltzmann equation for gas mixtures," in *Proceedings of the 29th International Symposium on Rarefied Gas Dynamics*, vol. 1628, (Xi'an, China), p. 1032, AIP Conference Proceedings, 2014.

[121] A. Raines, "Study of a shock wave structure in gas mixtures on the basis of the boltzmann equation," *European Journal of Mechanics B Fluids*, vol. 21, pp. 599–610, 2002.

[122] A. Gmurczyk, M. Tarczynski, and Z. Walenta, "Shock wave structure in the binary mixtures of gases with disparate molecular masses," in *Proceeding of the 11th International Symposium on Rarefied Gas Dynamics*, pp. 333–341, AIP Conference Proceedings, 1979.

[123] J. Dunham, "The energy levels of a rotating vibrator," *Physical Review*, vol. 41, pp. 721–731, 1932.

[124] G. Herzberg, *Molecular Spectra and Molecular Structure*. New York, NY: D. Van Nostrand Company, Inc., second ed., 1950.

[125] J. Hollas, *Modern Spectroscopy*. West Sussex, England: John Wiley & Sons, fourth ed., 2004.

[126] J. Parker, "Rotational and vibrational relaxation in diatomic gases," *Physics of Fluids*, vol. 2, pp. 449–462, 1959.

[127] G. Chernyi, S. Losev, S. Macheret, and B. Potapkin, "Physical and chemical processes in gas dynamics: Physical and chemical kinetics and thermodynamics of gases and plasmas - volume ii," in *Progresses in Astronautics and Aeronautics*, vol. 197, AIAA, 2002.

[128] F. Robben and L. Talbot, "Experimental study of the rotational distribution function of nitrogen in a shock wave," *Physics of Fluids*, vol. 9, no. 4, pp. 653–662, 1966.

[129] F. Robben and L. Talbot, "Measurements of rotational temperatures in a low density wind tunnel," *Physics of Fluids*, vol. 9, no. 4, pp. 644–652, 1966.

[130] M. Panesi, R. Jaffe, D. Schwenke, and T. Magin, "Rovibrational internal energy transfer and dissociation of $N_2(^1\Sigma_g^+) - N(^4S_u)$ system in hypersonic flows," *Journal of Chemical Physics*, vol. 138, p. 044312, 2013.

[131] R. Millikan and D. White, "Systematics of vibrational relaxation," *Journal of Chemical Physics*, vol. 39, pp. 3209–3213, 1963.

[132] C. Park, "Problems of rate chemistry in the flight regimes of aeroassisted orbital transfer vehicles," in *AIAA 19th Thermophysics Conference*, (Snowmass, CO), AIAA, 1984.

[133] B. Haas. PhD thesis, Department of Aeronautics and Astronautics, Stanford University, 1990.

[134] F. Lumpkin, B. Haas, and I. Boyd *Physics of Fluids*, vol. 3, p. 2282, 1991.

[135] B. Haas, D. Hash, G. Bird, F. Lumpkin, and H. Hassan, "Rates of thermal relaxation in direct simulation monte carlo methods," *Physics of Fluids*, vol. 6, pp. 2191–2201, 1994.

[136] B. Haas, J. McDonald, and L. Dagum, "Models of thermal relaxation mechanics for particle simulation methods," *Journal of Computational Physics*, vol. 107, pp. 348–358, 1993.

[137] N. Gimelshein, S. Gimelshein, and D. Levin, "Vibrational relaxation rates in the direct simulation monte carlo method," *Physics of Fluids*, vol. 14, pp. 4452–4455, 2002.

[138] J. Burt and I. Boyd, "Rotational and vibrational nonequilibrium in a low diffusion particle method for continuum flow simulation," in *41st AIAA Thermophysics Conference*, (San Antonio, TX), p. 3743, AIAA, 2009.